The University Of Sheffield.

Investigation of the Optical and Mechanical Properties of III-V Semiconductor Nanowires

John Patrick Bradley

Submitted for the degree of Doctor of Philosophy

Department of Physics and Astronomy

February 2017

Abstract

This thesis concerns the theoretical and experimental study of three applications of III-V semiconductor nanowires. First, a detailed overview of the catalyst-free bottom-up growth of GaAs and InP nanowire arrays is presented. Control of nanowire radial and axial growth is demonstrated through tailoring of growth conditions and pre-growth fabrication methods.

The limits of the catalyst-free growth technique are then investigated, leading to the establishment of an approach which allows for nanowire cross-section morphology to be precisely controlled. GaAs/InGaAs nanowire axial heterostructures are grown with elongated cross-section, resulting in the emission of strongly linearly polarised light from the nanowire top-facet. This represents the first demonstration of emission polarisation control in bottom-up semiconductor nanowires and provides a promising route for realisation of position-controlled linearly polarised single photon sources for quantum information applications.

Control of nanowire morphology is also leveraged to enable investigation of the mechanical properties of catalyst-free GaAs nanowires with different cross-section aspect ratios. Bottom-up semiconductor nanowires show great promise as ultrasensitive nanomechanical resonators owing to their high structural quality and small motional mass. A slight random asymmetry in the hexagonal cross-section of regular nanowires which commonly arises as a result of small differences in the growth rates of the nanowire side facets, however, means that the direction of motion of the non-degenerate nanowire flexural modes cannot be determined *a priori*. It is demonstrated that the ability to manipulate nanowire cross-section morphology allows for deterministic control of the direction of nanowire motion at the growth stage.

Finally, a nanocavity design comprising an InP nanowire placed in a partially-etched GaAs photonic crystal slot waveguide is developed. Optimisation of the cavity design is performed using a combination of frequency-domain and FDTD simulations. After fabrication of photonic crystal slot waveguide devices using a top-down etching process, experimental realisation of the nanocavity design is achieved through nanomanipulation of individual nanowires deposited on the photonic crystal device substrate using an atomic force microscopy system. Such a cavity design provides potential for creation of high quality position-controlled nanowire photon sources integrated in GaAs photonic circuitry.

Acknowledgements

I have been very fortunate to study in the Low Dimensional Structures (LDSD) group in the Department of Physics and Astronomy at the University of Sheffield, and I would like to acknowledge a number of my colleagues whose significant input made writing this thesis possible.

I would firstly like to sincerely thank Andrew Foster for the considerable support, guidance and knowledge he has imparted throughout my PhD study. I would also like to thank Andrey Krysa for always making the time for nanowire growth in the MOCVD reactor, Rikki Coles for his MEEP and MPB expertise and introducing me to Linux, Igor Itskevitch for demonstrating the virtues of being methodical, Ben Royall for his time and effort in training me (and many others) how to use the EBL systems and also his continued support and guidance during those long periods of time I spent in the cleanroom, and Nic Mullin for all of the work he put in to establish a successful nanowire manipulation technique. I would also like to extend my gratitude to Kirsty Gardener, Joseph Maguire and Thomas Lyons for all of their experimental endeavour and the staff of the EPSRC National Centre for III-V Technologies, in particular Paul Fry, Ken Kennedy, Saurabh Kumar and Rob Airey.

Finally, I would like to thank Maurice Skolnick, the head of the LDSD group, for the opportunity to develop myself as a researcher in the company of experts, and acknowledge the tremendous support and guidance of my supervisor Luke Wilson, from whom I have learnt a great deal.

This thesis is dedicated to my family, for whom I will forever be *The Boy*

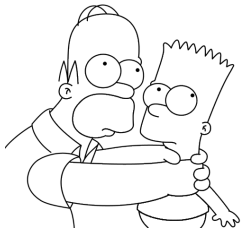

List of Publications

A.P. Foster, J.K. Maguire, **J.P. Bradley**, T.P. Lyons, A.B. Krysa, A.M. Fox, M.S. Skolnick and L.R. Wilson "*Tuning Nonlinear Mechanical Mode Coupling in GaAs Nanowires Using Cross-Section Morphology Control*" Nano Letters **16**(12), 414–7420 (2016)

A.P. Foster, **J.P. Bradley**, K. Gardner, A.B. Krysa, B. Royall, M.S. Skolnick and L.R. Wilson "*Linearly Polarized Emission from an Embedded Quantum Dot Using Nanowire Morphology Control*" Nano Letters **15**(3), 1559–1563 (2015)

J.P. Bradley, I.E. Itskevich, B. Royall, C. Bentham, N. Prtljaga, E. Clarke, A.M. Fox, M.S. Skolnick and L.R. Wilson "*Stark Tuning of Single Quantum Dots in an On-Chip Beam Splitter Device*" Oral Presentation, UK Semiconductors, Sheffield, UK, 2015

J.P. Bradley, A.P. Foster, M.N. Makhonin, K. Gardner, A.B. Krysa, B. Royall, P.W. Fry, T. Grange, T. Walther, M.S. Skolnick and L.R. Wilson "*Nano-Epitaxy as a Platform for Quantum Photonics*" Oral Presentation, ICPS, Austin, USA, 2014

J.P. Bradley, A.P. Foster, M.N. Makhonin, K. Gardner, A.B. Krysa, B. Royall, P.W. Fry, T. Grange, T. Walther, M.S. Skolnick and L.R. Wilson "*Nano-Epitaxy as a Platform for Quantum Photonics*" Oral Presentation, ICSNN, Savannah, USA, 2014

A.P. Foster, **J.P. Bradley**, M.N. Makhonin, A.B. Krysa, P.W. Fry, D.G. Davies, T. Grange, T. Walther, M.S. Skolnick and L.R. Wilson "*Nanowire-Embedded Quantum Light Emitters and Linearly Polarized Sources*" Oral Presentation, ICON2013, Annecy, France, 2013

A.P. Foster, **J.P. Bradley**, M.N. Makhonin, A.B. Krysa, B. Royall, P.W. Fry, T. Grange, T. Walther, M.S. Skolnick and L.R. Wilson "*Linearly Polarized Photon Emission from a Nanowire Heterostructure*" Poster Presentation, OECS2013, Rome, Italy, 2013

J.P. Bradley, A.P. Foster, M.N. Makhonin, A.B. Krysa, P.W. Fry, T. Grange, T. Walther, M.S. Skolnick and L.R. Wilson "*Position-controlled Quantum Light Emitters in Semiconductor Nanowire Arrays*" Oral Presentation, HETECH2013, Glasgow, UK, 2013

A.P. Foster, **J.P. Bradley**, M.N. Makhonin, A.B. Krysa, P.W. Fry, D.G. Davies, T. Grange, T. Walther, M.S. Skolnick and L.R. Wilson "*Quantum Light Emitters in Semiconductor Nanowire Arrays*" Oral Presentation, UK Semiconductors, Sheffield, UK, 2013

Contents

List of Figures

Chapter 1

Introduction

Owing to their reduced dimensionality, excellent structural properties and capability for assembly from the bottom-up, semiconductor nanowires have become the present focus of intense research interest for a wide range of fundamental and device physics. These include nanowire-based integrated photonic structures with potential for achieving efficient delivery of light to on-chip photonic circuitry [1–3] and nanowires as hosts for single photon sources [4–7] which are of great significance for a number of quantum information applications [8–10]. Research into nanowires has also been conducted for realisation of high brightness light emitting diodes [11], nanoscale lasers with efficient, directional and low-threshold emission [12], and ultra-sensitive vectorial force sensors [13, 14] which harness the exceptional mechanical properties of these structures. In addition, the large surface-to-volume ratio of nanowires has been exploited for a number of sensing applications [15, 16], while the ability to grow nanowires on lattice mismatched substrates provides a promising opportunity for monolithic integration of III-V semiconductors with silicon microelectronics [17, 18].

1.1 Properties of Semiconductor Nanowires

Nanowires may be defined as quasi-one dimensional columnar nanostructures, with a radial dimension of the order of nanometers and an unconstrained length, typically 1–10 µm. When formed from the bottom-up, they often exhibit a hexagonal cross-section, reflecting the crystal structure of the nanowire. If the diameter of the nanowire is sufficiently small, these structures can exhibit quantum confinement in two dimensions. For nanowires with large diameters (i.e. much greater than 100nm), the nanowire structure may influence optical and electrical properties via waveguiding and surface effects rather than by quantum confinement. Efficient waveguiding is of particular importance for lasing applications [12].

Semiconductor nanowires can be fabricated using either top-down or bottom-up approaches. The former typically begin with a bulk material from which nanowires are produced through a combination of lithography and etching, while in the latter, nanowires are formed most commonly using epitaxial growth techniques. Bottom-up growth is implemented in this work as it allows for the tuning of nanowire properties to a much greater extent than is possible using a completely top-down approach. Bottom-up growth also enables formation of nanowire structures with near atomically smooth surfaces, while the etching processes involved in top-down nanowire fabrication may result in damaged facets, which can adversely affect both the optical [19] and mechanical properties [20] of the final structures.

In addition to morphology, orientation and surface quality, the crystal structure of nanowires is an important consideration for device applications. Crystallographic imperfections can adversely impact the optical and mechanical properties of the nanowire which may limit the performance of nanowire-based devices. The nanowires grown during this course of research were formed from GaAs and InP on (111)B and (111)A oriented substrates, respectively using a catalyst-free bottom-up growth technique. Among the semiconductor materials available for nanowire growth, III-V materials show particular promise, owing to their superior opto-electrical properties, such as a direct bandgap and high electron mobility [21].

When grown in bulk, the crystal structure of both GaAs and InP adopts the zinc blende (ZB) arrangement [22]. For GaAs nanowires grown by the catalyst-free technique, the crystal structure is also typically (ZB). GaAs nanowires formed in this manner, however, usually contain rotational twinning planes, where a single crystal phase is rotated 180° about the (111) growth axis [23, 24]. A ZB twin can be thought of as a monolayer of wurtzite (WZ) crystal structure [25], and consecutive formation of twin planes in a ZB nanowire essentially forms a region of WZ nanowire. ZB and WZ have different bandgaps and electron affinities [26] and so there is a discontinuous band alignment at the interface between the two different crystal phases. The localisation of charge carriers that can result from this staggered type-II band alignment at the ZB-WZ interface may impair the optoelectronic performance of the nanowire structure. To date, there have been no reports of successful elimination of rotational twinning planes from GaAs nanowires grown in the (111)B direction by the catalyst-free technique.

Studies have shown that the structure of InP nanowires grown by the catalyst-free technique is generally different to that of GaAs. InP nanowires typically develop with the WZ crystal structure [27], but often consist of alternating WZ and ZB sections along the growth axis [28]. The resulting nanowires are therefore referred to as being polytypic. Polytypism is accompanied by a stacking fault perpendicular to the nanowire growth axis between the WZ and ZB crystal phases. It should be noted that the term stacking fault refers to a local interruption in the regular crystal stacking sequence that then continues in the same manner after the stacking fault, whereas a twinning plane results in a change of the crystal structure orientation and the stacking sequence is different before and after the twinning plane [29]. Like GaAs, the ZB and WZ crystal phases of InP have different bandgaps and electron affinities, which leads to a type-II band alignment in polytypic nanowires [30]. One consequence of this is that photoluminescence from polytypic nanowire structures spans a broad range of emission energies, due to radiative recombination occurring not only within a single crystal phase, but also between the two different crystal phases. In addition, it has been reported that the formation of alternating sections of different crystal phase along the nanowire length in this manner can also influence the mechanical properties of the nanowire structure [31].

1.2 Thesis Synopsis

This thesis focuses on the modelling and experimental study of III-V inorganic semiconductor nanowires and nanowire heterostructures produced using a selective-area catalyst-free growth approach. Three main applications are considered: nanowires as a means of tailoring the optical properties of quantum dots, nanowires as mechanical vectorial force sensors and nanowires as building blocks for future integrated photonic devices.

The extensive efforts undertaken to produce GaAs and InP nanowires by the catalyst-free growth technique are discussed in Chapter 2. Attempts at further developing the catalyst-free growth technique described in this chapter resulted in a new method by which to control the morphology of bottom-up GaAs nanowires. This morphology control is used to tailor the polarisation of emission from an embedded InGaAs structure in Chapter 3, and as a means of deterministically controlling the direction of motion of the flexural nanowire mechanical modes in Chapter 4. In Chapter 5, attempts at developing a moveable nanowire-based nanocavity arrangement consisting of an InP nanowire placed in the centre of a partially etched GaAs photonic crystal slot waveguide are discussed. Finally, Chapter 6 provides a summary of the conclusions drawn from each of the previous chapters and discusses the potential direction in which research in some of these areas can be continued.

Chapter 2

Growth of III-V Nanowire Arrays on (111) Substrates

2.1 Introduction

Semiconductor nanowires can be fabricated using a number of different approaches which are commonly grouped into two broad categories: top-down and bottom-up. Top-down methods typically begin with the deposition of a hard mask on a planar semiconductor wafer. A pattern determining the nanowire cross-section is transferred into the hard mask lithographically and nanowires are then produced via a subsequent top down etch using a highly anisotropic etchant [32, 33]. Although top-down methods are well established, a major downside of nanowire formation through this process is the potential development of etch damage on the nanowire sidewalls, which can negatively influence the optical [19] and mechanical [20] properties of the resulting structures. Bottom-up methods, on the other hand, involve the chemical synthesis of nanowires whose properties can be precisely controlled during growth. Bottom-up fabrication methods offer great scope in the tuning of nanowire characteristics, for instance through radial growth, and the ability to develop epitaxial quality surfaces, both of which are not possible with conventional top-down technologies.

The most commonly cited technique in the literature for bottom-up fabrication of semiconductor nanowires is the vapour-liquid-solid (VLS) mechanism, a catalyst-assisted process in which a nanoparticle (typically Au) is used to seed nanowire growth [34]. This process is depicted schematically in Figure 2.1(a). Initially, catalyst nanoparticles are deposited onto a suitable substrate surface, for instance a crystalline inorganic semiconductor (nanowire growth on non-crystalline substrates has also been demonstrated [35]). To initiate nanowire growth, gases or molecular beams containing suitable adatoms are then introduced over the surface of the heated substrate, incorporating within the molten catalyst nanoparticles and forming a supersaturated eutectic alloy. Following this, crystalline semiconductor precipitates out below the individual catalyst nanoparticles, leading to the formation of a nanowire structure at each nanoparticle site. Self-catalysed nanowire growth, in which the catalyst droplets are formed from a constituent element of the resulting nanowire structure (usually a group III element), has also been developed using a similar process [36].

The catalyst-free approach is an alternative bottom-up growth technique which enables nanowire formation without the use of a catalyst particle. In this approach, which is schematically depicted in Figure 2.1(b), a small aperture defined within a growth mask (e.g. SiO_2) deposited on a suitable semiconductor substrate surface is used to determine the nucleation site of the nanowire. When suitable adatoms are introduced to the surface, vertical free-standing nanowires are formed at the nucleation sites as a result of facet-dependent crystal growth rates [37, 38], provided the correct substrate crystal orientation is used. By relinquishing the need for a catalyst to drive nanowire growth, this approach offers a number of advantages over the VLS technique, including prevention of impurity incorporation in the nanowire from the catalyst [39, 40] and potential for higher quality interfaces in nanowire heterostructures, as nanowires formed via the VLS technique can be afflicted by the catalyst 'reservoir effect' [41, 42]. A number of heterointerfaces, such as quantum wells [43, 44], quantum dots [45] and radial core-shell structures [46, 47] have been realised to date using this growth approach, and devices that have been developed from the catalyst-free formation of nanowires include lasers [48, 49], light emitting diodes [50] and single photon sources [6, 7, 51]. Heterogeneous

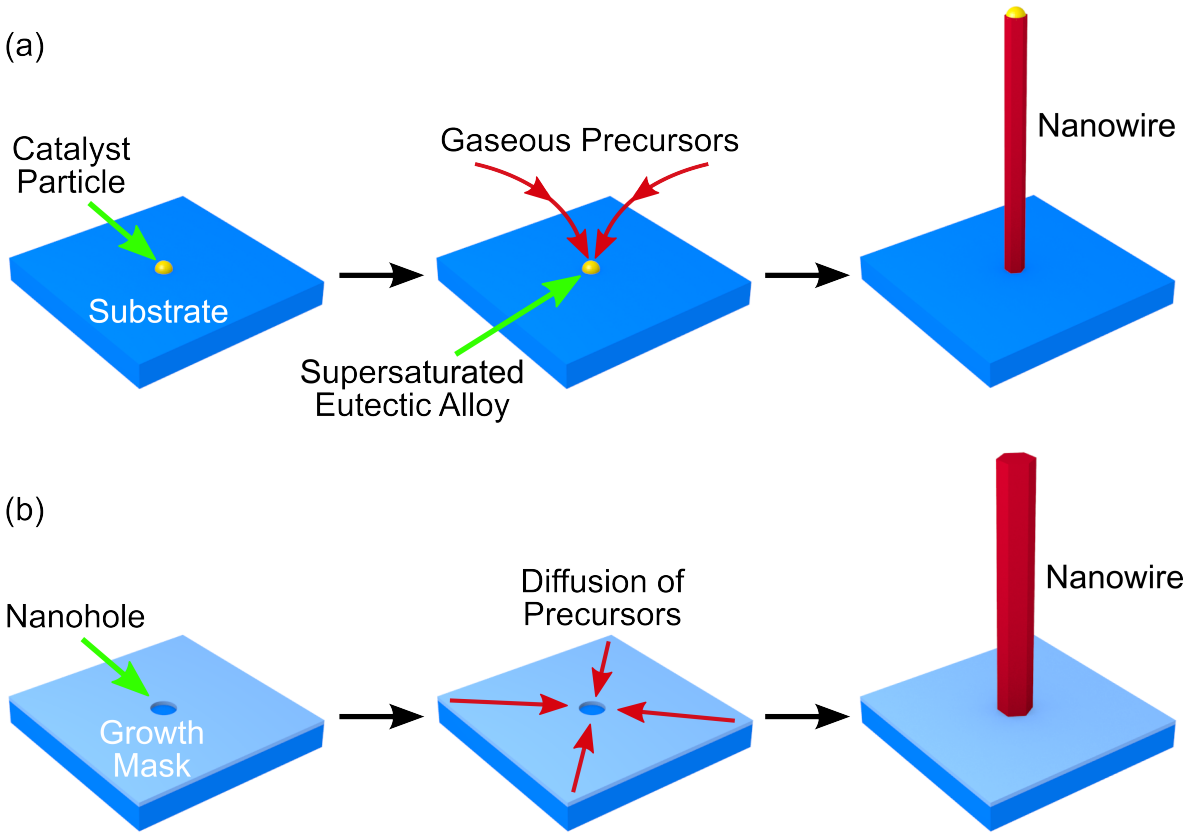

Figure 2.1: Overview of two main techniques employed for semiconductor nanowire growth. (a) Summary of the vapour-liquid-solid (VLS) growth mechanism. (left-to-right) A catalyst nanoparticle is deposited onto the substrate surface; Gaseous precursors containing the adatoms for initiation of growth incorporate within the molten catalyst at high temperature, forming a crystalline nanowire structure; As depicted here, the metal catalyst remains at the top of the nanowire after growth has been completed; (b) Summary of the catalyst-free procedure. (left-to-right) A small aperture is defined with a thin dielectric growth mask on a crystalline substrate; Precursors containing the adatoms for growth diffuse across the growth mask and incorporate within the aperture; a nanowire forms at the aperture site. Both growth processes depend on appropriate choice of growth conditions.

growth of nanowires on Si substrates using this technique has also been demonstrated, for example GaAs/AlGaAs on Si [52], InGaAs on Si [17, 18] and InAs on Si [53, 54]. The ability to form III-V nanowire structures on Si without anti-phase defects or misfit dislocations offers a promising route for the future monolithic integration of nanowire optoelectronic devices with established Si microelectronics technology.

In this chapter, the bottom-up epitaxial growth of GaAs and InP nanowires using selective area (catalyst-free) metal organic chemical vapour deposition (MOCVD) is described. Section

2.2 first provides an overview of the growth technique implemented for both III-V material systems. The details of the fabrication, growth process and characterisation of nanowires is then given for GaAs in Section 2.3 and InP in Section 2.4. Development of the GaAs nanowire growth approach discussed in this chapter allowed for the novel phenomena presented in Chapters 3 and 4, while growth studies performed with the InP materials system provided InP nanowires that were subsequently utilised for experimental studies of the nanowire-based nanocavity system presented in Chapter 5.

2.2 Overview of the Growth Technique

All of the III-V nanowire samples produced during this PhD project were grown by a catalyst-free MOCVD technique, wherein vertical nanowire structures were grown from nanoapertures in a thin SiO_2 dielectric film (~30nm) deposited on (111)B (for GaAs) and (111)A (for InP) orientated substrates. Nanoapertures were formed in square arrays using a combination of electron beam lithography (EBL) and reactive ion etching (RIE).

The fabrication procedure prior to nanowire growth and the growth process itself were both very similar for both GaAs and InP materials systems, and therefore, to minimise repetition, the pre-growth fabrication steps and growth scheme are described in detail only for GaAs nanowire growth on (111)B GaAs substrates in the following sections. For InP nanowire growth, only a brief overview of the notable differences in these processes is presented.

2.3 GaAs Nanowire Arrays on (111)B GaAs Substrates

In the following sections, the process by which selective-area GaAs nanowire arrays on partially masked (111)B GaAs substrates are formed is presented. First, the fabrication procedure used to prepare the (111)B substrates for nanowire growth is described. An overview of the

nanowire growth technique is then given, followed by a description of the growth parameters utilised for each nanowire growth in this instance. The structural properties of the grown nanowire samples are then discussed.

2.3.1 Fabrication of (111)B Substrates in Preparation for MOCVD Growth

2.3.1.1 Alignment Marker Development

The first pre-growth fabrication step involved the patterning and etching of alignment markers into a 2-inch diameter (111)B GaAs wafer. These markers were necessary to ensure accurate alignment between the wafer and the pattern exposed during EBL in a later fabrication step.

Fabrication began with the baking of a new wafer on a 100°C hotplate for 60s in order to evaporate any water on its surface. The wafer was then spin-coated with an optical resist, BPRS100, at ~4000rpm for 30s, to give a resist thickness of ~900nm (Figure 2.2(b)). It was then baked again for 5 minutes at 100°C to drive off the solvent in the spun resist. Alignment markers were transferred into the resist using a manual mask aligner system. The resist was exposed to ~300nm or ~400nm wavelength light through an optical mask for ~2s or ~10s, respectively (Figure 2.2(c)). For a particular resist thickness and exposure wavelength and time, the resolution of the transferred optical mask pattern depends primarily on the gap between the wafer and mask during exposure, and therefore minimising this gap as much as possible was attempted for each exposure run. However, as the gap size was manually controlled in the mask aligner system used in this instance, there was a possibility of unintentionally bringing the wafer into contact with the optical mask, resulting in smearing of the resist on the wafer and consequent contamination of the mask. To reduce the probability of this occurring here, the system settings that provided an appropriate wafer-mask separation for exposure were ascertained first using a bare 2-inch test wafer of similar thickness to that of the wafer being subsequently exposed.

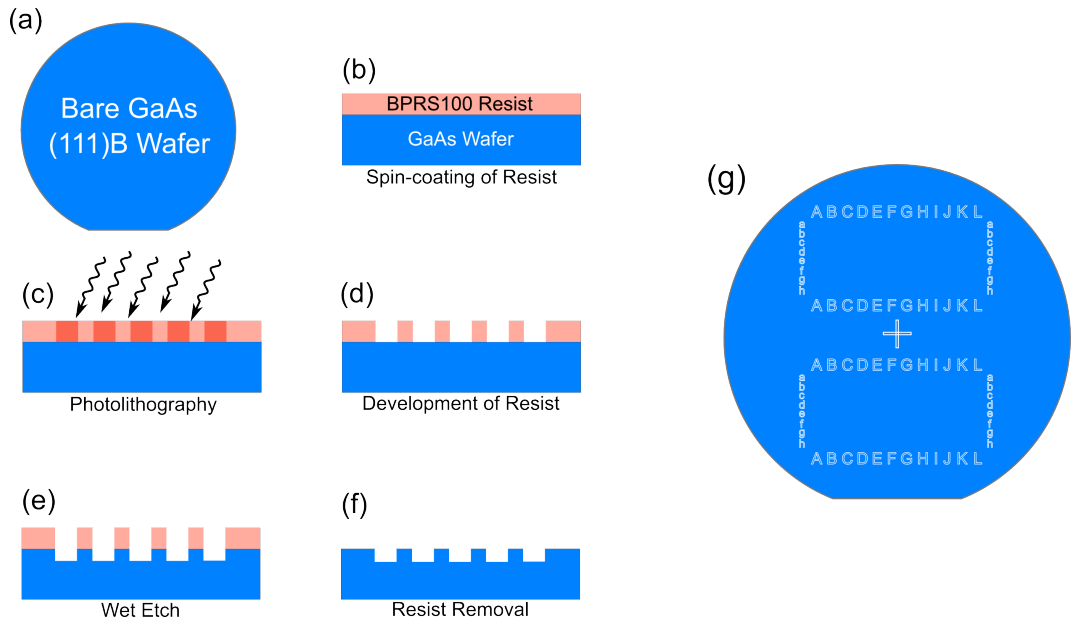

Figure 2.2: Schematic overview of the fabrication process used to produce alignment markers in a (111)B oriented GaAs wafer. (a) A bare GaAs wafer is (b) spin-coated with BPRS100 resist; (c) Photolithography is performed to expose the alignment marker pattern into the resist; (d) The resist is developed and exposed BPRS100 is removed; (e) The alignment marker pattern is transferred into the GaAs substrate using an acid echant; (f) The BPRS100 resist is removed. An overview of the alignment marker pattern produced after steps (b)–(f) is displayed in (g).

After pattern exposure, the BPRS100 resist was developed in a 3:1 H_2O:PLSI solution for 60s at room temperature (RT), with the wafer then rinsed in deionised (DI) water and dried with a nitrogen gun (Figure 2.2(d)). In an effort to ensure no resist remained in the exposed areas after developing, the wafer was then ashed in an oxygen plasma for 15s. Transfer of the mask pattern into the GaAs substrate was achieved by submerging the wafer in a 1:8:80 H_2SO_4:H_2O_2:H_2O etch solution for ~60s at RT (Figure 2.2(e)). The initial concentrations of H_2SO_4 and H_2O_2 were 98% and 30%, respectively, which, with these etching conditions, gave a typical etched marker depth of ~0.5µm. Confirmation of the etch depth was performed through the measurement of an etched feature using a Dektak surface profilometer. Where necessary, this etching step was repeated until the correct depth had been achieved. The remaining BPRS100 resist on the wafer was then removed using warm organic positve photoresist remover, EKC830 (Dow Chemical), followed by a rinse under running DI water and subsequent drying with nitrogen (Figure 2.2(f)).

2.3.1.2 SiO_2 Deposition and Square Definition

Plasma enhanced chemical vapour deposition (PECVD) of a ~30nm thick SiO_2 film on the wafer surface was then performed at 300°C, using SiH_4 and N_2O as the source gases and a RF power of 25W (Figure 2.3(a)). The role of this deposited film was to act as a growth mask, stimulating nanowire growth whilst restricting planar growth (as described in Section 2.3.2.2). Previous reports in the literature have shown that better control of selective area growth is achieved when the coverage of this deposited growth mask is reduced (below full coverage). For this reason the SiO_2 film was subsequently patterned into a set of individual squares with a side length of 130µm, using a similar combination of photolithography and wet etching that was presented in the previous section.

Before the spinning of BPRS100 in the fabrication procedure here, however, an adhesion promoter, Hexamethyldisilazane (HMDS) was first spun on the wafer for 30s at ~4000rpm to increase the adhesion of the BPRS100 to the previously deposited SiO_2 film. Photolithography was then performed with an optical mask consisting of a pattern that contained repeated 4 by 3 arrays of individual squares, which were not exposed during the exposure process. To ensure correct alignment of these patterned squares relative to the previously patterned alignment markers, this mask design also contained the same alignment marker pattern layout as that of the mask used in the previous lithography step. After exposure and subsequent developing of the resist, the exposed regions of the SiO_2 layer were removed by placing the wafer in a 1% solution of hydrofluoric acid (HF), followed by a DI water rinse and subsequent drying with nitrogen. The remaining BPRS100 resist on the wafer was then again removed using warm EKC830, followed by a rinse under running DI water and subsequent drying with nitrogen.

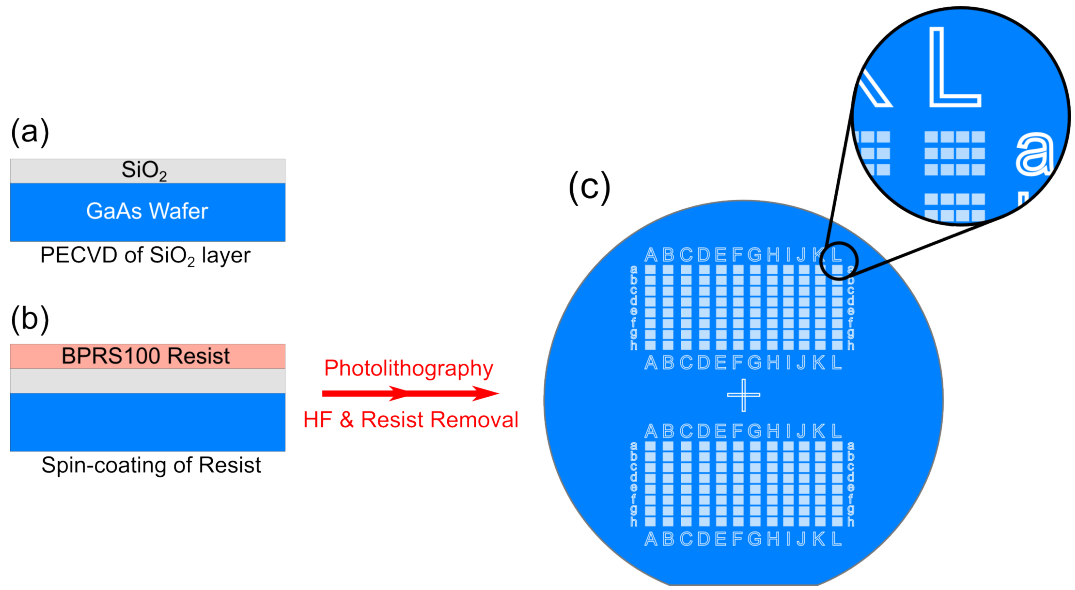

Figure 2.3: Definition of SiO_2 squares. (a) A thin SiO_2 layer is deposited onto the wafer using PECVD; (b) The wafer is spin coated with BPRS100 resist, and squares of SiO_2 are defined using photolithography and subsequent HF etching. The remaining resist is then removed; (c) Overview of SiO_2 square arrangement after steps (a)–(b), where each group of squares comprises 4 by 3 individual SiO_2 squares.

2.3.1.3 Nanohole Array Formation

After the second photolithography and etching process described above, the wafer was baked at 100°C for 60s and then spin-coated with an electron-sensitive resist, 1:2 anisole:poly(methyl methacrylate) (PMMA) at ~4000rpm for 30s, giving a resist thickness of ~90nm (Figure 2.4(a)). To drive off the remaining solvent in the resist after spin-coating, the wafer was then baked once more at 100°C for 5 minutes.

Square arrays of nanoholes, with a pitch of 4um, were then patterned into the resist using EBL* (Figure 2.4(b)). The electron accelerating voltage and beam aperture used for patterning was 30kV and 10um, respectively. A typical array in this design consisted of 20 by 20 nanoholes, all patterned with the same diameter. Between arrays, the diameter was varied, from 40nm upto 180nm.

*EBL system used for patterning – Raith 150.

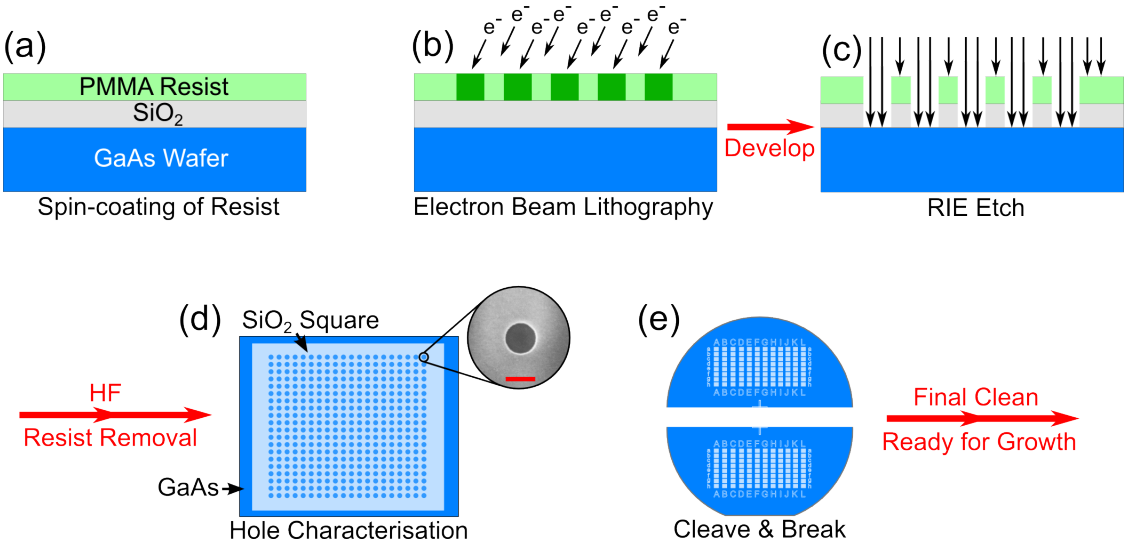

Figure 2.4: Formation of nanohole arrays in SiO_2 squares. (a) The wafer is spin-coated with PMMA resist; (b) EBL is performed to expose a nanohole array pattern into resist; (c) The resist is developed before the nanohole array pattern is transferred into the SiO_2 squares using RIE; (d) Any final remnants of SiO_2 present in the nanoholes after RIE are expelled using a HF 'dip', and the remaining resist is removed. SEM imaging is used to confirm that the nanohole pattern has successfully penetrated through to the substrate surface. Inset shows a typical SEM image of a nanohole produced after steps (a)–(d); (e) The wafer is cleaved in half and each half is cleaned a final time in preparation for nanowire growth. Scale bar 100nm.

Following EBL exposure of the array design, the PMMA resist was developed in a 1:3 methyl isobutyl ketone:isopropyl alcohol (MIBK:IPA) solution for 30s at 23°C, producing nanoholes in the resist at the locations previously exposed to the electron beam. Again, to remove any remaining resist in the exposed areas after developing, the wafer was then ashed in an oxygen plasma for 5–10s. This ashing time was reduced in comparison to that adopted previously in order to ensure that the developed nanoholes did not significantly increase in diameter, and, as the PMMA resist layer was much thinner than that of the BPRS100 used in the earlier photolithography steps, to prevent the complete removal of the unexposed resist from occurring.

Transfer of the developed nanohole pattern into the underlying SiO_2 film was then achieved using an anisotropic reactive ion etch (RIE) (Figure 2.4(c)). The wafer was dry etched at RT for ~150s, using a 40sccm flow of CHF_3, an RF power of 80W and a chamber pressure of 25mT. Following this, the wafer was again placed in 1% HF for a very brief period of time

(~2s), in an attempt to remove any final remnants of SiO_2 that may have been present in the nanoholes after the preceding RIE step. It has previously been demonstrated that the brief exposure of the wafer to HF (after RIE) in this manner, can significantly improve both nanowire yield and the overall uniformity of nanowires after growth, as a consequence of the complete removal of SiO_2 in the nanohole sites [55]. After subsequent rinsing of the wafer in DI water and drying with nitrogen, the remaining PMMA resist on the substrate surface was removed using warm EKC830 as described previously. To determine whether the nanohole pattern had been transferred successfully into the SiO_2 layer after the etching process, the wafer was then imaged using a scanning electron microscope (SEM). Although it could not be determined conclusively from this imaging that the nanohole pattern had been etched all the way through to the GaAs substrate as required, typically, it was observed that if there was a strong contrast difference between a nanohole and the surrounding SiO_2, subsequent nanowire growth from that nanohole site would be successful. An SEM image of an example nanohole produced after the pattern transfer procedure described above is displayed in Figure 2.4(d).

After confirming that the nanohole pattern had been successfully transferred into the SiO_2 film, measurement of the diameter of the etched nanoholes in each patterned array was performed. Following this, the wafer was cleaved in half in the direction parallel to the major flat orientation and each half wafer was then individually cleaned a final time using warm EKC830 in preparation for nanowire growth (Figure 2.4(e)).

2.3.2 Growth of GaAs Nanowires

2.3.2.1 Metalorganic Chemical Vapour Deposition

GaAs nanowire growth was performed using a horizontal flow MR350 MOCVD reactor housed in the EPSRC National Centre for III-V Technologies at the University of Sheffield[†]. The main components of the system, which is based on a tube furnace design, are depicted schematically in Figure 2.5.

[†]GaAs nanowire growth was performed by the author and Dr. Andrey Krysa.

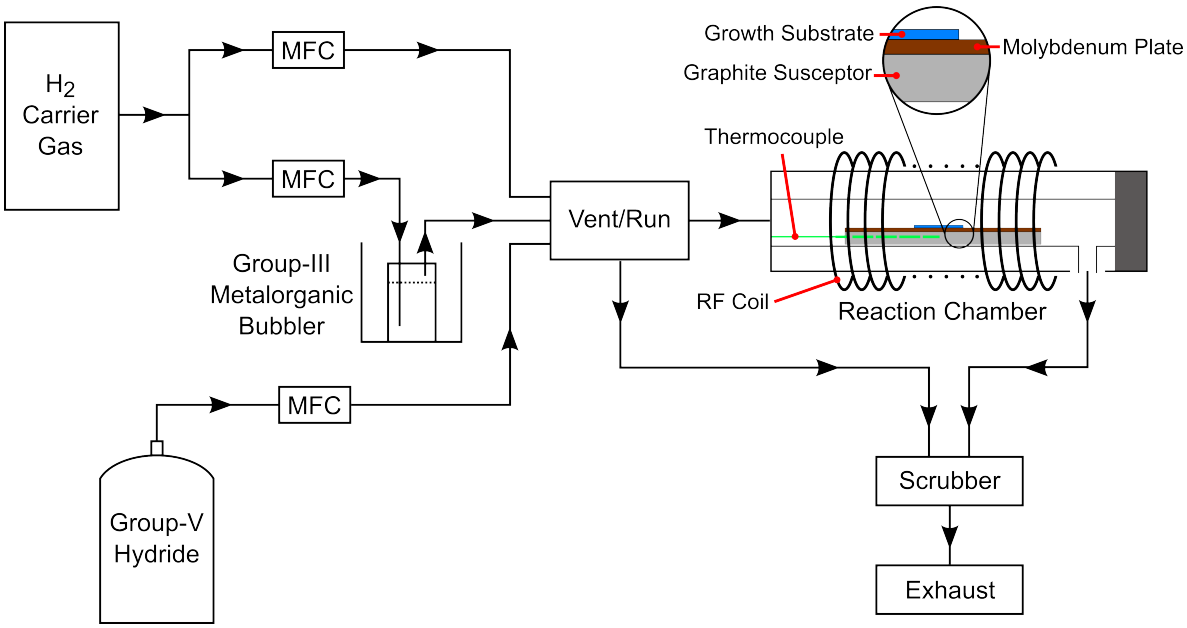

Figure 2.5: Schematic of the MR350 horizontal flow MOCVD system used for nanowire growth. Hydrogen gas is used to carry the hydride and metalorganic precursors to the reaction chamber. Black arrows indicate the direction of gas flow. The exhaust gas mixture, containing unreacted precursors and byproducts from the reaction chamber and the vent line, is passed through an activated charcoal scrubber, which filters the toxic compounds in this mixture and releases H_2 into the atmosphere. Upto four 2-inch wafer halves can be accommodated by the molybdenum substrate holder plate that sits atop the inductively heated stationary graphite susceptor block. MFC – mass flow controller.

The source materials supplied to the reaction chamber during GaAs nanowire growth were trimethlygallium (TMGa), arsine (AsH_3) and phosphine (PH_3), with H_2 implemented as the carrier gas. The volatile organometallic TMGa source was stored at a constant temperature and pressure in a sealed stainless steel cylinder (typically referred to as a bubbler), which was immersed in temperature-controlled bath. The hydride sources (AsH_3 and PH_3) were stored in high pressure cylinders and were directly supplied to the reaction chamber. Transport of the TMGa precursor was facilitated by the flowing of the high purity H_2 carrier gas through the bubbler. As the pressure and temperature of the bubbler were fixed, the amount of TMGa precursor entering the reaction chamber was determined by the H_2 flow, which was accurately monitored and controlled by an electronic mass flow controller (MFC). The hydride sources were also mixed with the hydrogen carrier gas and controlled by MFCs. Transport of the TMGa and hydride precursors to the reaction chamber occurred via separate supply lines to prevent pre-reaction before entering the chamber.

Inside the reaction chamber, the growth-prepared half wafer was held on a molybdenum substrate plate that sat atop a stationary graphite susceptor block, which was inductively heated by an external RF-supplied coil. Measurement of the graphite susceptor temperature was achieved using a thermocouple inserted into the centre of the susceptor. It is important to note therefore that readings from the thermocouple provided only an estimate of the temperature at the substrate surface.

In an attempt to achieve reproducible nanowire growth, a short GaAs growth run, using similar growth conditions as those for subsequent nanowire growth, was undertaken before loading of the half wafer into the reactor. This coated the interior walls of the inner quartz liner with GaAs, therefore presenting the same surface to the carrier gas in each nanowire growth run. The same quartz inner liner was also employed for each growth run, as it was possible that some variability in the carrier gas flow would occur between different liners. After loading, the half wafer was first annealed by ramping the measured susceptor temperature from RT upto 780°C over a time period of 9 minutes. The purpose of this annealing process was to remove the native oxide from the substrate, as well as any organic contaminants that may have been introduced during the previous processing of the wafer. To prevent desorption of arsenic from the substrate surface while this annealing process was taking place, an AsH_3 overpressure was maintained using a flow rate of 40sccm, which was introduced alongside the H_2 carrier gas (at a flow rate of 18,000sccm). Observation of thermocouple readings revealed that the substrate experienced these conditions at 780°C for approximately 3 minutes in total. The temperature was then lowered to the temperature selected for subsequent growth, which in this case was 750°C, with the AsH_3 overpressure maintained. Nanowire growth then proceeded through the pyrolysis (decomposition) of the TMGa and AsH_3 sources over the heated GaAs substrate ($Ga(CH_3)_3 + AsH_3 \longrightarrow GaAs + 3CH_4$). All nanowire growth presented in the following sections was performed at a pressure of 150 Torr.

2.3.2.2 Mechanisms of Selective-area MOCVD Nanowire Growth

In selective-area MOCVD, the morphology of polygonal semiconductor nanostructures that form within the openings of the mask layer is determined primarily by the relative growth rates of each of the semiconductor crystallographic growth planes (the directions of which are defined by the atomic arrangement of the semiconductor) during growth and the orientation of the growth substrate [38, 56–59]. Planes that grow more slowly typically develop as facets, leading to crystal structures surrounded by close packed planes with a minimum surface energy after growth [60].

For GaAs (and most other III-V semiconductors), there exists a family of six low index {110} growth planes which are oriented orthogonally to the (111)B growth plane. By promoting growth on the (111)B plane at the expense of growth on the six {110} planes, formation of a nanowire pillar with hexagonal cross-section can be achieved, terminated by a (111)B oriented top facet. Implementing a (111)B GaAs substrate means that the nanowire top facet after growth is oriented parallel to the substrate surface, and therefore the formed nanowire has a vertical geometry.

Previous demonstrations of successful nanowire formation using this approach have shown that the relative growth rates on the (111)B (axial) and {110} (lateral) planes depend strongly on the surface coverage of the group-V species during growth. This behaviour can be explained by considering the mechanisms of axial nanowire growth in selective-area MOCVD and the relationship between the surface chemical potential of the respective planes (i.e. the number of dangling bonds) and the effective coverage of the group-V species. Growth in the axial direction, as shown schematically in Figure 2.6(a), proceeds mainly through supply of reaction species adsorbed on the nanowire sidewall or surrounding growth mask which diffuse towards the advancing nanowire top (111)B surface. Surface diffusion in this manner is more significant for group-III adatoms as, relative to group-V adatoms, they have much larger diffusion lengths [61]. It is noted that reaction species may also directly incorporate on the (111)B surface from the vapour, but relative to the contribution from surface diffusion of species, the contribution

to axial growth from this direct incorporation process is negligible owing to the substantial difference in available surface area for adsorption (except at the nucleation stage of the growth process).

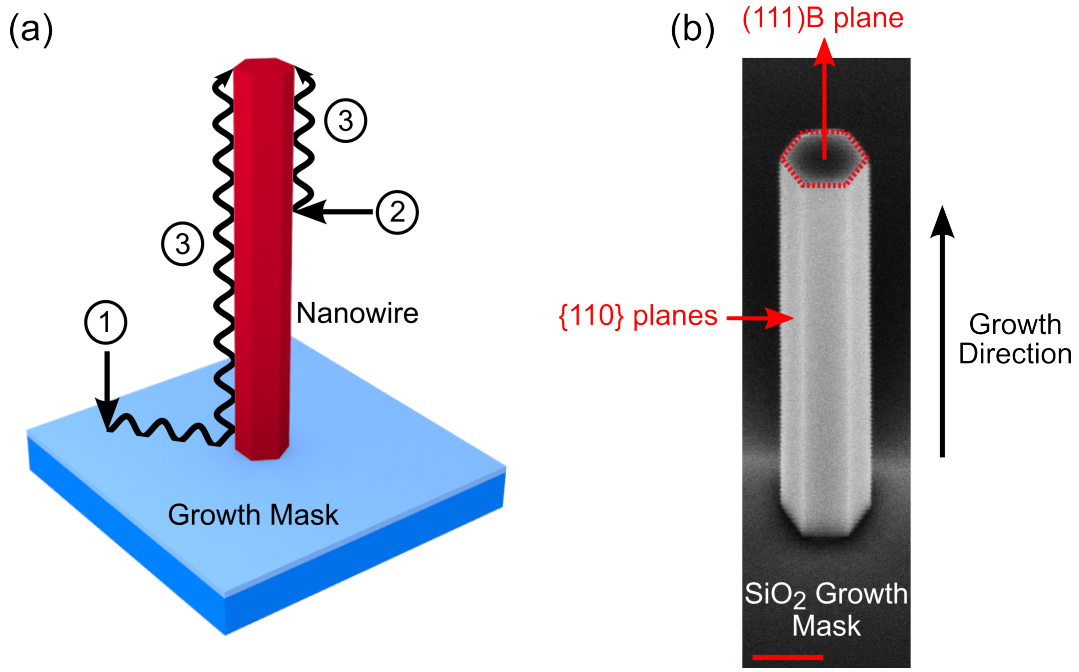

Figure 2.6: Selective-area nanowire growth by MOCVD. (a) Schematic overview of adatom contributions to axial nanowire growth. Adatom contributions include those (1) adsorbed on the growth mask and (2) nanowire sidewalls which (3) diffuse towards the advancing top (111)B surface; (b) SEM image of a GaAs nanowire formed on a (111)B substrate after growth. Scale bar 200nm.

For GaAs growth conducted at low growth temperatures and high AsH_3 flow rates, a large number of As species impinge onto the growing nanowire surfaces and the desorption probability of these species is low [62]. Under these conditions, the migrating Ga species are strongly adsorbed on the {110} planes as they contain both Ga and As atoms. The adsorbed As adatoms, which are bonded to the Ga atoms provide additional dangling bonds for the attachment of further Ga atoms, thereby enhancing growth on the {110} planes [57]. The high surface coverage of As species under these growth conditions also leads to the formation of energetically stable As-trimers on the As terminated (111)B surfaces [58, 63–65], which act to inhibit incorporation of Ga atoms on these surfaces. Therefore, at low growth temperatures and high AsH_3 flow rates, axial nanowire growth is suppressed and growth in the lateral direction is dominant.

Reducing the surface coverage of As species (i.e. increasing the probability of As desorption) can be achieved through a combination of decreased AsH_3 flow rate and higher growth temperature. Under these conditions, the number of dangling bonds available for binding of Ga atoms to the developing nanowire sidewalls is decreased and As-trimers on (111)B surfaces become less stable. In addition, owing to the reduction of surface coverage of As species, nucleation of polycrystalline GaAs structures on the growth mask is strongly suppressed under these conditions, and reactive species are selectively deposited in the mask openings. Studies of the temperature dependence of GaAs nanowire growth have demonstrated, however, that the rate of axial nanowire growth also decreases with increasing temperature. This is thought to be a consequence of increasing desorption of Ga species as temperature is increased, reducing the amount of Ga adatoms that successfully migrate from the mask region to the nanowire growth sites [23, 66].

The optimum conditions for selective-area GaAs nanowire growth therefore lie between the formation of As-trimers and the significant desorption of Ga species. Under these conditions, the axial growth rate is limited only by the flow rate of the TMGa precursor [67]. Figure 2.6(b) displays an SEM image of a typical nanowire produced after growth using this technique. In contrast to similar catalyst-free nanowire growth by MBE [68], nanowires produced by this growth approach are observed to have a minimum diameter limit that is set by the size of the nanohole from which it has nucleated (i.e. the nanowire diameter can never be smaller than the nanohole size). As reported in a previous study of selective-area GaAs nanowire growth, even under conditions optimised for hexagonal nanowire formation, the shape of the crystal at the initial stage of nanowire growth is observed to be tetrahedral, rather than hexagonal. This is considered to be due to the fact that tetrahedral growth does not need as much energy as hexagonal growth to overcome the energy barrier for nucleation [23]. The hexagonal shape is then thought to prevail as a result of preferential growth on the {110} planes. After the side facets of the hexagonal nanowire structure are developed, axial growth dominates as a result of the relatively slow growth rate of the {110} planes under these optimised growth conditions.

Owing to the mechanisms by which crystal growth proceeds in this selective-area approach, the properties of the patterned mask region also influence nanowire growth characteristics. For optimised growth conditions, it has been demonstrated that final nanowire height typically increases as the diameter of the nanohole from which it nucleates decreases [23, 65, 67, 69]. This is thought to be a result of the faster development of step sites at smaller diameter nanoholes, which present a larger surface area for adsorption of migrating reaction species. The relationship between nanowire growth rate and the pitch of patterned nanohole arrays is somewhat less well understood for this growth approach. Previous reports of VLS nanowire growth [61, 70] and selective-area nanowire growth using MBE [68] have shown that nanowire growth rate (both axial and radial) typically decreases with decreasing nanowire separation due to the increasing competition between adjacent nanowires for diffusing reaction species. A previous report of successful selective-area GaAs nanowire growth by MOCVD, however, demonstrated the opposite dependence of final nanowire height on nanohole pitch [65], though the origin of this contrasting behaviour was not clarified in this report, instead being left for future study. As, relative to a bare substrate, the effective surface area for adatom precipitation is greatly reduced by implementing a patterned growth mask, the growth rate of structures in the patterned regions is also strongly related to the total coverage of the mask. It has been demonstrated that better control over the morphology and uniformity of grown structures is generally achieved when growth is performed on partially rather than fully covered substrates [65, 71]. This is presumed to be due to the fact that growth species adsorbed on the mask are able to diffuse out to the exposed regions of the substrate surrounding the patterned mask regions, which results in a reduction of the growth rate in the selective growth sites. The choice of the patterned mask region size and geometry for growth in this instance was based on that reported in previous demonstrations of successful selective-area nanowire growth using this technique [65, 72, 73].

Taking into account the above discussion, it was expected that, given optimised growth conditions, vertical nanowires with hexagonal cross-section would be formed after growth, with individual nanowire growth rates inversely proportional to the diameter of the nanohole from

which the nanowire had nucleated. However, after nanowire growth here, two growth modes were actually observed, with the occurrence of each dependent on the treatment of the wafer during the pre-growth fabrication steps described previously. Discussion of these two growth modes is presented separately in the following sections. It should be noted that during each growth run, TMIn was introduced into the reactor for a short time (~2–4s) in an attempt to form a nanowire quantum dot (NWQD) within individual nanowires. However, discussion of NWQDs is left to Chapter 3, and the growth of these embedded structures was not thought to impact on the results presented in the following sections, which focus only on nanowire growth itself.

2.3.3 Nanowire Growth Mode 1: Rough Planar Surface Growth

For each sample presented in this section, growth on the regions of the GaAs substrate not covered by the SiO_2 squares (excluding the etched nanoholes) exhibited considerable surface roughness, which gave rise to a matte-like appearance of the wafer after growth. Figure 2.7 displays an SEM image of the boundary between a patterned SiO_2 square and the exposed substrate after a nanowire growth run, showcasing the typical surface profile of this rough planar growth. As will become clear subsequently, the presence of such growth had a notable impact on nanowire growth behaviour.

Following initial annealing of the substrate in the method described in the previous section, nanowire growth on Sample 2A[‡] was performed at 750°C for a total of 10 minutes using TMGa and AsH_3 flow rates of 33 and 15sccm, respectively. Such growth conditions had been previously shown to produce GaAs nanowires of high structural quality [55], and were therefore selected for growth on this sample. AsH_3 flow was maintained using a double dilution channel in this instance, as the available single dilution channel (for AsH_3) was controlled by 500sccm mass flow controller (and thus measurements of the flow rate with this channel would not have been accurate). At the end of the nanowire growth, with the TMGa channel closed, the

[‡]Sample 2A corresponds to growth sample reference MR3497.

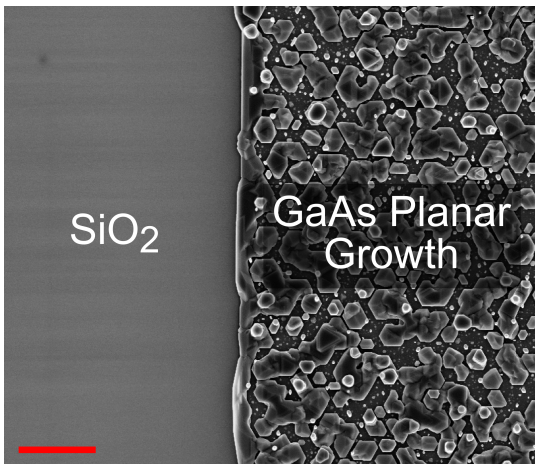

Figure 2.7: SEM image displaying rough planar growth on the regions of the GaAs substrate not covered by SiO_2 (right-hand side). No GaAs overgrowth is observed on the SiO_2 square (left-hand side). Scale bar 2µm.

AsH_3 flow rate was switched back to that used during the pre-growth annealing step (40sccm) and, in an effort to passivate the dangling bonds on the surfaces of each nanowire, a PH_3 flow of 300sccm was simultaneously introduced into the reactor as the sample cooled down. By introducing a PH_3 overpressure while the sample cooled, it was posited that a certain amount of arsenic/phosphorus exchange would occur at the surfaces of each nanowire, producing a thin enclosing GaAsP capping layer, which has previously been shown to improve the optical properties of GaAs nanowires [74].

Figure 2.8(a) displays an SEM image of an individual nanowire formed on Sample 2A after growth. It is observed that the nanowire has a hexagonal cross-section (recognised most prominently at the base of the nanowire), smooth sidewalls and is untapered. The diameter of the nanowire is ~145nm, while the diameter of the initial nanohole in the SiO_2 growth mask from which the nanowire formed was ~119nm, demonstrating that radial growth was strongly suppressed with these growth conditions. However, as illustrated by the red circles in Figure 2.8(c), contrary to previous reports of nanowire growth using this technique in the literature, average nanowire height (and hence growth rate) was observed to increase with increasing nanohole diameter. The maximum nanowire height in this instance (corresponding to the nanowires with the largest diameter) was found to be ~285nm.

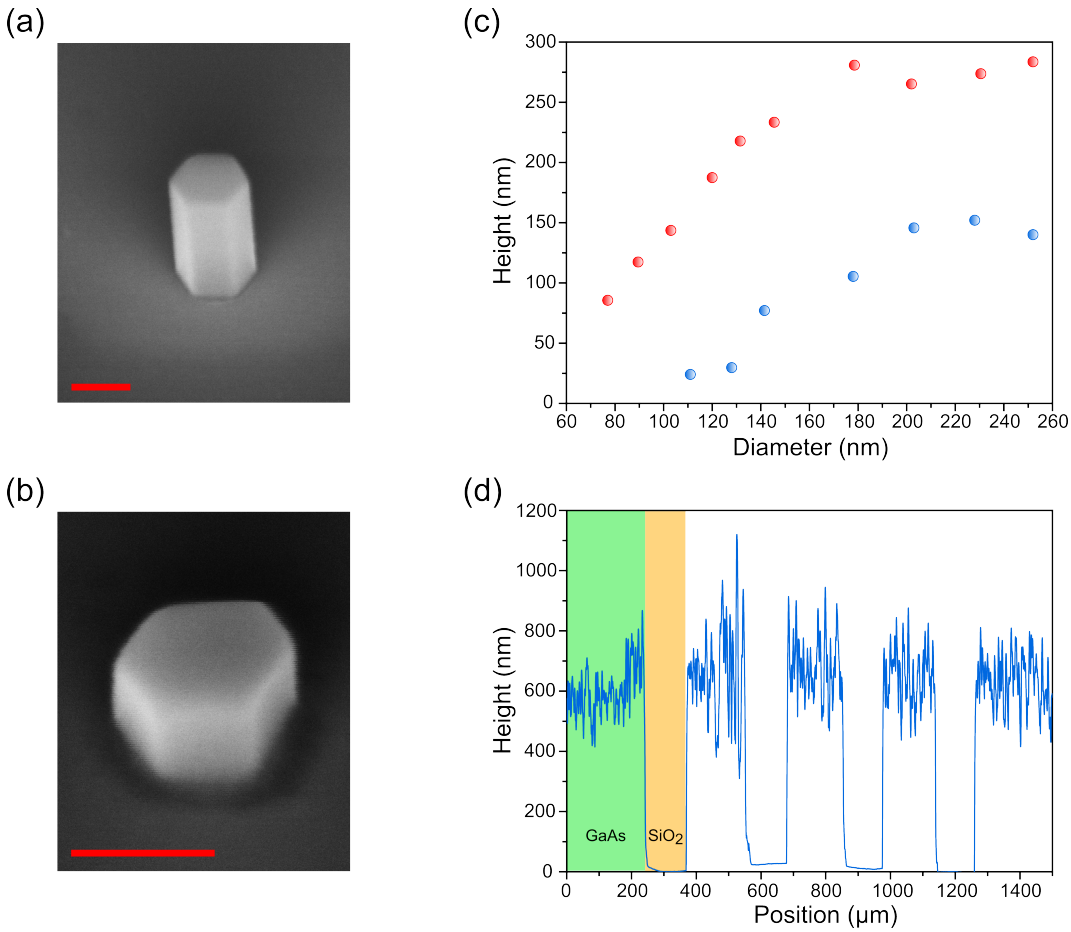

Figure 2.8: Structural characterisation of Samples 2A and 2B after nanowire growth. 45° angled SEM images show structure of individual nanowires (with similar diameters) from (a) Sample 2A and (b) Sample 2B; (c) Plot of nanowire height vs. nanowire diameter for nanowires grown on Sample 2A (red-circles) and Sample 2B (blue-circles); (d) Surface topography of Sample 2A after growth, measured using a Dektak surface profilometer. Region highlighted in green (and corresponding regions to the right) reveals surface profile of exposed GaAs area on substrate. Region highlighted in orange (and corresponding regions to the right) reveals surface profile across the SiO_2 growth mask. Scale bars 100nm.

In an attempt to increase average nanowire height, another sample (Sample 2B[§]) was grown at the same temperature as Sample 2A, using the same TMGa and AsH_3 flow rates, but with a longer overall GaAs growth time of 13 minutes and 30 seconds. Figure 2.8(b) displays an SEM image of an individual nanowire, located in the equivalent array to that of the nanowire displayed in Figure 2.8(a), formed on Sample 2B after growth. As for the previous sample, the nanowire was observed to have a hexagonal cross-section, and the radial growth was strongly

[§]Sample 2B corresponds to growth sample reference MR3540.

suppressed with the diameter of the nanowire and initial nanohole ~141nm and ~117nm, respectively. In comparison with the nanowire shown in Figure 2.8(a) however, the height of the nanowire is seen to be significantly smaller (~233nm vs. ~77nm), even though the total GaAs growth time for this sample was 35% longer. As illustrated by the blue circles in Figure 2.8(c), this held true for all nanowire diameters on Sample 2B. The relationship between height and initial nanohole diameter also followed the same trend as that observed previously for Sample 2A. It is noted that, owing to the slow growth rate of nanowires on this sample (and the observed relationship between nanowire diameter and height), there was no evidence of nanowire formation from arrays containing patterned nanoholes with a diameter below ~70nm. Therefore, for Sample 2B, the dataset shown in Figure 2.8(c) contains three fewer data points than that for Sample 2A.

For both samples described above, planar growth in the regions of the substrate not covered by the SiO_2 mask was observed to be extremely rough. Characterisation of the planar growth surface topography was achieved using a Dektak surface profilometer, where for a single measurement, the Dektak tip was moved in a straight line over a region of the sample surface that included four unpatterned SiO_2 squares. Figure 2.8(d) displays a Dektak surface profile measurement obtained for Sample 2A in this manner, which highlights both the large height difference between the regions covered by the SiO_2 squares (~0nm in this figure) and surrounding planar GaAs growth, and the significant variation in this planar GaAs growth height as a function of position. The exact growth rate of the rough epitaxial growth was not known, but based on a linear growth rate approximation, growth rates of over 1.5nm/s and 0.6nm/s were observed for Samples 2A and 2B, respectively. The high growth rate of the GaAs growth around the SiO_2 squares was thought to relate to the distinct fluctuations in height of the rough epitaxial growth (as a function of position) observed for both Sample 2A and 2B, which in turn appeared to be responsible for the unexpected height-diameter dependence of the nanowires on these samples. The similarly unexpected observation that nanowires formed on Sample 2B were smaller in comparison to those on Sample 2A, even though GaAs nanowire growth time was 35% longer, was also thought to be a result of rough planar growth, as both

the height and morphology of the rough planar growth was seen to differ between the two samples (with the growth rate of the rough planar growth lower for Sample 2B). Therefore, in an attempt to improve the reproducibility of subsequent nanowire growth samples and form nanowires with larger overall height which followed the expected height-diameter dependence reported previously, finding a way to reduce the surface roughness of the planar epitaxy was made a priority before any further growth was performed.

2.3.4 Nanowire Growth Mode 2: Smooth Planar Surface Growth

Owing to its observed effectiveness in removing both optically active (BPRS100) and electron-sensitive (PMMA) resists, wafer cleaning during the pre-growth processing steps described in Section 2.3.1 was undertaken principally using EKC830 photoresist remover. Exposure of the wafer surface to this photoresist remover was kept purposefully short (no longer than 5 minutes in total) for each individual cleaning process, as it was discovered during previous nanowire growth studies by Dr. Andrew Foster at the University of Sheffield, that EKC830 slowly etches through GaAs [55]. Prolonged use of EKC830 therefore, can result in the roughening of the substrate surface, for which the formation of a rough epitaxial surface after growth is thought to be associated. However, it was observed on a number of occasions during pre-growth fabrication that the wafer surface still contained residual resist after implementing this short cleaning time, even with pre-heating of the EKC830 before cleaning. Therefore, in these instances, the wafer was subsequently ashed in an oxygen plasma for a certain time period (usually 60s) to achieve appropriate sample cleanliness.

Although only very few high energy ions bombard the GaAs surface during the ashing procedure, it was hypothesised that some roughening of the sample surface may have occurred due to the multiple occasions this process was utilised during processing (and the duration for which it was undertaken in each instance) for both Sample 2A and 2B (as both samples originated from the same wafer, other than the final cleaning steps, they were subject to the same fabrication procedure). In an effort to reduce the necessity of these post-cleaning ashing

steps and also simultaneously further decrease the exposure time of the wafer surface to the EKC830 during each cleaning step, the wafer cleaning procedure during each cleaning step was altered slightly for subsequent pre-growth sample fabrication. Cleaning of the wafer from this point on involved first placing the wafer in a beaker containing a small amount of EKC830 (that had been pre-heated on a 100°C hotplate for ~3 minutes) and agitating the liquid by hand for 30s. The wafer was then immediately transferred to a separate beaker containing a small amount of fresh EKC830 (which again had been pre-heated for ~3 minutes) and agitated by hand for a further 3 minutes. Finally, as before, the wafer was rinsed in flowing DI water for 5 minutes and dried with nitrogen. Following the implementation of this cleaning procedure, no post-cleaning ashing steps were required, as a sufficient level of sample cleanliness was achieved after each cleaning step using the EKC830. Ashing, therefore was only utilised for removal of any residual resist in exposed areas after BPRS100 or PMMA resist exposure.

To determine whether the alterations made to the fabrication procedure described above resulted in a reduction in the roughness of the planar epitaxial GaAs growth, nanowire growth was performed on a half wafer where these alterations had been implemented, using the same growth conditions as those employed for Sample 2B.

Figure 2.9(a) displays the equivalent SEM image shown in Figure 2.7 for Sample 2C[¶] after growth, showing that the planar GaAs growth in the regions surrounding the SiO_2 squares for this sample exhibited a much reduced surface roughness in comparison to that seen for Samples 2A and 2B. This change in morphology was accompanied by a ~10 (~4) fold reduction in planar growth rate compared to Sample 2A (Sample 2B), and a greatly enhanced nanowire growth rate. The difference in nanowire growth rate in comparison to that observed for the previous samples is highlighted in Figure 2.9(b), which displays an SEM image of a nanowire with diameter of ~139nm formed after growth on Sample 2C. The height of this nanowire was measured to be ~2170nm, which is over ~8 (~28) times the height of individual nanowires with a similar diameter measured on Sample 2A (Sample 2B). It is posited that the much lower planar growth rate, which ostensibly resulted from the reduction in surface growth

[¶]Sample 2C corresponds to growth sample reference MR3575.

roughness, led to higher effective adatom flows for nanowire growth on this sample. As for the two previously grown samples, radial growth of this nanowire was strongly suppressed, with the diameter of the initial nanohole from which it had nucleated ~116nm. Nanowires on Sample 2C also exhibited the same hexagonal morphology and smooth sidewalls observed in the previously grown samples, which is illustrated more clearly by the SEM image in Figure 2.9(c) of a larger diameter nanowire (~178nm) grown on this sample.

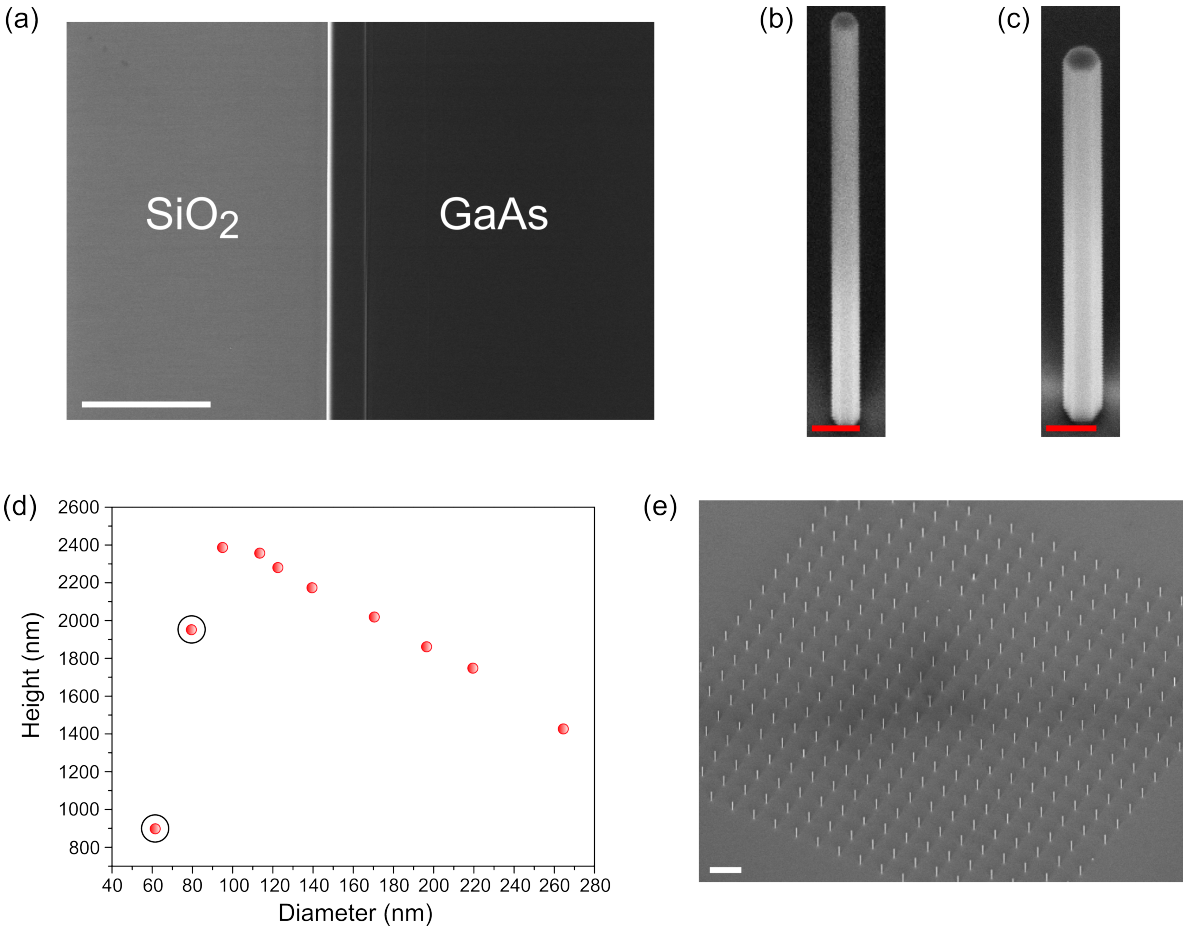

Figure 2.9: Structural characterisation of Sample 2C after nanowire growth. (a) SEM image of substrate after growth, revealing smooth GaAs planar growth (right) around regions covered by SiO_2 growth mask (left). Scale bar 5µm; 45° angled SEM images revealing structure of individual nanowires with a diameter of (b) ~139nm and (c) ~178nm. Scale bars 200nm; (d) Plot of nanowire height vs. nanowire diameter. Circled data points are discussed in the main text; (e) 45° angled SEM image showing overview of typical array containing nanowires with diameters of ~140nm. Scale bar 5µm.

Unlike the previous samples, however, in the presence of a much reduced planar growth rate, nanowire formation on Sample 2C followed the behaviour expected from previous reports in

the literature, with nanowire heights, on the whole, inversely proportional to the diameter of the nanohole from which they had nucleated. This is illustrated in Figure 2.9(d). The deviation from this behaviour exhibited by nanowires with diameters below ~90nm (two circled data points in Figure 2.9(d)) was thought to be due to an increased seeding time for these smaller diameter nanowires, caused by the incomplete removal of SiO_2 from the nanohole sites from which the nanowires had nucleated. As described in Section 2.3.1, the brief dipping of the wafer in 1% HF was performed in an effort to remove any final remnants of the SiO_2 that may have been present in the nanoholes after the RIE etching process, but on this sample it appears that the exposure time of the substrate to the HF was not sufficiently long enough to allow for complete removal of the remaining SiO_2 in these smaller diameter nanohole sites. This is perhaps further supported by the observation that nanowire yield and uniformity in arrays containing nanowires with diameters less than 90nm was poorer than for those that contained nanowires with larger diameters. Figure 2.9(e) shows an SEM image of a typical nanowire array containing nanowires with a diameter ~140nm on Sample 2C. The nanowire yield for this array is over 98%, and nanowire heights and diameters are observed to be extremely uniform across the entire array.

2.3.5 Developing the Catalyst-Free Growth Technique

In addition to the single nanowire structures discussed in the previous sections, nanowire growth from a number of more intricate nanohole arrangements was also achieved on Sample 2C. These included closely spaced nanohole pairs and triplets. Whilst the pitch between the pairs or triplets within a particular array was fixed at 4µm, the separation between each member of the pair or triplet was reduced from ~200nm to ~0nm. An example of the structures formed after growth from these nanohole pair and triplet sites are displayed in Figure 2.10.

As illustrated in Figures 2.10(a) and (d), growth of individual nanowire structures in pair arrangements was observed for edge-to-edge nanowire separations down to ~20nm. It is noted that on GaAs nanowire samples grown previously, successful growth of individual nanowire

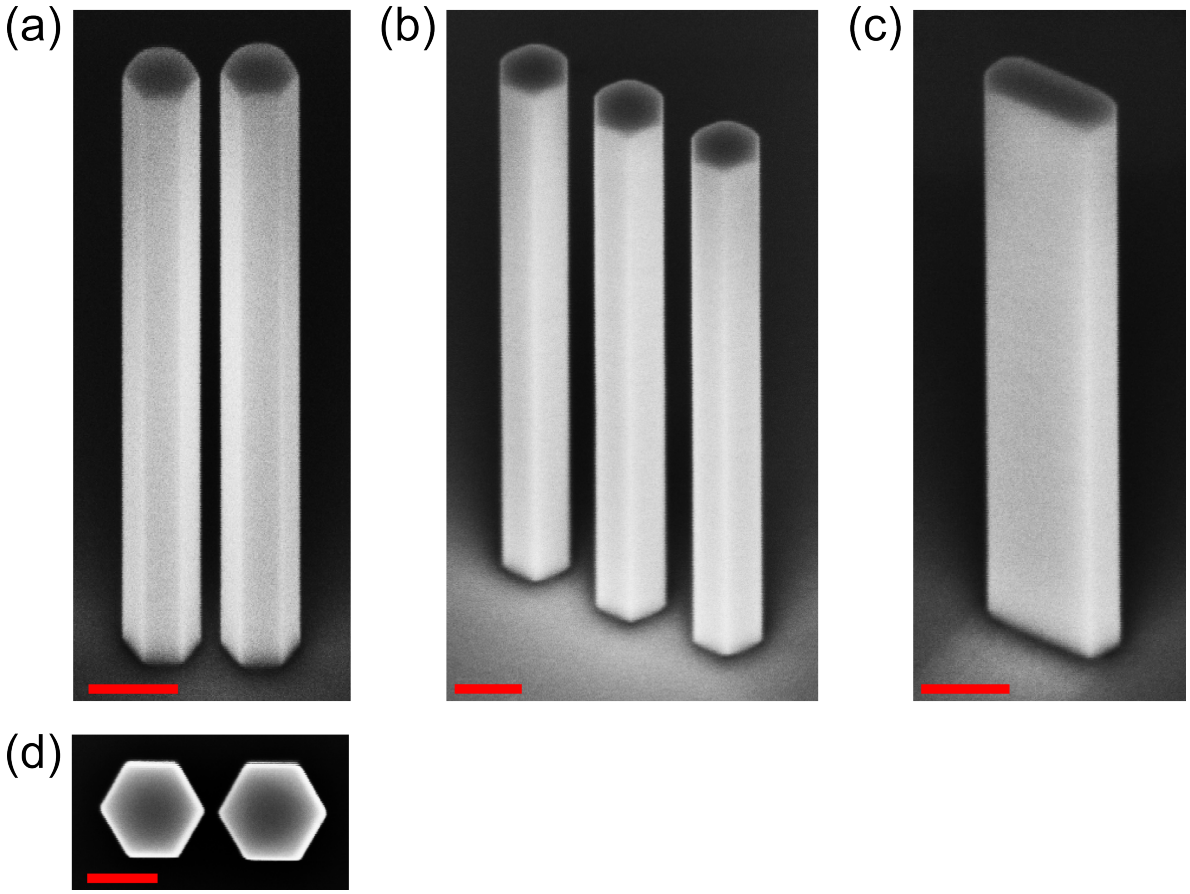

Figure 2.10: Development of the catalyst-free growth technique. Angled SEM images show closely spaced individual nanowires forming a (a) nanowire pair and (b) nanowire triplet; (c) An angled SEM image showing an elongated nanowire with a cross-section aspect ratio of ~2 formed from an elongated nanohole (nanodash) site; (d) Top down SEM image of the nanowire pair in (a). Scale bars 200nm.

structures in pair arrangements has been demonstrated for even smaller edge-to-edge nanowire separations of ~10nm. These structures are referred to in Chapter 3.

For nanowires seeding from more closely spaced nanohole clusters, a mix of regular and amorphous growth was observed until a critical nanohole separation was reached whereby the resulting structure formed from the cluster of nanohole sites after growth was a single elongated nanowire, with an elongated dimension similar to that of the combined width of the nanohole cluster. Although these closely spaced nanohole clusters provide a means by which nanowire morphology can be successfully manipulated, control over the cross-section dimensions of the resultant elongated nanowire structures is fundamentally limited by the maximum separation

between nanoholes in the cluster that will produce a properly formed elongated structure. In addition to this, on previously grown samples with similar pair and triplet arrangements, it has been observed that for nanohole separations that were smaller than this 'critical' separation, the incidence of single elongated nanowire formation rather than a mixture of random growth was significantly higher for structures grown from nanohole pairs than for those grown from nanohole triplets. Therefore, to enable better control of the cross-section dimensions of single elongated structures, elongated nanoholes (nanodashes) were also patterned on Sample 2C. The cross-section dimensions of the nanodashes was varied across each array while, again, the pitch between nanodashes was fixed at 4µm. Figure 2.10(c) displays an SEM image of an example elongated structure formed after growth from a nanodash site with a cross-section aspect ratio of ~2 on Sample 2C.

The ability to form individual nanowire clusters with a controllable separation down to ~20nm presents a promising opportunity for investigation of the coupling between embedded NWQDs in nanowire structures as a function of their lateral separation, while control of the nanowire cross-section aspect ratio provided by the closely spaced nanohole clusters and nanodashes described above, enables tailoring of the polarisation properties of light collected from the top facet of the nanowire emitted by an embedded NWQD. This structural tailoring of light polarisation is the subject of Chapter 3.

2.4 InP Nanowire Arrays on (111)A InP Substrates

In the following sections, the process by which selective-area InP nanowire arrays on full coverage (111)A InP substrates are formed is presented. First, the fabrication procedure used to prepare the (111)A substrates for nanowire growth is briefly described. This is followed by an overview of the growth parameters utilised for each nanowire growth in this instance. Both the structural and optical properties of the grown nanowire samples are then discussed.

2.4.1 Fabrication of (111)A Substrates in Preparation for MOCVD Growth

Fabrication prior to InP nanowire growth was undertaken on 2-inch diameter (111)A n-type InP wafers. This substrate orientation was chosen for nanowire growth with this materials system as it has been demonstrated previously that the direction of preferential growth for InP nanowires is along the <111>A crystal direction [37].

Fabrication began with the patterning of alignment markers on the wafer using the photolithography procedure described in Section 2.3.1.1. However, markers in this case were formed through metal deposition instead of direct etching into the wafer. Marker formation in this way was necessitated by the fact that a suitable etchant chemistry could not be determined for (111)A InP. The distances between the alignment markers and the areas subsequently patterned for nanowire growth on the wafer was at least 1mm (and in general significantly more), and therefore it was assumed that the decision to use metal markers here was unlikely to have any influence on nanowire growth.

The process used for metal alignment marker definition is depicted schematically in Figure 2.11. Following transfer of the alignment marker pattern into the previously spun BPRS100 resist via photolithography, the wafer was developed in 3:1 H_2O:PLSI for 60s at RT. The wafer was then ashed in an oxygen plasma for 15s to remove any resist remaining in the exposed areas after developing, and loaded into a metal evaporator. During the evaporation process, ~5nm of Ti was evaporated onto the wafer, followed by ~50nm of Au. The initial Ti layer was deposited on the wafer to improve the adhesion of the Au to the exposed InP surface. The thickness of each of the deposited metal layers was measured by monitoring the oscillation frequency of a quartz crystal placed adjacent to the wafer. After unloading the wafer from the evaporator, warm EKC830 was used to remove both the resist and metal from the regions of the wafer not previously exposed during photolithography, leaving behind a pattern of metal markers on the wafer surface.

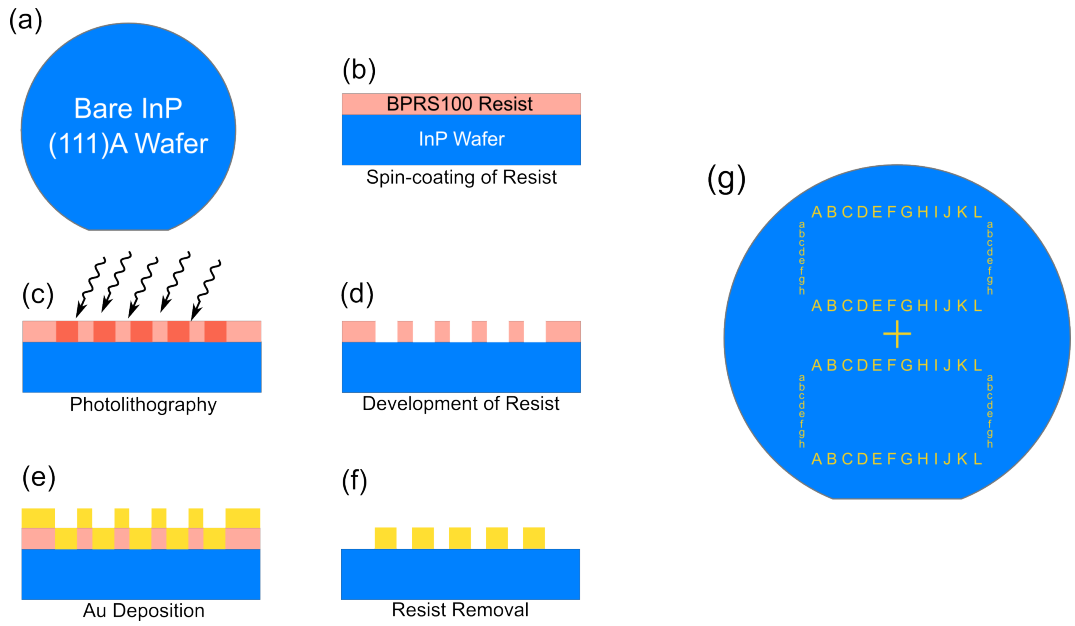

Figure 2.11: Schematic diagrams showing fabrication process used to produce alignment markers in a (111)A oriented InP wafer. (a) A bare InP wafer is (b) spin-coated with BPRS100 resist; (c) Photolithography is performed to expose the alignment marker pattern into the resist; (d) The resist is developed and the exposed BPRS100 is removed; The alignment marker pattern is transferred onto the InP substrate through (e) evaporation of Ti and Au onto the substrate surface and (f) subsequent removal of the remaining BPRS100 resist. An overview of the alignment marker pattern produced after steps (b)–(f) is displayed in (g).

PECVD of a 30nm thick layer of SiO_2 on the InP wafer surface was then performed in the manner described in Section 2.3.1.2. For previous GaAs nanowire growth, it was observed that nanowire growth was heavily influenced by the surrounding surface growth on the exposed wafer surface. With this in mind, it was decided that InP nanowire growth would be undertaken with the substrate fully covered by the deposited SiO_2 growth mask, where only a very little amount of growth away from the patterned arrays of nanoholes would be anticipated, resulting in nanowire growth that was expected to be more reproducible. The impact that implementing a full coverage growth mask had on nanowire growth rates is discussed later in Section 2.4.3. A second photolithography step was therefore used simply to pattern markers into the SiO_2 mask, whose role was to help in navigating across a wafer sample during optical characterisation of nanowires after growth. Transfer of this marker pattern into the SiO_2 layer was achieved by placing the wafer into a 1% HF solution for 30s, followed by a rinse in DI water and drying with nitrogen.

Arrays of nanoholes were then patterned into the growth mask using a combination of EBL and RIE etching as described in Section 2.3.1.3. No growth of InP nanowires had been performed in the MR350 reactor previously, and therefore as part of the optimisation of the nanowire growth conditions, the nanohole arrays were patterned with a wide range of pitches. A previous demonstration of InP nanowire growth in the presence of a full coverage SiO_2 mask using a similar growth approach showed that nanowires at the edges of an array had a higher growth rate relative to those closer to the centre, due to a lower competition for adatoms that diffuse inwards from the surrounding growth mask [75]. To investigate this positional dependence on nanowire growth rate, larger arrays than those on the previous GaAs substrates were patterned on the InP substrates. 100nm diameter nanoholes were patterned in arrays with a side length of 400µm, with pitches of 1, 2, 3 and 4µm. Nanohole arrays with a pitch of 0.5µm were also patterned, but had a comparatively reduced side length of 200µm. SEM imaging showed that the typical nanohole diameter after patterning and etching ranged from ~100–130nm. Following measurement of the nanohole diameter, the wafer was cleaved in half in the direction parallel to the major flat orientation and each half wafer was then individually cleaned a final time using warm EKC830 in preparation for nanowire growth.

2.4.2 Growth of InP Nanowires

The growth study of InP nanowires at the University of Sheffield was initiated by Dr. Andrew Foster. The two main aims of this growth study were to initially grow pure phase, stacking-fault free nanowires and then once this had been achieved, incorporate a NWQD within each nanowire through growth of a few nms thick region of InAsP. However, owing to time constraints, growth of InP/InAsP heterostructures was performed for each nanowire sample so that both aims could be addressed at the same time. In this section, only discussion of the results from InP samples collaboratively grown and characterised by the author and Dr. Andrew Foster are presented. Discussion of NWQDs is left to Chapter 3, and so reference to the attempted incorporation of a thin InAsP emitter within individual nanowires is included only to help describe the structural and optical features that are observed as a consequence of

the inclusion of this embedded region. As for GaAs nanowire growth, all InP nanowire growth discussed in the following sections was performed under the supervision of Dr. Andrey Krysa.

Initial nanowire growth conditions for this study were based upon a report in the literature, which described that a transition from polytypic nanowires containing many stacking faults to pure phase InP nanowires could be induced through an appropriate change of both the growth temperature and the ratio of the III/V source flows [28]. Simply copying the growth conditions presented in this report, however, was unlikely to yield the same nanowire growth, given the variability in the growth environment between different MOCVD reactors. Moreover, the wafers used for nanowire growth in this instance were entirely covered by the SiO_2 growth mask, and so it was assumed that nanowire growth rates would be much higher than those for the partially covered substrates utilised in Ref [28] (and in the GaAs nanowire growth presented previously), as a result of the reduced surface area for adatom precipitation. A range of different growth conditions around those described in Ref [28] were therefore utilised for nanowire growth here.

Table 2.1 summarises the growth conditions used for three InP nanowire growths performed during this growth study. Herein they will be referred to as Sample 2D, Sample 2E and Sample 2F. The source materials supplied by the reactor during InP/InAsP nanowire growth were trimethlyindium (TMIn), phosphine (PH_3) and arsine (AsH_3), with H_2 implemented as the carrier gas. Prior to nanowire growth, all samples were first annealed for 9 minutes under a PH_3 overpressure to remove the native oxide from the substrate, along with any organic contaminants that may have been introduced during the previous processing of the wafer. It is noted that this annealing time included the time taken to ramp from RT up to the target annealing temperature. In the following sections, the structural and optical properties of the nanowires formed on each sample is presented.

Reference in text	Sample MR No.	Anneal time (s)	Anneal Temp (°C)	Growth Temp (°C)	Source flows (sccm)			Growth time (s)		
					TMIn	PH3	AsH3	InP	InAsP	InP
2D	3388	540	670	620	0.125	60	12	600	5	60
2E	3389	540	680	680	0.125	60	12	600	5	60
2F	3428	540	680	680	0.13	50	12	240	1.5	60

Table 2.1: Summary of InP sample growth conditions. The anneal time includes the time taken to ramp to the annealing temperature from RT. Growth times refer to, from left-to-right, the InP nanowire base, the InAsP segment and the top InP section of the nanowire.

2.4.3 InP Nanowire Characterisation

Figure 2.12 displays representative SEM images of the nanowires formed after growth on Samples 2D and 2E. These samples were grown using the same precursor flows and growth times but at different growth temperatures (620°C and 680°C, respectively) to investigate the impact of temperature on nanowire formation. The nanowire growth direction on both samples was observed to be perpendicular to the plane of the substrate, with the nanowire structures composed of hexagonal facets. The relative side lengths for a number of imaged nanowires were seen to be different, however, resulting in a variety of nanowire geometries that deviated from the regular hexagonal structures observed after growth of GaAs nanowires in Section 2.3.2. In the most extreme cases, growth on three of the side facets was almost entirely suppressed, leading to the formation of nanowires with quasi-triangular cross-section. As seen in Figure 2.12(d), a number of nanowires with 4µm pitch on these samples also developed numerous additional facets. Although the exact origin of this variation in nanowire geometry is unknown, it is posited that it may be a consequence of relatively high nanowire growth rates. Around the edges of each array, where the growth rate was highest [75], structures with morphology unlike that seen in the rest of the array were observed on both samples. An example of this anomalous edge growth is displayed in the inset of Figure 2.12(a).

Another prominent feature of the nanowires grown on these samples was the abrupt change in the morphology of the InP growth after the introduction of AsH_3 to form the InAsP segment

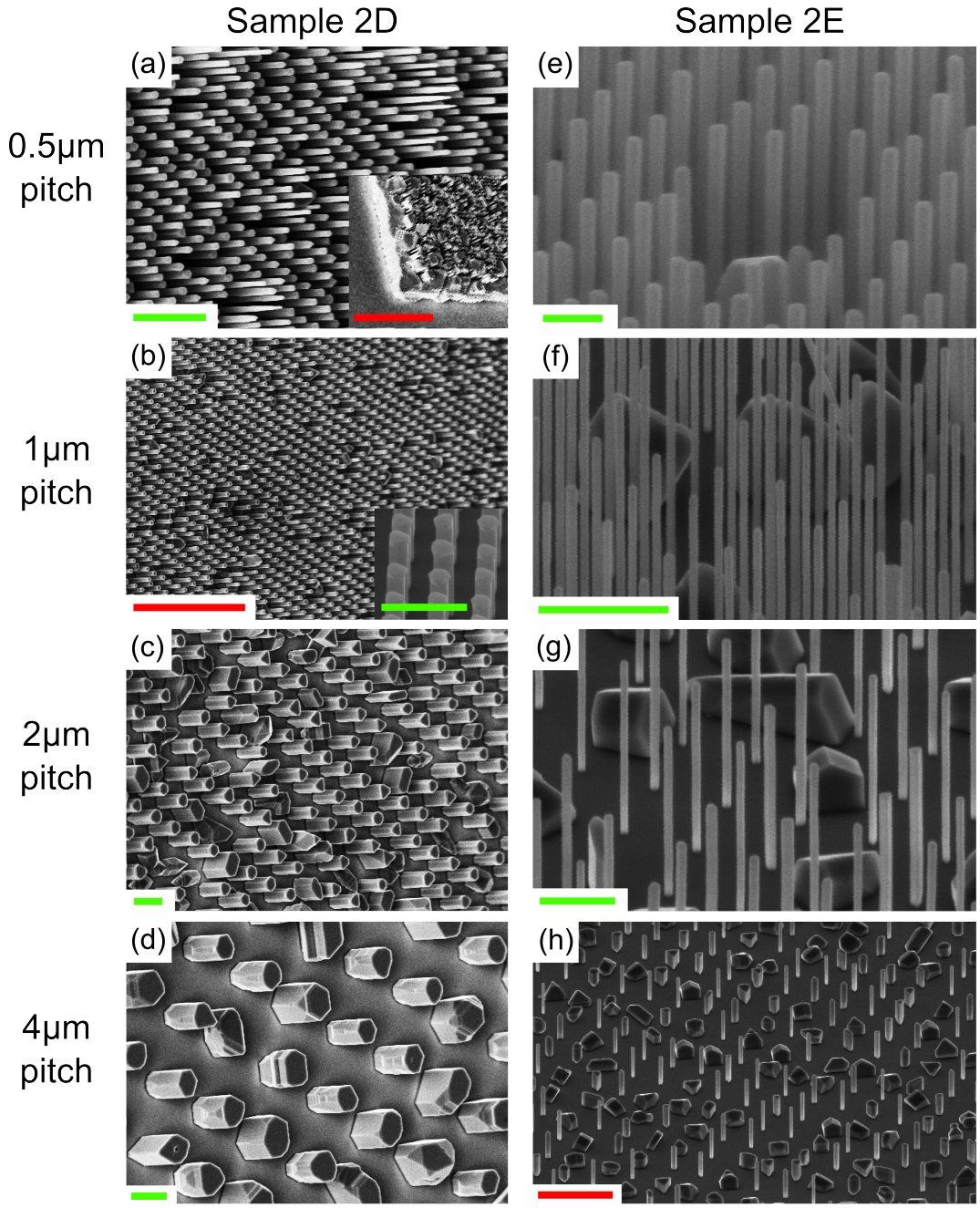

Figure 2.12: SEM images of nanowire growth on Samples 2D and 2E. (a,b,c,d) Tilted SEM overview images of Sample 2D for a nanowire pitch of 0.5µm, 1µm, 2µm and 4µm, respectively; (a) (Inset) Edge of 0.5µm pitch array showing anomalous growth. Scale bar 10µm; (b) (Inset) Zoomed image of nanowires in array with 1µm pitch highlighting abrupt change in morphology of InP growth observed after introduction of AsH_3 to form the InAsP segment in each nanowire. Scale bar 2µm; (e,f,g,h) Equivalent images for Sample 2E. Scale bars (a,c-g) 2µm (b,h) 10µm.

within the nanowires. This is illustrated most clearly in the inset of Figure 2.12(b), although it was a feature of all nanowires on both samples. It is observed here that the change in morphology occurs very close to the top of the nanowire, and this is due to the fact that the introduction of AsH_3 into the reactor for this purpose was intentionally left until just one minute before the end of the nanowire growth, so as to have the least impact on the structural morphology of the nanowire as possible, whilst still allowing sufficient time for adequate capping of the InAsP segment. In addition to increasing the nanowire diameter, after formation of the InAsP segment, a rotation of the hexagonal nanowire cross-section by 90° was observed for a number of nanowires, changing the sidewall orientation from parallel to the $[\bar{1}00]$ direction to the $[\bar{2}11]$ direction of the InP (111)A substrate [28]. An increase in nanowire diameter when InP growth is resumed after formation of a thin InAsP region has been observed previously for nanowire growth using a similar growth approach, although with a lower temperature during InAsP formation and slightly higher temperature during InP nanowire growth [4]. Determining the origin of the increased radial growth and observed structural transformation for these nanowires after InAsP formation will be the subject of future work with this materials system.

Due to the increased nanowire growth rate at the edges of each array, it was not possible to determine the heights of nanowires with a pitch of 0.5µm on either sample, but a noticeable variation in height was clearly observed across the array for this pitch on Sample 2D. Additionally, tapering close to the nanowire tip was seen for nanowires with this pitch on Sample 2D, but this also varied from nanowire to nanowire. In terms of nanowire morphology, the 1µm pitch nanowires showed the best uniformity on Sample 2D, although there were still some obvious defects. For the pitches of 2–4µm, the number of defects and variation in general nanowire morphology increased with increasing pitch. On Sample 2E, nanowire height was relatively uniform for all pitches. However, in comparison to Sample 2D, the defect density was much higher.

The relationship between nanowire pitch and the axial and radial growth rates of nanowires was noticeably different for the two samples. The axial growth rate for nanowires on Sample

2D showed no obvious dependence on the pitch for 1µm to 4µm, with an average nanowire height of ~2.3µm. Using a linear growth rate approximation, this corresponded to a linear growth rate of ~3.5nm/s, which is comparable to that reported in the literature for a similar growth approach [4]. Nanowires on Sample 2E were considerably taller, with an average height of over ~6µm for a pitch of 2µm (due to edge effects, nanowire heights could not be determined accurately for a pitches below 2µm on this sample), and the axial growth rate of nanowires on this sample showed a weak dependence on nanowire pitch, increasing with decreasing nanowire pitch.

The radial growth rate for nanowires on Sample 2D showed an approximately linear relationship with nanowire pitch, with the average nanowire diameter ranging from ~225nm for nanowires with a pitch of 0.5µm to ~1600nm for those with a pitch of 4µm. For sample 2E, the radial growth rates were considerably smaller in comparison to those for Sample 2D, and the relationship between radial growth rate and pitch showed a more non-linear behaviour, with a relatively smaller increase in radial growth rate from 0.5µm pitch nanowires to those with a pitch of 4µm. Average nanowire diameters on Sample 2E ranged from ~150nm (0.5µm pitch) to ~870nm (4µm pitch). While the more non-linear dependence of the diameter on nanowire pitch observed for nanowires on Sample 2E is more promising for realisation of nanowires with diameters small enough that formation of an embedded NWQD is possible at a pitch that allows for interrogation of individual structures (greater than or equal to ~2µm), the much faster axial growth rate observed for nanowires on this sample may have an adverse impact on the ability to form sharp InAsP/InP interfaces within the nanowire structure.

Optical characterisation of nanowires on Samples 2D and 2E was performed using a low temperature non-resonant µ-PL setup. A schematic outline of the setup is displayed in Figure 2.13. Each sample was installed in an evacuated continuous flow helium cryostat operating at T≈10K, with nanowires excited by a 632.8nm HeNe laser. The laser was focused onto the sample using a 50X microscope objective lens with an NA of 0.42, giving an excitation spot size of ~2µm. PL spectra was observed to be similar across both samples for all nanowire pitches.

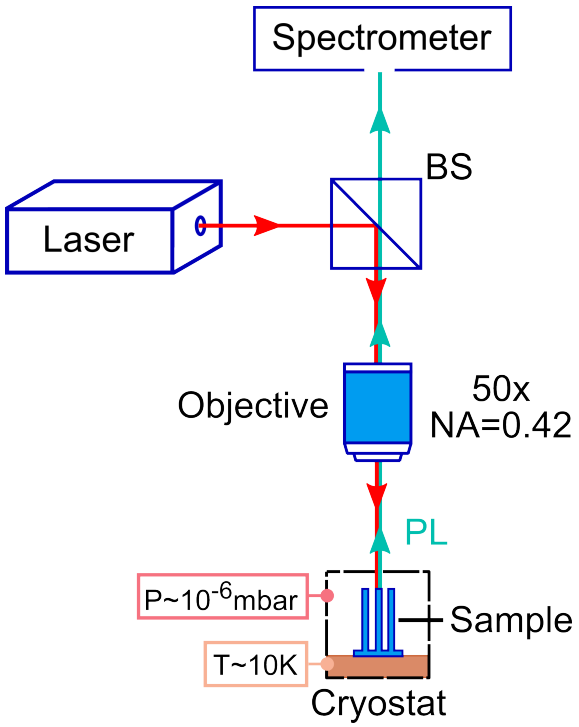

Figure 2.13: Simplified schematic diagram of the non-resonant, low-temperature µ-PL setup used for optical characterisation of nanowire samples. The incident non-resonant laser is directed by a beam splitter (BS) to an objective lens (50x, NA=0.42) which focuses the light onto the nanowire sample. The emitted PL from the sample is collected by the same objective lens, transmitted through the BS and then spectrally resolved using a single grating, 0.5m focal length spectrometer with a liquid nitrogen cooled charge coupled device (CCD). The spectrometer in this case had two gratings with 600 lines/mm and 1200 lines/mm, respectively, the latter providing a spectral resolution of ~130µeV. Each nanowire sample was mounted on the copper coldfinger of an evacuated continuous flow helium cryostat (Cryoindustries) in a vertical geometry, to enable excitation of and PL collection from the top facet of nanowires. During PL measurements, the coldfinger temperature was ~10K, with the pressure inside the evacuated chamber ~10^{-6}mbar.

Figure 2.14(a) displays representative PL spectra obtained from a number of separate locations across an array containing nanowires with 0.5µm pitch on Sample 2D. A broad range of emission energies were observed in all of the spectra, indicating that the nanowires were polytypic and consisted of both zinc-blende (ZB) and wurtzite (WZ) InP crystal phases. Emission occurs over this large spectral range due to the smaller bandgap and large negative band offset of ZB relative to WZ, which leads to the formation of a type-II heterojunction at each of the segment interfaces (along the growth direction). The lowest energy PL emission is governed by recombination of the electron in a bulk ZB region with a hole in the neighbouring WZ section of the nanowire, whilst the highest energy PL emission corresponds to the direct

recombination of an electron-hole pair in a WZ segment of the nanowire. Between these two limits, transitions can take place at any energy, dependent on the axial extent of each of the ZB/WZ segments in the nanowire. This is illustrated schematically in Figure 2.14(c). Based on low temperature band offsets presented previously in the literature, the lower and upper energy transition limits for polytypic InP nanowires are ~1.36eV and ~1.49eV, respectively [76]. If any of the ZB or WZ segments in the nanowire are sufficiently short, axial carrier confinement can occur. Therefore, for a nanowire with an appropriately small diameter, recombination of confined states in neighbouring ZB/WZ segments may resemble that of a quantum dot. Indeed, both single photon emission and cascaded photon emission has recently been demonstrated from such structural arrangements in InP nanowires, which are commonly referred to as crystal phase quantum dots [30, 77].

The PL emission at energies lower than ~1.36eV observed in Figure 2.14(a) is thought to correspond to collected photons originating from the lower bandgap InAsP section embedded within the nanowires. A clearer example of the PL emission detected at energies below this minimum energy associated with exciton recombination in polytypic InP nanowires is shown in Figure 2.14(b). No excited states were observed at higher pump powers in this case, so it is possible that the sharp line emission seen here was due to stacking faults within the InAsP region.

During SEM imaging of Sample 2E after growth, a number of broken nanowires on the sample surface that had originated from a nearby 0.5µm pitch array were observed. The exact cause of this localised detachment of nanowires from the substrate was unknown, but it provided the opportunity to undertake PL measurements on individual nanowires from this array. In addition, as the nanowire axis of these broken nanowires was oriented parallel to the plane of the substrate, probing of the nanowire structure as a function of length could be attempted, albeit with limited resolution owing to the relative size of the excitation spot (~2µm) and nanowire length in each case. PL spectra obtained at a number of different locations along the lengths of three separate broken nanowires (labelled NW-2A, NW-2B and NW-2C) on Sample 2E are displayed in Figure 2.15. For each nanowire, the excitation spot was manually

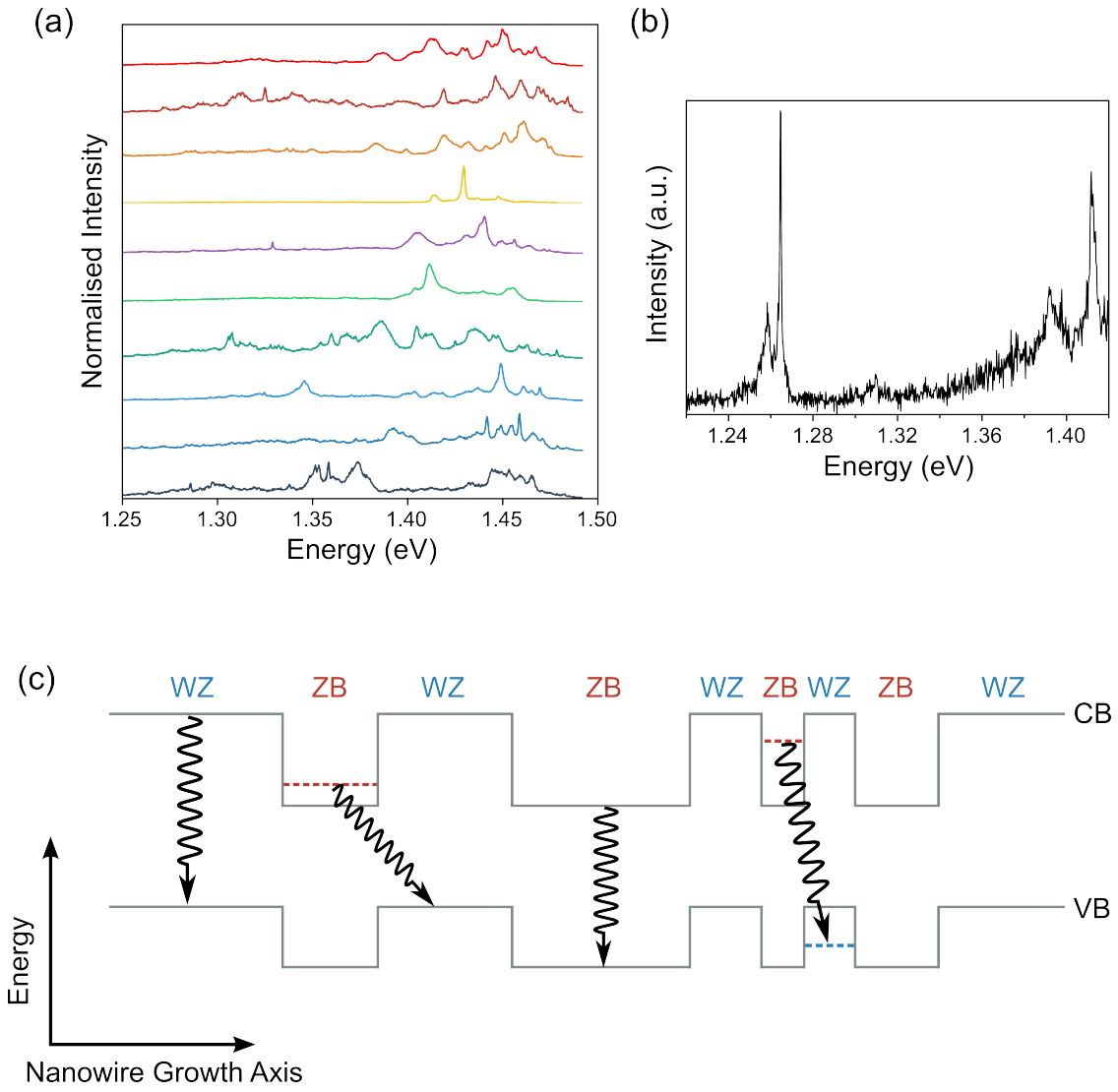

Figure 2.14: InP nanowire PL spectra. (a) Normalised PL spectra collected from different locations on a 0.5µm pitch array. For clarity, spectra are offset in y; (b) PL spectrum obtained from a 2µm pitch array; (c) Schematic band diagram illustrating carrier recombination in a polytypic nanowire. Four possible optical transitions are displayed. Dashed lines denote the confined energy states within the respective crystal phase. WZ – wurtzite, ZB – zinc-blende, CB – conduction band, VB – valence band.

scanned along its length using a set of piezo transducers attached to the microscope objective, which provided full motional control in the x, y and z directions over a small scanning area. The approximate location along the nanowire of the centre of the excitation spot from which the the associated PL spectrum was captured is indicated in Figure 2.15(d).

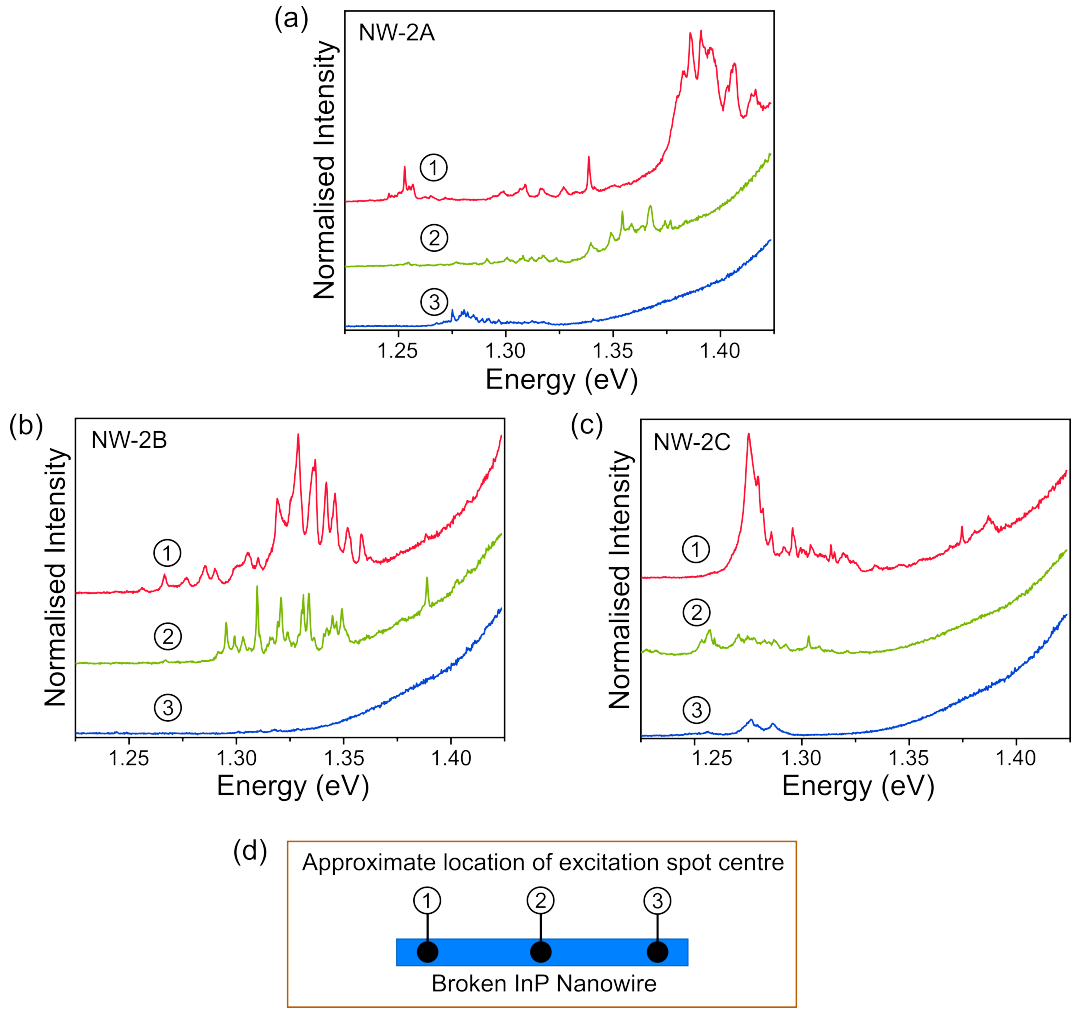

Figure 2.15: PL spectra from individual broken InP nanowires. (a) Normalised PL spectra obtained from NW-2A as the excitation spot was scanned along its length; (b,c) Equivalent PL spectra for NW-2B and NW-2C, respectively; (d) Schematic diagram showing the approximate location along the nanowire length of the excitation spot centre from which the associated PL spectra for each nanowire in (a,b,c) was obtained.

For each of the three nanowires, emission at energies lower than ~1.36eV was observed to become considerably more prevalent as the excitation spot was scanned from one end of the nanowire to the other. This indicated firstly that each nanowire contained an InAsP segment and that, as expected from the growth procedure and previous structural characterisation discussed above, it was localised in a region close to the nanowire tip. Similar to the spectrum presented in Figure 2.14(b), when exciting the nanowires at location ① (where the InAsP region was presumed to approximately reside) no evidence of state filling behaviour

was observed at energies below ~1.36eV. Coupled with the fact that there was such a large spectral range of emission below ~1.36eV when exciting at this location, it was assumed that the emission seen here was again due to stacking faults within the InAsP region. Due to the polarisation dependence of light absorption for nanowires in this horizontal orientation [78, 79], relative to the PL measurements on as-grown nanowires presented previously, higher excitation powers were required to observe PL emission from the broken nanowires. At these higher excitation powers, and with a comparitvely larger fraction of the excitation spot absorbed by the substrate, the emission from the substrate inhibited the characterisation of the rest of the internal nanowire structure for all three of the nanowires. Some emission corresponding to InP WZ/ZB transitions was observed however, most noticeably when exciting NW-2A at location ① where the InAsP segment was thought to be (roughly) located. Whilst in-depth structural characterisation of the individual broken nanowires on Sample 2E was restricted by substrate emission, the description of the nanowire internal structure provided by the PL measurements on the as-grown vertically oriented nanowires was clear enough that time consuming TEM measurements were not required in this instance.

The observed structural and optical properties of the nanowires on Samples 2D and 2E demonstrated that further optimisation of the growth conditions was required in order to achieve the overall aims of the growth study with this materials system. With this in mind, a new sample was grown utilising a double dilution PH_3 channel, which enabled flow rates between 5sccm and 50sccm to be measured. The previously employed flow rate of 60sccm, in contrast, was at the lower limit of what the mass flow controller monitoring the single dilution PH_3 channel could measure. In the report from which the initial growth conditions for this materials system were based upon, it was demonstrated that, along with an increase in growth temperature like that between Samples 2D and 2E, the transition from polytypic to pure single phase nanowires was induced through a reduction in the V/III ratio of the precursors. Sample 2E therefore was grown with a similar TMIn flow rate to that used in Samples 2D and 2E, but with a reduced PH_3 flow rate of 50sccm. A reduction in the V/III ratio was also observed to lead to a lowering of both the radial and axial growth rates of nanowires in this

report. In addition to a change in the V/III ratio, the growth time for the first InP section of the nanowires was reduced from 9 minutes to 4 minutes on Sample 2F, in an attempt to reduce the number of defects that were present on Sample 2E.

Figure 2.16 displays representative SEM images of nanowires formed after growth on Sample 2F. While nanowires in the 0.5µm and 1µm pitch arrays showed good height uniformity, the number of defects in these arrays had increased considerably in comparison to Sample 2E. Growth was not observed on the SiO_2 mask away from the patterned arrays on this sample, which implies that the defects nucleated within the nanoholes, but for a reason that is unclear, failed to produce the facets required for nanowire formation. As illustrated in Figure 2.16, the density of defects was observed to increase with increasing nanowire pitch. For the 0.5µm and 1µm pitch arrays, average nanowire diameters were similar to those on Sample 2E, although a number of nanowires in the 0.5µm pitch arrays were seen to have diameters down to ~110nm. The average height of nanowires with 1µm pitch on this sample was measured to be ~3.5µm.

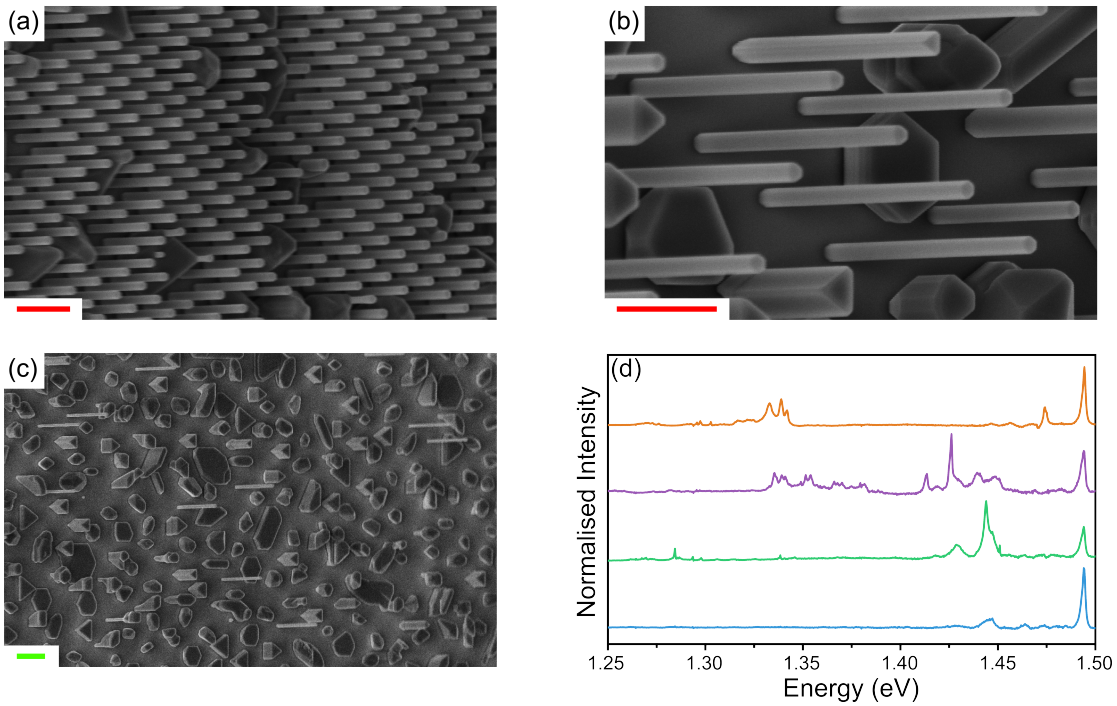

Figure 2.16: Characterisation of nanowires on Sample 2F. Angled SEM images show overviews of (a) 0.5µm pitch, (b) 1µm pitch and (c) 2µm pitch nanowire arrays. Scale bars (a,b) 1µm (c) 2µm; (d) Normalised PL spectra obtained from four separate locations across a 0.5µm pitch array. For clarity, spectra are offset in y.

The significant increase in defect formation observed for Sample 2F relative to 2E, indicates that there may only exist a very narrow range of conditions for which the PH_3 flow rate can be modified in the pursuit of reducing the nanowire radial and axial growth rates and still obtaining high nanowire yield on a substrate fully covered by the SiO_2 mask. Growth temperature and the TMIn flow rate are therefore left as the main controls on the nanowire growth rate in this case. However, another reason for the limited success of this growth run may have been that the 60sccm flow rate measured by the mass flow controller for Samples 2D and 2E was not accurate (being that it was at lower limit of what could be measured by this mass flow controller), and the difference in flow rates between the samples was actually considerably greater. Unfortunately, due to time constraints, it was not possible to address this issue here.

PL spectra obtained from nanowires with a 0.5µm pitch on Sample 2F are shown in Figure 2.16(d). An emission peak corresponding to the direct InP WZ free exciton transition at ~1.49eV is clearly seen in each spectrum, but the nanowires are once again recognised as polytypic, with emission observed over a broad range of energies below this transition energy, including emission at energies lower than ~1.36eV which may again be attributed to the InAsP segment embedded in each of the nanowires.

The results obtained from structural and optical characterisation of Sample 2F show that further optimisation of the growth conditions is evidently required. However, it is possible that a combination of pure phase nanowires growing with lower growth rates than was observed for Samples 2D–2F is simply unattainable on full coverage SiO_2 wafers. This is further discussed in Chapter 5.

2.5 Conclusion

The fabrication and growth of vertical GaAs and InP nanowire arrays using a catalyst-free approach has been described. For GaAs nanowires, two distinct growth modes were observed depending on the surface roughness of the planar GaAs growth surrounding the regions covered

by the SiO_2 growth mask. In contrast to most reports in the literature, when planar growth was observed to be rough, average nanowire height was observed to increase with increasing nanowire diameter. The high planar growth rate in this growth mode (>0.6nm/s) also influenced the nanowire growth rate, resulting in a height variation across individual arrays and a maximum average nanowire height of ~285nm. Through alteration of the fabrication procedure, smooth planar growth with a much reduced growth rate (<0.2nm/s) was accomplished. Nanowire formation in this growth mode followed the expected height-diameter dependence behaviour, and height uniformity was dramatically improved in comparison to that observed when planar GaAs growth was rough. Nanowires were also considerably taller in this growth mode, a result thought be caused by the decreased planar growth rate. Unlike axial growth, the influence of the planar growth surface roughness on nanowire radial growth was minimal, with radial growth observed to be strongly suppressed for all GaAs nanowire samples.

Taking into account the influence of planar growth on the reproducibility of GaAs nanowire growth, InP nanowire growth was performed on substrates fully covered by the SiO_2 growth mask. Control of nanowire growth rate on these full coverage substrates, however, proved to be much more challenging. Considerable variation in nanowire geometry across individual arrays was observed and at the edges of arrays, where the growth rate was highest, normal nanowire growth was typically replaced by unstructured growth. Although nanowire radial growth rate was observed to decrease with increasing growth temperature, both axial growth rates and defect density were seen to increase. A first attempt at reducing the axial growth rate and formation of defects at the highest growth temperature through reduction of the PH_3 flow during growth did not succeed. PL measurements also revealed that nanowires on all InP samples were polytypic. Therefore, further growth studies are required in order to obtain uniform arrays of pure phase nanowires with a much reduced defect density.

Chapter 3

Tailoring the Emission Properties of GaAs/InGaAs Nanowire Heterostructures Using Cross-Section Morphology Control

3.1 Introduction

Bottom-up growth techniques provide a number of appealing properties which make them of great interest for the development of nanowire-based light sources. These include the ability to both incorporate within the nanowire quantum dots (NWQD) exhibiting very narrow line-widths [5] and lithographically define the nanowire growth sites to enable formation of position-controlled single photon sources [6, 51] at the array-scale [7]. The layer-by-layer nature of bottom-up nanowire growth also naturally leads to the formation of an on-axis NWQD, ensuring efficient coupling of the NWQD emission to the fundamental guided mode of the nanowire. In addition, the incorporation of a NWQD within a nanowire enables tailoring of the optical emission properties of the NWQD through appropriate engineering of the

surrounding structure. Significant progress has been made in this regard, with the collection efficiency of NWQD emission into a single mode fibre exceeding 90% for deliberately tapered nanowire structures possessing dimensions optimised for a high photon emission rate into the fundamental optical mode [80].

As well as enhancing NWQD brightness and photon extraction efficiency, nanowire parameters can also be modified to tailor the polarisation properties of NWQD emission. Typically, nanowires formed through epitaxial growth exhibit a nominally cylindrical symmetry within the limits determined by the crystalline side facets developed during the growth process. As a consequence, the fundamental mode of the nanowire is quasi-degenerate and the nanowire structure supports two orthogonal linearly polarised modes. By altering the aspect ratio of the nanowire cross-section, the confinement strength of each mode within the nanowire structure can be controlled, providing potential for funnelling of the NWQD emission exclusively into a single linearly polarised mode. Coupling of single photons to a single optical mode of well defined energy and polarisation constitutes a model system for quantum optics experiments and provides the basis for attainment of advanced quantum information processing networks [10, 81, 82]. Experimental demonstration of nanowires with anisotropic cross-section has been achieved by top-down etching through a planar wafer [83], but this type of approach cannot produce the high quality nanowire facets enabled by bottom-up nanowire growth, nor can it easily allow for radial overgrowth of a shell passivation layer for reduction of the rate of non-radiative recombination via surface states.

In this chapter, polarisation control of the emission from an embedded on-axis NWQD in nanowires formed using a (catalyst-free) selective-area growth technique is demonstrated for the first time. Polarisation control is provided through the ability to determine the cross-section morphology of the nanowire prior to growth. The EBL patterning scheme and growth conditions that enable formation of nanowires with anisotropic cross-section are discussed in Section 3.3. PL measurements reveal that light emitted by an embedded quantum emitter within these elongated structures is strongly linearly polarised. As a means of describing the origins of this observation, the modal properties of infinite waveguides with anisotropic cross-

section are analysed in Section 3.4. In Section 3.5, the development of the growth scheme based on this modal analysis is described and results from PL measurements undertaken on NWQDs formed in optimised structures with elongated cross-section are presented. Finally, the broadband nature of the polarisation control exhibited by these elongated nanowire structures is demonstrated through 3D FDTD simulations in Section 3.6.

In the next section, a brief overview of NWQDs is presented, along with a discussion of the methods by which NWQD emission can be tailored through manipulation of the surrounding nanowire structure.

3.2 Background

3.2.1 Nanowire Quantum Dots

The unique optical properties of semiconductor quantum dots (QD) make them excellent building blocks for quantum photonic applications and their use has become widespread in the development of new light sources for nano-optoelectronic devices over the past few decades. Semiconductor QDs are most commonly formed via the Stranski-Krastanow (SK) technique [84], which involves the bottom-up epitaxial growth of a layer of semiconductor material on the surface of a lattice mismatched substrate composed of a semiconductor material that has a larger bandgap energy. SK growth enables formation of well-confined QDs exhibiting high quality optical properties [85], and successful demonstrations of single photon emission [86], quantum entanglement of emitted photons [87, 88] and measurements of cavity quantum electrodynamics [89] have been achieved with QD structures formed using this approach. However, although SK growth provides an ideal platform for study of novel phenomena from individual QDs, the random distribution of both size and location of QDs formed in this manner requires cumbersome post-selection of QDs with a desired location and emission properties for device integration. This presents an insurmountable barrier to significant scale-up, which is necessary, for example, to realise solid state implementations of quantum information pro-

tocols [9]. Consequently, much recent research in this area has centred around alternative QD growth techniques which allow for control over QD location and size.

One system that holds great promise in this regard involves incorporation of a QD within a vertical nanowire structure. As described in Chapter 2, deterministic control of nanowire location may be enabled through lithographic definition of the nanowire growth location, which in turn also grants the ability control the location of the incorporated nanowire quantum dot (NWQD). Although NWQDs have been demonstrated in a number of different configurations [90, 91] the most prominent consists of an axial heterostructure in the arrangement A/B/A, where the B section exhibits quantum confinement. NWQDs in this configuration grow epitaxially in a layer-by-layer fashion, and so control of the NWQD dimensions is provided in the lateral direction by the diameter of the nanowire at the time of NWQD formation and the axial direction by the NWQD growth time. The combination of this layer-by-layer growth and the small diameter range of the host nanowire structure also means that any lattice mismatch in heteroepitaxy is relieved much more effectively compared to SK QD growth. This allows for a much wider choice of material combinations as, unlike for SK QD growth which always produces a strained QD, lattice mismatch between the nanowire and NWQD materials is not a pre-requisite [92]. Another advantage of incorporating a QD in a nanowire is that the columnar structure of the nanowire acts to enhance the efficiency of light extraction from the NWQD. In contrast, photonic coupling to external optics for QDs embedded in a bulk matrix (SK growth) is highly inefficient on account of the large disparity between the refractive index of the matrix material and air/vacuum [90]. It has also been demonstrated that NWQDs grown in the (111) direction can have a theoretically vanishingly small fine structure splitting [93], which is an essential requirement for obtaining entangled photon pairs through the biexciton-exciton cascade.

Irrespective of the specific growth process (MBE, MOCVD, catalysed or non-catalysed, etc.) formation of a NWQD in an axial heterostructure configuration proceeds in the following manner: Nanowire growth is started with material A. After a certain time and for a selected nanowire length, the growth sources are altered and axial growth continues with a different

lower bandgap material B. When the desired length of the segment of material B is reached, the growth conditions are switched back to those used for nanowire formation. Growth eventually stops, leaving a nanowire composed of material A containing an embedded segment composed of material B. This formation process is depicted schematically in Figure 3.1. In order to realise a QD within the nanowire, the diameter of the nanowire at the point at which growth of the embedded segment occurs must be sufficiently small such that carriers are confined radially with the segment. Axial confinement is achieved by restricting the segment growth time so that it does not exceed ~1–10nm in height.

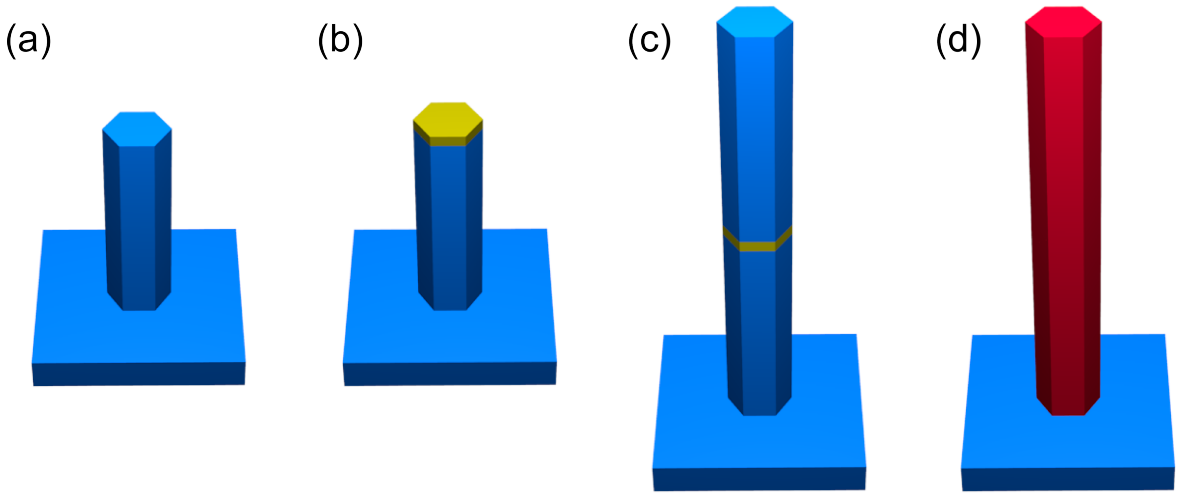

Figure 3.1: Schematic overview of the growth process for formation of an axial NWQD. (a) Initially, a nanowire is grown on a host substrate; (b) different elements are then introduced into the growth reactor for a short time to form a small region of semiconductor that has a lower bandgap than the nanowire base – this constitutes the NWQD; (c) following formation of the NWQD, growth continues with the original nanowire material; (d) if desired, after the targeted nanowire height is reached it may then be radially capped to passivate surface states.

The majority of axial NWQDs reported in the literature are those formed via the VLS growth mode, with demonstrations spanning a wide range of semiconductor materials combinations, including InGaAs/GaAs [94], GaAsP/GaP [95], GaN/AlN [96] and InAsP/InP where the most promising results with regards to exciton coherence times have been achieved to date [5, 97, 98]. Typically, however, properties of only a few NWQDs are described in these reports, and there is no reference to the overall uniformity of the sample. In addition, nanowires

are either randomly distributed on the sample or grown in very close proximity (a notable exception of this situation are the NWQD samples characterised by the Delft group [5, 97, 98]). With respect to both scale-up and isolation of single QDs for device applications, this presents challenges similar to those experienced for QDs formed by SK growth. In contrast, as nanowire growth locations are lithographically defined prior to the growth process, catalyst-free NWQD growth is an inherently position-controlled growth approach. Catalyst-free growth also offers the potential for higher quality axial interfaces and thus better confinement of carriers within the NWQD as it does not suffer from the catalyst 'reservoir effect' typically observed in VLS growth [41, 42]. In addition, using a catalyst-free growth approach for NWQD formation prevents the possibility of catalyst contamination of the nanowire, which may have a negative impact on the optoelectronic properties of both the nanowire and NWQD [39, 40].

Although, in comparison to VLS growth, progress in catalyst-free NWQD growth has been markedly slower, NWQDs exhibiting narrow emission linewidths in the InP/InAsP [4] and InGaAs/GaAs [6, 45] materials systems have been demonstrated. Furthermore, evidence of photon antibunching from individual InGaAs NWQDs embedded in homogeneous arrays of GaAs nanowires has been observed [7], providing a promising route for growth of uniform, readily scalable single photon sources. A similar growth approach to that described in Ref [7] is utilised for formation of the axial heterostructures presented in the following sections.

3.2.2 Tailoring of NWQD emission

In addition to providing deterministic control over the shape and location of QDs, the axial heterostructure configuration described in the previous section also enables tailoring of the optical properties of an embedded NWQD through modification of the surrounding nanowire structure.

In the most simple case, a dramatic transformation in the brightness and emission directionality of an on-axis NWQD can be achieved by varying the diameter of the nanowire host. Such a transformation occurs as a result of the change in the fraction of NWQD emission that

is coupled to the fundamental waveguide mode of the nanowire when the nanowire diameter is varied [99–101]. Calculations show that when the ratio between the nanowire diameter and NWQD emission wavelength is equal to 0.22, the coupling of the NWQD emission to the fundamental waveguide mode is at its highest and the brightness and directionality of the QD is maximised. For a particular nanowire diameter, the fraction of NWQD emission coupled to the fundamental mode also remains high (>90%) over a broadband wavelength range. This configuration therefore offers an advantage over placing a QD in a nanocavity, where enhancement of the QD emission rate can only typically be sustained over a very small wavelength range.

Although appropriate tailoring of the nanowire diameter can enhance the NWQD brightness and emission directionality, photons strongly confined in this sub-wavelength sized waveguide will scatter at large angles when leaving the nanowire end facet, severely limiting the collection efficiency of the emitted light [99]. For realisation of a truly deterministic single-photon source, a near-unity light collection efficiency is a fundamental requirement [98]. A significant increase in collection efficiency can be achieved by smoothly reducing the nanowire diameter from the NWQD location to the top facet the nanowire diameter [102]. In these needle-like structures, adiabatic conversion of the fundamental mode into a strongly deconfined mode occurs, resulting in the production of a comparatively narrower and more Gaussian far-field emission pattern [101]. The smoother the tapering of the structure is, the greater the enhancement of the collection efficiency, and structures with tapering angles down to ~1° have been experimentally realised, resulting in a reported single-mode fibre collection efficiency above 90% [80].

Nanowire morphology can also be engineered to manipulate the polarisation of NWQD emission. Owing to the cross-section symmetry of the structure, the fundamental optical mode of a waveguide with a cylindrical cross-section consists of two degenerate guided modes with orthogonal linear polarisation. By implementing a nanowire with anisotropic cross-section, the relative coupling strength of the NWQD emission to each of the two orthogonal modes can be controlled. Experimental demonstration of nanowires with anisotropic cross-section, formed

by top-down etching through a semiconductor mesa structure, has been previously reported and showed that only a relatively small increase in lateral aspect ratio is required for emission from an embedded QD to be strongly linearly polarised when collected from the nanowire top-facet [83]. Such a system would be particularly advantageous for a number of quantum information processing applications requiring linearly polarised photons for their operation, such as entanglement based protocols for quantum key distribution [103, 104], reducing the inevitable losses introduced by using linear polarisation optics. As described in the previous section, however, the random location of the self-assembled QDs in this type of approach necessitates considerable time searching for a nanowire-QD combination with suitable structural and optical properties, and is thus incompatible with scale-up. The inability to control QD location also results in a suppression of the QD emission rate, which is maximised when the emitter is centred on the nanowire axis [98]. In addition, the surface damage resulting from the etching process can reduce the optical quality of the embedded QD by creating a defective interface which acts as a trap for fluctuating charges [105]. Subsequent surface passivation is also difficult to achieve for these etched structures.

In the following sections, a technique for bottom-up growth of GaAs nanowires with anisotropic cross-section is presented. Appropriate tailoring of the nanowire cross-section dimensions is shown to result in the observation of strongly linearly polarised emission from an InGaAs axial segment grown within these elongated structures. This work represents the first demonstration of emission polarisation control in this manner using a catalyst-free growth approach and presents a promising route for the formation of uniform arrays of linearly polarised single photon sources. It should be noted that some of the results presented in the following sections have been published elsewhere [106].

3.3 Linearly Polarised Emission from Elongated GaAs/InGaAs Nanowire Heterostructures

3.3.1 Sample Fabrication and Growth

Catalyst-free bottom-up growth of GaAs/InGaAs nanowire heterostructures has been extensively studied at the University of Sheffield, resulting in the experimental demonstration of position-controlled NWQDs which show evidence of single photon emission [7]. Of interest therefore, was investigating methods by which this bottom-up growth technique could be developed further. An initial attempt at developing this growth approach (outlined in Chapter 2) involved the fabrication of pairs of nanoholes with varying separation to determine the minimum separation between pairs that could be implemented and still achieve successful individual nanowire growth. For nanowires in appropriately close proximity, there is the potential for optical interaction between single NWQDs in each individual structure. It is noted that growth of multiple spatially separate NWQDs along the axial direction of a single nanowire structure has been previously demonstrated using the same growth approach [7].

A schematic overview of the nanohole pair arrangement adopted for nanowire growth on Sample 3A* is displayed in Figure 3.2(a). As was the case for single nanowire growth presented in Chapter 2, the separation between each nanohole pair was set at 4µm, whilst the separation, x, between individual nanoholes forming the pair was varied from 0nm upto 200nm. As a result of the small separation between them, enlargement of individual nanoholes caused by EBL patterning proximity effects was observed after fabrication. This enlargement was of particular importance for patterned pair separations of zero, as it caused the resultant holes to be overlapped. For a patterned nanohole diameter of ~100nm, a final nanohole diameter of ~130nm was typically observed.

*Sample 3A corresponds to growth sample reference MR3352 grown by Dr. Andrew Foster [55].

Nanowire growth on Sample 3A followed the same bottom-up growth process utilising low pressure MOCVD as described previously in Chapter 2. The substrate was first annealed for 9 minutes under an AsH_3 overpressure at 780°C. In preparation for growth, the temperature was then lowered to 750°C, with the AsH_3 overpressure maintained. Nanowire growth commenced with the simultaneous closure of the AsH_3 overpressure supply channel, and introduction into the reactor of TMGa with a flow rate of 33sccm and AsH_3 with a flow rate of 15sccm maintained by a double dilution channel. After 3 minutes of GaAs growth, TMIn was then introduced into the reactor for ~3s in an attempt to form an InGaAs NWQD within individual nanowire structures. Unlike TMGa (and AsH_3), TMIn is a solid source, and therefore the concentration of indium within a certain (H_2) carrier gas flow can fluctuate over time. This meant that, between growth runs, the the carrier gas flow through the TMIn source bubbler had to be varied in order to achieve the measured concentration of TMIn that was desired for NWQD formation. For this growth run, the measured TMIn concentration was approximately 0.02% in a total H_2 flow of 200sccm. Based on the results from previously characterised InGaAs quantum wells grown in the MR350 reactor used for nanowire growth, this concentration was estimated to produce an InGaAs NWQD with a ~20% indium fraction. Nanowire growth was then completed by switching off the TMIn source and continuing GaAs growth, using the same TMGa and AsH_3 flow rates as those used previously, for a further 7 minutes. At the end of the nanowire growth, with the TMGa channel closed, the AsH_3 flow rate was switched back to that used during the pre-growth annealing step (40sccm) and, in an effort to to provide a degree of surface passivation of the nanowire sidewalls, a PH_3 flow of 300sccm was simultaneously introduced into the reactor as the sample cooled down. Using these growth conditions, a sequence of growth modes correlating to the separation between a nanohole pair were observed.

When the nanohole pair separation was sufficiently large, individual nanowires were successfully realised with measured edge-to-edge separations down to ~10nm. An example of a nanowire pair formed in this configuration after growth is shown in Figure 3.2(b). The nanowires in this instance had a height of ~2µm and a diameter of ~190nm, corresponding

to radial growth of ~30nm. It was found that, for the same fabricated nanohole size, the diameter and height of an individual nanowire forming a pair was not the same as that for an isolated single nanowire grown on the same sample. This is thought to be a result of the close proximity of the individual nanowires in a pair, which alters the growth dynamics around the pair site [65].

As nanohole separation was decreased, the resulting nanowire growth initially became random, switching between formation of non-uniform pairs and single amorphous structures as displayed in Figure 3.2(c). Further reduction of the nanohole separation beyond a critical point, however, led to complete suppression of pair growth and instead single structures with an elongated cross-section were formed. An example of one of these elongated structures is shown in Figure 3.2(d).

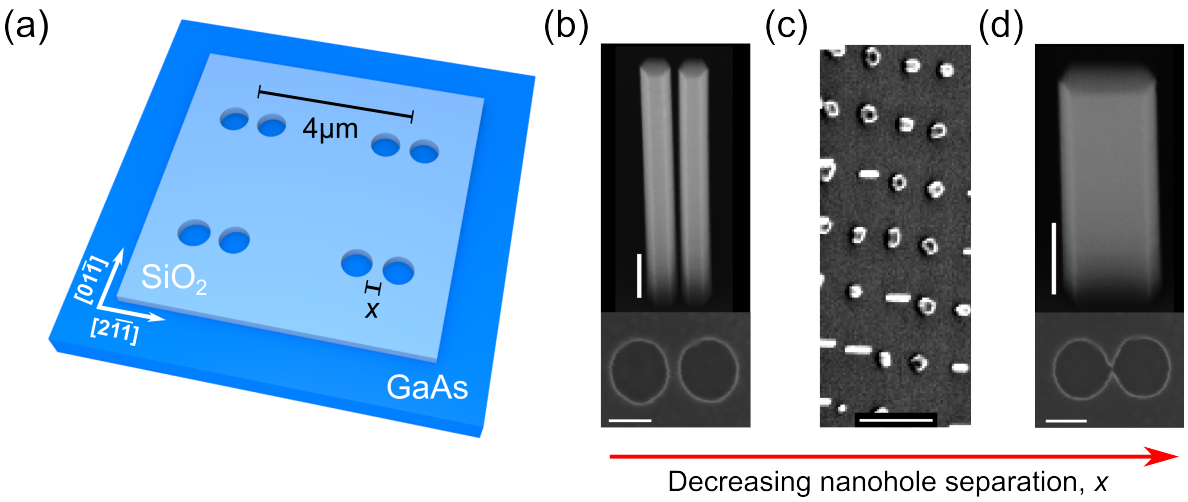

Figure 3.2: Nanowire growth from closely spaced nanohole pairs. (a) Schematic diagram of nanohole pair arrangement adopted for nanowire growth on Sample 3A. The edge-to-edge separation between individual nanoholes constituting a pair, x is varied from 0nm upto 200nm, with the separation between each pair fixed at 4μm; SEM images show, as a function of decreasing x, (b) a nanowire pair with edge-to-edge separation of ~10nm, (c) random growth, with formation of non-uniform pairs and single amorphous structures, (d) a single structure with elongated cross-section. The lower panels in (b) and (d) display the nanohole pair layout from which the resulting structures above were formed. (b,d) Upper scale bars 200nm, lower scale bars 100nm. (c) Scale bar 5μm. Image reproduced with permission from [55].

Comparison of fabricated nanohole separation and resulting nanowire structure after growth revealed that an elongated nanowire was only formed if either the edges of the nanoholes were touching or they were overlapped. In the first case, the initial pyramidal islands which form separately within the nanoholes are thought to coalesce immediately upon the development of the vertical nanowire facets, which leads to a single elongated nanowire rather than the unstructured growth observed in Figure 3.2(c). As well as those oriented in the $[2\overline{1}\overline{1}]$ direction (90° relative to the major-flat orientation), nanohole pairs were also fabricated in the $[01\overline{1}]$ (0° relative to the major-flat orientation) direction on this sample. For the elongated structures formed along the $[2\overline{1}\overline{1}]$ direction, the dimension in the direction perpendicular to this orientation (and the nanowire axis) was defined by the nanohole diameter (and radial growth), and was measured to be ~180nm.

In the direction of elongation, the length was a function of the extent to which the nanoholes were overlapped and was found to have a maximum value of ~300nm (nanohole edges just touching). The volume of material deposited for the single elongated structures formed along this direction was therefore approximately the same as that for a pair of nanowires in close proximity. For structures formed along the $[01\overline{1}]$ direction, the development of {110} facets during growth leads to elongated structures with a different cross-section profile when compared to those in the $[2\overline{1}\overline{1}]$ direction and more importantly a much reduced cross-section aspect ratio. Figure 3.3 displays top-down SEM images of elongated nanowires formed along the $[2\overline{1}\overline{1}]$ and $[01\overline{1}]$ direction (from a nanohole pair), respectively, alongside a schematic outline of the posited arrangement of the individual nanowires that constitute the single elongated structure in each instance. It is important to note here that as nanowire formation proceeds via layer-by-layer assembly of material during growth, the InGaAs axial structure in an elongated nanowire is likely itself to have a cross-section which is anisotropic, with the level of anisotropy dependent on the dimensions of the surrounding nanowire.

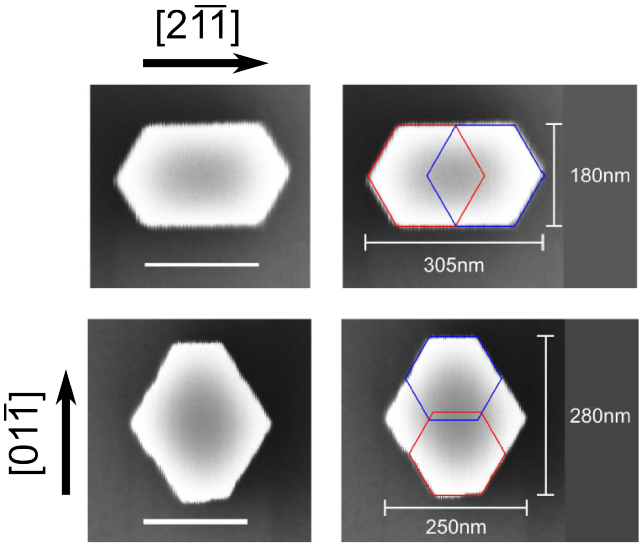

Figure 3.3: Top-down SEM images of nanowires with elongated cross-section formed from orthogonally oriented nanohole pairs with $x \approx 0$nm (i.e. edges just touching). The coloured outlines in the right hand panels depict the posited arrangement of the individual nanowires that constitute the single elongated structure in each of the left hand panels. It is observed that as well as possessing a different cross-section profile, the nanowire elongated along the [01$\bar{1}$] direction (bottom-panels) also has a much reduced cross-section aspect ratio when compared to the structure formed along the [2$\bar{1}\bar{1}$] direction (top-panels). SEM images taken with permission from [55].

3.3.2 PL Measurements

To characterise the influence of nanowire morphology on the emission properties of the embedded InGaAs region, polarisation-dependent PL measurements were undertaken on two orthogonally oriented elongated nanowires with the same dimensions as those labelled in Figure 3.3, and a nanowire with normal hexagonal cross-section from the same sample. Measurements were obtained using the µ-PL setup shown in Figure 2.13, with the addition of a linear polariser with high extinction ratio ($>10^8$) and a half-wave plate into the collection path. The half-wave plate was included to take into account the polarisation sensitivity of the spectrometer and ensure all light passing through the polariser (at a particular polarisation angle) was collected by the CCD.

The non-polarised, low power PL emission obtained from the embedded InGaAs region in each of the elongated nanowires is displayed in the left hand panels of Figure 3.4(a) and Figure 3.4(b). Overall, the fraction of elongated nanowires that were observed to contain an optically active emitter on this sample was less than 50%, indicating that further optimisation of the growth procedure for these structures was needed. For each orientation, the ground state PL emission peaks at low excitation powers are relatively broad with a FWHM on the order of several meV. This was thought to be a result of a reduction in carrier confinement caused by the radial extension of the InGaAs region in these elongated structures.

For each of the three nanowire morphologies, polarisation-resolved PL spectra were taken in 15° angular steps, using a ~5s accumulation time. The instability of the optical setup meant that, at each angular step, it was necessary to realign the excitation laser spot onto the nanowire through observation of a maximised signal on the CCD. Realignment of the laser on each nanowire was only possible however, by increasing the excitation power (to obtain an adequate count rate in ~1s), which resulted in additional broadening of each ground state emission line as illustrated in the right hand panels of Figure 3.4(a) and Figure 3.4(b). The acquired spectra at each angular step were then integrated (with the background count rate subtracted) over the wavelength range encompassing the observed PL emission peak from the InGaAs structure in each nanowire.

Figure 3.5 displays a plot of the normalised polarisation-dependent (integrated) PL intensity for each of the three nanowire morphologies. The scatter in data points was caused by the instability of the optical system used for PL measurements as described above. From this figure, it is clearly observed that the emission behaviour from the InGaAs region in the nanowires with elongated cross-section is notably different from that of a normal hexagonal nanowire. Light emitted from a nanowire with elongated cross-section is observed to be strongly linearly polarised, with the orientation of polarisation coincident with the axis of elongation. Similar emission behaviour has been reported previously in the case of SK grown QDs embedded in etched nanopillars with anisotropic cross-section [83]. For a normal hexagonal nanowire, the emission shows instead only weak linear polarisation.

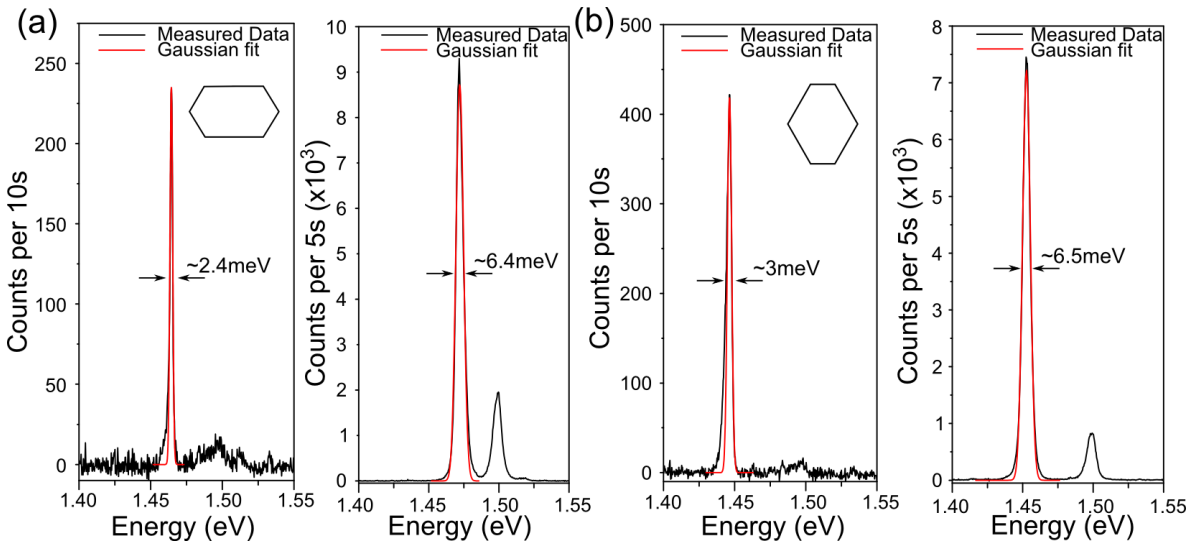

Figure 3.4: Non-polarised PL emission from an embedded InGaAs region within an elongated nanowire structure. (a) PL spectrum obtained from a elongated nanowire formed in the $[2\bar{1}\bar{1}]$ direction at (left-panel) low excitation power (~2nW) and (right-panel) higher excitation power (~230nW) corresponding to that used for polarisation-dependent measurements; (b) Same as (a) but for an elongated nanowire formed in the $[01\bar{1}]$ direction. Excitation powers used for this nanowire were (left-panel) ~1nW and (right-panel) ~80nW, respectively. Images taken with permission from [55].

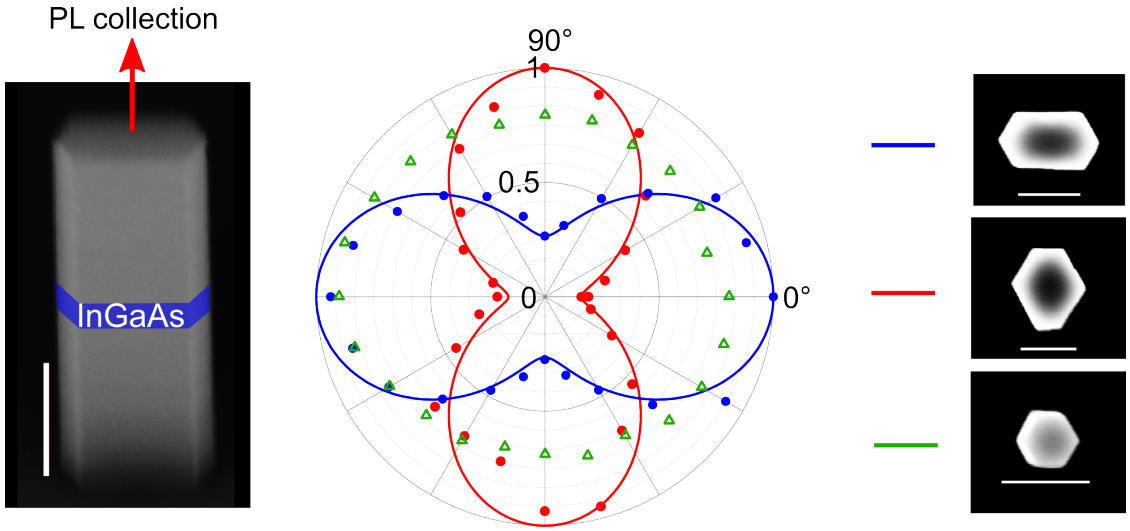

Figure 3.5: Normalised, polarisation-resolved PL measurements for three different nanowire morphologies. Integrated PL intensity for a normal hexagon (green triangles) and elongated nanowires oriented in the $[2\bar{1}\bar{1}]$ direction (blue circles) and $[01\bar{1}]$ direction (red circles) is displayed as a function of polariser collection angle. Solid lines depict cosine curve fits to the data. Emission is collected from the top facet of each nanowire, as illustrated in the annotated SEM image on the left of the figure. Scale bars 200nm. SEM images taken with permission from [55].

The degree of polarisation (DOP) for the three nanowire morphologies is quantified using the ratio DOP = $(I_{\max} - I_{\min})/(I_{\max} + I_{\min})$, where $I_{\min}$ and $I_{\max}$ are the minimum and maximum integrated PL intensities, respectively. For the elongated nanowire oriented along the $[2\overline{1}\overline{1}]$ direction, this value was calculated to be ~61%, while for the nanowire oriented along the $[01\overline{1}]$ direction it was ~72%. The DOP value calculated for a normal nanowire was observed to vary slightly from nanowire to nanowire, with an average value of ~10%. This agrees with previous observations made for hexagonal nanowires containing InAsP NWQDs [107].

In order to explain the results obtained above, and determine the dependence of nanowire cross-section anisotropy on the extent to which emission from the embedded InGaAs region is linearly polarised, analysis of the modal properties of these structures was performed. The results of this analysis are presented in the following section.

3.4 Modal Properties of Infinite Waveguides with Hexagonal Cross-Section

The angular frequency, w and wavevector, k of an electromagnetic mode are related by $\omega = c|\mathbf{k}| = c\sqrt{k_x^2 + k_y^2 + k_z^2}$, where k_x, k_y and k_z are orthogonal components of $|\mathbf{k}|$ and c is the speed of light. In free-space, electromagnetic modes correspond to plane waves; for a certain value of k_z, k_x and k_y can take any value, meaning ω is always greater than or equal to the light line $\omega = ck_z$. This continuous spectrum of electromagnetic modes forms the light cone, a region which defines solutions of Snell's law [108].

Introduction of a planar structure with refractive index, n_s leads to the generation of a new set of electromagnetic modes that exist below the light line. As $n_s > n_{\text{free-space}}$, these modes have lower frequencies relative to the corresponding modes in free-space and are localised within the region of the structure. Defining $k_{||}$ and $k_{\perp}$ as the wavevectors parallel and perpendicular to the interface between the planar structure and free-space, the only modes in free-space

below the light line $\omega = ck_{\parallel}$ are those with imaginary $k_{\perp}$, which correspond to fields that decay exponentially away from the structure. This localisation of the fields in the direction perpendicular to the interface leads to the formation of a set of discrete 'index-guided' modal frequencies below the light line, $\omega_m(k_{||})$.

Consider first as a simple nanowire approximation, an infinite cylindrical GaAs (n_{GaAs}=3.45) waveguide with circular cross-section surrounded by an air (n=1) cladding. The series of lowest-order index-guided modes for this system, calculated using the MIT photonic bands (MPB) software package [109], are displayed in Figure 3.6(a). For quantum information applications, coupling of the emission from a quantum emitter into a single electromagnetic mode is desired [110–113], but here the fundamental guided mode (diameter to wavelength ratio, $a/\lambda < 0.233$) is two-fold degenerate as a result of the symmetry of the structure. This symmetry can be broken through elongation of the structure along one of its cross-section axes, which lifts the fundamental mode degeneracy and creates two orthogonally linearly polarised modes oriented along the major and minor axes, M_x and M_y. For a particular wavelength, changing the aspect ratio of the elongated structure by only a moderate amount ($\sim$2:1) leads to a large optical anisotropy; the majority of M_y is expelled into the air cladding whilst M_x remains tightly confined inside the structure. The dispersion relation and modal electric field profiles for this situation are depicted in Figure 3.6(b) and Figure 3.6(c). A dipole emitter within this structure will therefore preferentially couple to this single mode, with the coupling efficiency being maximised when the emitter is on-axis, where the strength of the electric field of M_x, E_x is greatest.

The experimental realisation of linearly polarised quantum light sources that exploit the optical anisotropy described above, has been reported for the case of etched nanowires [83]. In this top-down approach, there is potential for bright, high quality single photon emission from the top of the nanowire structure as QDs can be grown using well-established techniques (e.g. SK growth by MBE) and their axial location within the structure can easily be defined, allowing integration of a distributed Bragg reflector or equivalent [114] However, due to the limitations in controlling the radial position of the embedded QD in this type of system,

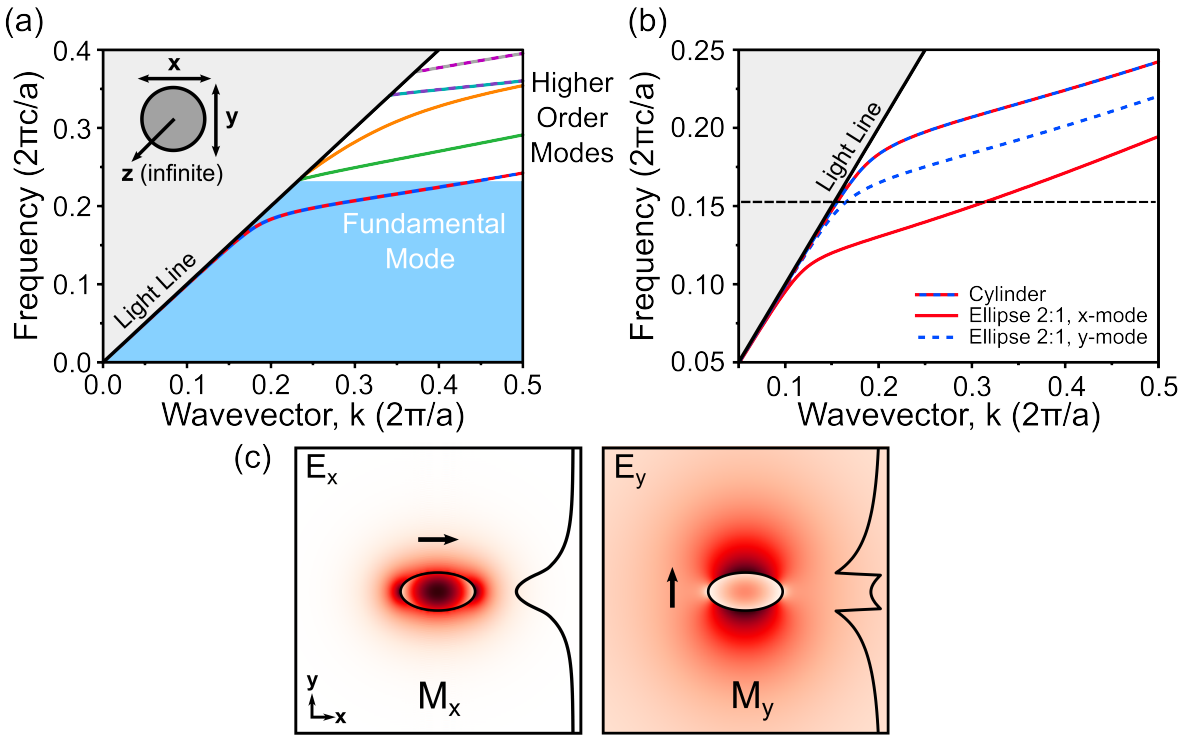

Figure 3.6: Modal analysis for infinite GaAs waveguides (surrounded by air cladding) with circular and elliptical cross-section. (a) Dispersion relation for a cylindrical waveguide with diameter a. The x-axis and y-axis are in dimensionless units, with wavevector k spanning the range of the first Brillouin zone. Two-tone dashed lines correspond to doubly degenerate modes and the blue shaded region indicates the frequency range in which only the fundamental mode is supported by the waveguide; (b) Fundamental mode dispersion relation for an elliptical waveguide with minor axis length a and aspect ratio of 2:1 (x-polarised mode red line, y-polarised mode blue dashed line). The fundamental mode for the cylindrical waveguide in (a) (red and blue dashed line) is displayed for comparison; (c) In-plane electric field components associated with the x and y polarised modes, M_x and M_y, for the elliptical waveguide modelled in (b) at frequency $f{=}a/\lambda{\approx}0.151$ (indicated by black dashed line in (b)). The field components are normalised in such a way that $\int\epsilon|\mathrm{E}\ x,y|^2\,d^2x{=}1$, where the integral is calculated over the infinite plane perpendicular to the waveguide axis, z and ϵ is the relative dielectric permittivity at each point across the plane. The development of the electric field for M_x and M_y in the y-direction at $x{=}0$ is depicted on the right of each plot.

efficient coupling between the QD and the fundamental M_x mode is difficult to achieve. The surface damage induced by the etching process can also degrade both the optical quality and emission rate of the embedded QD.

Bottom-up growth of nanowire-QD structures in contrast, naturally leads to the creation of an on-axis embedded emitter and high quality sidewalls. The facet-led growth process in this system however, restricts the extent to which the morphology of the nanowire can be modified, and so a cylindrical nanowire cannot be obtained. Figure 3.7(a) displays the dispersion relation

for an infinite wire with hexagonal cross-section, along with that for the previously modelled cylindrical wire above for comparison. It is observed that the shift to a hexagonal morphology only marginally lifts the degeneracy of the fundamental mode, and so the previous modal analysis carried out on the cylindrical wires above provides an appropriate approximation for these faceted structures. This is illustrated in Figure 3.7(b) and Figure 3.7(c), which display the dispersion relation and modal electric field profiles for an elongated hexagonal structure with an aspect ratio of 2:1. Although the x and y modes are shifted slightly in frequency when compared to an elliptical structure of the same aspect ratio, the evolution of the modes with wavevector k, is almost identical.

The dispersion relations and modal electric field profiles above are useful in providing a qualitative description of the degree of confinement at a particular wavelength for each of the linearly polarised modes, but in order to better characterise how the aspect ratio of the cross-section influences this degree of confinement, it is more relevant to measure the fraction of the mode energy that is contained within the nanowire (FME). Figure 3.8 displays the FME as a function of frequency for nanowires with an aspect ratio of 1.5:1, 2:1 and 3:1 respectively. Though the modification of one of the lateral dimensions of the nanowire affects the degree of confinement of the mode along the other (i.e. they are not entirely independent parameters), as the nanowire becomes more anisotropic, the relative confinement of the two modes becomes progressively disparate. Therefore, increasing the aspect ratio should presumably lead to a more efficient coupling between an embedded emitter and the single linearly polarised mode along x. However, the radial dimensions of catalyst-free NWQDs are governed primarily by the dimensions of the surrounding nanowire, and so in order to successfully realise a NWQD with appropriate lateral confinement of carriers, there must be a limitation on the length of the longest dimension of the nanowire. The facet-led nature of nanowire formation may also prohibit the maximum aspect ratio that can be achieved during growth.

To illustrate both the rise in the disparity between the FME for the two linearly polarised modes as the aspect ratio is increased and how modifying one of the lateral dimensions of the nanowire affects the degree of confinement of the mode along the other, the approximate FME

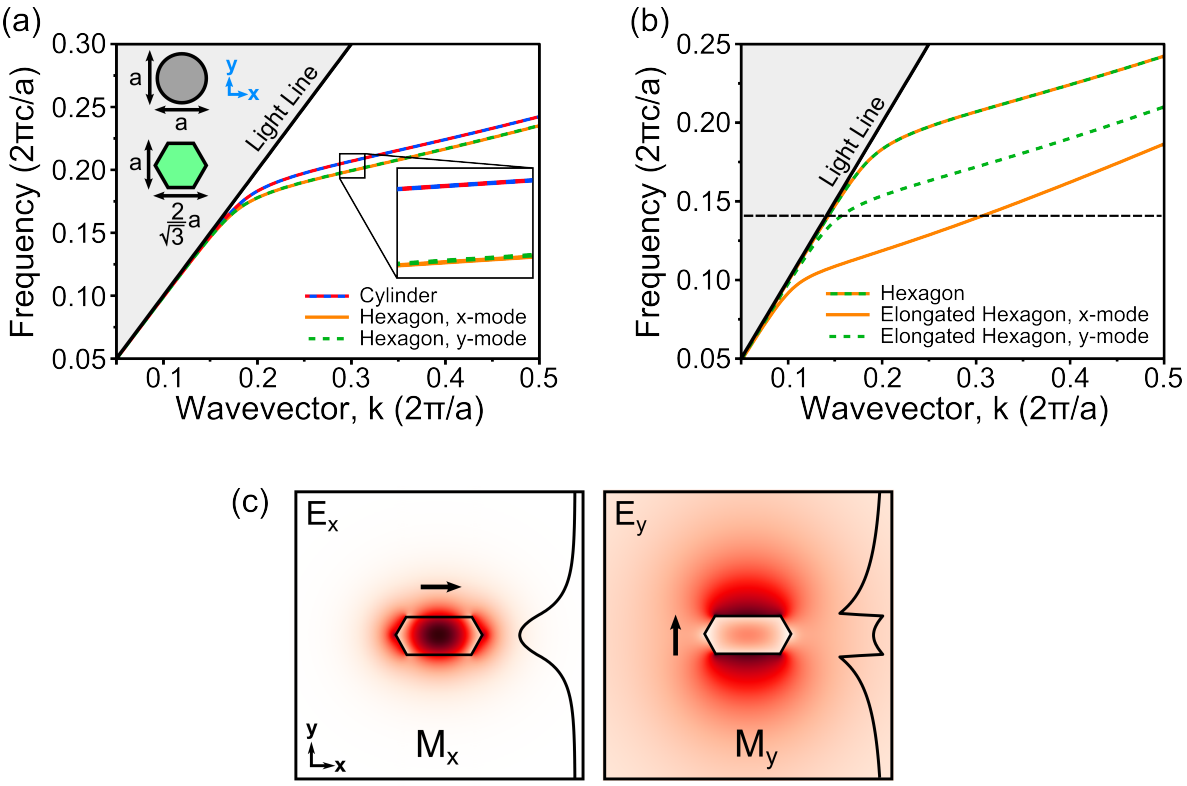

Figure 3.7: Nanowire fundamental mode analysis. (a) Dispersion relations for the fundamental modes of infinite nanowires with circular and hexagonal cross-sections. The inset highlights the weak non-degeneracy of the fundamental mode in the hexagonal case; (b) Fundamental mode dispersion relation for an elongated hexagonal nanowire with short axis length a and aspect ratio of 2:1 (x-polarised mode: orange line, y-polarised mode: green dashed line). The fundamental mode for the regular hexagonal nanowire in (a) (green and orange dashed line) is displayed for comparison; (c) In-plane electric field components associated with the x and y polarised modes, M_x and M_y, for the elongated nanowire modelled in (b) at frequency $f{=}a/\lambda{\approx}0.140$ (indicated by black dashed line in (b)). Again, the development of the electric field for M_x and M_y in the y-direction at $x{=}0$ is depicted on the right of each plot.

values for each mode associated with a nanowire structure of minor axis length a=100nm at the mode wavelength λ_M=860nm, for each of the aspect ratios displayed in Figure 3.8, are presented in Table 3.1. These parameters were chosen to reflect the intended minor axis length of the structures (from the patterned nanohole sizes) in Section 3.3.1 and the approximate PL emission wavelengths measured in Section 3.3.2.

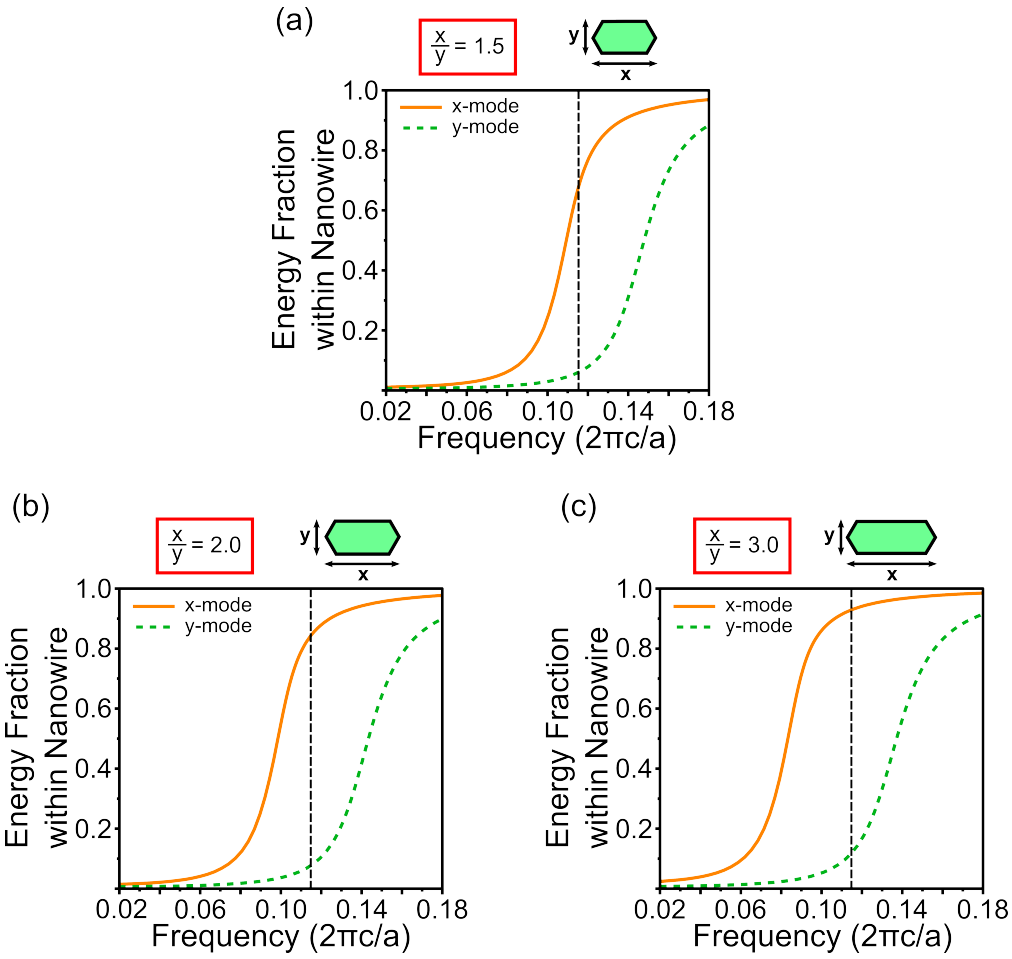

Figure 3.8: Fraction of modal energy for M_x and M_y contained inside nanowires with aspect ratios of (a) 1.5:1, (b) 2:1 and (c) 3:1 (where 1=a=100nm), as a function of frequency. The black dashed lines on each plot signify the relative mode energy fractions, FME at $f=a/\lambda_M$=100nm/860nm≈0.116 for each aspect ratio, the values of which are stated in Table 3.1.

Aspect Ratio	x_{FME} (%)	y_{FME} (%)
1.5:1	10	3
2:1	67	6
3:1	94	11

Table 3.1: Approximate values of FME for x and y modes associated with nanowire structures of varying cross-section aspect ratios at λ_M=860nm. Here 1=a=100nm.

The calculated values in Table 3.1 suggest that the aspect ratio which best satisfies the conditions of maximum emitter-mode coupling efficiency combined with reduced NWQD size is the ratio of 2:1. Although there is only a small difference in size along the long axis,

the difference between x_{FME} and y_{FME} (and also the confinement of x_{FME} at this mode wavelength) for the ratio of 1.5:1 relative to 2:1 is significant, whereas those of 3:1 and 2:1 are comparatively small considering the larger difference in size.

The modal analysis presented above provides an insight into the origins of the linearly polarised PL emission observed from the elongated nanowire structures described in the previous section. However, the DOP value calculated for the structure oriented along the $[01\bar{1}]$ direction is both much higher than expected from the results determined here and higher than the DOP value calculated for the more anisotropic structure oriented along the $[2\overline{11}]$ direction. One plausible explanation for this discrepancy between theory and experiment is that the intrinsic properties of the embedded InGaAs emitter also have an influence on the form of the PL emission that is collected from the top of the nanowire. Linearly polarised PL emission has previously been reported for the case of elongated QDs [10, 115], and due to the nature of NWQD formation in bottom-up growth, it is reasonable to assume that the NWQDs in these structures are themselves elongated to a certain degree. Tailoring the degree of elongation for a NWQD in this system is challenging though, and the extent to which a particular NWQD geometry influences the emission is not clear. The ability to control the polarisation through nanowire morphology therefore is a more appealing option, and recognising the limits on morphology control that could be achieved with the previously implemented growth approach, a new scheme was developed as discussed in the following section.

3.5 Development of the Growth Scheme

It was observed in the previous sample (Sample 3A) that formation of a single elongated structure only occurred during growth when the separation between the nanoholes constituting a nanohole pair was smaller than a certain threshold value (~10nm). This therefore sets an upper boundary on the amount of cross-section anisotropy that can be achieved for an individual nanowire in this patterning scheme.

One apparent way of overcoming this fundamental restriction with respect to nanowire morphology control would be to simply pattern arrangements containing more than two closely spaced nanoholes, with the desired cross-section anisotropy defining the amount of extra nanoholes required. It was observed, however, that the incidence of single elongated nanowire formation (rather than random unstructured growth) for nanohole triplet arrangements, which were also patterned on Sample 3A, was significantly smaller than for nanohole pairs with equivalent patterned separation. With this in mind, single elongated nanoholes (nanoslots) were patterned on a new sample (Sample 3B[†]) as an alternative method to overcome this limitation in controlling nanowire morphology. As elongated nanowires were found to form from overlapped nanohole pairs in Section 3.3.1, it was reasonable to assume that growth of such a structure from a single elongated site was possible.

3.5.1 Sample Fabrication and Growth

Both nanohole pairs and nanoslots were patterned along $[01\bar{1}]$ and $[2\bar{1}\bar{1}]$ directions as in the previous sample, and also additionally along the $[\bar{1}12]$ direction (60° relative to the major-flat orientation). Elongated nanowires formed along the $[\bar{1}12]$ direction were expected have the same morphology as those formed along the $[2\bar{1}\bar{1}]$ direction by virtue of how the facets develop during growth (see Figure 3.9), and therefore could provide a further demonstration of the modelling results described in the previous section. The $[01\bar{1}]$ direction was included again so that a comparison between the emission from weakly and strongly anisotropic nanowire structures could be made.

PL measurements on Sample 3A revealed that less than half of the formed nanowires on this sample contained an optically active InGaAs emitter. In an effort to try and increase this fraction on Sample 3B, the process of forming an InGaAs region during growth of the nanowires was repeated four times, with slight alterations in the conditions for each repeat. The first two InGaAs regions were grown with a TMIn concentration of 0.02% in a total H_2

[†]Sample 3B corresponds to Sample 2C described in Chapter 2 (growth reference, MR3575).

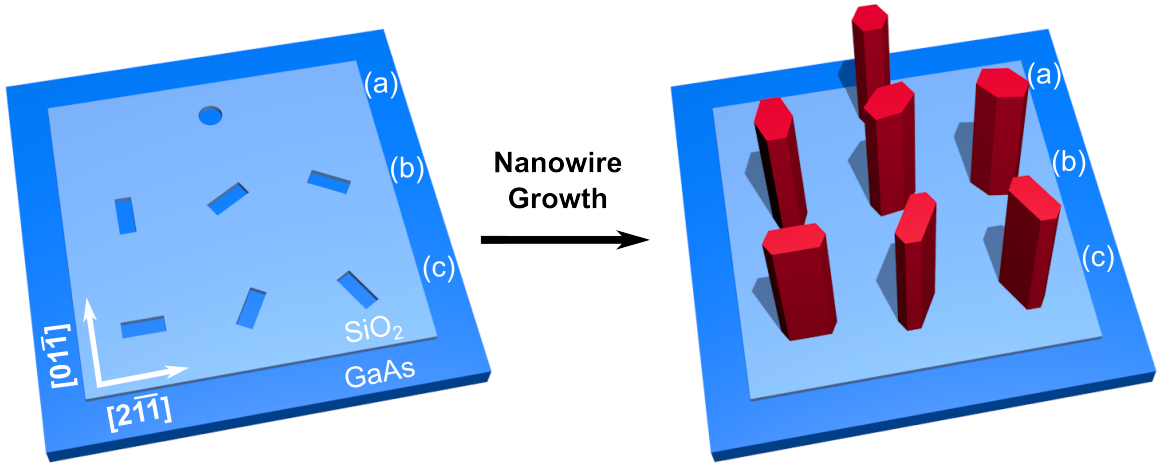

Figure 3.9: Nanowire morphology control. Considering the crystal orientation of the substrate, there are six most logical orientations of the patterned nucleation sites (depicted here as nanoslots) to form elongated nanowires after growth. (a) Reference: a nanohole patterned in the SiO_2 dielectric layer leads to formation of a regular hexagonal nanowire with six {110} facets; (b) Nanoslots elongated along the [01$\bar{1}$], [10$\bar{1}$], and [$\bar{1}$10] directions lead to formation of nanowires with low cross-section aspect ratio; (c) Nanoslots elongated along the [2$\bar{1}\bar{1}$], [$\bar{1}$12], and [$\bar{1}$2$\bar{1}$] directions lead to formation of nanowires with high cross-section aspect ratio.

flow of 200sccm, with growth times of 2s and 4s, respectively. The subsequent two InGaAs regions had growth times of 2s and 4s respectively again, but with a TMIn concentration of 0.04% in 200sccm of H_2. Each InGaAs region was separated by 180s of GaAs growth, and a final 90s of GaAs growth was used to cap the uppermost InGaAs region. Finally, as in all other previous nanowire growths, the sample was cooled under an overpressure of PH_3 and AsH_3. The TMGa and AsH_3 precursor flows during nanowire growth and the AsH_3 and PH_3 precursor flows during the cooling stage were the same as those used in the growth of Sample 3A. For reference, the conditions used for nanowire growth on Sample 3B are summarised in Table 3.2.

Figure 3.10 displays representative SEM images of nanowires grown from nanoslot sites oriented along [2$\bar{1}\bar{1}$], [$\bar{1}$12] and [01$\bar{1}$] directions on Sample 3B. As predicted (and illustrated in Figure 3.9) nanowires oriented along the [2$\bar{1}\bar{1}$] and [$\bar{1}$12] directions maintain the geometry of the underlying sites, whereas those grown along the [01$\bar{1}$] direction deviate from the patterned contours as an inevitable consequence of the facet-led growth process. The narrowest high-aspect ratio nanowires had heights of ~2µm and cross-section dimensions of ~100x210nm

NW Core Source Flows (sccm)	TMGa 33 AsH_3 15		
Total NW Core Growth Time (s)	810		
Parameters for NWQD Formation	NWQD	TMIn Concentration (%)	Formation Time (s)
	1	0.02	2
	2	0.02	4
	3	0.04	2
	4	0.04	4

Table 3.2: Summary of conditions used for nanowire growth on Sample 3B.

(pictured in Figure 3.10), corresponding to radial overgrowth of only ~10nm. Based on a linear growth rate approximation, the InGaAs regions within each elongated structure had heights of ~5nm (2s growth time) and ~10nm (4s growth time) respectively, with the GaAs barrier between each InGaAs region measuring ~440nm thick. For reference, SEM images confirming that nanowires grown from typical (non-elongated) circular sites on this sample had a regular hexagonal cross-section, are also included in Figure 3.10.

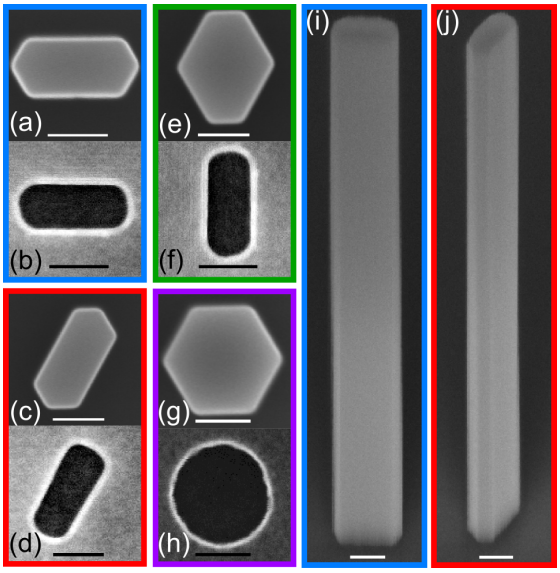

Figure 3.10: SEM images of nanoslots produced along the (b) $[2\bar{1}\bar{1}]$, (d) $[\bar{1}12]$ and (f) $[01\bar{1}]$ directions and (h) a regular circular nanohole. The rounded corners observed for all nanoslot orientations are a byproduct of the EBL patterning and etching steps. Top down SEM images of nanowires grown with cross-section anisotropy along the (a) $[2\bar{1}\bar{1}]$, (c) $[\bar{1}12]$ and (e) $[01\bar{1}]$ directions and also (g) no anisotropy in the cross-section. 45° titled SEM images of nanowires grown in the (i) $[2\bar{1}\bar{1}]$ and (j) $[\bar{1}12]$ directions. All scale bars 100nm.

3.5.2 PL Measurements

Optical characterisation of the elongated nanowires on Sample 3B followed a similar procedure to that employed for Sample 3A, with the PL setup described in Section 3.3.2. As the narrowest elongated nanowires on Sample 3B discussed above had the most desirable properties in terms of aspect ratio and potential NWQD size, these structures were the main focus of the measurements.

In general, a single PL emission line was observed at low excitation powers (~1nW) for individual nanowires on this sample, suggesting that only one of the four grown InGaAs regions was optically active. However, the overall fraction of nanowires that showed PL emission (~75%) was substantially greater than was observed on sample 3A. Figure 3.11(a) displays a representative non-polarised power dependent PL spectra from a single elongated structure (in this case oriented along the $[2\overline{1}\overline{1}]$ direction). At low excitation powers, a single PL emission line is seen at 1.445eV (~860nm). As the excitation power increases (upto ~1.4μW), state filling of excited states is observed, demonstrating behaviour expected for PL emission from a NWQD. The measured state separation of ~3.6meV, however, is somewhat larger than expected from a simple model of the NWQD as a square infinite potential well (~1meV). In addition, contrary to the predictions of an infinite square potential model, the energy separation between successive excited states in Figure 3.11(a) is approximately constant. Similar NWQD emission behaviour has been reported previously for non-elongated GaAs/InGaAs nanowire heterostructures formed using the same growth technique, and is thought to result from the formation of a harmonic potential in the radial direction of the NWQD caused by a reduction in the incorporation of indium across the nanowire width [7, 55]. Such a potential leads to greater radial confinement of carriers and therefore higher energy levels relative to a square potential, and it also produces approximately equally spaced energy levels in the large NWQD radius limit. It is noted that no evidence of NWQD emission was observed for any of the elongated structures in the previous sample.

Polarisation-dependent PL measurements on individual elongated nanowires were undertaken at energies corresponding to the saturation point of the NWQD ground state transition (typically ~50–100nW) to maximise the collected signal. Figures 3.11(b) and (c) display polarisation-resolved measurements obtained for nanowires oriented along the $[2\bar{1}\bar{1}]$ and $[\bar{1}12]$ directions respectively. As for Sample 3A, the spectral accumulation time for each angular step was 5s, but here the angular step size was reduced to 10° in order to better characterise the relationship between emission intensity and polariser angle and improve the accuracy of the calculated DOP value. The PL emission from both high-aspect ratio orientations is observed to be strongly linearly polarised along the axis of elongation, similar to what was seen previously in Figure 3.5. In contrast to the results obtained for Sample 3A however, PL emission from structures oriented along $[01\bar{1}]$ direction show much weaker and generally more random polarisation, approaching that observed previously for nanowires grown from regular circular holes. This emission behaviour was also observed for a small fraction of structures in the $[2\bar{1}\bar{1}]$ and $[\bar{1}12]$ directions, where one of the six {110} facets did not develop correctly during growth, leading to the formation of a more weakly anisotropic structure.

Using the same ratio defined previously to quantify the DOP, the calculated DOP values for the individual structures displayed in Figures 3.11(a) and (b) were ~96% and ~92%, respectively. These values are significantly higher than determined for the elongated structures on the previous sample. DOP values were calculated for a total of twelve strongly-elongated nanowires on this sample — six each in the $[2\bar{1}\bar{1}]$ and $[\bar{1}12]$ orientations — and are summarised in Figure 3.11(d). The average DOP for nanowires oriented in the $[2\bar{1}\bar{1}]$ direction was found to be (95 ± 1)%, while for those in the $[\bar{1}12]$ orientation it was (93 ± 1)%. For comparison, the average DOP value calculated for nanowires oriented in the $[01\bar{1}]$ direction was ~15%.

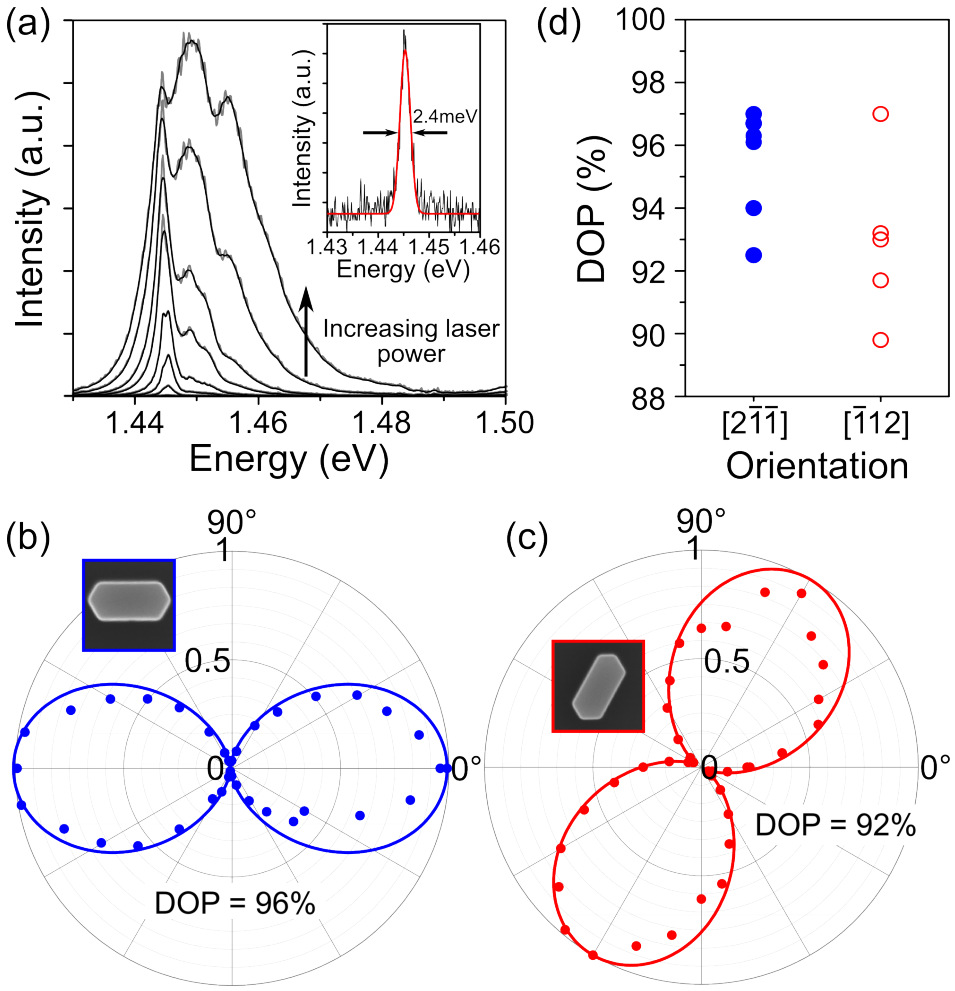

Figure 3.11: Overview of PL measurements performed on the narrowest elongated nanowires oriented along the [2$\bar{1}\bar{1}$] and [$\bar{1}$12] directions on Sample 3B. (a) Representative power-dependent PL spectra collected from an individual nanowire oriented along the [2$\bar{1}\bar{1}$] direction using excitation powers of ~10nW, ~40nW, ~85nW, ~200nW, ~350nW, ~700nW and ~1.4µW, respectively. Three confined states are visible at the highest excitation power (grey line – raw data, black line – smoothed data). Inset displays ground state PL spectrum of NWQD collected using an excitation power of ~1nW (black line) and Gaussian fit of data (red line); (b) Normalised, polarisation-resolved NWQD PL intensity for an elongated nanowire oriented along the [2$\bar{1}\bar{1}$] direction. Circles represent the integrated intensity measured using an excitation power of ~60nW at a particular polariser collection angle and the solid line depicts a cosine curve fit to the data. Inset provided as a reminder of nanowire orientation; (c) Same as (b) but for a single nanowire oriented in the [$\bar{1}$12] direction measured using an excitation power of ~100nW; (d) Calculated DOP values for a total of twelve elongated nanowires oriented in [2$\bar{1}\bar{1}$] and [$\bar{1}$12] directions measured using excitation powers of ~50–100nW.

In order to verify that the experimental results obtained above were predominately a result of the structural properties of the nanowires, and not instead those of the embedded emitter, polarisation-resolved measurements were also undertaken on structures with a cross-section

of ~200x400nm (oriented along the $[2\bar{1}\bar{1}]$ and $[\bar{1}12]$ directions) as these have approximately the same aspect ratio as the narrowest structures measured above, but owing to their larger size, confine both orthogonal modes at the emission wavelength (see Figure 3.12). It was found that the emission from these larger structures was similar to that observed for weakly anisotropic structures, with an average calculated DOP of ~25%.

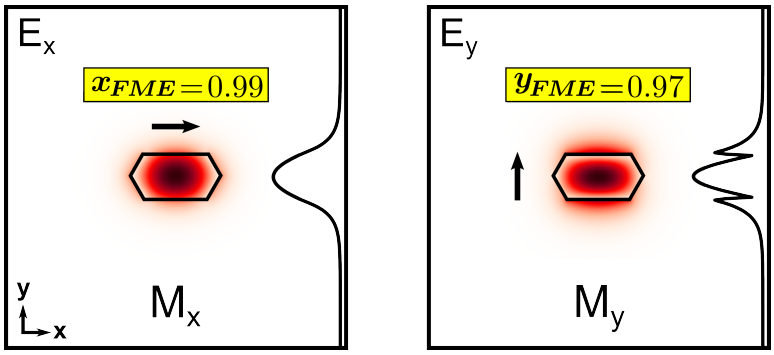

Figure 3.12: Simulated in-plane electric field components associated with M_x and M_y, for an elongated nanowire with cross-section dimensions of 200x400nm at the mode wavelength λ_M=860nm. The development of the electric field for M_x and M_y in the y-direction at x=0 is depicted on the right of each plot. Fraction of mode energy within nanowire (FME) is displayed for both polarised modes.

3.6 FDTD Simulations of Elongated Nanowire Structures

The modal analysis presented in Section 3.4 provides a useful explanation of the origin of the linearly polarised emission that is observed experimentally from the elongated nanowires in Section 3.3.2 and Section 3.5.2, and its dependence on nanowire cross-section and emission wavelength. It does not, however, take into account the finite size of the actual grown nanowires, the axial location of the embedded emitter or the influence of the substrate the nanowire sits atop.

To give a more comprehensive description of the emission behaviour observed from these structures experimentally, and to substantiate the experimental results, three-dimensional finite difference time domain (3D FDTD) simulations were performed using the commercial-grade simulator 'FDTD solutions' from Lumerical [116]. The simulation domain, shown in Figure 3.13(a), consisted of an elongated nanowire with cross-section of 100x210nm and a height of 2µm, placed upon a semi-infinite GaAs substrate and 30nm layer of SiO_2. For both the nanowire and substrate, a real refractive index of 3.45 was used. A broadband electric-dipole emitter was positioned on the nanowire axis at an axial distance, d from the substrate.

Polarisation-resolved far-field intensity profiles, determined from emission collected above the top facet of the nanowire, were obtained separately for a dipole polarised along the direction of elongation, and one perpendicular to this direction (both perpendicular to the nanowire growth axis) before summing the results. Figure 3.13(b) displays the polarisation-resolved far-field emission profile, with the electric field polarisation oriented along the direction of elongation, for a dipole located at d=1000nm at the emission energy E=1.445eV (λ~860nm). The cross-polarised far-field emission profile when plotted on the same scale shows no features, demonstrating the disparity between emission intensity for the two modes. This disparity is more clearly illustrated in Figure 3.13(c), which shows a plot of the normalised, polarisation-resolved far-field intensity as a function of polarisation angle for this arrangement, assuming a NA of 0.42 (to reflect the angular collection range of the objective lens used in PL measurements).

Since it was not apparent which one of the four grown InGaAs regions was optically active within an individual nanowire measured on Sample 3B, from the far-field emission profiles, DOP values were calculated as a function of dipole location, d at the emission energy E=1.445eV. As displayed in Figure 3.13(d), these calculations reveal that DOP values are greater than 90% for 680nm $< d <$ 1480nm, and remain high for the majority of dipole locations along the nanowire. The variation in DOP values observed in Figure 3.13(d) is caused by weak Fabry-Perot modes forming within the nanowire, plus reflection from the underlying

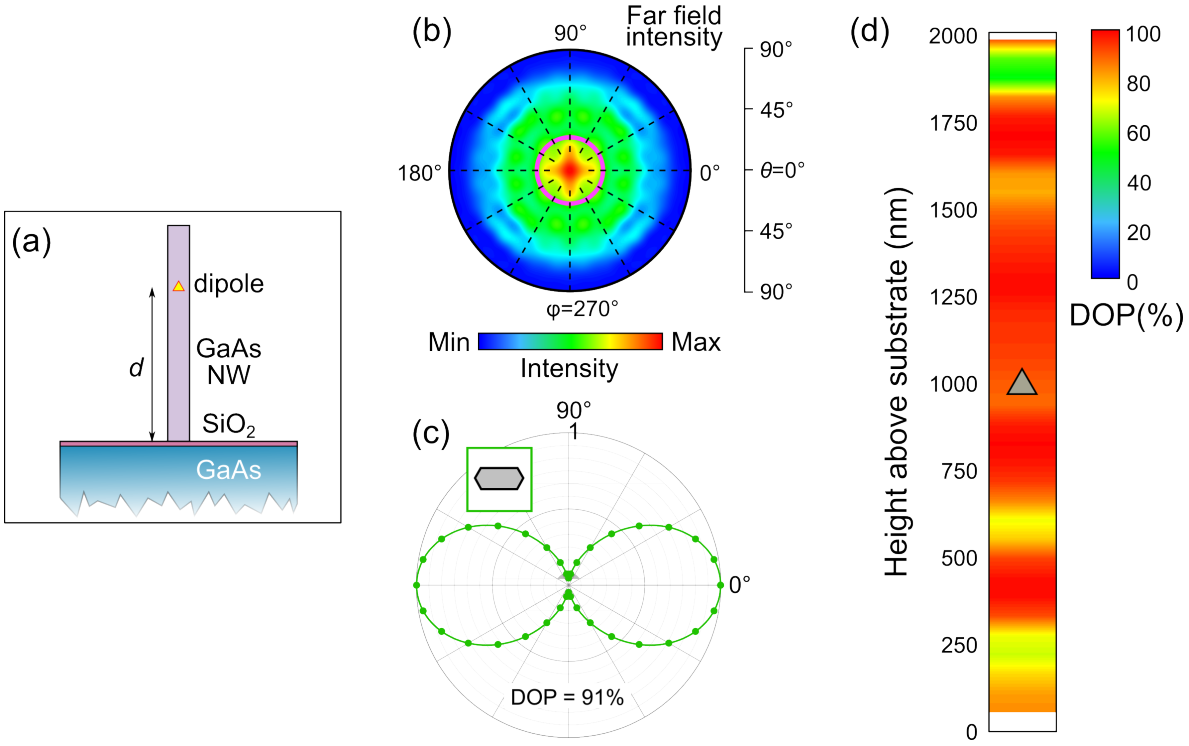

Figure 3.13: 3D FDTD simulations of an elongated nanowire containing an on-axis embedded dipole emitter. (a) Schematic of simulation domain. A dipole emitter is placed a distance d above a semi-infinite GaAs substrate and far-field emission profiles are generated from emission collected from the top facet of the nanowire; (b) Normalised, polarisation-resolved far-field emission profile for d=1000nm, with the electric field polarisation oriented along the direction of elongation, at the emission energy E=1.445eV (λ~860nm). The pink circle represents the collection angle of an objective lens with the same NA=0.42 as used in experimental measurements. On this scale, the cross-polarised far-field profile contains no observable features; (c) Normalised, polarisation-resolved far-field intensity as a function of polariser collection angle (10° steps) for the arrangement detailed in (b). Circles represent total calculated far-field intensity at a particular collection angle and solid line depicts cosine curve fit to data. Inset provided as a reminder of nanowire orientation; (d) DOP as a function of dipole position, d at the emission energy E=1.445eV.

substrate and dipole emission into leaky modes, which becomes especially significant when the dipole is located near the top of the nanowire. Adopting an objective lens with a larger NA than used in the above experiments would both reduce the variation in DOP values along the nanowire and lead to higher overall DOP values, even at this location. Figure 3.14(a) displays DOP values as a function of d assuming a NA=1, with that for NA=0.42 alongside for comparison. Polarisation-resolved far-field intensity profiles, with electric field polarisation oriented along the direction of elongation, for four uniformly spaced emitter locations along the nanowire are displayed in Figure 3.14(b). It is observed that the influence of reflections

from the substrate (location ①) and emission into leaky modes (location ④) leads to emission from the nanowire top facet at steeper angles than for an emitter located closer to the centre of the nanowire (locations ② and ③). Even at these relatively large displacements from the centre of the nanowire however, this effect is small and calculated DOP values are >95% for both NA=0.42 and NA=1.

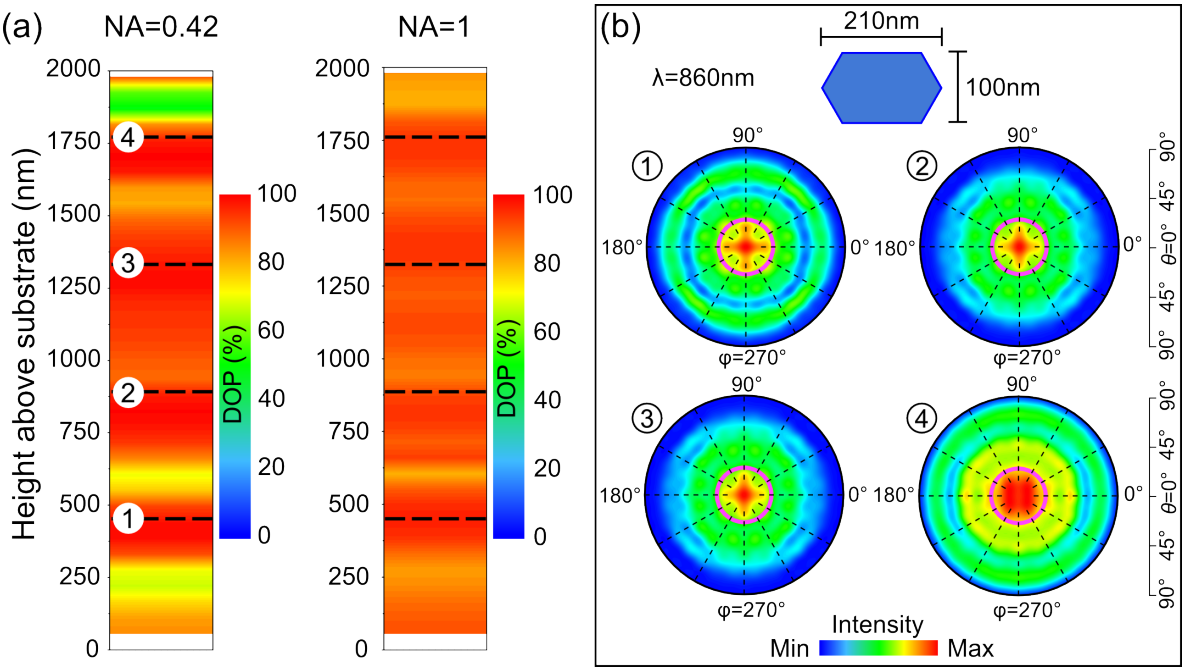

Figure 3.14: Simulated emission behaviour of an on-axis dipole emitter embedded in an elongated nanowire as a function of dipole axial location. 3D FDTD simulations show, (a) DOP as a function of dipole height above the substrate (on-axis), for an objective lens with NA of 0.42 and 1, at the emission energy E=1.445eV (λ~860nm); (b) Normalised, polarisation-resolved far-field intensity profiles for the axial locations labelled in (a). The electric field is polarised along the axis of elongation (inset provided as a reminder of nanowire orientation). On this scale, the cross-polarised component cannot be observed. Inner pink circles denote the experimental NA of 0.42.

The bottom-up approach used for nanowire growth facilitates the formation of an embedded emitter with radial dimensions similar to that of the surrounding nanowire structure, therefore it is relevant to analyse how DOP values vary laterally across the nanowire as well as axially along it. Figure 3.15(a) shows calculated DOP values assuming collection from an objective lens with NA=0.42 at λ=860nm for a dipole emitter placed separately at four different radial locations across the nanowire, repeated for the axial locations ① – ④ labelled

in Figure 3.14(a). For each of the individual axial locations, it is observed that movement of the dipole emitter away from the nanowire axis leads to only a small variation in the calculated DOP value, even for relatively large radial displacements (~70nm). It should be noted however, that any radial displacement from the nanowire axis would diminish the coupling of emitter to the dominant confined optical mode, resulting in a reduced photon emission rate.

To emulate the emission wavelength observed experimentally, all of the above DOP analysis was done for λ=860nm. However, it is observed that polarisation control of the emission from a nanowire with these structural properties is inherently broadband. Figure 3.15(b) displays calculated DOP values as a function of wavelength in the wavelength range λ=860–900nm, again for the axial emitter locations ① – ④ labelled in Figure 3.14(a). Calculated DOP values in this wavelength range remain above 96% for the experimental NA=0.42 at all axial locations and remain high for NA=1. For potential elongated structures containing more than one optically active emitter, this broadband polarisation control is a key asset.

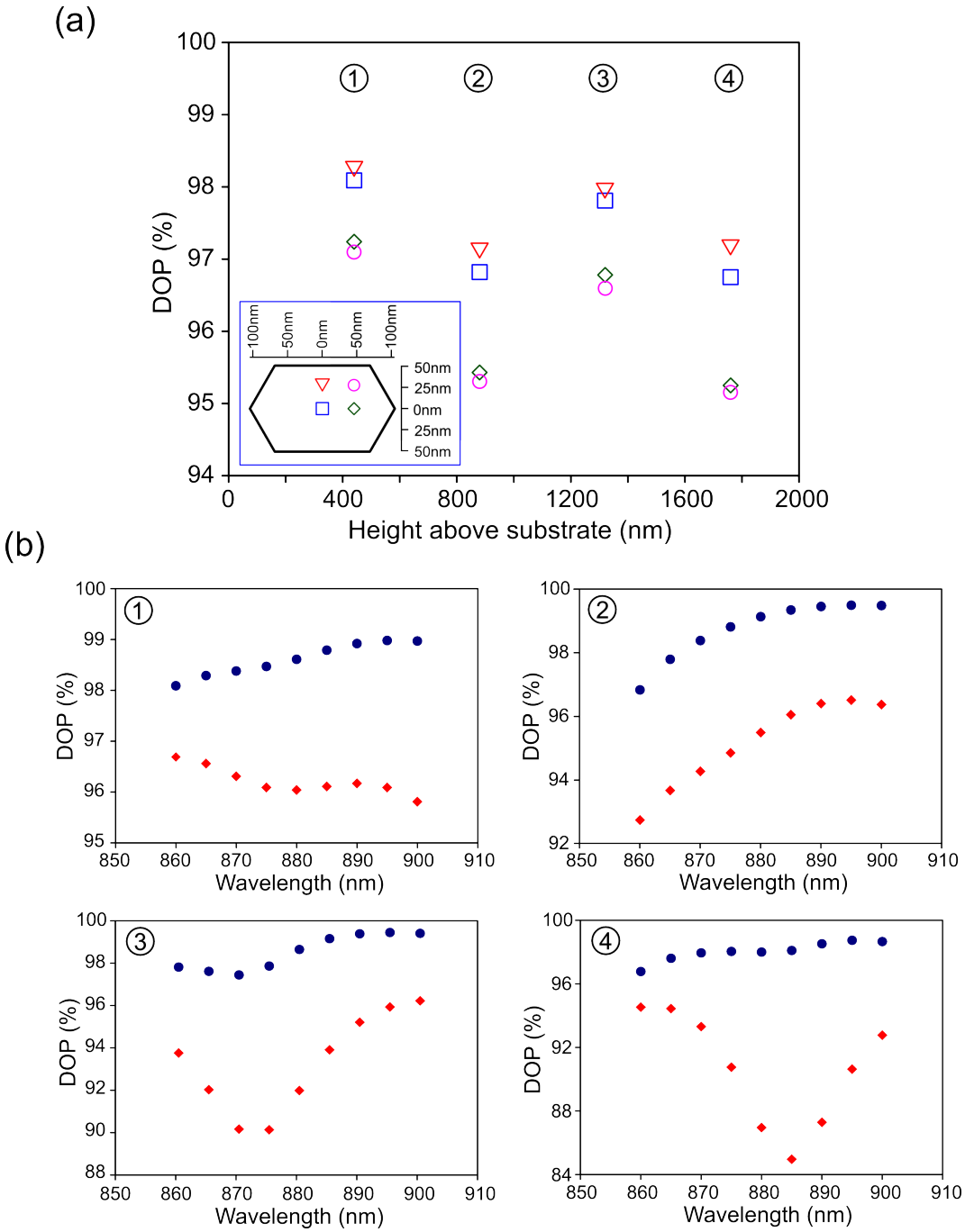

Figure 3.15: 3D FDTD analysis of the polarisation control provided by a highly anisotropic nanowire containing an embedded quantum dot. (a) DOP values for a dipole emitting at E=1.445eV (λ~860nm) as a function of radial position of the emitter within the nanowire, using an objective lens NA=0.42. The emitter coordinates (x,y)nm are shown in the inset: blue square (0,0)nm, red triangle (0,25)nm, green diamond (50,0)nm, pink circle (50,25)nm. The axial location is given on the x axis, where numbers refer to locations labelled in Figure 3.14(a); (b) Wavelength dependence of DOP values for an on-axis dipole at the axial locations within the nanowire numbered in Figure 3.14(a). Blue circles and red diamonds denote NA=0.42 and NA=1, respectively.

3.7 Conclusion

The ability to precisely manipulate nanowire morphology has enabled polarisation control of the emission from an embedded on-axis NWQD in nanowires formed using a catalyst-free growth approach to be demonstrated for the first time. Reduction of the separation between a closely spaced nanohole pair was observed to lead to nanowire growth changing from the formation of two separate nanowires to the formation instead of a single nanowire with an elongated cross-section, where the direction of elongation was determined by the orientation of the patterned nanohole pair. Pairs of individual nanowires with edge-to-edge separations down to ~10nm were realised and single elongated structures were successfully formed in $[2\overline{1}\overline{1}]$ and $[01\overline{1}]$ directions. Through the patterning of single elongated nanoholes (nanoslots), further control over the dimensions of nanowires with an elongated cross-section was achieved. PL emission from InGaAs axial structures embedded within the narrowest elongated nanowires formed from these nanoslot sites (collected from the nanowire top facet) exhibited QD-like properties and was observed to be strongly linearly polarised (>90%), with the polarisation direction coincident with the elongation axis of the nanowire cross-section. Preferential coupling of the emission from the embedded InGaAs structure to a single linearly polarised optical mode within the nanowire was investigated as the possible origin of this observed linearly polarised emission. This explanation was further supported by experimental results along with results from 3D FDTD simulations. FDTD simulations also showed that the degree of polarisation (DOP) of the emission from the nanowire top facet is largely independent of emitter location within the nanowire, both radially and axially, and remains above 90% over a broad wavelength range. This system therefore provides a promising route to the bottom-up growth of position controlled linearly polarised single photon sources.

Chapter 4

Tuning the Mechanical Properties of GaAs Nanowires Using Cross-Section Morphology Control

4.1 Introduction

In addition to providing a valuable platform for the study of quantum optical phenomena, semiconductor nanowires formed using a bottom-up growth approach show great promise as nanomechanical resonators capable of ultrasensitive detection of mass [117] and force [118]. Assembly from the bottom-up produces structures with atomically sharp facets and atomically abrupt clamping at the nanowire-substrate interface, therefore reducing the surface [20] and clamping [119, 120] induced losses that may be suffered by cantilever systems processed through top-down methods. As a result, mechanical damping rates in grown nanowires have been demonstrated to be significantly lower than that for their etched counterparts [118]. The small motional mass of nanowires also leads to relatively high mechanical resonance frequencies, which decouples the nanowire motion from common sources of noise whilst improving force sensitivity [121].

Nanowires grown by bottom-up techniques typically have a regular hexagonal cross-section. However, it is very common for a slight asymmetry in the cross-section dimensions to exist, thus altering the optical and mechanical properties of the nanowire. From a mechanical perspective, this results in non-degenerate flexural mechanical mode doublets, which oscillate with similar frequencies in orthogonal directions [122–124]. This is analogous to the splitting of the fundamental optical modes in the same structures [106] as discussed in Chapter 3. Simultaneously monitoring the orthogonal mode amplitudes and/or frequencies may enable vectorial detection of in-plane forces and spatial force derivatives. Measurements of the magnitude and direction of the static tip-sample force derivatives in a 2D scanning plane have been recently demonstrated using grown GaAs nanowires in an atomic force microscopy setup [13], while suspended SiC nanowires coupled to a strongly focused laser beam have been used to demonstrate the non-conservative nature of radiation pressure [14]. Moreover, the optical transitions of embedded self-assembled quantum dots in nanowires have been shown to couple to the mechanical motion of their host nanowire through strain [125], and measurements on two perpendicular flexural modes would add the unique possibility of obtaining vectorial information on force and strain fields. As the asymmetry present in the nanowire cross-section develops arbitrarily, however, the direction of motion of the non-degenerate orthogonal nanowire flexural modes cannot be determined *a priori*. To take full advantage of the nanowire as a vectorial force transducer, therefore, necessitates considerable time either characterising many nanowires to locate individual structures that oscillate in the desired orthogonal directions or carefully orientating the nanowire substrate until the motion of a selected nanowire is optimised for a particular measurement.

In the previous chapter, control over the confinement of the fundamental non-degenerate orthogonally polarised optical modes in individual GaAs nanowires was achieved through appropriate tuning of the nanowire cross-section aspect ratio. This enabled the demonstration of linearly polarised emission from an incorporated InGaAs NWQD, with the polarisation of the emitted light observed to be co-incident with the elongation axis of the nanowire cross-section. In this chapter it is shown that, by utilising the same catalyst-free nanowire growth

approach, the precise direction of motion of the orthogonal flexural nanowire modes can be deterministically controlled through choice of nanowire elongation axis at the growth stage. The ability to deterministically control the direction of nanowire motion, combined with the array-scale uniformity that can also be achieved with this growth approach [7] offers potential for development of a highly sensitive multi-nanowire force transducer arrangement, collectively oscillating in the same orthogonal directions with well defined frequencies.

A brief overview of the growth conditions used to produce the nanowire samples discussed in this chapter is given in section 4.2. In section 4.3, the measurement technique used to characterise the frequency response of nanowire motion is described. The thermomechanical flexural mode spectra measured for individual nanowires with three different cross-section aspect ratios at room temperature and at cryogenic temperatures are then presented in sections 4.4 and 4.5, respectively. Finally, in an effort to observe non-linear nanowire oscillatory behaviour, the amplitude response of a resonantly driven fundamental thermomechanical nanowire mode is investigated in section 4.6. It should be noted that some of the results presented in the following sections have been published elsewhere [126].

4.2 Sample Fabrication and Growth

In Chapter 3, it was shown that control of GaAs nanowire morphology could be achieved through the patterning of elongated aperture sites (nanoslots) in the SiO_2 growth mask. Using the same approach, nanoslots with varying cross-section dimensions were patterned on Sample 4A, in addition to regular circular apertures (nanoholes). It was also shown in Chapter 3 that there were three equivalent directions for which the elongation of the nanowire cross-section remained true to the elongation of the growth mask aperture (Figure 3.9). For Sample 4A, the major axis of the patterned apertures was arbitrarily chosen to be oriented parallel to the major flat of the GaAs wafer ($[2\overline{1}\overline{1}]$ direction). As for previous GaAs nanowire samples, the apertures on Sample 4A were patterned with a pitch of 4µm. Aperture dimensions were fixed within a particular array and varied from array to array. In order to reduce the probability

of measuring vibrational motion of multiple nanowires simultaneously, only a single row of 20 apertures was patterned in each individual array.

Growth on Sample 4A followed the scheme for Sample 2C (3B) described in Chapter 2 (3), but the nanowire growth time was increased by a factor of four to a total of ~54 minutes. The intention of this increase in the growth time was to produce nanowires tall enough to make optical detection of individual nanowire motion achievable. In addition, as only the mechanical properties of the nanowire structures on Sample 4A were under investigation, NWQD formation was not attempted during growth and the sample was cooled in an overpressure comprising AsH_3 only.

Figure 4.1(a) shows an SEM image of a representative row of 20 nanowires grown from circular aperture sites on Sample 4A. The average height, L of nanowires in this row was measured to be ~14.5um which is ~7 times taller than the equivalent structures formed on Sample 2C (3B). Radial growth was again found to be strongly suppressed with the chosen nanowire growth conditions, with the average nanohole and nanowire diameter in this row measured as ~120nm and ~130nm, respectively. As for Sample 2C (3B), planar growth in the regions of the substrate not covered by the SiO_2 mask was observed to be smooth on this sample. Nanowire heights were also found to decrease as nanowire diameter increased, with the average height of structures formed from apertures with the largest patterned cross-section dimensions (400x150nm) measured to be ~8.1µm.

An angled SEM image of an individual elongated nanowire structure on Sample 4A with a cross-section aspect ratio (AR) equal to 2.25 is shown in Figure 4.1(b), alongside the nanoslot in the SiO_2 mask from which the nanowire was grown. The AR in this case is defined as the maximum width (w_{major}) along the major axis (the elongation direction) of the nanowire divided by the width along the minor axis (w_{minor}). Therefore, for a nanowire with regular hexagonal cross-section, the orthogonal widths lead to an AR of $2/\sqrt{3} \approx 1.155$. Similar to all previous GaAs nanowire growths, nanowires on Sample 4A had six smooth {110}-oriented sidewalls, and were untapered. To further facilitate optical detection of nanowire motion, the sample substrate was cleaved parallel and as close as possible to the line of nanowires in

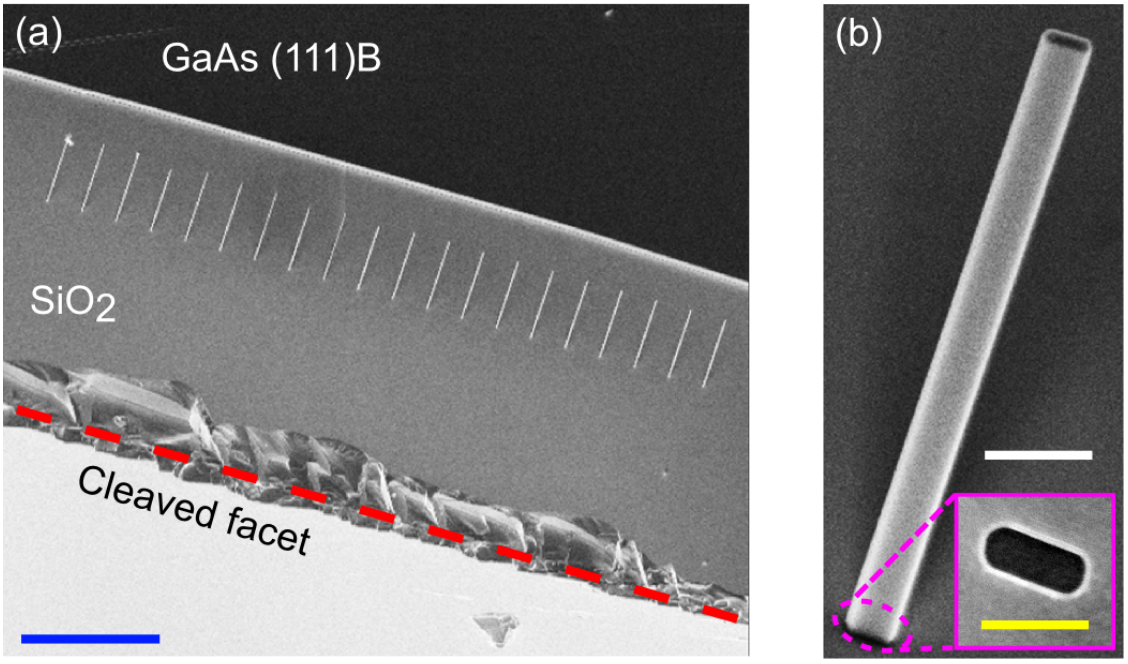

Figure 4.1: GaAs nanowire growth on Sample 4A. (a) Angled SEM image of an array containing a row of 20 vertical nanowires formed from nanohole sites, with the substrate cleaved along the $[2\bar{1}\bar{1}]$ direction (parallel to the row) ~30µm away (illustrated by the dashed red line). The nanowire growth axis is orthogonal to the substrate plane. Scale bar 20µm; (b) Angled SEM image of an individual nanowire with an elongated cross-section (from a different array to that shown in (a)). Scale bar 400nm (Inset) A top down SEM image of the nanoslot site from which the nanowire in (b) was grown. Scale bar 200nm.

each array. For the nanowires discussed in the following sections, the distance between the cleave line (highlighted by the red dashed line in Figure 4.1(a)) and each nanowire row was ~30µm. The significance of reducing the separation between individual nanowires and the substrate edge with respect to detection of nanowire mechanical motion is described further in Section 4.3.

4.3 Experimental Setup

Characterisation of nanowire motion was performed using a home-made free-space Michelson interferometer* utilising a continuous wave sensing laser. A schematic overview of the ex-

*Michelson interferometer setup used for characterisation of nanowire mechanics in this chapter was constructed by Dr. Andrew Foster.

perimental setup is shown in Figure 4.2(a). In this setup, light reflected from the nanowire sample (in the probe arm) interferes on a fast photo-diode with light reflected from the reference mirror (in the reference arm). Changes in the relative phase of the two reflected beams due to nanowire motion are monitored through intensity fluctuations of the detected optical signal. The magnitude of the relative phase change is proportional to the amplitude of the nanowire displacement, and therefore, in the case of a nanowire excited only by the Langevin force, the largest fluctuations in the detected signal occur at frequencies corresponding to the mechanical resonance frequencies of the nanowire. Fluctuations in the intensity of the interfering reflected beams are detected in this setup utilising a balanced detection scheme, whereby the combined reflected photons from each of the two arms are split equally and fed into the two inputs of a balanced photodetector, which outputs a voltage proportional to the difference between the optical power impinging on each of the photodetector inputs. One of the advantages of employing this scheme over a more simple single-detector arrangement is that it enables detection of nanowire motion without having to use a high power beam in the probe arm which could perturb the nanowire mechanical frequencies through heating of the sample. The output differential signal corresponding to nanowire motion scales with the input laser power from each of the two arms in this scheme, meaning that a reduction in the signal-to-noise ratio (SNR) of the differential signal caused by a decrease in the optical power in the probe arm can be compensated for by an increase in power in the reference arm [127]. Another advantage of the balanced detection scheme is that any common-mode laser noise is strongly suppressed when the path length difference between the probe and reference arms is minimised.

The nanowire sample was mounted on a right angled copper bracket attached to a piezo transducer (PZT) inside an evacuated flow cryostat chamber, with the nanowire growth axis oriented orthogonally to the optical axis of the interferometer probe arm. The PZT was used to investigate the dynamical properties of nanowires as described in Section 4.6.

Due to the cross-section anisotropy of the elongated nanowires, two orthogonal flexural modes exist for each harmonic (fundamental, second order, etc.). Therefore, in order to enable

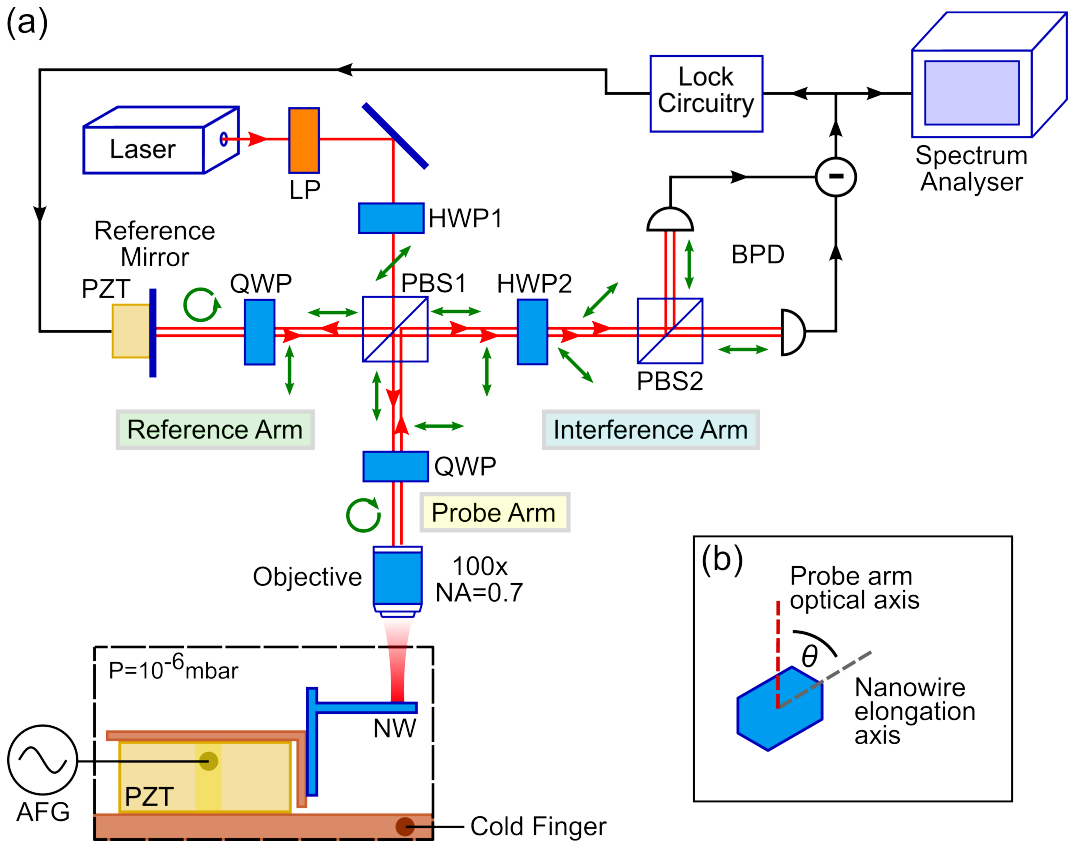

Figure 4.2: Detection of GaAs nanowire motion. (a) Schematic diagram of the interferometer setup. A linear polariser (LP) and a half-wave plate (HWP1) are used to determine the ratio of optical power delivered to the reference and probe arms after the first polarising beam splitter (PBS1). Quarter wave plates (QWP) are used to ensure that light returning to PBS1 is cross-polarised with the incident light in the probe and reference arms, and therefore is directed to the interference arm. The second half-wave plate (HWP2) is used in combination with the second polarising beam splitter (PBS2) to send half of the light to each of the two balanced photodetector (BPD) inputs, with the light in each path thus having the same polarisation allowing it to interfere on the photodetector. The high frequency differential signal output from the BPD is sent to a spectrum analyser, while the low frequency signal output by the BPD is sent to a lock circuit that drives a piezo transducer (PZT) attached to the reference mirror which is used to stablise the path length difference between the reference and probe arms. Red arrows indicate beam paths in the interferometer setup, with green arrows specifying the polarisation degree of freedom of the light after it passes through each optical component; (b) Schematic diagram showing the relative orientation of the nanowire elongation axis (major-axis) and probe arm optical axis in this setup.

detection of both modes simultaneously, the sample was rotated such that the cross-section major axis was at ~60° relative to the optical axis of the probe arm (Figure 4.2(b)). As described in Section 4.2, nanowire samples after growth were cleaved parallel and as close as possible to the row of individual nanowires selected for subsequent measurements. This meant that focusing of light from the probe arm onto a single nanowire could be performed

using a high NA objective (NA=0.7, 100x magnification) without the incident and reflected beams being obscured by the remaining substrate.

To determine the frequency response of the nanowire motion, the high frequency differential signal output by the balanced photodetector was directed to a spectrum analyser (Agilent N9000A CXA Signal Analyser). The low frequency differential signal was sent to a lock circuit, which was used to stabilise the interferometer against low frequency drift of the reference and probe arms, resulting from noise and temperature fluctuations.

4.4 Characterisation of Nanowire Flexural Modes

To determine the influence of nanowire morphology on the frequency response of nanowire motion, measurements of the flexural mode frequencies for a nanowire with regular hexagon cross-section (grown from a circular aperture) and two nanowires with differing cross-section aspect ratios on Sample 4A were performed using the interferometer setup described in the Section 4.3. The structural dimensions of these three nanowires, herein referred to as NW-4A, NW-4B and NW-4C, are presented in Table 4.1. All measurements in this section were undertaken at room temperature and a pressure of ~10^{-6}mbar. The sensing laser used for the interferometer was a wavelength stabilised diode operating at 633.1nm, with the maximum laser power incident on a nanowire limited to ~2μW to minimise heating of the sample. It is noted that a change in the Q-factor of the second order flexural mode resonances was only observed in these measurements when the laser power incident on the nanowire surpassed ~10μW, with even higher powers required to induce a similar perturbation of the fundamental mode resonances.

	w_{major} (nm)	w_{minor} (nm)	AR	Axial Length, L (μm)
NW-4A	156	133	1.17	14.4
NW-4B	196	114	1.72	14.3
NW-4C	244	123	1.98	12.9

Table 4.1: Structural dimensions of three representative nanowires on Sample 4A selected for flexural mode characterisation. AR=w_{major}/w_{minor}.

Figure 4.3(a) shows the fundamental thermomechanical mode spectra for each of the three nanowires described in Table 4.1. The detected signal for the higher frequency modes in each spectrum was observed to decrease when the sample was rotated in a manner that increased the angle θ between the nanowire elongation axis (major-axis) and probe arm optical axis. These higher frequency modes, therefore, were attributed to vibration of the nanowire in the plane formed by the nanowire growth axis and the major-axis of the nanowire cross-section, as in this case the nanowire vibration is perpendicular to the optical axis of the probe arm and its motion cannot be resolved. This mode is referred to as the major fundamental mode ${f_1}^{\mathrm{major}}$, with the lower frequency mode correspondingly referred to as the minor fundamental mode ${f_1}^{\mathrm{minor}}$. Schematic diagrams of the mode shapes for ${f_1}^{\mathrm{major}}$ and ${f_1}^{\mathrm{minor}}$ determined from finite-element method simulations are shown in Figure 4.3(b), illustrating that these two modes are indeed orthogonal. As is highlighted by Figure 4.3(c), even for NW-4A, which has a nominally regular hexagonal cross-section, there is a slight non-degeneracy of the fundamental vibrational modes. This small frequency separation between modes is commonly observed for these structures [123–125, 128, 129], and originates from an apparently unavoidable anisotropy in the hexagonal cross-section of the nanowire.

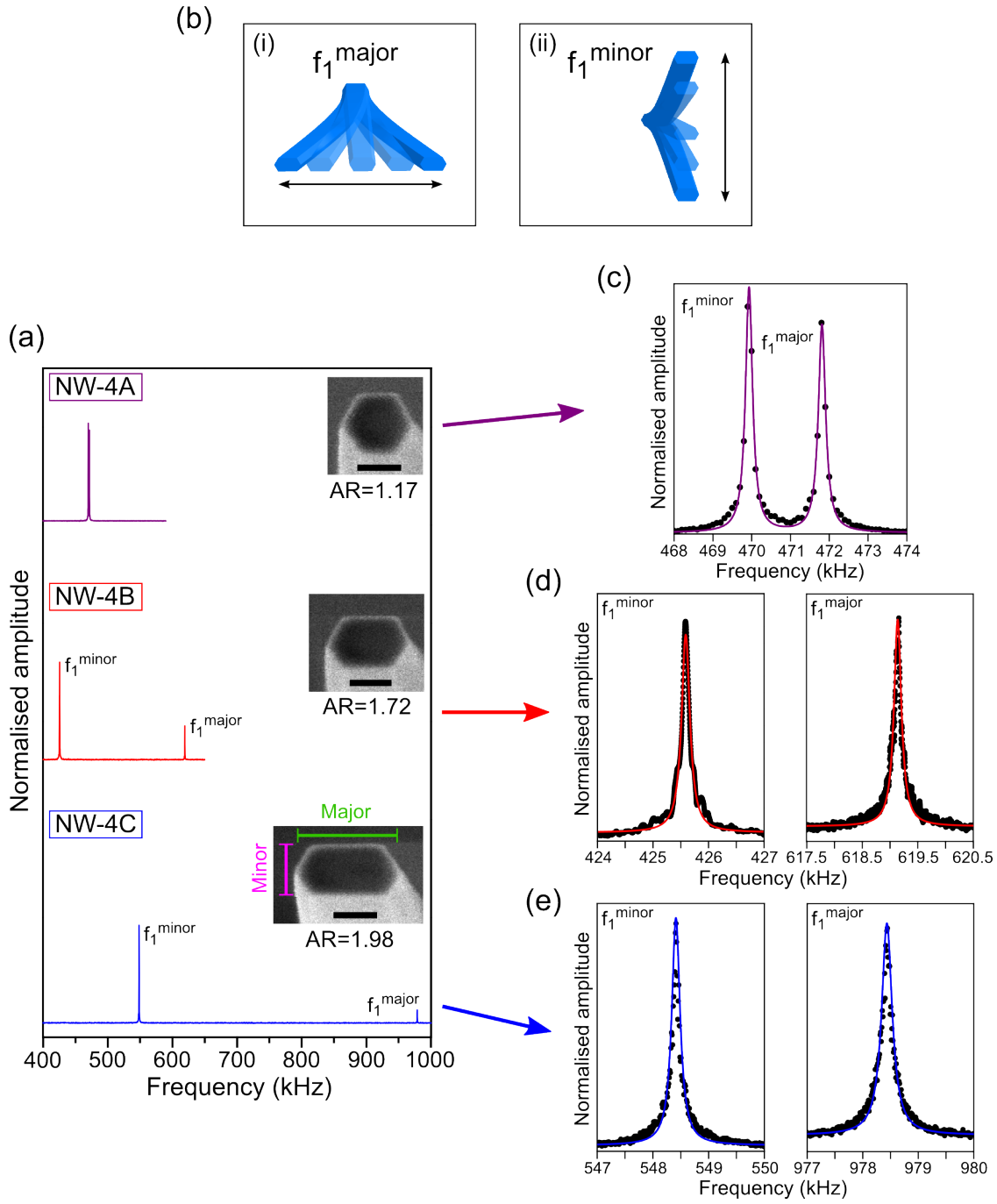

Figure 4.3: Fundamental flexural mode spectra for nanowires with different cross-section aspect ratio. (a) Fundamental thermomechanical mode spectra for NW-4A, NW-4B and NW-4C. Spectra are offset for clarity. Insets show shallow angle SEM images of the respective nanowires. Scale bars 100nm; (b) Schematic diagrams show the two orthogonal fundamental flexural mode shapes, (i) f_1^{minor} and (ii) f_1^{major} for a nanowire with an aspect ratio of ~2, where $f_1^{major} > f_1^{minor}$; Narrower bandwidth fundamental mode spectra for (c) NW-4A, (d) NW-4B and (e) NW-4C. Experimental data for individual modes (circles) in (d) and (e) were fitted with a single Lorentzian function (lines), while, due to the close proximity of the mode peaks, a double Lorentzian function was used to fit the data in (c). Cross-sectional dimensions of each nanowire are presented in Table 4.1.

The fundamental flexural resonance frequencies for NW-4A, NW-4B and NW-4C are summarised in Table 4.2. f_1^{minor} for the three nanowires ranged from ~430–550kHz, while the frequency separation between modes, f_1^{major}–f_1^{minor}, increased from ~2kHz for NW-4A to ~430kHz for NW-4C. The increase in mode separation is largely a consequence of the increasing width of the nanowire in the major axis direction, as the minor axis width varies only a little between the three nanowires. In addition to the fundamental flexural modes, the second order orthogonal flexural modes of the three nanowires, f_2^{minor} and f_2^{major}, were also detected. The measured resonance frequencies of these modes for each nanowire are summarised alongside the fundamental mode frequencies in Table 4.2. An example of the f_2 mode spectra obtained for NW-4C is shown in Figure 4.4. The Q-factors of the orthogonal modes of these nanowires ranged from ~2000 to ~3000. These values are similar to those previously reported for GaAs nanowires [124].

	f_1^{minor} (kHz)	f_1^{major} (kHz)	f_2^{minor} (kHz)	f_2^{major} (kHz)
NW-4A	469.8	471.7	2947.0	2958.8
NW-4B	425.6	619.1	2668.1	3880.2
NW-4C	548.4	978.4	3438.2	6128.6

Table 4.2: Resonance frequencies for the first four flexural modes of nanowires with differing cross-section aspect ratio. Measurements were performed using a spectrum analyser with a resolution of ~1Hz.

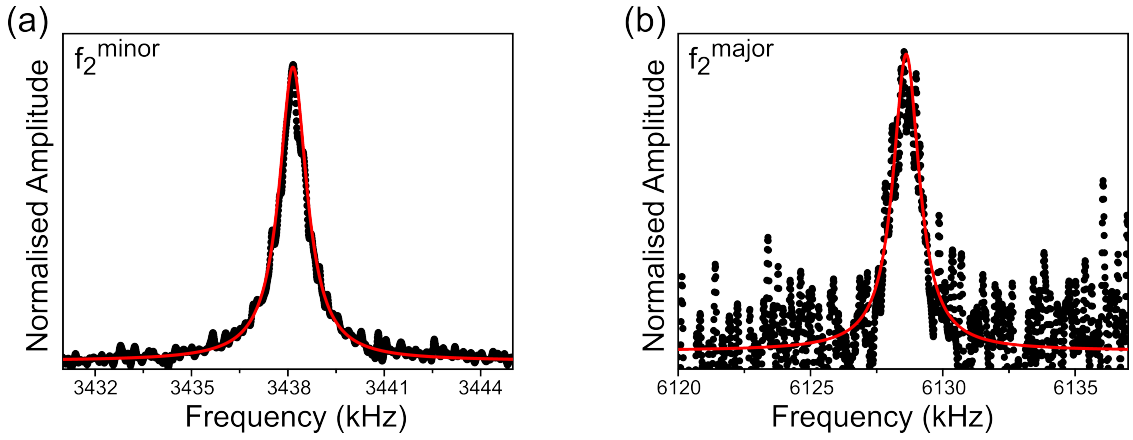

Figure 4.4: Narrow bandwidth mode spectra for the orthogonal first order flexural modes of NW-4C. Experimental data (circles) in (a) and (b) was fitted with a single Lorentzian function (lines).

As the cross-section dimensions of the nanowires in this instance are much smaller than the nanowire length (i.e. w_{major}, $w_{minor} \ll L$), Euler-Bernoulli beam theory may be used to describe the nanowire motion [130]. From this theory, the equation of motion for the vibrating nanowire is defined as

$$\frac{\partial^2}{\partial x^2}\left(\mathrm{EI}\frac{\partial^2 w}{\partial x^2}\right) + \mu\frac{\partial^2 w}{\partial t^2} = 0 \tag{4.1}$$

where $w(x,t)$ describes the displacement of the nanowire in the direction of vibrational motion at a position x along the nanowire axis at a time t, E is the Young's modulus of the nanowire, I is the second moment of area related to bending of the nanowire in the vibration direction and μ is the nanowire mass per unit length. If the nanowire cross-section is constant along its length, the product EI is constant and the equation of motion reduces to

$$c^2\frac{\partial^4 w}{\partial x^4} + \frac{\partial^2 w}{\partial t^2} = 0 \tag{4.2}$$

where

$$c = \sqrt{\frac{EI}{\mu}}. \tag{4.3}$$

The boundary conditions for a nanowire with length L which is fixed at one end are

$$w = 0 \quad \text{and} \quad \frac{\partial w}{\partial x} = 0 \quad \text{at } x = 0 \text{ (fixed end)} \tag{4.4}$$

$$\frac{\partial^2 w}{\partial x^2} = 0 \quad \text{and} \quad \frac{\partial^3 w}{\partial x^3} = 0 \quad \text{at } x = \mathrm{L} \text{ (free end).} \tag{4.5}$$

The linear, homogeneous boundary conditions of this system allow for the equation of motion to be solved using the method of separation of variables

$$w(x,t) = W(x)T(t). \tag{4.6}$$

Inserting 4.6 into 4.2 and re-arranging gives

$$\frac{c^2}{W(x)}\frac{\partial^4 W(x)}{\partial x^4} = -\frac{1}{T(t)}\frac{\partial^2 T(t)}{\partial t^2} = \omega^2 \tag{4.7}$$

where ω is a constant that corresponds to the angular frequency of the nanowire vibration. This equation can then be separated into the two ordinary differential equations

$$\frac{d^4 W(x)}{dx^4} - \lambda^4 W(x) = 0 \tag{4.8}$$

$$\frac{d^2 T(t)}{dt^2} + \omega^2 T(t) = 0 \tag{4.9}$$

where

$$\lambda^4 = \frac{\omega^2}{c^2}. \tag{4.10}$$

The general solutions to Equations 4.8 and 4.9 are

$$W(x) = C_1 \mathrm{sin}\lambda x + C_2 \mathrm{cos}\lambda x + C_3 \mathrm{sinh}\lambda x + C_4 \mathrm{cosh}\lambda x \tag{4.11}$$

and

$$T(t) = d_1 \mathrm{sin}\omega t + d_2 \mathrm{cos}\omega t \tag{4.12}$$

where d_i and C_i are constant coefficients. The boundary conditions in Equations 4.5 can be expressed entirely in terms of the spatial function $W(x)$. Non-trivial solutions to Equation

4.11 when applying these boundary conditions exist only if

$$\cosh(\lambda L)\cos(\lambda L) + 1 = 0. \tag{4.13}$$

However, this solution is not unique and depends on ω. Equation 4.13 therefore becomes

$$\cosh(\lambda_i L)\cos(\lambda_i L) + 1 = 0 \quad \text{with} \quad \lambda_i = \left(\frac{\mu\omega_i^2}{\mathrm{EI}}\right)^{1/4} \tag{4.14}$$

The quantities ω_i refer to the linear resonance frequencies of the nanowire in the direction of vibrational motion and are given by

$$\omega_i = \lambda_i^2\sqrt{\frac{\mathrm{EI}}{\mu}} \tag{4.15}$$

where the first few numerically calculated roots of Equation 4.14 are $\lambda_1 L \approx 1.875$ and $\lambda_2 L \approx 4.694$. Using the previously defined flexural mode notation, the ratio of orthogonal mode frequencies of the same flexural order is therefore given by

$$\frac{f_1^{\text{major}}}{f_1^{\text{minor}}} = \sqrt{\frac{\mathrm{I}^{\text{major}}}{\mathrm{I}^{\text{minor}}}} \tag{4.16}$$

where ${f_1}^j = {\omega_1}^j/2\pi$ (and j=major, minor). Orienting the nanowire cross-section so that the major and minor axes lie along x and y, respectively and centring the cross-section at (x=0,y=0), the values for $\mathrm{I}^{\text{major}}$ and $\mathrm{I}^{\text{minor}}$ can be calculated from

$$\mathrm{I}^{\text{minor}} = \frac{1}{12}\sum_{n=1}^{n=6}(y_n^2 + y_n y_{n+1} + y_{n+1}^2)(x_n y_{n+1} - x_{n+1} y_n) \tag{4.17}$$

and

$$\mathrm{I}^{\text{major}} = \frac{1}{12}\sum_{n=1}^{n=6}(x_n^2 + x_n x_{n+1} + x_{n+1}^2)(x_n y_{n+1} - x_{n+1} y_n) \tag{4.18}$$

where (x_n,y_n) specify the co-ordinates of each of the nanowire cross-section vertices (relative

to the origin). For co-polarised modes of differing order, I^j is the same for each ${f_i}^j$ (where i=1,2..) and the ratio of flexural mode frequencies is equal to a constant value which depends on the selected mode orders. For f_1 and f_2,

$$\frac{{f_2}^j}{{f_1}^j} = \frac{(\lambda_2/L)^2}{(\lambda_1/L)^2} \approx 6.267. \tag{4.19}$$

Table 4.3 summarises the experimentally determined values of ${f_1}^{major}/{f_1}^{minor}$ and ${f_2}^{major}/{f_2}^{minor}$ for NW-4A, NW-4B and NW-4C alongside the values of this ratio calculated using Equation 4.16. It is observed that there is reasonable agreement between the calculated and experimental values for each mode order for all three nanowires (columns 2 and 3). The experimentally determined co-polarised mode ratios are also summarised in Table 4.3. For each nanowire, there is very good agreement between experimental values and the value of ≈6.267 calculated from Equation 4.19. These two results demonstrate that nanowire motion here is described well by the Euler-Bernoulli theory presented above. Schematic diagrams of the nanowire flexural mode profiles ${f_1}^{minor}$ and ${f_2}^{minor}$ calculated using this model are shown in Figure 4.5.

	${f_1}^{major}/{f_1}^{minor}$	${f_2}^{major}/{f_2}^{minor}$	E-B Theory	${f_2}^{minor}/{f_1}^{minor}$	${f_2}^{major}/{f_1}^{major}$
NW-4A	1.004	1.004	1.017	6.273	6.273
NW-4B	1.455	1.454	1.539	6.269	6.269
NW-4C	1.784	1.783	1.797	6.270	6.264

Table 4.3: Frequency ratios for the first four flexural modes of nanowires with varying cross-section aspect ratios. Values of ${f_i}^{major}/{f_i}^{minor}$ (where i=1,2) calculated using E-B theory in column 4 show reasonable agreement with the experimentally determined ratios in columns 2 and 3 for each nanowire. Experimental values of the frequency ratio of co-polarised modes of differing order in columns 5 and 6 agree well with the value of ≈6.267 calculated using Euler-Bernoulli theory.

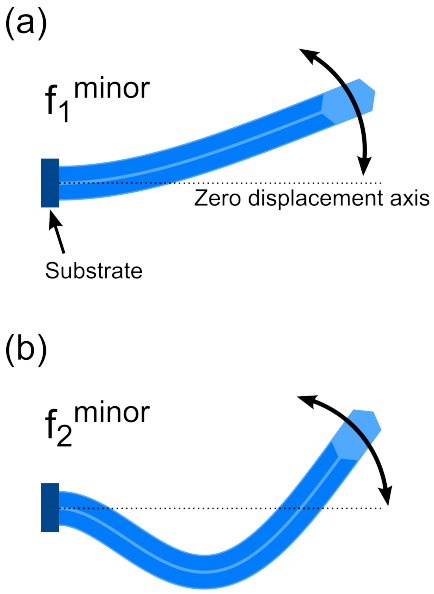

Figure 4.5: Schematic diagrams showing the mode profiles of the first two flexural modes along the minor-axis direction of a nanowire with an elongated cross-section.

4.5 Temperature Dependence of Nanowire Motion

A significant increase in cantilever mechanical Q-factor is commonly observed when operating at cryogenic temperatures [131–133]. This increase in Q is primarily a result of the reduction in the thermoelastic damping of the cantilever at these temperatures [133, 134], and has particular relevance for cantilever-based force sensing, where the minimum resolvable force (on resonance), F_{min} scales as $Q^{-1/2}$ [121, 132, 135]. As a consequence of the temperature dependence of the Young's modulus E, reduction of the cantilever temperature can also lead to a shift in the resonance frequency of the vibrational modes [136].

In order to investigate how nanowire motion was affected by temperature, measurements of the resonance frequencies and Q-factors of nanowires on Sample 4B at room temperature and T≈10K were performed using the interferometer setup described in Section 4.3. To ensure heating of the sample was minimised when performing measurements at low temperatures, the 633.1nm laser used previously was replaced by a Ti:Sapphire laser tuned to 900nm. The maximum laser power incident on each nanowire under investigation was ~10μW.

A comparison of the fundamental thermomechanical mode spectra for a nanowire with a cross-section aspect ratio of ~1.4 (length x w_{major} x w_{minor} = 13µm x 205nm x 150nm), at RT and T≈10K is shown in Figure 4.6. A significant increase in the Q-factor is observed as well as a change in the resonance frequency of each mode when the temperature of the nanowire is reduced from RT to cryogenic temperatures. In addition to the described reduction in the thermoelastic damping of the nanowire when the temperature is lowered to cryogenic temperatures, the reduction of the pressure in the cryostat vacuum chamber as a result of the 'freezing out' of any remaining gaseous species present in the chamber may have also contributed to the observed improvement in the Q-factor for each mode of this nanowire at T≈10K. Referring back to Eq. 4.15, the red-shifting of the fundamental mode resonances at lower temperature suggests that the value of E for this nanowire was larger at RT than at T≈10K (i.e. the nanowire structure became less rigid with decreasing temperature) [136, 137].

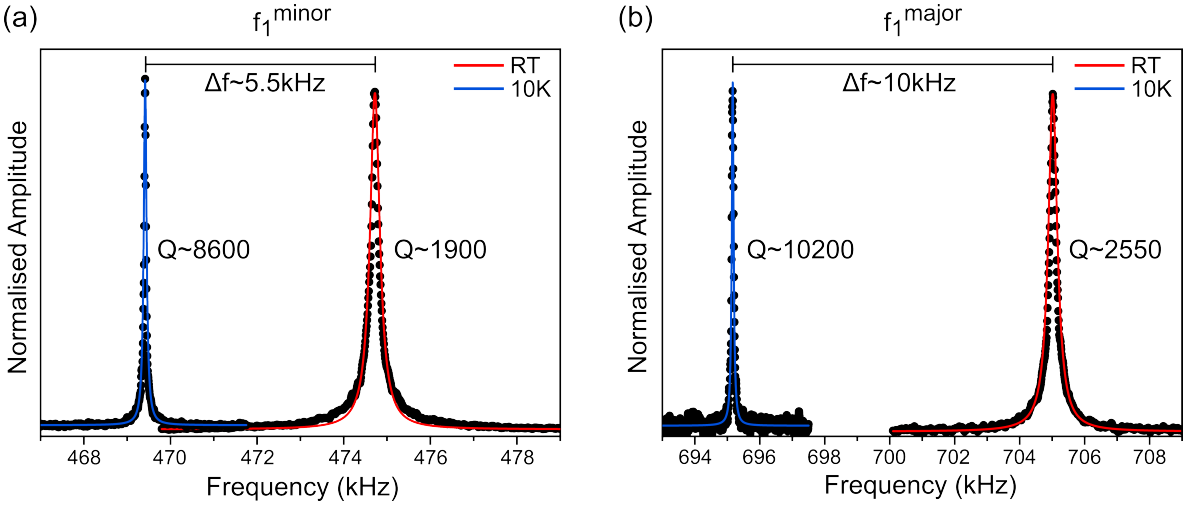

Figure 4.6: Comparison of the fundamental flexural mode spectra (a) f_1^{minor} and (b) f_1^{major} obtained for a nanowire with a cross-section aspect ratio ~1.4 at RT and T≈10K. Experimental data (circles) for each temperature in (a) and (b) was fitted with a single Lorentzian function (lines).

To determine whether the temperature dependent behaviour presented in Figure 4.6 was typical of all nanowires on Sample 4B, fundamental thermomechanical mode spectra at RT and T≈10K were obtained for three groups of six nanowires with each group having different cross-section aspect ratio. The three groups contained nanowires with nominal aspect ratios of ~1.17 (14µm x 175nm x 150nm), ~1.37 (13µm x 205nm x 150nm) and ~1.77 (12.3µm x

265nm x 150nm). Table 4.4 summarises the average experimentally determined fundamental resonance frequencies and Q-factors for each group of nanowires described above. The results demonstrate that the behaviour presented in Figure 4.6 is indeed typical for all nanowires on this sample, with a red-shifting of the average fundamental mode resonance frequencies and a significant increase in average fundamental mode Q-factors observed for each nanowire group when the temperature is reduced from RT to cryogenic temperatures.

	Aspect Ratio	f_1^{minor} (kHz)	Q (f_1^{minor})	f_1^{major} (kHz)	Q (f_1^{major})
RT	1.17	440±10	1470±100	460±10	1790±200
	1.37	469±8	1750±50	700±10	2450±50
	1.77	568±9	1900±40	1110±20	5730±360
T≈10K	1.17	433±6	7490±270	450±10	10740±1220
	1.37	464±8	8600±610	690±10	12300±800
	1.77	564±9	8830±160	1030±10	18430±990

Table 4.4: Resonance frequencies and associated mechanical Q-factors for the fundamental flexural modes of nanowires with three different average cross-section aspect ratios at RT and T≈10K. Averages are taken over six nanowires for each nominal aspect ratio. Errors are equal to one standard deviation.

Although the fundamental mode Q-factors for each group of nanowires here significantly increase when the temperature is reduced from RT to cryogenic temperatures, reports in the literature suggest that the thermoelastic damping of a cantilever does not typically decrease monotonically with decreasing temperature [132, 133, 135]. A slight temperature instability of the nanowire sample in the experimental setup utilised here, however, meant that it was not possible to obtain nanowire mode spectra at other temperatures in the range T≈10K – RT. The temperature instability of the nanowire sample was thought to arise from the poor thermal conductivity of the PZT to which the copper bracket housing the nanowire sample was attached. In an attempt to improve the thermal contact between the cryostat coldfinger and copper bracket, copper wires were used to connect the coldfinger to the bracket. Unfortunately this still did not completely eliminate the temperature instability of the setup. As described in the next section, the PZT was used in this setup to enable investigation of the dynamical properties of nanowires on Sample 4B.

4.6 Response of a Resonantly Driven Nanowire Mode

Previous studies of the dynamical properties of nanowire cantilevers have demonstrated that these small resonator structures commonly exhibit non-linear oscillatory behaviour at relatively small driving amplitudes [123, 124]. Although this can complicate the analysis of sensing experiments conducted with these structures, non-linearities in general also give rise to a wealth of interesting phenomena, including signal amplification [138, 139], mechanical frequency mixing [140] and noise squeezing [141].

With this in mind, the dynamical properties of individual nanowires on Sample 4B were investigated using the PZT as a mechanical excitation source. All measurements were undertaken at RT, using the 633.1nm wavelength stabilised diode laser for interferometric read-out. An arbitrary function generator (AFG – B&K Precision 4064) was used to drive the PZT with a sinusoidal excitation. The frequency of the sinusoidal excitation was adiabatically swept across the linear resonance frequency of a single flexural mode, whilst the response amplitude was monitored on the spectrum analyser. In the linear regime, the frequency at which the maximum nanowire response amplitude is observed is approximately that of the thermomechanical resonance frequency, and an increase in sweep amplitude leads only to an increase in the nanowire response amplitude and the area under the driven resonance peak. For sufficiently large PZT driving amplitudes, the deviation from the linear to non-linear regime is signalled by a shifting of this maximum response amplitude frequency with increasing driving amplitude until a point at which the nanowire oscillation enters a bistable regime, which is characterised by a step change in the response amplitude at a critical sweep frequency [123, 124].

Figure 4.7 displays the amplitude response of the fundamental flexural mode, $f_1{}^{minor}$, under swept mechanical excitation for a nanowire on Sample 4B with a cross-section aspect ratio of ~1.17, but a slightly smaller height in comparison to the group of nanowires with the same nominal aspect ratio (in the same array) described above (~12.3µm). Although the

area under the resonance peak was observed to increase with increasing driving amplitude, for nanowire oscillation amplitudes upto the interferometer fringe width ($\lambda/4$), there was no evidence of non-linear oscillatory behaviour for this mode. For a detection laser wavelength of 633.1nm, this fringe width equates to ~160nm. When the nanowire oscillation amplitude becomes larger than the fringe width, the measured response saturates and is accompanied by the appearance of harmonics of the fundamental mode in the differential signal. This complicates measurements such as this where larger driving amplitudes are required.

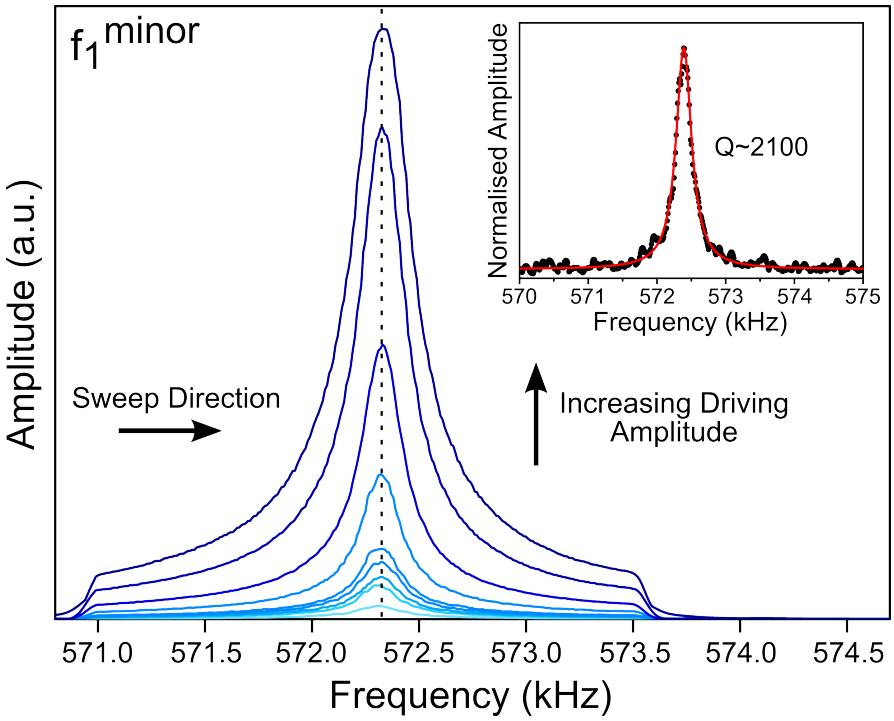

Figure 4.7: Nanowire response amplitude under swept excitation for the fundamental mode $f_1{}^{minor}$, of a nanowire with an AR of ~1.17. The drive amplitude increases from the bottom trace (light blue) to the top trace (dark blue). Inset shows the (non-driven) thermomechanical spectrum of $f_1{}^{minor}$ for this nanowire. Experimental data (circles) was fitted with a single Lorentzian function (line).

Observation of non-linear oscillatory behaviour of one of the fundamental flexural modes under swept excitation has been previously reported in the literature for GaAs nanowires with regular hexagonal cross-section and commensurate dimensions to those grown on Sample 4B. These were grown using a similar bottom-up technique and their motion was detected using an interferometer with a comparable fringe width [123]. However, as reported in Ref

[142], the critical amplitude for which oscillatory behaviour of the fundamental flexural mode of a cantilever fixed at one end becomes non-linear is approximately equal to $6.3(L/\sqrt{\mathrm{Q}})$, where L is the length of the cantilever and Q corresponds to the thermomechanical Q-factor of the fundamental flexural mode that is under excitation. The critical amplitude, therefore, for this nanowire was ≈1.7µm, which is significantly larger than the interferometer fringe width. For the measurements displayed in Figure 4.7 the incident laser spot from the probe arm was positioned as close to the clamping point of the nanowire as possible whilst still being able to detect the thermomechanical motion, but this still did not enable detection of non-linear behaviour for this mode. No instances of non-linear oscillatory behaviour of the fundamental flexural modes was observed on any of the nanowires measured on this sample. Due to the slight temperature instability of the sample when cooled to cryogenic temperatures as described in the previous section, it was not possible to perform these measurements at lower temperatures where the critical amplitude would be reduced by a factor of ~2 as a consequence of the increase in the mechanical Q-factor of the fundamental flexural modes. It is noted that the non-linear behaviour reported in Ref [123] was observed when operating the nanowire at a cryogenic temperature.

As stated in Ref [142], the critical amplitude for the second order flexural modes is reduced by a factor of ~18 relative to that for the fundamental modes. In terms of observing non-linear oscillatory behaviour, another advantage of the second order modes is that there is an additional node in the flexural mode profile (Figure 4.5(b)), around which the incident laser spot from the probe arm could be positioned. This measurement will therefore be undertaken in the future.

4.7 Conclusion

The mechanical properties of GaAs nanowires with varying cross-section aspect ratio grown using a catalyst-free bottom-up growth approach have been presented. Nanowire vibrational motion was characterised using a home-made free-space Michelson interferometer, and was

observed to closely follow the behaviour described by Euler-Bernoulli theory for a singly clamped beam. For elongated nanowires, attribution of a detected thermomechanical mode to a particular orthogonal vibrational direction was made possible by selecting the orientation of the elongation axis prior to nanowire growth. In agreement with previous reports in the literature, the mechanical Q-factor of the fundamental vibrational modes was observed to significantly increase when the operating temperature was reduced from RT to cryogenic temperatures (~10K). A full description of the Q-factor as a function of temperature, however, was not possible due to a slight temperature instability in the experimental setup utilised for detection of nanowire motion. The dynamical properties of individual nanowires were also investigated using a PZT as a mechanical excitation source. Initial attempts at detecting non-linear nanowire oscillatory behaviour through resonant mechanical excitation of the fundamental vibrational modes were unsuccessful. It has been reported in the literature that, in comparison to the fundamental modes, the onset of non-linear oscillatory behaviour for second order modes occurs at much smaller vibrational amplitudes. Future attempts at observing non-linear nanowire motion, therefore, will focus on resonant driving of these second order vibrational modes.

Chapter 5

Position-Controlled High-Q III-V Nanocavity System Formed by InP Nanowires on a GaAs Photonic Crystal Platform

5.1 Introduction

As described in Chapter 3, semiconductor nanowires formed from the bottom-up provide a versatile platform for the development of solid-state quantum light sources. The small diameters of these structures allow for the realisation of many heterostructure configurations, including quantum wells [43, 44] and quantum dots [6, 7, 45], from a wide variety of materials combinations [70], while the layer-by-layer nature of the epitaxial growth process naturally results in to the formation of an embedded emitter that is centred on the nanowire axis [102, 106]. The brightness and directionality [99–101], polarisation [83, 106] and collection efficiency [80, 102] of the emission from the embedded light source can also all be tailored through appropriate modification of the surrounding nanowire morphology. Bottom-up nanowires

have therefore attracted a great deal of interest in the pursuit of realising ultra-compact integrated photonic systems.

However, the vertical configuration of these structures after growth presents a significant barrier to achieving strong light confinement and efficient injection of emitted photons into on-chip photonic circuitry, especially for nanowires with dimensions optimised for high photon emission rates. Previous attempts at realising a highly localised integrated nanowire-based light source have involved transfer of nanowires from the growth substrate and subsequent fabrication of a photonic crystal device around a selected individual nanowire with desirable optical properties [1, 2]. Photonic crystal devices offer the ability to both guide light from one location to another efficiently and concentrate light into extremely small volumes [143–145], and therefore provide a promising route for the strengthening of nanowire light confinement and efficient incorporation of photonic emission with on-chip photonic elements. In these demonstrations, however, enhancement of light confinement is limited by the relatively small overlap of the confined mode of the photonic crystal and the nanowire volume.

In this chapter the theoretical and experimental study of a novel alternative means of achieving highly localised nanowire emission in an integrated photonic system is presented. The system in this case consists of an InP nanowire placed in a partially etched GaAs photonic crystal slot waveguide. For appropriate nanowire and photonic crystal structural parameters, a nanocavity mode with a very high Q-factor and a mode volume, V comparable to a cubic wavelength inside the nanowire can be realised at the nanowire location. In Section 5.2, a detailed description of this nanocavity design, originally proposed by Birowosuto *et. al* [146], is presented. Also included in this section is a discussion of another nanowire-photonic crystal integrated design proposed by Larrue *et. al* [147], which provides a potential means of enhancing light confinement in nanowires without removal of the nanowire from the growth substrate. As both designs presented in this section involve integration of a nanowire with a photonic crystal device, the basic properties of photonic crystals are introduced in Section 5.2 as well. In Section 5.3 frequency-domain and 3D FDTD simulations are used to demonstrate how the properties of the nanocavity resonance in the design proposed in Ref [146] are influenced by

modification of the nanowire and photonic crystal slot waveguide parameters, with the aim of achieving a high-Q, low V cavity resonance at a wavelength coinciding with the approximate centre of the broadband PL emission spectrum observed from the InP nanowires discussed in Chapter 2. Following this, the experimental methods utilised to produce nanocavity devices based on the optimised design determined in Section 5.3 are discussed in detail in Section 5.4. Results from the optical characterisation of these experimental nanocavity structures using PL and reflectivity measurements are then presented in Sections 5.5 and 5.6, respectively. The results obtained in Section 5.5 show that PL emission from individual InP nanowires occurs predominately at an energy corresponding to the low-temperature WZ band energy. Therefore, 3D FDTD simulations are used to determine the photonic crystal parameters that yield a high-Q, low V cavity resonance at a wavelength coinciding with this energy. A modified experimental procedure is then implemented for photonic crystal production to improve the prospect of realising an experimental cavity device with parameters matching that of optimised design. Finally, growth of a new InP nanowire sample is attempted with the aim of forming arrays of nanowires of a single crystal phase, which by virtue of being free of stacking faults, would all emit around the resonance wavelength of the optimised cavity design. The details regarding all of the processes related to this modified design are included in Section 5.7.

5.2 Background

5.2.1 Photonic Crystals

Photonic crystals are structures consisting of a periodic arrangement of materials with different dielectric constants. The periodicity of the structures causes Bragg reflections which control the propagation properties of light through the crystal. Through appropriate tailoring of the dielectric constant of the materials, the length of the periodicity and the type of symmetry the photonic crystal exhibits, propagation of certain wavelengths of light can be

prohibited as a result of destructive interference caused by the Bragg reflections [148]. These reflections lead to the formation of a photonic bandgap in the dispersion relation for in-plane light propagation, analogous to the electronic bandgap in semiconductors [108]. The type of photonic crystal structures used for realisation of the nanocavity arrangement described in this chapter consisted of a periodic triangular lattice of air holes etched into a suspended membrane of high index material (GaAs). This slab design is commonly adopted for these structures owing to the relative ease with which it can be fabricated and its potential for integration with other photonic elements on-chip [149]. A scanning electron microscope (SEM) image of such a device is shown in Figure 5.1.

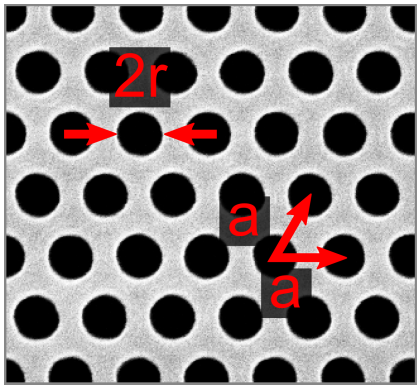

Figure 5.1: Top-down SEM image of a two-dimensional photonic crystal slab structure formed by etching of a triangular lattice of air holes (black) with radius r and lattice constant a through a semiconductor membrane (grey).

A defect state within the photonic bandgap of the photonic crystal slab can be created by filling in one or more of its air holes. As this defect mode is forbidden in the surrounding crystal lattice, it is well confined in two dimensions and a cavity is formed. Total internal reflection at the semiconductor-air interface provides further confinement of the cavity mode in the direction perpendicular to the photonic crystal plane. One of the most well studied types of cavity in this slab architecture is the L3 cavity design, which is formed when three air holes are removed in a line. L3 cavities were the first type of photonic crystal cavity arrangements in which quality factors greater than 10^4 were demonstrated experimentally [145] and have subsequently been implemented for a number of applications, including creation of efficient single photon sources [150] and measurements of quantum electrodynamics [89]. Omission

of air holes along a complete row of a photonic crystal slab creates defect states within the photonic bandgap of the structure which are free to propagate along the length of the defect axis (see Figure 5.5). This type of linear defect, known either as a line-defect or W1 waveguide, provides a means of coupling and guiding the emission from an emitter efficiently from one location to another on-chip and is thus one of the key components in the future realisation of integrated photonic circuits [151].

In the following sections, two alternative approaches for enhancing light confinement in small diameter nanowires through integration with photonic crystal devices are presented. The first involves the growth of a single vertical nanowire at the antinode location of a resonant L3 cavity mode, proposed by Larrue *et. al* [147], and in the second, proposed by Birowosuto *et. al* [146], a nanocavity system is formed through the transfer and placement of an individual nanowire into a partially etched slot at the centre of a photonic crystal line-defect.

5.2.2 Bottom-Up Growth of a Nanowire at the Centre of an L3 Photonic Crystal Cavity

For a nanowire grown by bottom-up growth techniques, the small refractive index contrast between the nanowire and the substrate dramatically affects the reflection co-efficient of the bottom facet mirror, leading to a large majority of emitted nanowire photons being lost to the substrate region. These losses can be somewhat compensated for by either increasing the diameter of the nanowire (with lasing demonstrated for single vertical nanowires with large lateral cross-sections [152, 153]), transferral of the nanowire from its growth substrate onto another host substrate [154, 155], or a combination of both. However, the multimode confinement in larger diameter nanowires typically leads to the formation of a complex far-field radiation pattern and low spontaneous emission rates for each of the confined modes [156], and nanowires transferred from the growth substrate are randomly dispersed on the host substrate, which can be a major obstacle for large-scale assembly and integration with other photonic elements on-chip.

In the scheme proposed by Larrue *et. al* [147], the loss mechanism at the nanowire-substrate junction is significantly reduced by instead incorporating the vertical nanowire structure with a high-Q low V L3 photonic crystal cavity. In this arrangement, the cavity acts as photon reservoir that recycles photons into the nanowire volume and prevents them from being surrendered to the surrounding substrate region. The design and resulting mode profile of the L3 photonic crystal cavity are displayed in Figure 5.2(a) and Figure 5.2(b). The L3 design is selected owing to the spatial distribution of the cavity mode, which has a maximum intensity at the centre of the cavity (predominately polarised in the direction perpendicular to the defect orientation, y) [157]. In addition, an L3 cavity provides strong modal selectivity as a result of optical losses in higher order modes [158, 159]. Shifting of the two holes terminating the cavity in the direction parallel to the defect orientation further enhances the confinement of the normal L3 fundamental cavity mode and a Q-factor of ~40000 is achieved for this modified cavity design [147, 160].

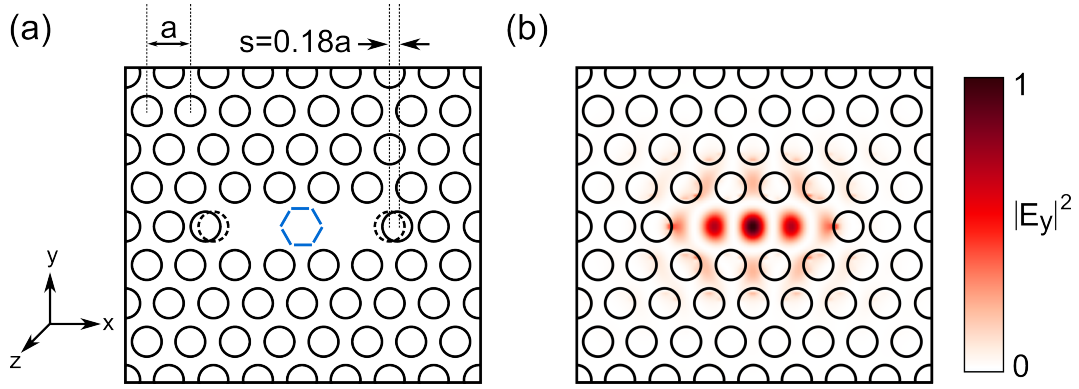

Figure 5.2: Modified L3 photonic crystal cavity design for a coupled nanowire-cavity system. Here the photonic crystal slab material is GaAs (n=3.4). (a) Schematic diagram of the modified L3 cavity design. The two holes terminating the cavity along x are displaced by an amount s=0.18a, where a is the lattice constant of the photonic crystal (the nearest neighbour periodicity of the air holes). (b) Calculated $|E_y|^2$ intensity distribution of the fundamental resonant mode of a bare L3 cavity. Placement of the vertical nanowire on the photonic crystal slab, illustrated by the blue dashed line in (a), is chosen to coincide with the maximum field intensity region of the cavity mode.

The introduction of the vertical nanowire at the centre of the L3 cavity breaks the symmetry of the slab structure and leads to a perturbation of the resonant photonic crystal cavity mode. With increasing nanowire diameter, the vertical confinement of cavity mode steadily reduces until a point at which guided modes are allowed to propagate freely through the nanowire

structure. This increase in the overlap of the electric field of the coupled mode with the nanowire, however, also naturally leads to a decrease in the Q-factor of the resonator. FDTD simulations carried out with the freely available software package MEEP [161], show that for a hexagonal GaAs nanowire with optimised parameters, placed at the centre of a GaAs L3 photonic crystal cavity, a high spontaneous emission factor (the fraction of the spontaneous emission funnelled into the resonant mode with respect to that into all other modes) β, of 0.3 can be achieved whilst maintaining a comparatively much larger Q-factor (~300) than is possible for a vertical nanowire sitting on a bare substrate.

Although this system has been engineered with optimal tailoring of the vertical emission properties of the nanowire in mind, funnelling of NWQD emission from the nanowire region back into the photonic crystal slab may be achieved through increasing the reflectance of the nanowire top facet. These photons directed back into the photonic crystal cavity region could then be routed into other coupled photonic elements on-chip. Increasing the reflectance of the top facet can be performed by first embedding the nanowire in a polymer matrix (e.g benzocyclobutene), exposing the top facet of the nanowire through controlled etching of the polymer layer and subsequent deposition of a thin layer of metal (e.g. Au), before removal of the remaining polymer material [162]. The coupled resonant mode profile calculated for the optimised nanowire design shown in the right panel of Figure 5.3(b) with a thin perfect metal (100% reflection, no absorption) top layer is shown in Figure 5.3(c). It is found that introduction of the top metal layer leads to a greater proportion of the coupled cavity mode to reside in the photonic crystal slab for these nanowire dimensions, reducing the value of β by approximately a half. Further optimisation of the nanowire parameters is required then for this modified design, but it has potential for providing a means of integrating cavity-enhanced single photon nanowire emission with photonic elements on-chip.

The simple design and cavity-enhanced emission properties of this nanowire-cavity system make it a particularly attractive means of realising highly efficient, low threshold nanolasers and high quality single-photon sources that are compatible with large scale integration. Methods of photonic crystal cavity fabrication in a number of III-V materials systems are well

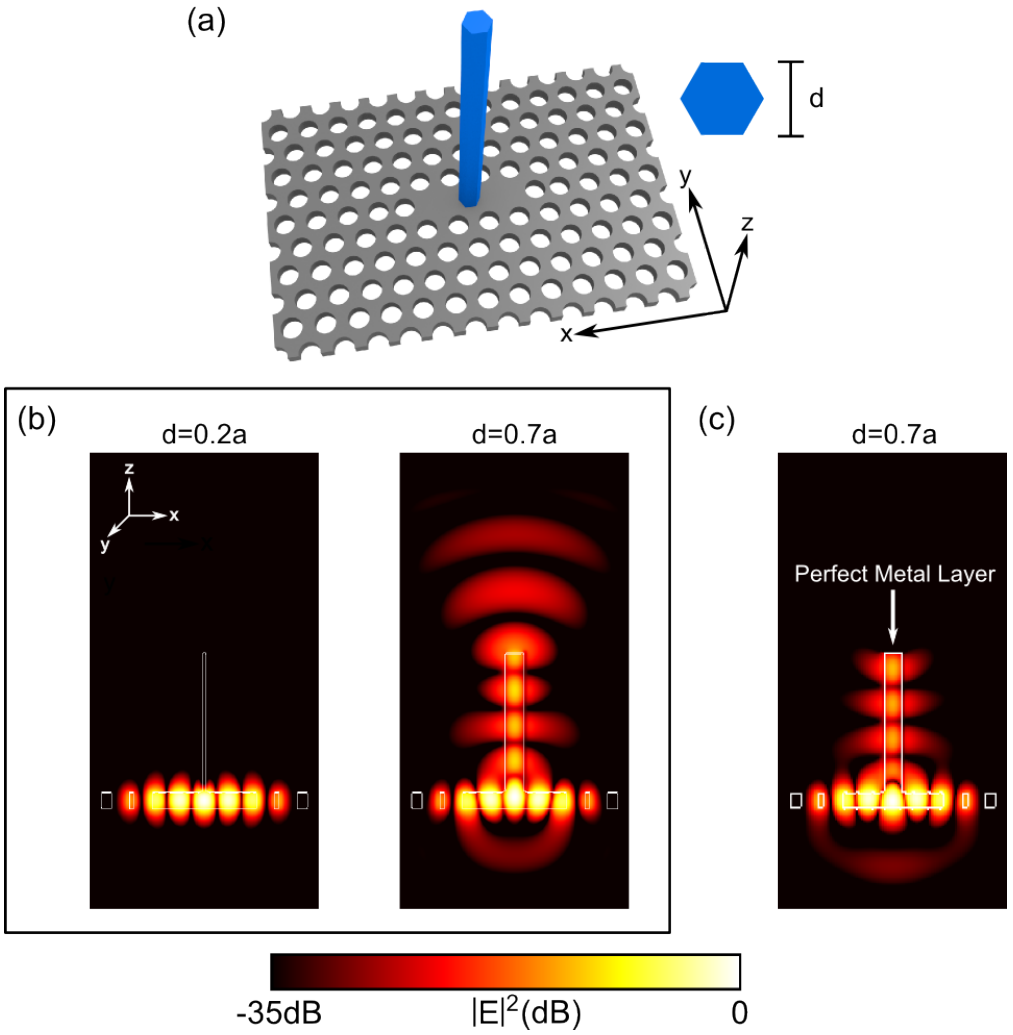

Figure 5.3: Optimisation of nanowire dimensions for enhanced overlap of the coupled cavity mode with the nanowire volume. The nanowire material is set to be the same as that for the photonic crystal slab (GaAs). (a) Schematic diagram of the coupled cavity system, consisting of a single vertical hexagonal nanowire with diameter d, and height h placed at the centre of a modified L3 photonic crystal cavity; Calculated $|E|^2$ intensity distribution of the fundamental coupled cavity mode for a nanowire with h=5a and (b) d=0.2a (left-hand panel), d=0.7a (right-hand panel), (c) d=0.7a with a thin perfect metal layer on the top facet. For a mode wavelength $\lambda_M \approx$860nm, the nanowire dimensions both in the right-hand panel of (b) and in (c) correspond to $d \approx$160nm and $h \approx$1.2µm.

established and control of nanowire position (at the centre of the L3 cavity mode anti-node in this case) in bottom-up growth techniques is enabled through lithographic definition as described in Chapter 2. Experimental realisation of this system, however, is greatly complicated by the fact that, whereas formation of III-V nanowires in the vertical direction requires the use of a (111)A or B substrate [38, 73], owing to the difficulties associated with realising smooth,

high quality surfaces in the (111)A or B direction [163, 164], semiconductor photonic crystal structures are typically fabricated from membranes epitaxially grown on (100) substrates. As a consequence of these differing substrate crystal orientation requirements, the feasibility of successful vertical nanowire growth on a photonic crystal cavity in the manner proposed here is low, and although experimental realisation of one similar system has been reported [165], to date there have not been any demonstrations of this coupled cavity arrangement in the III-V materials system.

5.2.3 Nanowire Placed in a Partially Etched Photonic Crystal Slot Waveguide

The unconventional (111)A or B substrate orientation required for bottom-up III-V nanowire growth, and losses associated with the low index contrast between the nanowire and underlying growth substrate mean that enhancement of nanowire light confinement is typically pursued through removal and transfer of the nanowire onto a host substrate, where a tailored cavity architecture can then be fabricated around it [2, 155, 166]. However, as the nanowire is randomly dispersed on the host substrate after transfer, highly precise nanofabrication techniques are required to align exactly the cavity location and orientation with that of the deposited nanowire. Experimental demonstration of successful coupling between nanowires and small photonic cavity systems fabricated after nanowire transfer have been reported [2] but the confined mode volume (at the modal wavelength) in these systems is too large to achieve strong overlap of the confined mode with the nanowire volume.

In the scheme proposed Birowosotu *et. al*, [146] strengthening of light confinement in a small diameter nanowire is achieved by transfer and placement of the nanowire into a partially etched slot at the centre of a photonic crystal line-defect which has been pre-fabricated on the host substrate. In this arrangement, depicted schematically in Figure 5.4, cavity losses associated with a horizontal nanowire lying on a bare substrate are greatly diminished by the surrounding photonic crystal waveguide structure, which leads to the formation of a coupled

nanocavity at the nanowire position that exhibits high-Q and an effective mode volume, V of $\sim(\lambda/n)^3$ for suitably optimised structures. Strong light confinement in a small volume is a result of the small refractive index modulation in the photonic crystal line-defect generated by the placement of the nanowire in the partially etched slot. The nanowire also acts to suppress electric field losses associated with the large vertical asymmetry of the photonic crystal slab in the partially etched slot region.

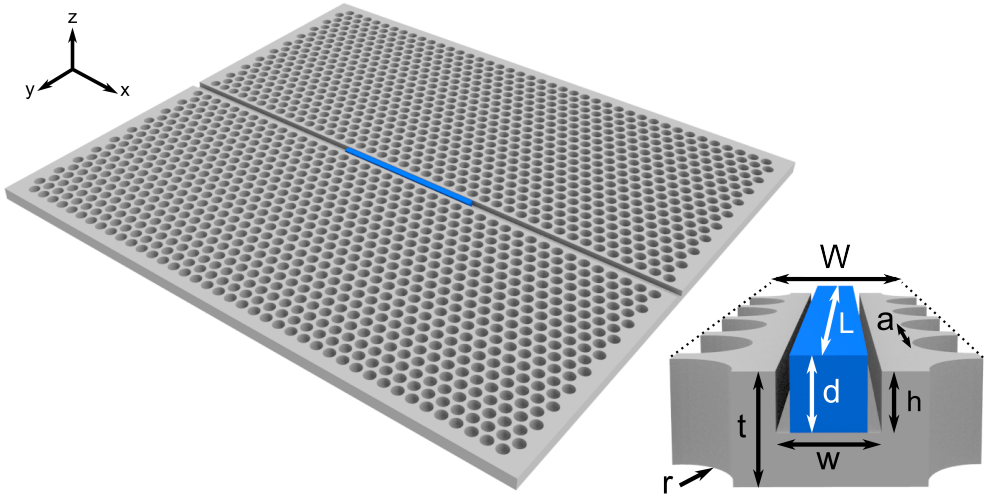

Figure 5.4: Schematic of a high-Q low-V position-controlled nanocavity design proposed by Birowosotu *et. al.* The nanocavity is formed by placement of a subwavelength sized nanowire at the centre of a partially etched slot in the middle of a photonic crystal line-defect. The inset displays a cross-section of the nanocavity arrangement. White text labels refer to nanowire parameters (d = nanowire diameter, L = nanowire length), while those in black refer to surrounding photonic crystal device parameters (a = nearest neighbour periodicity of air holes, W = line-defect width, r = air hole radius, t = slab thickness, h = slot height, w = slot width).

Due to the fact that the nanowire structure is not bound to the surrounding photonic crystal device after placement in the slot, one of the most attractive features of this system is the potential ability to control the position of the cavity along the line-defect after device fabrication, which provides the possibility of realising position-controlled on-demand high quality quantum light sources for photonic integrated circuits. Post-fabrication formation of high-Q low-V nanocavities in photonic crystal waveguides has been demonstrated elsewhere with the use of scanning probe lithography, [167] however, in this scheme, once the cavity has been 'written', the cavity location cannot be subsequently re-positioned. Re-writeable photonic crystal nanocavities have been reported in the case of water/polymer micro-infiltration of

photonic crystal air holes [168, 169] but as well as the high level of complexity involved in cavity formation using this method, the feasibility of incorporating this type of cavity with other integrated photonic circuit elements is low.

As described above, strong confinement of light in the region of the nanowire is provided by the spatial index modulation of the photonic crystal line-defect resulting from the placement of the nanowire in the partially etched slot waveguide. The origin of this high-Q, low-V cavity mode can be explained by considering the dispersion characteristics of the line-defect photonic crystal waveguide design in this scheme and how these are modified by the introduction of the partially etched slot and subsequent placement of an individual nanowire inside the slot. The band structure of a photonic crystal slab structure with a line defect, calculated using the MIT photonic bands (MPB) software package [109], is displayed in Figure 5.5. Removal of a complete row of air holes from the photonic crystal creates a series of regularly spaced point defects within the crystal which couple to form a series of guided modes in the photonic bandgap (PBG) which are free to propagate along the defect axis. These TE-like gap-guided modes are confined laterally by the periodic air hole arrangement either side of the defect and vertically by total internal reflection (TIR).

It is observed that the group velocity ($d\omega/dk$) of the fundamental gap-guided mode (labelled (i) in Figure 5.5) decreases monotonically and tends to zero as it reaches the Brillouin zone (BZ) edge. The evolution of this gap-guided mode as the wavevector progresses from the light cone to the BZ edge is a result of coupling between the fundamental gap-mode and a second category of guided TE-like 'index-modes' that arise as a consequence of the waveguide having a higher refractive index than the surrounding air [108]. Coupling of the highest energy index-guided mode (labelled (iv) in Figure 5.5) with the fundamental gap-guided mode induces an anti-crossing between the two, creating a region close to the BZ edge where the group velocity tends to zero (termed the 'slow-light' region) [170].

Introduction of a partially etched slot that sits at the centre of the line-defect and extends along its length reduces the effective refractive index in the line-defect region, which induces a modification of the group velocity profile of the fundamental gap-mode and causes it to

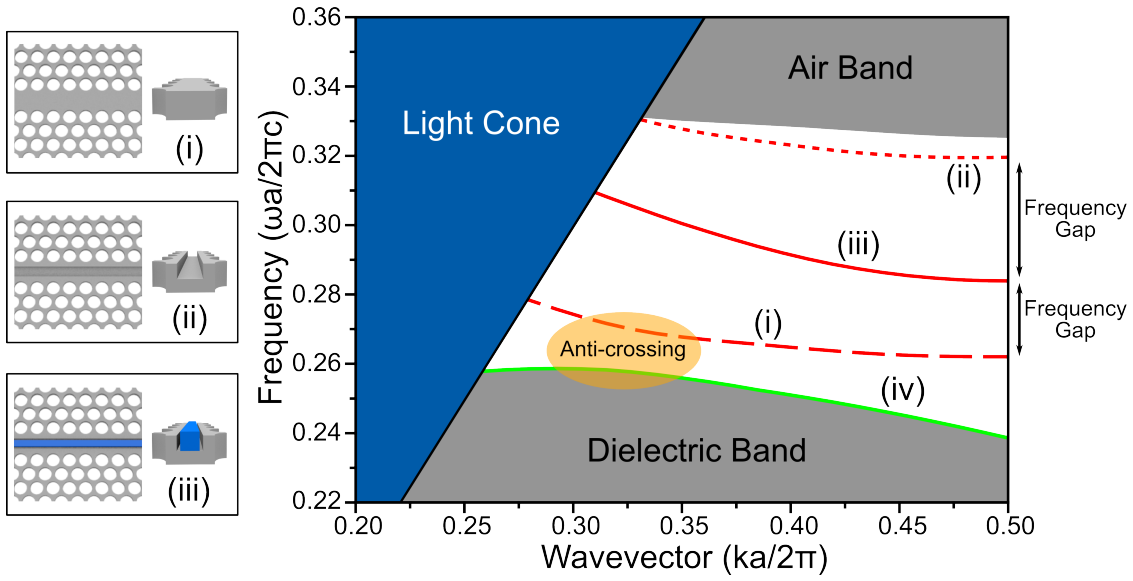

Figure 5.5: Calculated band structure showing the TE-like fundamental PBG modes for a photonic crystal (i) line-defect (ii) line-defect with a partially etched slot and (iii) nanowire (with square cross-section) at the centre of a partially etched slot. Anti-crossing of highest energy index-guided mode (iv) and PBG mode (i) causes group velocity of (i) to tend towards zero near BZ edge. Left hand panels display schematic diagrams of the device arrangements that produce modes (i), (ii) and (iii).

be pulled up towards the higher frequency air band (consisting of the extended slab modes propagating in air) [171]. This slot waveguide gap-guided mode is depicted by the curve labelled (ii) in Figure 5.5. Subsequent placement of a nanowire with similar refractive index to the surrounding photonic crystal device at the centre of the partially etched slot waveguide restores a fraction of the original effective refractive index of the line-defect and red-shifts the fundamental gap-mode into a region in the PBG that lies in-between that of the original gap-guided and slot waveguide modes (labelled (iii) in Figure 5.5). As this nanowire-slot waveguide mode is surrounded by a complete frequency gap inside the line-defect PBG, light is strongly confined to the nanowire region, resulting in the formation of a high-Q low-V cavity. Similar designs exploiting this 'mode-gap' effect to create high-Q low-V nanocavities in photonic crystal line defect structures have been reported elsewhere [167, 172–177].

The coupled nanowire-photonic crystal system designed by Birowosuto *et. al* is optimised for cavity operation in a wavelength range for telecommunications applications (1.3µm–1.55µm) and employs Si as the materials system for fabrication of the photonic crystal slot waveg-

uide. Recently, there have been a number of reports demonstrating growth of embedded quantum dots in small diameter InP nanowires that exhibit very narrow emission line-widths and spectrally pure, bright single-photon emission at sub-micron emission wavelengths [5, 77]. Therefore tailoring of the cavity parameters in this design to achieve a cavity resonance at sub-micron wavelengths provides the opportunity for realisation of an extremely high quality source of indistinguishable single photons and also measurements of cavity quantum electrodynamics using a single NWQD. In addition, such a system has the potential to provide sufficient optical gain to demonstrate lasing operation from nanowires with sub-100nm diameters. Optimising the cavity resonance to sub-micron wavelengths also offers the advantage that the fundamental optical properties of the cavity system can be extensively characterised by commercially available high performance silicon photodetectors. Additionally, as device size requirements scale with wavelength, a cavity design optimised for operation at shorter wavelengths offers the possibility of a more compact structural arrangement.

As the bandgap energy of Si is ~1.1eV (at RT) [178] however, achieving cavity operation with this design at sub-micron wavelengths requires utilisation of a different materials system for the photonic crystal slot waveguide device. In the following sections of this chapter, a detailed investigation into the design and experimental realisation of a movable high-Q, low-V nanowire cavity system, consisting of an InP nanowire placed inside a partially etched GaAs photonic crystal slot waveguide, optimised for cavity resonance at sub-micron wavelengths is presented. As well as possessing a more appropriate bandgap energy for a sub-micron cavity resonance wavelength, GaAs was selected as the materials system for photonic crystal device fabrication in this case due to the fact that fabrication methods for these devices in this materials system are well established in the LDSD group at the University of Sheffield. Manufacture of a number of other high quality photonic devices in the GaAs materials system have also been demonstrated by the LDSD group [143, 179], providing the potential for future integration of this optimised cavity arrangement with other photonic devices on-chip.

5.3 Optimisation of Nanocavity Design for Cavity Resonance at Sub-Micron Wavelengths

The scale invariance of Maxwell's equations allowed, as a first step in optimisation with the GaAs materials system, the translation of the photonic crystal slot waveguide parameters in Ref [146] to those appropriate for a cavity mode resonance at shorter wavelengths. To maximise the probability of spectral overlap of nanowire emission and the cavity resonance in this first instance, a target cavity resonance wavelength of $\lambda_R \approx 870$nm for this system was selected, as this corresponds approximately to the centre of the broadband PL energy distribution observed from low temperature PL measurements on the previously grown polytypic InP nanowire samples presented in Chapter 2. Conversion of the photonic crystal waveguide parameters to those more suitable for $\lambda_R \approx 870$nm led to selection of the following starting values: a=246.5nm, r=70nm, t=140nm and again $W=0.98\sqrt{3}a$ (~418nm). The value of t here was chosen based on a compromise between strong modal confinement in the z-direction via TIR at this resonant wavelength [108] and the structural integrity of the photonic crystal slab. As the narrowest nanowire diameter achieved in previous InP nanowire growth was on the order of ~100nm, this value was chosen as the nanowire diameter in this adapted design. It is noted that although this adapted design does not take into account the slight refractive index difference between Si (n_{Si}=3.48) and GaAs (n_{GaAs}=3.4), it was deemed a suitable starting point for design optimisation here.

Optimisation of the nanowire-photonic crystal cavity system was performed using both frequency-domain and FDTD simulation approaches. Frequency-domain simulations were employed to investigate the shift in frequency of the fundamental PBG mode of the nanocavity arrangement when parameters of the photonic crystal were modified, in order to ascertain the structural arrangement which produced a PBG mode coinciding in frequency with the desired cavity resonance. The cavity properties of this structural arrangement, such as the Q-factor and V at the resonant wavelength were then subsequently obtained using 3D FDTD simulations.

Initial optimisation steps were carried out using frequency-domain simulations, as these are much less computationally demanding than equivalent FDTD simulations of the same structural system (owing to the fact that calculations are performed in the frequency-domain with a periodically repeating supercell) and allowed for the structural parameters corresponding to the approximate desired cavity resonance wavelength to be obtained in a much shorter time-frame than would have been possible using only FDTD simulations.

Frequency-domain simulations commenced with consideration of the most straightforward cavity design, where the slot width and height of the photonic crystal slot waveguide were set to match that of the nanowire diameter (100nm). The band structure for this arrangement, calculated using MPB with the supercell depicted schematically in Figure 5.6(a), is displayed in Figure 5.6(b). Here, the refractive index for the InP nanowire is set to n_{InP}=3.17 (with the refractive index of the photonic crystal slot waveguide set to n_{GaAs}=3.4 as mentioned above). As the nanowire in this case completely fills the partially etched slot region in all directions, the fundamental PBG mode of this system, depicted by the curve labelled (i), resembles that observed for an unmodified line-defect in terms of its evolution with wave-vector k and relative position to the dielectric band edge (see Figure 5.5). In a real experimental design however, placement of a nanowire in a partially etched slot with the same width as the nanowire diameter would be challenging, and so the frequency shift of the fundamental PBG mode as a function of expanding slot width (in increments of 2.5nm) was determined. Curves (ii) and (iii) in Figure 5.6(b) depict the PBG modes calculated for a slot width of 115nm and 135nm, respectively. The reduction in effective refractive index caused by the increasing fraction of air in the slot waveguide leads to an expected blue-shifting of the fundamental mode, but it is observed that even a relatively small increase of 35nm causes a considerable frequency shift of the PBG mode from the initial position of (i) ($\Delta\omega\approx0.043(2\pi c/a)$) and a large deviation from the desired cavity mode resonance frequency ($\Delta\omega\approx0.029(2\pi c/a)$), illustrated by the black dashed line in this plot.

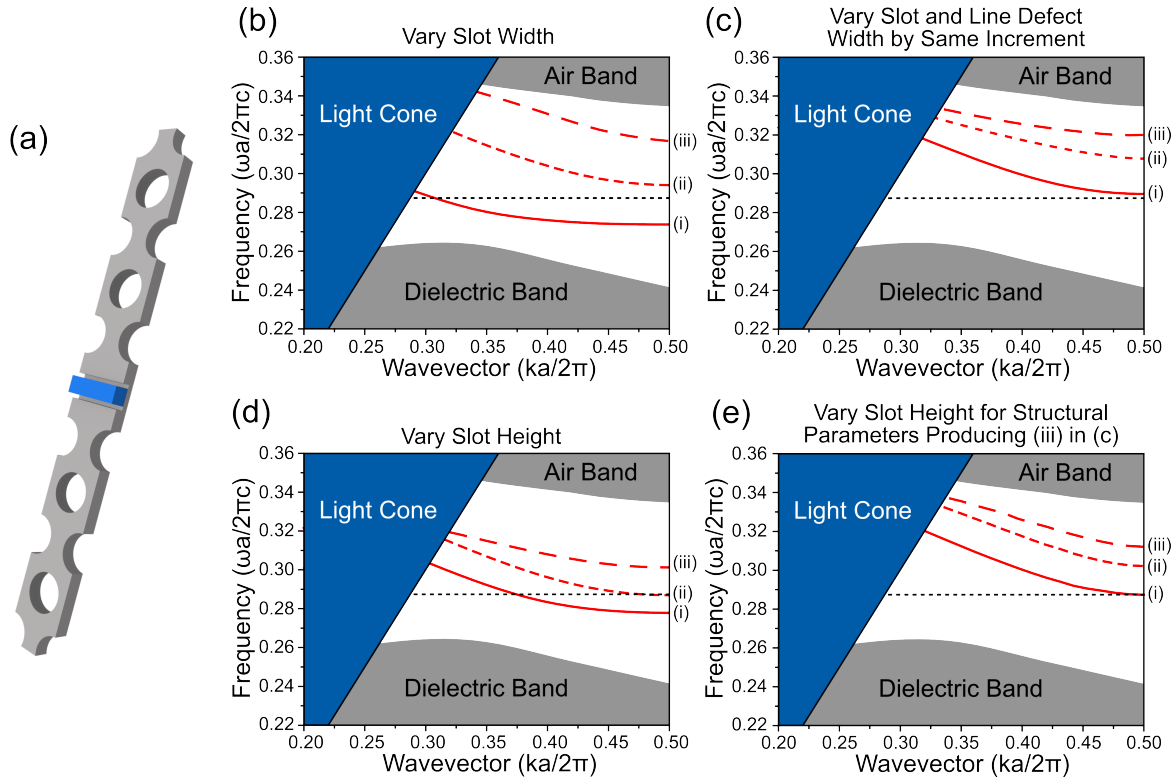

Figure 5.6: Frequency-domain simulations for characterisation of the frequency shift of the fundamental nanowire-photonic crystal slot waveguide PBG mode with varying photonic crystal device parameters. (a) Schematic diagram of supercell utilised for frequency-domain simulations, consisting of a nanowire with square cross-section placed in the centre of a partially etched photonic crystal slot waveguide. The refractive indices of the nanowire and photonic crystal for all calculations were set at n_{InP}=3.17 and n_{GaAs}=3.4, respectively; Calculated band structure diagrams show how the fundamental PBG mode of the system shifts in frequency when the (b) slot waveguide width is varied, (c) slot waveguide and line defect width are varied simultaneously by the same dimensional increment, (d) slot height is varied, (e) slot height is varied for the structural arrangement producing the highest frequency PBG mode (iii) observed in (c). In all band structure plots, the dashed black line indicates the frequency equivalent to λ_R≈870nm. Structural parameters that correspond to the calculated band structures in (b), (c), (d) and (e) are presented in the main text.

In an attempt to compensate for the reduction in the effective refractive index induced by the increasing slot width, for each slot width increment, the line-defect width was simultaneously increased by the same step size (2.5nm). Figure 5.6(c) displays the fundamental PBG modes for a slot width and corresponding line-defect width of (i) w=115nm, W=0.98$\sqrt{3}a$+7.5nm; (ii) w=135nm, W=0.98$\sqrt{3}a$+17.5nm and (iii) w=150nm, W=0.98$\sqrt{3}a$+25nm. It is seen that, as well as causing a red-shift of the fundamental PBG modes, the complementary increase in the line-defect also leads to a small reduction in the frequency shift as the slot width is

increased ($\Delta\omega_{(i)-(ii)}\approx0.018(2\pi c/a)$ compared to $\Delta\omega_{(ii)-(iii)}\approx0.023(2\pi c/a)$ in Figure 5.6(b)). Red-shifting of the fundamental PBG modes was also observed when the depth of the slot was reduced below the diameter of the nanowire. Figure 5.6(d) shows the calculated fundamental PBG modes for the structural arrangement that produced mode (i) in Figure 5.6(d) with a varying slot depth of (i) 60nm, (ii) 90nm and (iii) 115nm. As the nanowire diameter has been set to 100nm in this design, matching the slot depth with nanowire diameter means that approximately 70% of the suspended photonic crystal device is removed in the slot region. In an experimentally realised structure, the removal of this amount of material in the slot region has the potential to greatly weaken the structural integrity of the suspended device. However, reducing the depth of the slot will lead to a reduction in the spatial overlap of the cavity mode with the nanowire volume. Determining a slot depth that provides an adequate comprise between these two opposing conditions is therefore important in this design.

Taking into consideration the observations from the previous three optimisation steps, red-shifting of the most blue-shifted PBG mode in Figure 5.6(c) towards the desired cavity resonance was attempted through varying the slot depth of the corresponding structural arrangement. This structural arrangement was chosen for further optimisation as it possesses the largest studied slot width (150nm), and experimentally, a larger slot width will facilitate easier placement of the nanowire inside the slot waveguide. Figure 5.6(e) displays the calculated fundamental PBG modes for this structural arrangement with a slot depth of (i) 60nm, (ii) 70nm and (iii) 85nm. For the smallest slot depth, it is observed that the frequency of the fundamental PBG mode coincides with the desired cavity resonance frequency in the region close to the BZ edge. The parameters of this structural arrangement, therefore, were selected as the initial parameters for nanocavity optimisation using FDTD simulations.

3D FDTD simulations were performed using the commercial-grade simulator 'FDTD solutions' from Lumerical [116]. The simulation domain, depicted schematically in Figure 5.7, consisted of a GaAs photonic crystal slot waveguide (n_{GaAs}=3.4) with an InP nanowire (n_{InP}=3.17) of finite length, L=2µm at its centre. Investigation of the cavity properties of this system began by determining the fundamental cavity resonance wavelength λ_R, using a broadband electric

dipole source placed at the centre of the nanowire. The Q-factor and V of the cavity system were then subsequently calculated using a narrowband excitation range (~2nm) around this previously calculated resonance wavelength. In the FDTD software package utilised for these calculations, the Q-factor is determined by the slope of the envelope of the decaying signal using the formula

$$Q = \frac{-2\pi f_R \log_{10}(e)}{2m} \tag{5.1}$$

where f_R is the resonance frequency of the mode, and m is the slope of the decay [116]. V is calculated according to the conventional Purcell definition

$$V = \frac{\int_V \epsilon |\mathbf{E_y}(r)|^2 dV}{\max[\epsilon |\mathbf{E_y}(r)|^2]} \tag{5.2}$$

where $|\mathbf{E_y}(r)|^2$ is the electric field intensity at point r, and $\max|\mathbf{E_y}(r)|^2$ is the maximum field intensity value inside the simulation domain [180].

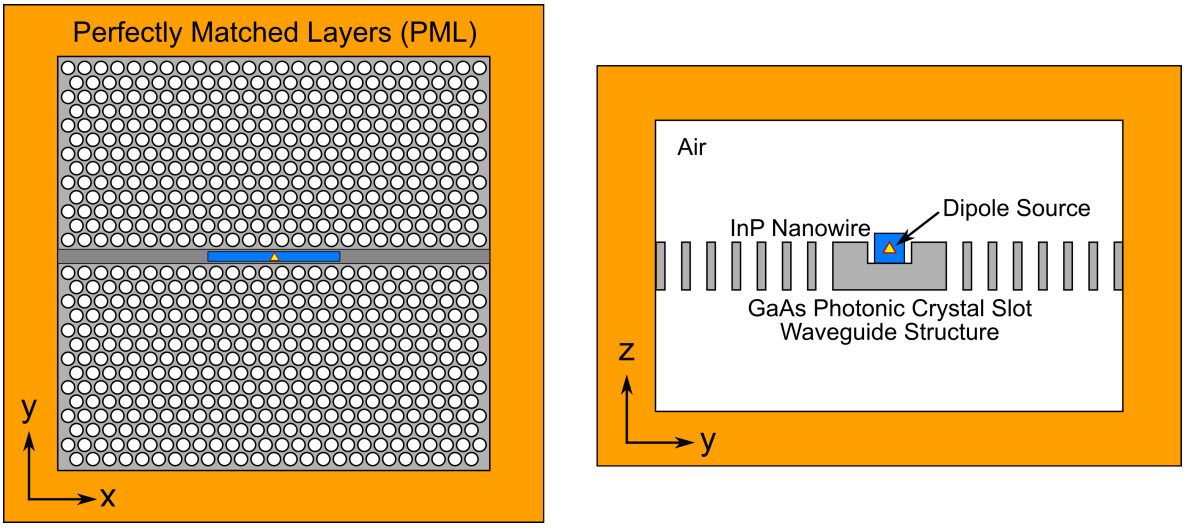

Figure 5.7: Schematic illustration of the 3D FDTD simulation domain utilised for optimisation of the nanowire nanocavity design. An electric dipole is placed in the middle of a finite length InP nanowire (n_{InP}=3.17) with square cross-section, which is located at the centre of a GaAs photonic crystal slot waveguide (n_{GaAs}=3.17). The simulation domain measures 37 (x-axis) by 30.5 (y-axis) by 7.9 (z-axis) lattice periods (a) and is surrounded by perfectly matched layers (PML) to ensure complete absorption of the electric fields (without any reflection) at the boundaries.

For the optimised structural arrangement described above, the value of the cavity resonance wavelength calculated from FDTD simulations was found to be significantly red-shifted in comparison to that determined previously from frequency-domain simulations ($\lambda_R \approx 920$nm). Using equations 5.1 and 5.2, the Q-factor and V of this cavity resonance were calculated to be ~43500 and ~$0.71(\lambda/n)^3$ (where $n = n_{\mathrm{InP}}$), respectively. However, as is observed from the calculated mode profile of the cavity mode in Figure 5.8(a), because the main component of the electric field of the (TE) cavity mode ($\mathbf{E_y}$) is oriented perpendicularly to the nanowire/slot interface along most of the nanowire length, the majority of the mode residing outside of the photonic crystal slab is concentrated in the slot region around the nanowire. This is further illustrated in Figure 5.9(a)(i), which shows the development of $|\mathbf{E_y}|$ in the y-direction at a position in x and z corresponding to the centre of the nanowire (x=0μm, z=0.06μm). The maxima of $|\mathbf{E_y}|$ are clearly located in the slot region around the nanowire, with the field intensity changing abruptly at the slot boundaries. It is also observed that the fraction of the field confined within the nanowire is comparatively small compared to that residing outside. The fraction of electric field confined within the nanowire for this cavity resonance, C_y was calculated using

$$C_y = \frac{\int_{-L/2}^{L/2}\int_{-d/2}^{d/2}\int_{-d/2}^{d/2} \varepsilon_{\mathrm{NW}}|\mathbf{E_y}|^2 dxdydz}{\sum_{i=1}^{N}\int_{-\infty}^{\infty}\int_{-\infty}^{\infty}\int_{-\infty}^{\infty} \varepsilon_i|\mathbf{E_{y}}_i|^2 dx_i dy_i dz_i} \tag{5.3}$$

where i refers to each of the materials within the simulation domain (i.e. air, GaAs and InP) and $\varepsilon_{\mathrm{NW}}$ is the dielectric constant of the nanowire. Using Equation 5.3, C_y was determined to be ~0.07. This is approximately a factor of 3 smaller than that reported for a similar cavity system with a comparable slot width and nanowire diameter by Birowosuto *et al.* in the supplementary information of Ref [3]. As expected, when the slot width is matched to the nanowire diameter (w=100nm), the electric field profile of the cavity resonance, shown in Figure 5.8(c), is more like that of an unmodified photonic crystal line-defect mode. Along the y-direction, $|\mathbf{E_y}|$ develops gradually across the nanowire boundaries and significantly more of the field resides within the nanowire volume compared to that for w=150nm, with the

maxima of $|\mathbf{E_y}|$ located at x=0 (Figure 5.9(a)(iii)). This comparative increase in the fraction of the field inside the nanowire observed in Figure 5.8(c) and Figure 5.9(a)(iii) is reflected in the value of C_y, which was calculated to be ~0.15 for this arrangement.

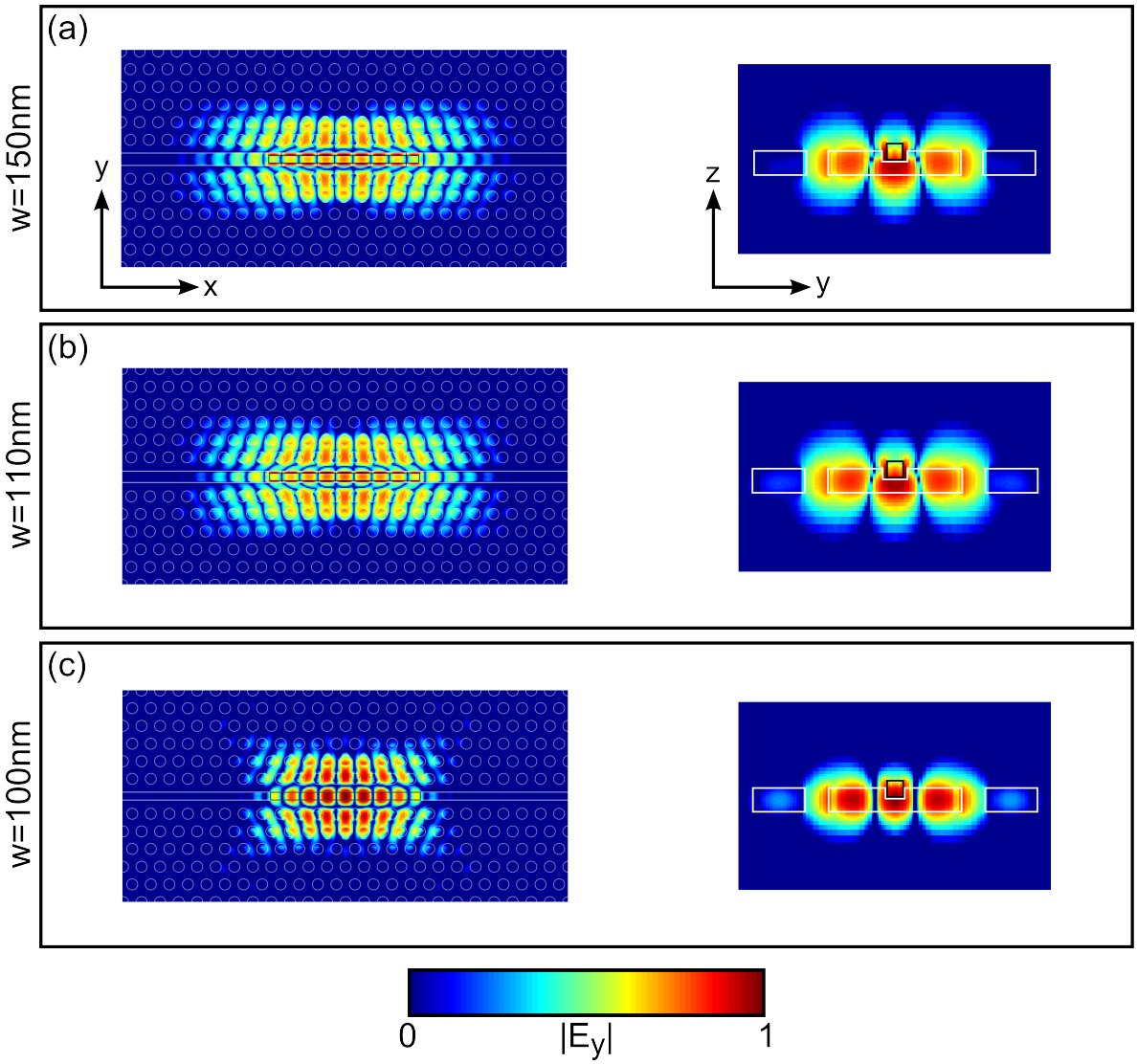

Figure 5.8: FDTD simulations for characterisation of the resonance properties of the fundamental cavity mode for a nanowire-photonic crystal nanocavity arrangement when varying the slot width, w relative to the nanowire diameter, d. Calculated 2D $|\mathbf{E_y}|$ field-profiles of the fundamental cavity mode in the x-y plane (left) and y-z plane (right) are shown for d=100nm and (a) w=150nm, (b) w=110nm, (c) w=100nm. For all calculations, the other nanocavity parameters have fixed values of t=140nm, a=246.5nm, r=70nm, W=0.98$\sqrt{3}a$+25nm and h=60nm. The colour scale in each image is logarithmic and the field profiles are normalised to the source power. Photonic crystal and nanowire structures are depicted by white and black solid lines, respectively. Properties of the simulation domain are described in Figure 5.7.

The increased confinement of the field inside the nanowire for this arrangement slightly reduces V relative to that for w=150nm ($V \approx 0.66(\lambda/n)^3$), but this decrease in V is accompanied by a comparatively larger reduction in the Q-factor of the cavity resonance (Q≈30000). It is thought that the main contributor to this decrease in Q is the reduction in vertical confinement of the cavity mode when w=100nm. Figure 5.9(c) and Figure 5.9(d) show the spatial Fourier transforms (FT) of the cavity mode electric fields displayed in Figure 5.8(a) and Figure 5.8(c), respectively. For decomposed plane waves which have in-plane momentum components (k_x, k_y) inside the light cone (represented by the white circles at (0,0) with a radius of $2\pi/\lambda_R$), the condition for TIR is broken [145, 146, 181]. When w is reduced from 150nm to 100nm, it is observed that the number of in-plane momentum components inside the light cone increases, resulting in a comparatively weaker vertical confinement of the cavity mode. The reduction in w from 150nm to 100nm also leads to a red-shifting of the cavity resonance, with λ_R≈954nm for w=100nm.

Although C_y was observed to reduce considerably with an increase in w from 100 to 150nm (and as is shown in Figure 5.8(b) and Figure 5.9(a)(ii), the electric-field outside of the photonic crystal slab resides mainly in the slot region around the nanowire even for only a infinitesimal width mismatch between nanowire diameter and slot width), experimental observation of cavity enhanced emission from a similar nanowire cavity system where w is greater than the nanowire diameter has been recently reported by Birowisuto *et al.* [3]. With this in mind, the structural parameters of the photonic crystal waveguide were modified in order to realise a cavity resonance at the target wavelength λ_R≈870nm for the ideal scenario where w=d=100nm. Taking into consideration observations made from the previous frequency domain simulations, this was achieved by increasing r to 80nm and decreasing both a to 242.5nm and W to $0.98\sqrt{3}a$ with h and L remaining as 60nm and 2µm, respectively. These structural changes also resulted in a significantly increased Q-factor, relative to the previously described arrangements, of ~76000 and a small decrease of V to ~$0.65(\lambda/n)^3$. The value of C_y, however, remained at ~0.15.

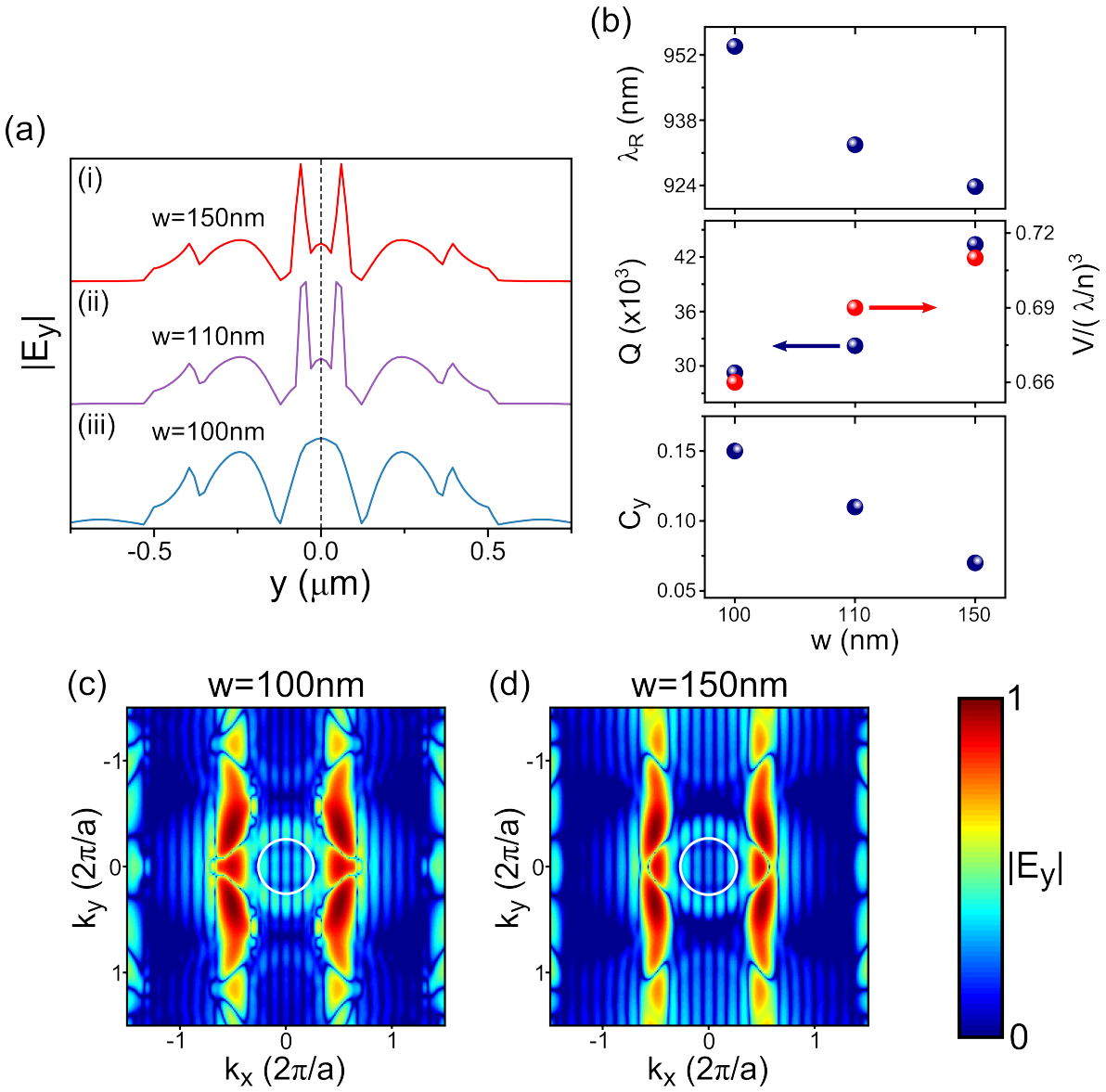

Figure 5.9: Variation in the properties of the fundamental nanocavity mode as a function of slot waveguide width, w. (a) Development of $|\mathbf{E_y}|$ along the y-direction at the centre of the nanowire in x and z (x=0μm, z=0.06μm) for (i) w=150nm, (ii) w=110nm, (iii) w=100nm; (b) Summary of the calculated λ_R, Q, V and C_y values for each of the values of w; Spatial Fourier transformation spectra obtained from the y-component of the electric field ($|\mathbf{E_y}|$) in the x-y plane for (c) w=100nm, (d) w=150nm. The colour scale in each image is logarithmic and the light cone is depicted by the white circle with a radius, $r_{LC}=2\pi/\lambda_R$. For all calculations, the other nanocavity parameters have fixed values of t=140nm, a=246.5nm, r=70nm, $W=0.98\sqrt{3}a$+25nm, h=60nm and L=2μm.

One way of improving the value of C_y for the ideal w=d system described above, is through an increase in the value of h. A slot depth of 60nm was chosen for all of the previous FDTD simulations, as in the preceding frequency-domain simulations this resulted in a λ_R

which coincided with the target wavelength of 870nm. The original reason for reducing the slot depth relative to the nanowire diameter was that in an arrangement where h=d, the suspended photonic crystal slab, with only ~40nm of material remaining in the slot region, would be very susceptible to collapse during nanowire transfer and placement. To ascertain in more detail how modification of the slot waveguide depth for this arrangement affected the properties of the cavity mode and its spatial overlap with the nanowire volume, C_y, Q, V and λ_R were calculated for h values of 30, 50, 70 and 90nm. For each of these values of h, Figure 5.10(a) shows the calculated cavity mode profile in the y-z plane at x=0. As expected, it is observed from the mode profiles that as h increases, the amount of field confined within the nanowire also increases. A plot of the calculated C_y values for each slot depth (in addition to h=60nm calculated previously) is plotted in Figure 5.10(b), and shows that the fraction of the field confined within the nanowire increases from ~0.07 for h=30nm upto ~0.24 for h=90nm. However, although the mode volume of the cavity mode does not change significantly when h is modified ($0.62 \lesssim V \lesssim 0.69$), the Q-factor of the resonance decreases from ~250000 for h=30nm to ~20000 for h=90nm. To highlight this contrary trend in the relationship of C_y and Q to h, the values of Q/V for each slot depth are also plotted in Figure 5.10(b). Taking into consideration the mode profiles displayed in Figure 5.10(a), the decrease in the Q-factor with increasing h is thought to be a result of the increased perturbation of the photonic crystal waveguide mode as the slot depth increases, which leads to a reduction in the vertical confinement of the mode in the photonic crystal slab. The spatial FTs of the cavity mode electric fields for h=60nm and h=90nm displayed in Figures 5.10(c) and (d) further support this explanation. It is clearly observed that for h=90nm, the number of in-plane momentum components inside the light cone (white circle) is increased compared to that when h=60nm. For this range of h values, λ_R was found to change by only ~10nm ($865\text{nm} \lesssim \lambda_R \lesssim 875\text{nm}$).

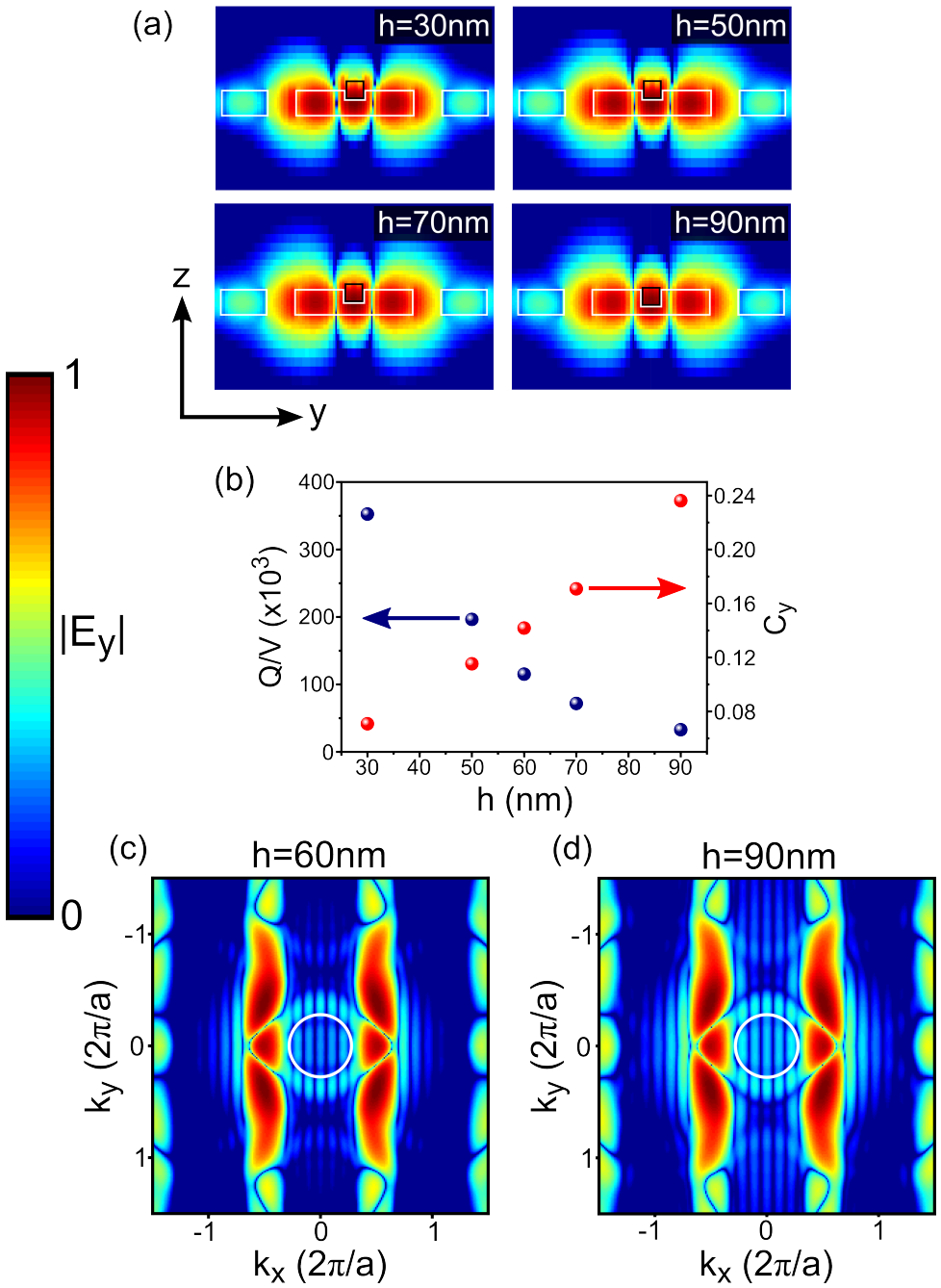

Figure 5.10: Calculation of the fundamental cavity mode properties when varying the slot waveguide depth, h. (a) Calculated 2D $|\mathbf{E_y}|$ field-profiles of the fundamental cavity mode in the y-z plane for d=w=100nm and h=30, 50, 70, 90nm. The colour scale in each image is logarithmic and the field profiles are normalised to the source power. Photonic crystal and nanowire structures are depicted by white and black solid lines, respectively; (b) Summary of the calculated Q/V and C_y values for each of the different values of h, including h=60nm for comparison; Spatial Fourier transformation spectra obtained from the y-component of the electric field ($|\mathbf{E_y}|$) in the x-y plane for (c) h=60nm, (d) h=90nm. The colour scale in each image is logarithmic and the light cone is depicted by the white circle with a radius, r_{LC}=$2\pi/\lambda_R$. For all calculations, the other nanocavity parameters have fixed values of t=140nm, a=242.5nm, r=80nm, W=$0.98\sqrt{3}a$ and L=2µm.

As the structural parameters of individual nanowires transferred to the photonic crystal substrate will vary somewhat in experiment, the effect on the properties of the fundamental cavity mode when changing the nanowire diameter and length was also investigated using FDTD simulations. Maintaining the ideal scenario where w=d, and setting h to the previous value of 60nm, it was found that an increase (decrease) in the nanowire diameter resulted in a decreased (increased) resonance Q-factor and an increased (decreased) V and C_y relative to d=100nm. A summary of the calculated values of Q, V and C_y for d values ranging from 50nm to 150nm in 25nm increments (including that for d=100nm for comparison) is displayed in Figure 5.11(b). Inspection of the mode profiles in the y-z plane at x=0 for the largest and smallest d values (50 and 150nm, respectively) which are displayed in Figure 5.11(a), show that the decrease in Q as d increases is again a result of the reduction in vertical confinement of the mode in the photonic crystal slab caused by an increase in the perturbation of the photonic crystal waveguide mode. The combination of this increased mode perturbation and an increased nanowire volume as d increases also leads to a greater amount of the overall electric field to be confined within the nanowire, which results both in the increase in C_y observed in Figure 5.11(b) and the decrease in V. The variation in λ_R for this diameter range is also displayed in Figure 5.11(b). Figure 5.11(c) shows the mode profiles in the x-z plane at y=0 for a nanowire with d=100nm and a length of 1, 2 and 3µm. It is observed that the spread of the cavity mode distribution is proportional to L, and becomes more uniform as L increases. As a result, the calculated values of Q and V were both found to increase with increasing L. C_y and λ_R, however remained comparatively unchanged. A summary of the calculated values of λ_R, Q, V and C_y for L=1, 2 and 3µm are shown in Figure 5.11(d). Although the mode profiles in Figure 5.11(d) provide an insight into the origin of the variation in Q and V with L, it is not clear exactly why the increase in Q when L is increased from 2µm to 3µm is so much larger in comparison to when L is increased by the same magnitude from 1µm to 2µm.

Taking into account all of the simulation results presented above, the base photonic crystal design chosen as the best candidate for experimental realisation of a nanocavity system with a λ_R≈870nm, which has both a high Q-factor and low V was that where t=140nm, a=242.5nm,

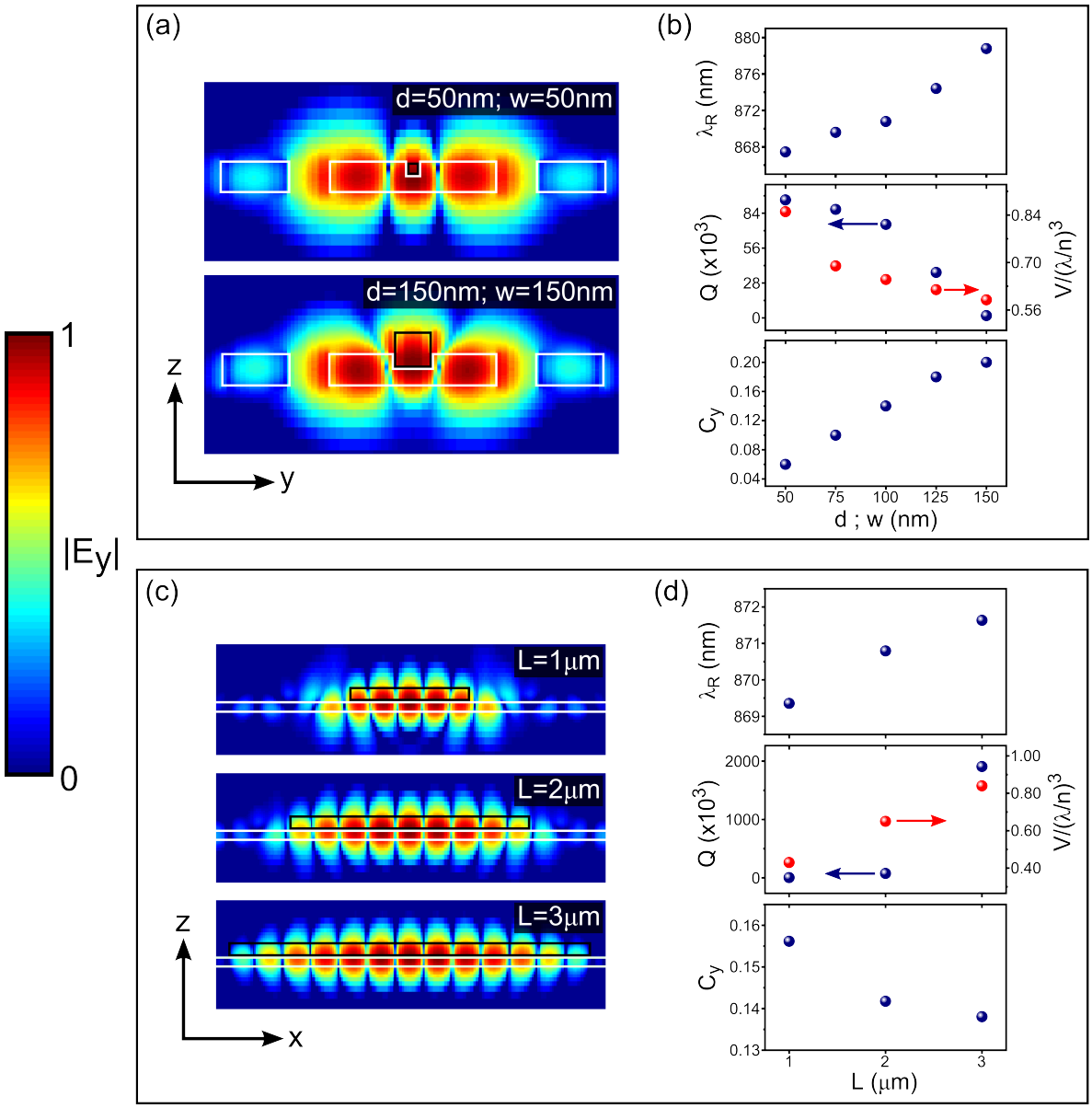

Figure 5.11: Calculation of the fundamental cavity mode properties when varying dimensions of the nanowire situated in the slot waveguide. Calculated 2D $|\mathbf{E_y}|$ field-profiles of the fundamental cavity mode in the (a) y-z plane for d=w=50nm and d=w=150nm with L fixed at 2μm and in the (c) x-z plane for L=1, 2 and 3μm with d=w fixed at 100nm. The colour scale in (a,c) is logarithmic and the field profiles are normalised to the source power. Photonic crystal and nanowire structures are depicted by white and black solid lines, respectively; A summary of the calculated λ_R, Q, V and C_y values for (b) d=w values ranging from 50nm to 150nm in 25nm increments with L fixed at 2μm and (d) L=1, 2 and 3μm with d=w fixed at 100nm. For all calculations, the other nanocavity parameters have fixed values of t=140nm, a=242.5nm, r=80nm, W=0.98$\sqrt{3}a$, h=60nm and L=2μm.

r=80nm, W=0.98$\sqrt{3}a$. In terms of the nanowire and slot parameters, it was shown that a value of h in the range 50–70nm provided the best compromise between maintaining both a

high Q/V and C_y value, and the ideal situation for maximum spatial overlap of the cavity mode with the nanowire volume in the x-y direction is when w=d. Therefore, a h value of 60nm was aimed for in the cavity design, and in recognition of the fact that the diameter of individual nanowires transferred onto the device substrate will vary somewhat, devices with a range of w values would be required.

5.4 Experimental Realisation of the Nanocavity Design

5.4.1 Fabrication of a GaAs Photonic Crystal Slab with a Partially Etched Slot Waveguide

The optimised photonic crystal slot waveguide designs described in the previous section were fabricated using a top-down approach that involved a repeated lithography and etching process, to first produce the holes establishing a particular photonic crystal device with a line defect and then subsequently define the partially etched slot waveguide. A schematic diagram of the wafer layer structure (Growth Reference: VN2782) used in device fabrication is shown in Figure 5.12. It comprised of a 140nm-thick GaAs region containing a layer of InAs QDs deposited on a 1µm $Al_{0.6}Ga_{0.4}As$ layer, grown on a GaAs substrate cleaved along the [100] plane. This particular wafer was selected for device fabrication as the QD density was measured to be low after optical characterisation, reducing the probability of exciting a QD at the location of a deposited nanowire in or around a photonic crystal device, which may potentially obscure observation of successful cavity enhanced nanowire emission. The thickness of the $Al_{0.6}Ga_{0.4}As$ sacrificial layer in this wafer structure was chosen so that after removal, the vertical separation between the remaining GaAs membrane and underlying substrate was large enough to prevent light leakage to the substrate once the sacrificial layer has been removed.

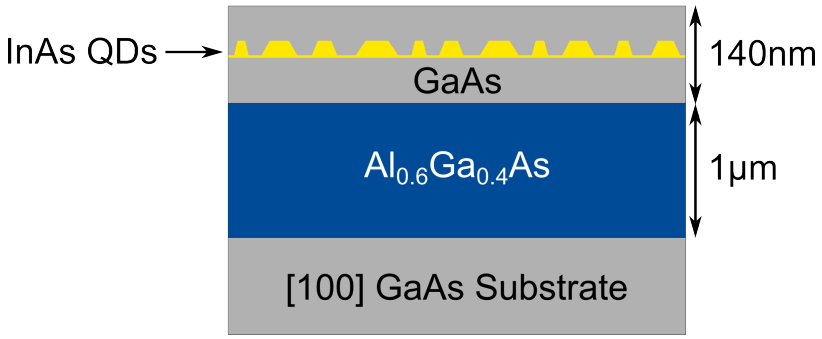

Figure 5.12: Schematic diagram of the epitaxially grown wafer structure used for photonic crystal slot waveguide device fabrication.

Fabrication commenced with the baking of a cleaved piece of the VN2782 wafer on a 180°C hotplate for 60s to evaporate any water on its surface. This sample (PCslots-5A) was then spin-coated with an electron-sensitive resist, ZEP520A (Zeon Chemicals), at ~5000rpm for 30s to give a resist thickness of ~340nm (Figure 5.13(b)). It was then baked again for 5 minutes at 180°C to drive off solvent in the spun resist.

Arrays of photonic crystal designs with a pitch of 50µm were then patterned into the resist (Figure 5.13(c)) using electron-beam lithography (EBL)*. The electron accelerating voltage and beam aperture size used for device patterning on this sample was 30keV and 7.5µm, respectively, giving a feature resolution limit (with this resist thickness) of ~60nm. A typical array consisted of 5 columns by 5 rows of devices, with the patterned air hole radius varied from row to row (bottom-to-top) in order to increase the probability of realising a fabricated structure with parameters corresponding to those of the optimised design described in the previous section. To further augment this probability, multiple device arrays were patterned on PCslots-5A, with the exposure dose of the beam varied from array to array. In addition to the photonic crystal designs, alignment markers were patterned at the edges of each write-field (50x50µm^2 here) in this patterning run, to prepare the sample for subsequent overlay of the slot waveguide patterns.

The ZEP520A resist was then developed in Xylene for 60s at 23°C after EBL exposure, leaving an etch mask defined by the exposed areas of resist (Figure 5.13(d)). Transfer of the etch mask

*EBL system used for device patterning – Raith 150.

pattern into the underlying 140nm GaAs layer was achieved using a highly anisotropic inductively coupled plasma (ICP) etch, with CHF_3 as the etching gas (Figure 5.13(e)). Etching was performed until all of the 140nm GaAs layer in the exposed areas was expelled (penetrating slightly into the AlGaAs layer), using an endpoint sample to monitor the etch time required to achieve this etch depth. The remaining ZEP520A resist on the sample after etching was then removed using warm 1-Methyl-2-Pyrrolidinone and a subsequent IPA rinse (Figure 5.13(f)). Figure 5.14 displays SEM images of example photonic crystal devices produced using the described fabrication procedure, along with the layout of the alignment markers patterned at the edges of each write-field. The number of air hole repeats in x for these structures was 43, and in y the number of repeats, separated by the line defect, was 20.

After fabrication of the photonic crystal devices, the sample was respun with ZEP520A (in the same manner as outlined above) and using the previously patterned alignment markers in each write-field as a guide, the slot waveguide designs were patterned into the resist using EBL once more. Similar to the photonic crystal designs, the patterned slot widths were varied along each column of devices within in a particular array, with the dose value for each width varied from array to array. Again, after patterning, the resist was developed and the resulting etch mask was transferred into the 140nm GaAs layer using an ICP etch with CHF_3.

Unlike for the photonic crystal structures however, to obtain a slot depth matching that of the optimised design required a very precise etch time, and as the exposed GaAs region for an individual slot is small relative to that of the air holes comprising the surrounding photonic crystal, the etch rate was expected to be slower than was observed previously. To characterise the relationship between etch time and etch depth for a particular slot width, slots with varying widths were patterned on separate pieces of the VN2782 and each separate piece was etched for a different etch time using the same ICP recipe as before. These test pieces were then cleaved along the direction perpendicular to the slot length, as shown in Figure 5.15(a), mounted on a 90° mount and imaged using an SEM. An SEM image of a group of slots with different widths etched for the same period of time is shown in Figure 5.15(b). The two main observations from these slot tests were that, for a particular etch time, the small variation

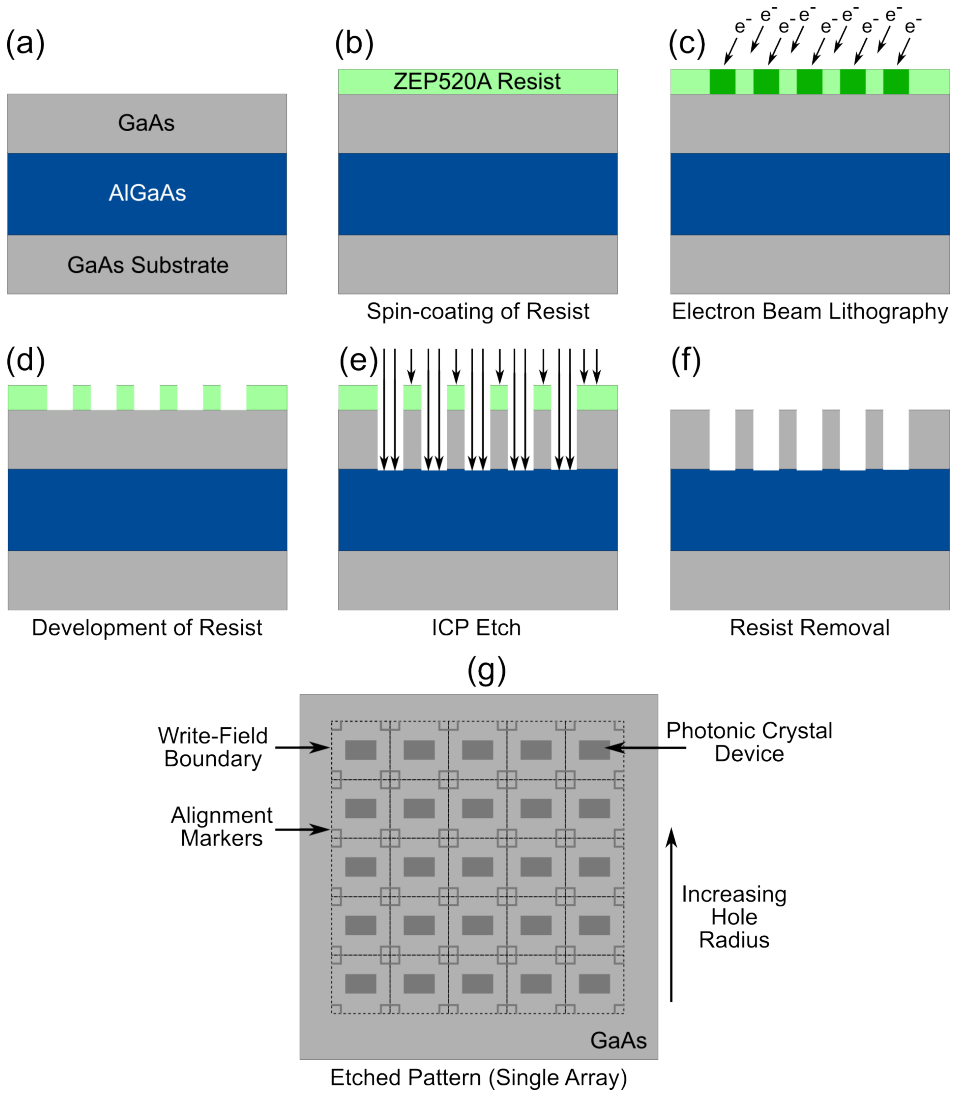

Figure 5.13: Top-down fabrication process used to create photonic crystal devices containing a line-defect. Schematic diagrams show, (a) The sample (PCslot-1A) before processing; (b) Spin-coating of ZEP520A onto the sample surface; (c) Pattern exposure of resist by electron beam lithography; (d) Development of ZEP520A resist in Xylene, removing exposed regions; (e) ICP etching of sample to transfer the resist pattern into underlying GaAs region; (f) Removal of resist; (g) An overview of a single (5x5) device array pattern etched into the top GaAs layer after steps (a)–(f). Alignment markers sit in each of the four corners of an individual write-field (illustrated here by black dashed lines), with a photonic crystal device positioned in the centre.

in slot width did not affect the resulting slot depths (i.e. the slot depth for each patterned width was approximately the same) and using the same ICP recipe as that for the photonic crystal devices led to the production of slots with straight and smooth sidewalls.

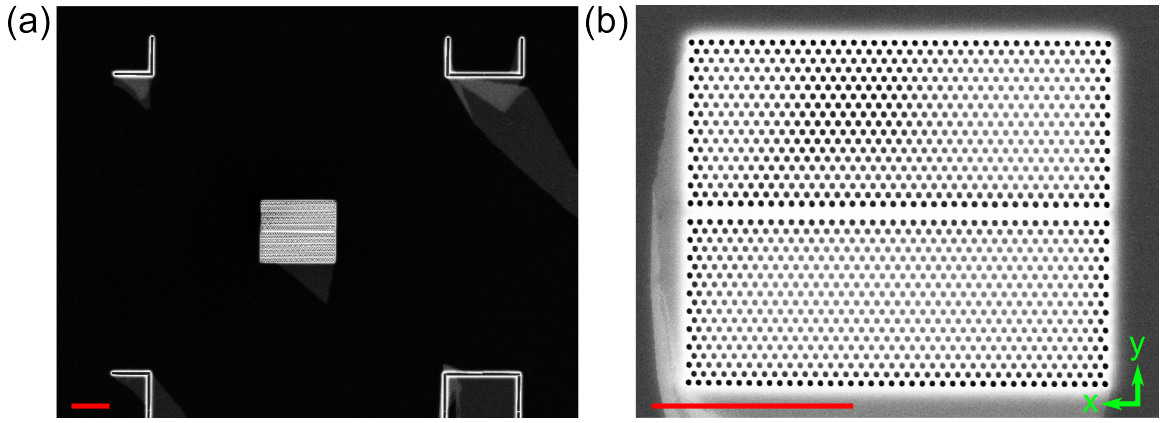

Figure 5.14: Top-down SEM images of photonic crystal devices containing a line-defect after fabrication. (a) A single device sits (approximately) in the centre of four surrounding alignment markers, which outline the dimensions of an individual EBL write-field; (b) The number of air hole repeats for each device in x and y is 43 and 20, respectively, giving overall lateral dimensions of ~10.5x9µm on average. Scale bars 5µm.

Following transfer of the slot waveguides into the GaAs layer, the remaining ZEP520A resist on the sample was again removed using warm 1-Methyl-2-Pyrrolidinone and a subsequent IPA rinse. The sample was then selectively wet-etched with hydrofluoric (HF) acid to remove the sacrificial AlGaAs layer, rinsed in deionised (DI) water and dried with a nitrogen gun to leave a final free-standing membrane containing arrays of patterned photonic crystal plus slot waveguide devices (Figure 5.16(a)). Figures 5.16(b)–(e) display SEM images of a selection of photonic crystal slot waveguide devices produced using the described fabrication procedure. Even with the adoption of alignment markers at the edges of each write-field to ensure the overlaid slots were patterned relative to the previous photonic crystal patterns, it was found that the slot position relative to the centre of the photonic crystal waveguide varied slightly in both x and y from device to device within a particular array. This slight random variation in slot position was attributed to the limits in overlay positional accuracy that could be achieved with the EBL system used for device patterning, which was ~50nm. For a small number of devices, overlap of the slot with a row of holes was observed, as shown in Figure 5.16(e). This substantial misalignment of the slot from the targeted position was thought to be a result of one or more of the four alignment markers within a write-field not being detected during the overlay process. As seen in Figure 5.16(c), another artefact discovered after device fabrication

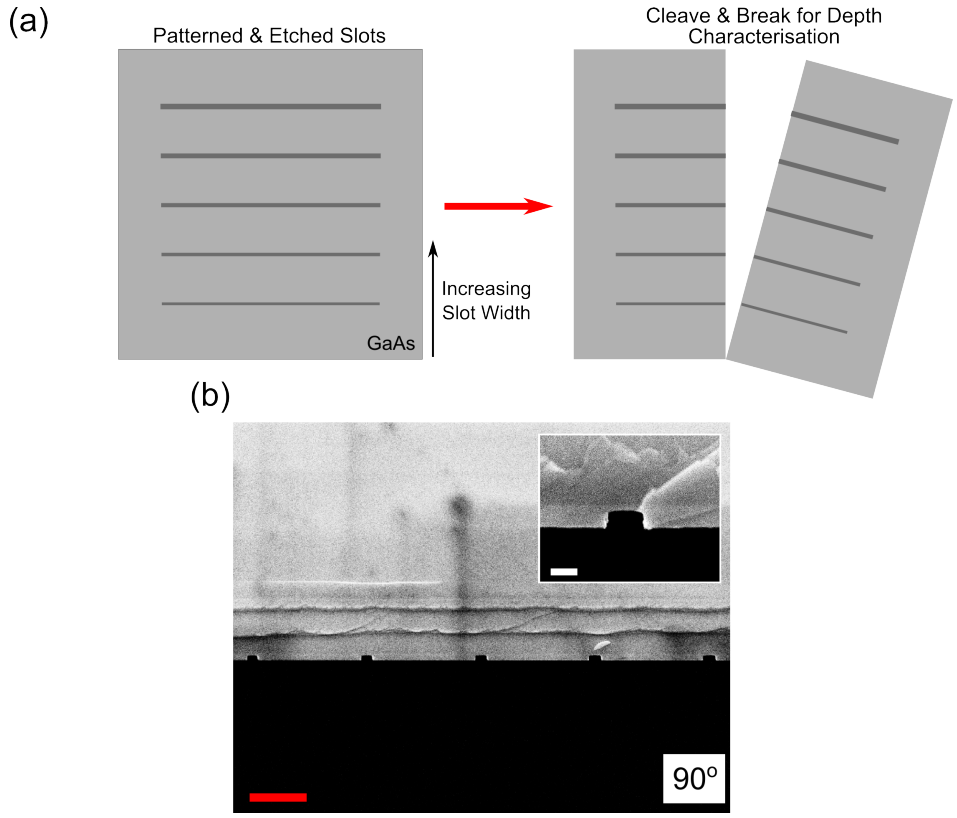

Figure 5.15: Characterisation of the relationship between ICP etching time and resulting slot etch depth. Schematic diagrams in (a) and (b) show the patterned slot design, comprising of slots with varying widths, transferred into a test piece of wafer by ICP etching. The test piece is cleaved perpendicularly to the slot orientation and broken to allow for measurement of the slot depth corresponding to a particular ICP etch time; (c) SEM image of a cleaved test piece orientated at 90° to the scanning electron-beam. For a particular etch time, the depth of each patterned slot in (a) is approximately the same. Scale bar 1µm. Inset: profile of a typical slot produced after ICP etching. Scale bar 100nm.

was the appearance of small periodically repeating nodules along the length of a slot. These were assumed to originate from the calculated proximity corrections incorporated into the slot design before patterning, which were included in an attempt to realise slots with sharp square edges after fabrication. Although nodule size was found to vary from device to device, they did not exceed a maximum of a few nm in dimension. This sample therefore, was utilised for subsequent nanowire deposition and manipulation.

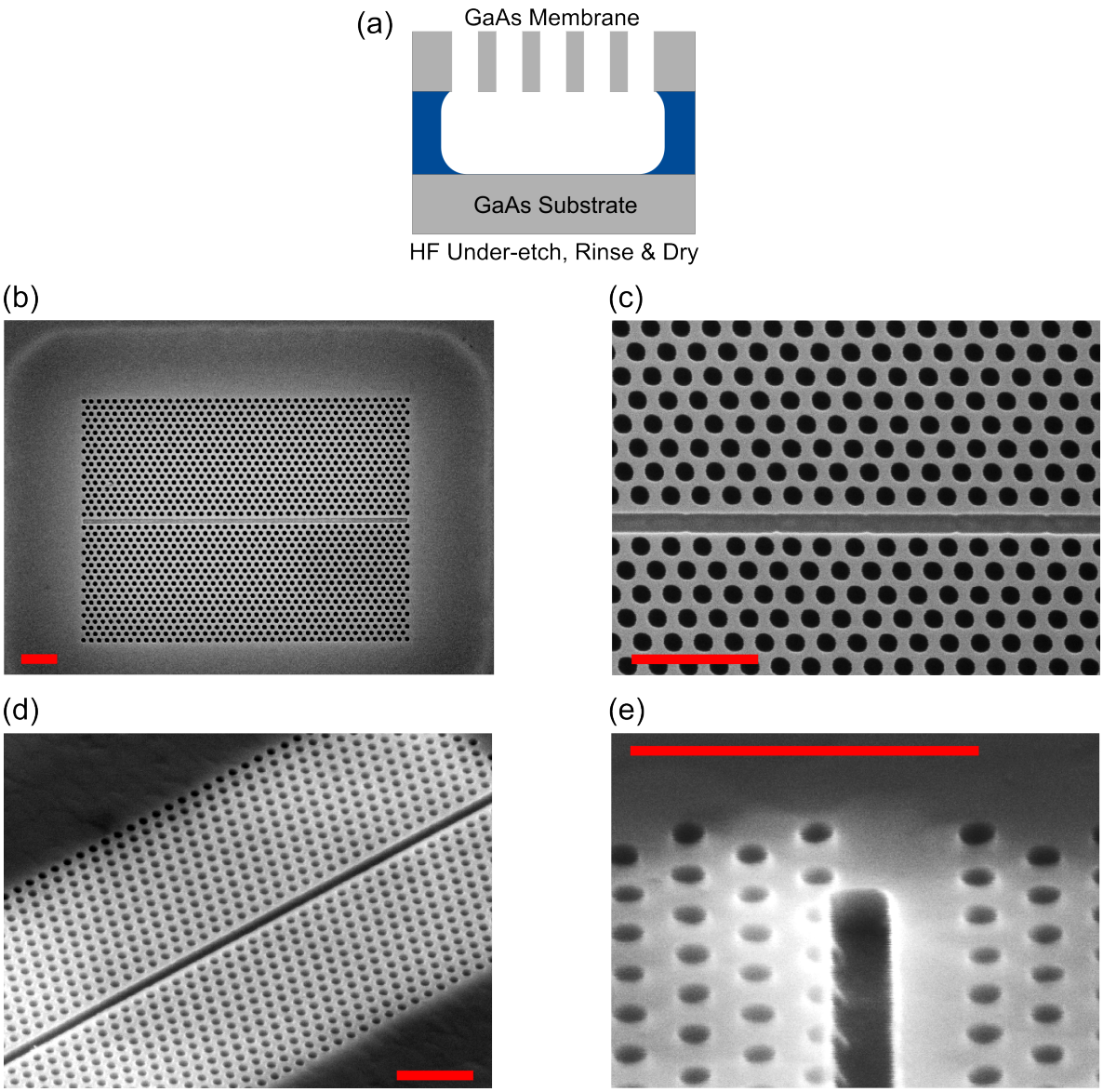

Figure 5.16: Creation of suspended GaAs photonic crystal slot waveguide devices. (a) Schematic diagram showing the resulting layer structure after the sacrificial AlGaAs layer is selectively etched with HF acid; Top-down SEM images show, (b) a free-standing photonic crystal slot waveguide device, where the light grey rounded edges around the periphery of the device outline the region of AlGaAs that has been under-etched and (c) nodules of material a few nm in size not removed after ICP etching of the slot, which repeat periodically along the slot length; Angled SEM images show, (d) depth of the slot waveguide and air holes comprising the surrounding photonic crystal and (e) a device where the etched slot overlaps the first row of holes on one side of the line defect. Scale bars 1µm.

5.4.2 Nanowire Transfer

Optimisation of the nanowire cavity design described in Section 5.3 was based on a nanowire diameter of ~100nm, as this corresponded to the approximate smallest InP nanowire diameter measured on Sample 2F (MR3428) in Chapter 2. In order to transfer these smallest diameter nanowires from the growth substrate to the suspended photonic crystal slot waveguide devices on PCslots-5A, a method was required to first detach the nanowires from the growth substrate and then deposit them (horizontally) on the surface of PCslots-5A in the vicinity of devices with parameters closest to those of the optimised design. Typically, nanowire transfer in this manner is achieved by sonication of nanowires from the growth substrate into a solution (usually a solvent) and subsequent deposition of a small amount of this solution containing suspended nanowires onto the device substrate [1, 182]. The success of this method depends primarily on the density and coverage of nanowires on the growth substrate being high enough to create a suspended nanowire solution that requires minimal repeated deposition steps to deliver an appropriately high number of nanowires onto the device substrate. Multiple depositions may cause damage to pre-fabricated devices on the device substrate and lead to the removal of nanowires transferred in prior deposition attempts. This transfer method was attempted with cleaved pieces containing nanowire arrays from other areas of MR3428 without success (even after repeated deposition steps), and was thought to be a consequence of the nanowire density and coverage not being high enough on this sample.

Nanowire transfer with Sample 2F therefore, was instead performed using a dry mechanical dispersion technique, which is outlined schematically in Figure 5.17(a). In this technique, the growth substrate is turned upside down and swept across the surface of the device substrate, causing the nanowires to detach from the growth substrate and disperse onto the device substrate. In an attempt to ensure only the region of nanowires with diameters ~100nm on Sample 2F were deposited onto the area of PCslots-5A containing the device structures with parameters closest to those of the optimised design, great care was taken in trying to bring into contact only these specific regions during transfer. It is noted that this nanowire transfer

selectivity would not have been feasible with the sonication method described above. Great care was also taken in trying to minimise as much as possible the contact between the two sample substrates during transfer, in order to reduce the probability of damaging any of the suspended device structures. As a result of this, a number of transfer attempts were required before the majority of ~100nm diameter nanowires on Sample 2F were successfully dispersed onto PCslots-5A. Figure 5.17(b) and Figure 5.17(c) display SEM images of a two regions in close proximity on PCslots-5A after successful nanowire deposition using this technique. It is observed from these SEM images that due to the prolonged contact and relative motion between the two substrates during the transfer process, the dispersed nanowires formed a pronounced trail along the surface of the device substrate, with the density of nanowires fluctuating randomly across the length of the trail.

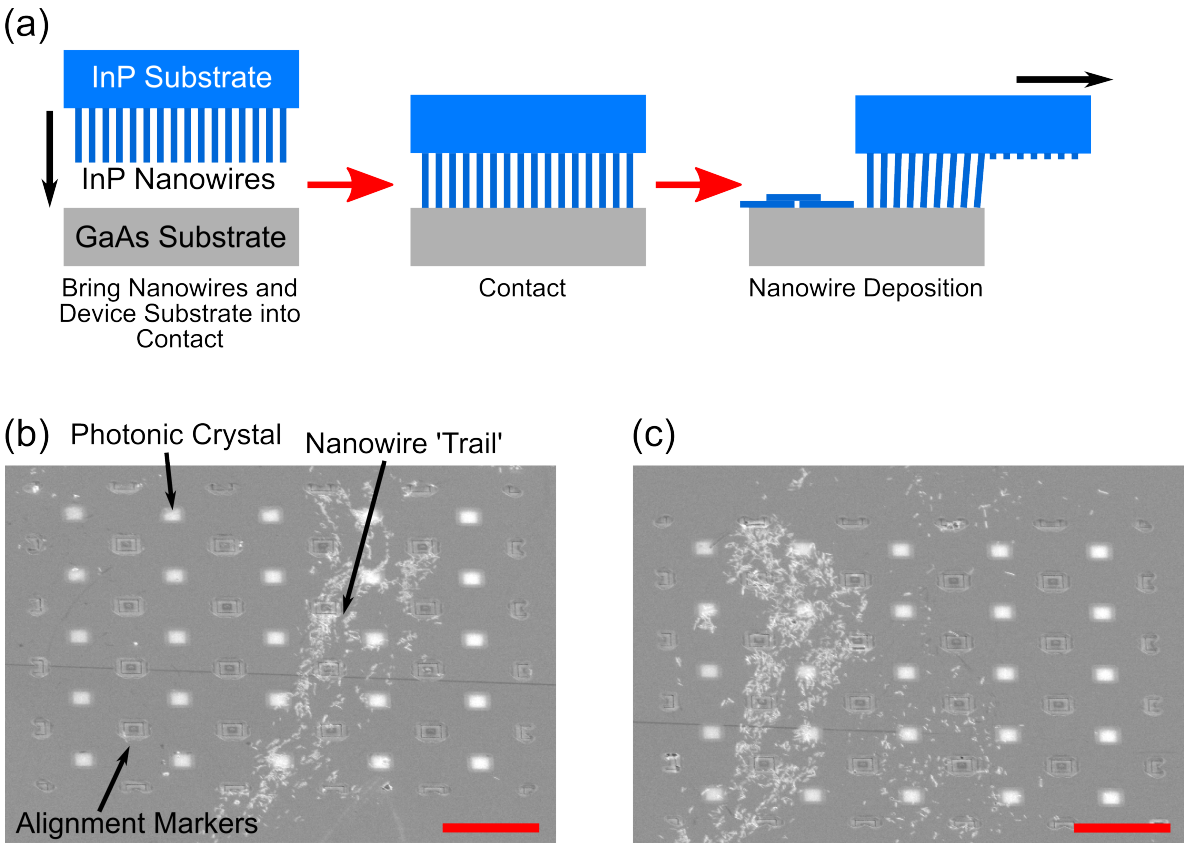

Figure 5.17: Deposition of small diameter InP nanowires from Sample 2F onto the surface of Sample PCslots-5A. (a) Schematic outline of the dry mechanical dispersion technique used for nanowire deposition; Angled SEM images in (b) and (c) show typical nanowire distribution after deposition. Scale bars 50µm.

Following successful nanowire deposition using the dry mechanical dispersion technique described above, PCslots-5A was inspected to determine the most suitable nanowire candidates for subsequent nanomanipulation. As this was a first attempt at manoeuvring nanowires on the device substrate, the most suitable candidates were deemed as individual nanowires that were on or in close proximity to a photonic crystal device with parameters similar to those of the optimised design which were mostly free of debris, as these provided the best opportunity for successful nanowire placement into the slot waveguide with minimal damage to the surrounding photonic crystal. SEM images of the three devices, herein referred to as Devices 1, 2 and 3, containing nanowires that satisfied these criteria best are displayed in Figure 5.18. The measured parameters of these devices and dimensions of the corresponding highlighted nanowires selected for nanomanipulation are presented in Table 5.1. Measurements of the slot waveguide depth, h after fabrication of these devices was not possible due to the slot being bounded by the GaAs slab on either side, and therefore as slot etching on PCslots-5A was performed using etch parameters optimised for creation of a slot with a depth of ~60nm, for each of these devices (and all other devices on PCslots-5A) h was also assumed to be ~60nm.

	a (nm)	r (nm)	W (nm)	w (nm)		d (nm)	L (µm)
Device 1	250	78	418	175	NW-1A	135	1.9
Device 2	248	75	415	167	NW-2A	122	2.3
Device 3	255	80	420	165	NW-3A	133	1.8
					NW-3B	140	0.9
					NW-3C	137	0.8

Table 5.1: Summary of measured dimensions of nanowires selected for nanomanipulation and parameters of surrounding photonic crystal devices displayed in Figure 5.18. For each device, it is assumed that $h \approx 60$nm.

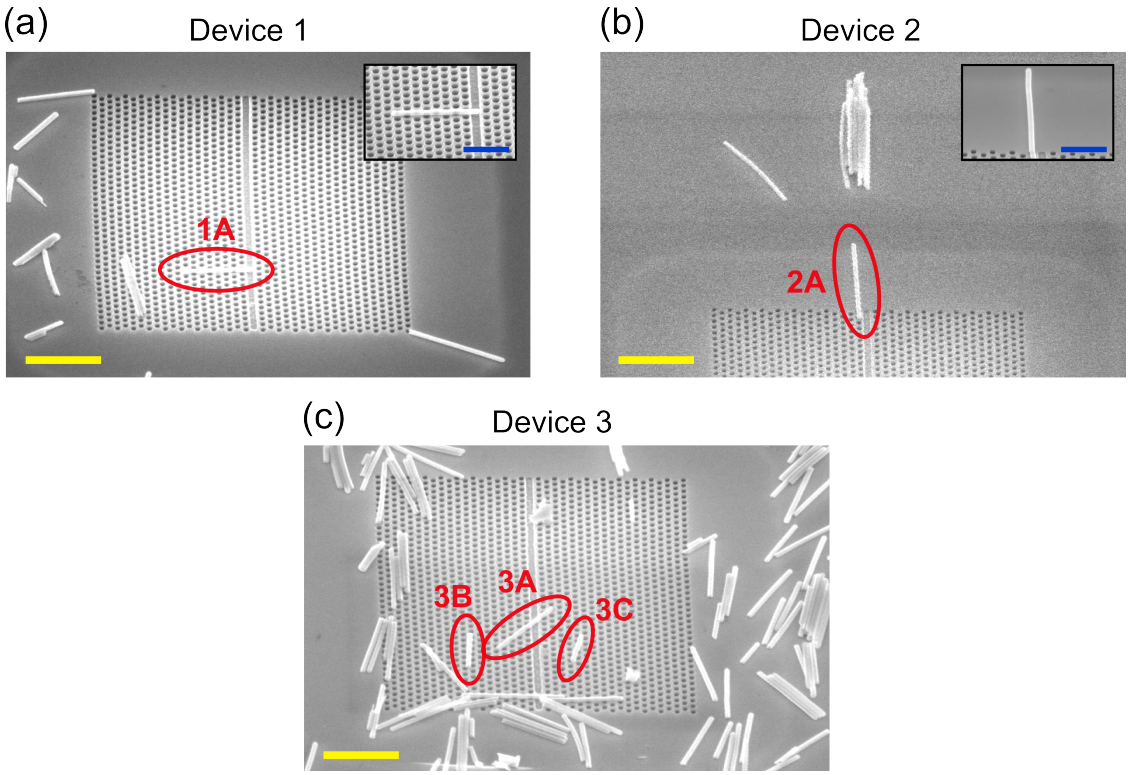

Figure 5.18: Angled SEM images of regions around photonic crystal slot waveguide devices on PCslots-5A containing deposited nanowires from Sample 2F selected for nanomanipulation (circled in red). Scale bars 2µm. Insets in (a) and (b) display higher magnification images of selected nanowires. Scale bars 500nm.

5.4.3 Nanomanipulation of Transferred Nanowires Using Atomic Force Microscopy

Nanomanipulation of the selected nanowires displayed in Figure 5.18 was performed using atomic force microscopy (AFM)[†]. The main elements of the AFM system are depicted schematically in Figure 5.19(a)[‡]. Deflection of a silicon tip attached at the end of a flexible cantilever as it interacts with the sample surface is measured via an optical lever, whose basic constituents comprise a laser and photodiode that is split into four quadrants. Laser light reflects off the side of the cantilever opposite to that attached to the tip, and as the cantilever bends under the action of sample-tip forces, the resulting motion of the reflected spot on

[†]All surface topography imaging and manipulation of nanowires presented in this section was carried out by Dr. Nic Mullin.

[‡]AFM system used for nanomanipulation — Bruker Dimension Icon.

the photodiode creates a differential (electronic) signal, which relays information about the current position of the tip relative to a zero deflection point. Movement of the reflected laser spot in the vertical direction corresponds to height variations in the sample, with horizontal displacements relating to frictional forces between the tip and sample as they move relative to one another. Relative motion between the tip and surface is achieved using a scanning arrangement, which consists of piezoelectric actuators that are capable of moving the tip in x, y and z directions over the sample.

Nanomanipulation in this case proceeded in the following manner: first an area of PCslots-5A corresponding to one of the best candidate regions depicted in Figure 5.18 was imaged using the AFM cantilever tip to determine the approximate co-ordinates of the selected nanowire on the sample surface relative to the boundaries of the imaged area; second, with this positional information, the AFM cantilever tip was then used to 'push' the nanowire from its current location along a desired trajectory; lastly, the same area imaged in the first step was re-imaged to establish whether or not the nanowire had been successfully displaced from its starting position, and what its resulting position was after this displacement.

Images of the sample surface presented here were obtained with the AFM system set up in *tapping mode*. One of the main advantages of this mode is that there is little to no lateral force exerted on the sample during imaging (which can lead to surface damage or undesirable movement of objects on the surface) as the cantilever tip is only in contact with the sample surface for a very short period of time. In tapping mode, the cantilever tip, before engaging on the sample surface, is tuned to a frequency just below resonance (typically on the order of 200-400 kHz in air for the cantilever tips used here [183]) in the direction perpendicular to the cantilever axis by a dedicated piezo drive installed at the base of the cantilever (separate to the piezo actuators controlling the movement of the sample in x, y and z directions). As the cantilever oscillates up and down, the reflected laser spot moves in a regular pattern vertically over the photodiode quadrants, generating a sinusoidal AC (electronic) signal, which is analysed by a lock-in amplifier and converted into an amplitude value, A_{free}. After determining A_{free} for a particular piezo driving voltage (in this case $A_{\text{free}}\approx$20nm), the

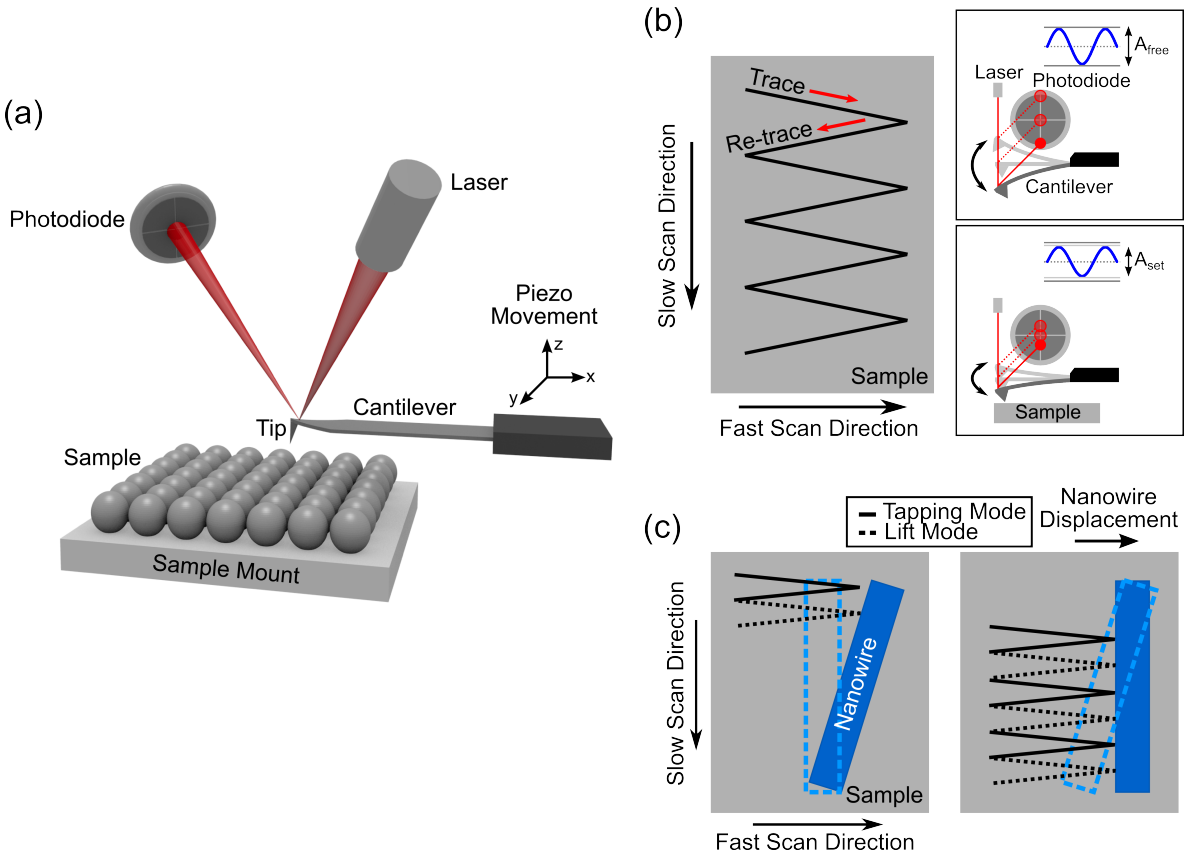

Figure 5.19: Nanowire nanomanipulation using AFM. Schematic diagrams show: (a) The main elements comprising the AFM system used for nanomanipulation. Motion of the cantilever tip relative to the sample is driven by a set of piezo actuators connected to the cantilever base. An optical detection system incorporating a laser and photodiode measures deflection of the tip in response to changes in topography of the sample surface; (b) The raster scan type motion utilised for imaging a region of the sample surface while in tapping mode. Owing to the relative speed of tip motion along the orthogonal scanning axes during the raster scan trace-retrace steps, x and y are referred to as the fast and slow scan directions, respectively. Right hand panels illustrate how a change in cantilever oscillation amplitude is detected in the AFM system when the tip is brought in close proximity to the sample surface. A particular damped oscillation amplitude can then be selected and maintained through use of a feedback loop; (c) The method employed to reposition nanowires from a location on or around a photonic crystal device into the slot waveguide. The cantilever tip is first positioned in close proximity to the nanowire and an initial single trace-retrace step is performed in tapping mode. The cantilever tip is then driven into the sample with a selected negative lift value. With the tip and sample surface in contact, another trace-retrace step is performed, and if the negative lift value is large enough, the lateral force exerted on the nanowire by the tip causes the nanowire to be displaced from its original position. Compared to normal tapping mode operation, each trace-retrace step in this procedure only spans a half line spacing in the y-direction, and so twice as many scan traces are performed in the same scanning area. The final position and orientation of the nanowire after a full scan with the AFM in lift mode operation is determined by the location and number of points along the nanowire pushed by the tip and the negative lift value that is assigned in lift mode operation.

oscillating tip is then brought into contact with the sample again, leading to a damping of the free oscillation. As damping increases when the tip is pressed harder into the sample, the amount of interaction between the tip and sample in this mode can be set by defining a damped amplitude setpoint value, A_{set} that is maintained by a proportional-integral-differential (PID) controller, which adjusts the voltage applied to the scanning piezo (in the z-direction) in response to amplitude variations of the sinusoidal motion of the reflected laser spot on the photodiode [184, 185]. Using this feedback loop, the value of A_{set} was fixed at ~90% of A_{free}, and with this value defined, a specified area of the sample surface was then characterised by the oscillating tip through lateral displacement of the cantilever relative to the sample in the raster scan type motion depicted in Figure 5.19(b). AFM images resulting from scans using this technique for the regions encompassing the nanowires of interest shown in Figure 5.18 are displayed in Figure 5.20. All image scans consisted of 512x512 pixels, spanning a scan area of 15µm by 15µm, captured with a scan speed of ~1 line per second.

After obtaining a topographic image of an area encompassing a nanowire of interest, the cantilever tip was laterally translated to a location adjacent to the nanowire (with the tip out of contact with the sample surface) in preparation for nanomanipulation. The AFM system was then switched to *lift mode*, and a negative lift scan height value was assigned. In lift mode operation, the cantilever tip first performs a single trace-retrace raster scan in tapping mode as described above. It is then lifted in z by a chosen displacement and another trace-retrace scan is performed. By choosing a negative lift value, the tip and sample are brought closer together in this subsequent trace-retrace step, and for a particular negative lift value the amplitude of the oscillating cantilever can be damped completely. If the cantilever-tip ensemble is considered as a point-mass spring, and tip-surface forces are ignored (which is a reasonable assumption when the separation between the tip and sample is large enough that the oscillation amplitude of the cantilever=A_{free}) then the tip-sample force required to completely damp the free oscillatory motion is given by $F_{\text{damp}}=kA_{\text{free}}/Q$, where k and Q are the spring-constant and quality factor of the cantilever-tip ensemble, respectively [186]. For this cantilever-tip ensemble, k~40N/m and Q~400, and therefore the force required to

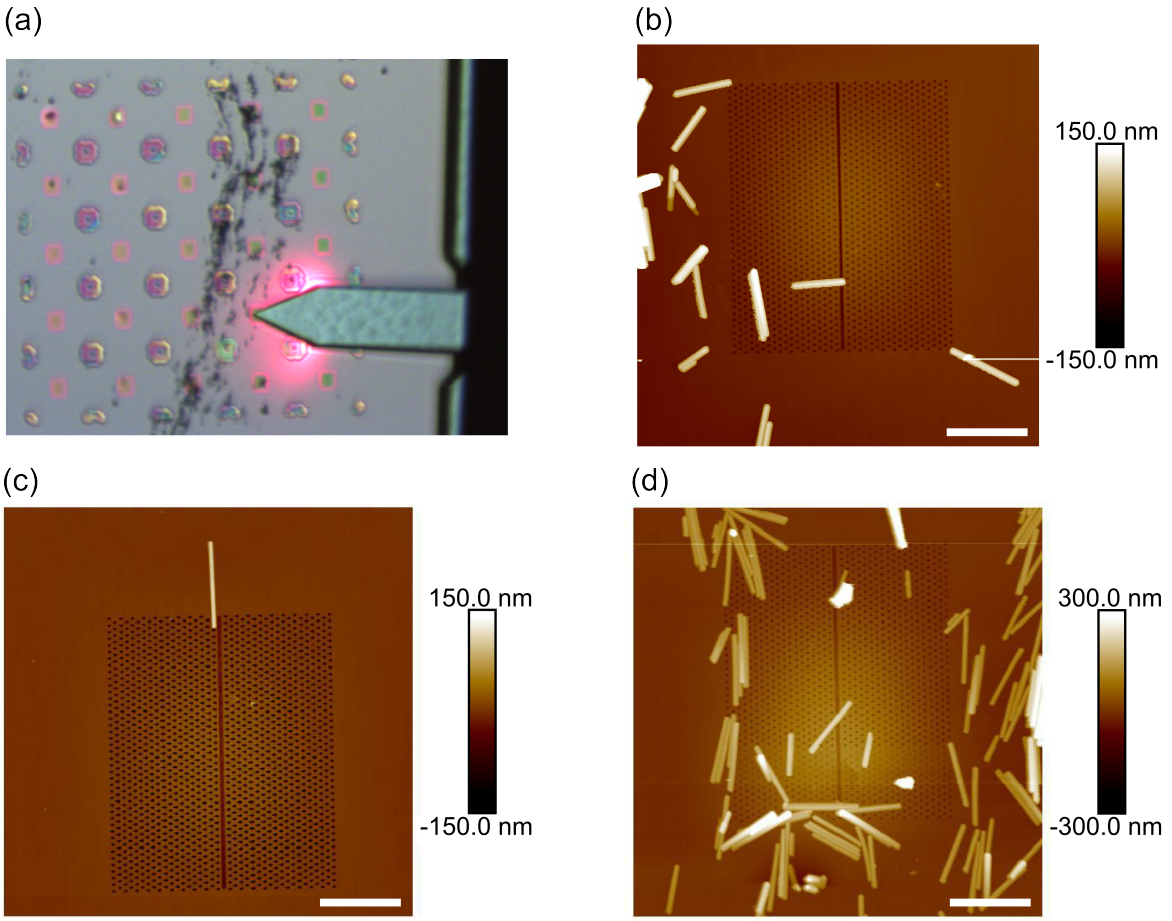

Figure 5.20: Surface imaging of sample PCslots-5A using AFM in tapping mode operation. (a) Optical image of cantilever and tip during surface raster scan of region encompassing a single photonic crystal device; Topographic images of regions encompassing devices (b) 1, (c) 2 and (d) 3 that contain nanowires selected for nanomanipulation. Colourmaps refer to tip position in z relative to the surface of PCslots-5A sample. Scale bars 3µm.

completely damp A_{free} is $F_{\text{damp}}\approx$2nN. With the cantilever motion completely damped, the trace-retrace motion of the tip in lift mode exerts a lateral force on the nanowire, which if large enough can cause the nanowire to be displaced from its original position. The approach used for 'pushing' individual nanowires on this sample is illustrated schematically in Figure 5.19(c).

Increasing the lateral force exerted on the nanowire by the tip during trace scans in lift mode was achieved by increasing the negative lift value and driving the tip further into the sample. After cantilever oscillation is completely damped, the additional force between the sample and tip as the tip is driven further into the sample is given by $F_{\text{Z}}=-kZ$ (Hooke's law),

where Z is the cantilever deflection. Negative lift values in the range 50–200nm were utilised for nanomanipulation on these samples (with these values including the 20nm required to completely damp A_{free}), corresponding to tip-sample forces of F_{total}≈1200–7200nN (where $F_{\text{total}} = F_{\text{damp}} + F_{\text{Z}}$). AFM images depicting the successful nanomanipulation of NW-1A from the surface of Device 1 into the centre of the slot waveguide, as well as the clearing of other non-relevant nanowires on its surface, using the approach described above are displayed in Figure 5.21. In addition to providing the ability to move nanowires residing on or around the device surface into the slot waveguide, it is observed from the images in this figure that once placed into the slot waveguide, subsequent repositioning of the nanowire along the slot waveguide is also possible with this approach, demonstrating its potential for the successful realisation of a nanocavity system that can be position-controlled.

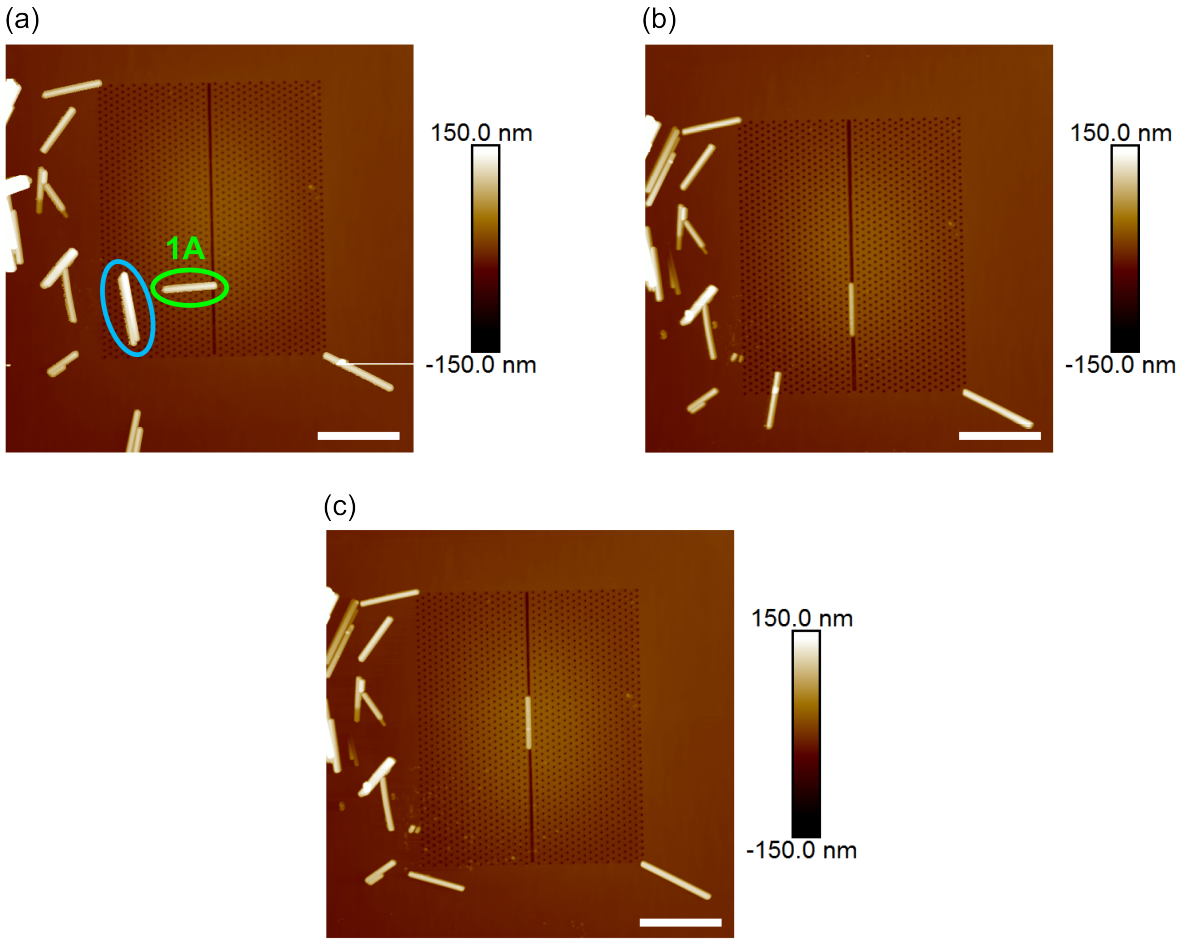

Figure 5.21: Nanomanipulation of nanowires on the surface of PCslots-5A using AFM in lift mode operation. AFM images show (a) the starting position of NW-1A (circled in green), which is then (b) rotated and placed into slot waveguide using the AFM tip. Once placed in the slot waveguide, the AFM tip is then used to (c) nudge the nanowire along its length and into the approximate centre of the photonic crystal device. The AFM tip was also used to clear away other nanowires in close proximity to NW-1A on the surface of Device 1 (circled in blue) in this nanomanipulation run. Colourmaps refer to tip position in z relative to the surface of PCslots-5A sample. Scale bars 3µm.

5.5 PL Measurements to Determine Cavity Resonance Wavelength

Confirmation of nanowire cavity formation after placement of a candidate nanowire into the slot waveguide of the surrounding photonic crystal device was performed using low temperature µ-PL measurements with the setup presented in Figure 2.13. Successful cavity formation

in this case would be evidenced by the appearance of a bright, narrow spectral peak on the background of the nanowire emission, which sharply increases in intensity (with only a negligible increase in peak width) with increasing excitation power. PL measurements therefore were taken on candidate nanowires before and after nanomanipulation so that a comparison of the emission spectra could be performed. Measurements were undertaken using a CW Ti:Sapphire laser tuned to 700nm, focused into a ~2µm spot by a microscope objective lens with an NA of 0.42. To ensure maximum collection of light scattered by the nanowire under excitation, the collection path in each measurement was aligned to coincide with one of the nanowire ends [187].

The PL emission spectra obtained from NW-2A before (Figure 5.22(a)) and after nanomanipulation (Figure 5.22(b)) is displayed in Figure 5.22(c). Before placement of the nanowire into the slot waveguide (black-trace), a broad emission peak centred at 855nm was observed, along with a four other lower intensity peaks at longer wavelengths, the most prominent of which approximately overlapped the cavity resonance wavelength of the optimised design (λ~868nm). Emission in the spectral range encompassed by the broad peak (850–860nm) was seen to occur from all locations excited on PCslots-5A, and was therefore attributed to emission from the embedded wetting layer in the GaAs membrane. Consequently, the only emission that could be associated with NW-2A with any certainty consisted of the four lower intensity peaks at longer wavelengths. After placement of the nanowire into the slot (blue-trace), strong quenching of nanowire emission was observed, with only the peak at λ~865nm remaining visible in the spectrum. No evidence of cavity-enhanced emission at this or any other wavelength encompassing the original nanowire emission spectrum was identified.

Collection of the individual emission spectra from each of the three nanowire candidates on Device 3 was not possible as the separation between them was smaller than the diameter of the PL laser excitation spot. The PL spectrum obtained with the excitation spot centered at the approximate mid-point of NW-3B before nanomanipulation is displayed by the black trace in Figure 5.23(d). Although low intensity emission in the wavelength range associated with InP ZB/WZ transitions in the nanowire was observed in this spectrum, it was seen

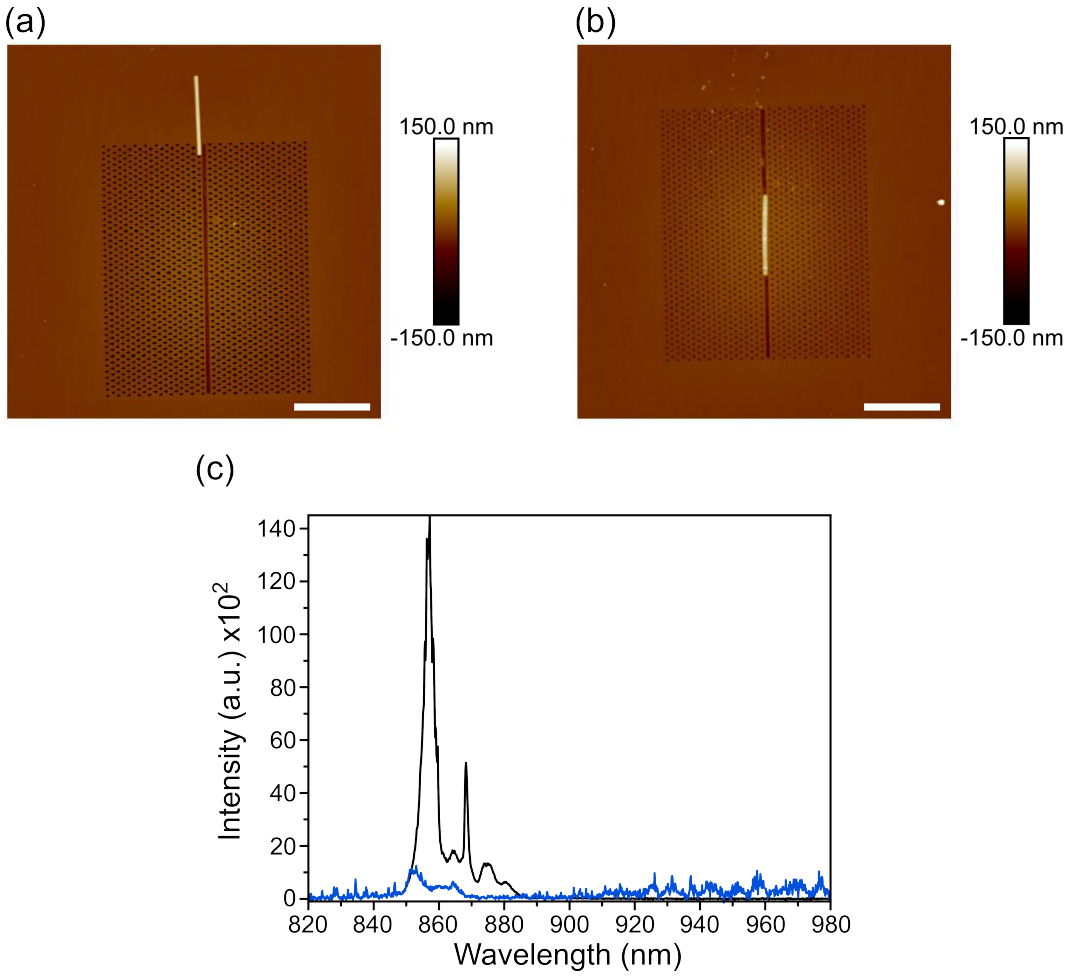

Figure 5.22: Optical characterisation of NW-2A on Device 2 before and after nanomanipulation. AFM images show location of NW-2A (a) before and (b) after nanomanipulation; (c) PL spectra obtained from NW-2A before (black-trace) and after (blue-trace) placement of the nanowire into the slot waveguide. For both spectra, an excitation power of ~500nW was used. Scale bars 3µm.

to be dominated by a bright broad feature at longer wavelengths (900–940nm) consisting of several overlapping single peaks. As this feature appeared at energies lower than the lowest energy InP ZB/WZ transition [30], it was thought to correspond to emission from the InAsP layer formed during the growth of these nanowire structures (see Chapter 2). Due to the fact that it was not possible to discern the exact contribution each of the three nanowires had made to this measured spectrum, all three were placed into the slot waveguide of the device to maximise the potential of spectral overlap of nanowire emission with the resonance of the constructed nanowire cavity, resulting in the configuration displayed in Figure 5.23(b). Before

performing PL measurements on each of the three nanowires moved into the slot waveguide, an attempt was made first to move the nanowire clumps and other debris away from the surface of the photonic crystal device and onto the surrounding bare GaAs region. Although most of the debris was successfully cleared with a tip-sample force in the range previously used for the nanomanipulation of the candidate nanowires on this device, displacement of a number of fragments of other debris was not possible in this force range (owing to the larger adhesion between these debris fragments and the device surface). In an effort to remove these remaining pieces of debris, the tip-sample force was therefore incrementally increased upto ~10μN (corresponding to ~250nm of negative lift) during the removal procedure. The increase in the force exerted on the device surface as the tip was further driven into the sample, however, led to the photonic crystal membrane in these regions being damaged and also inadvertently led to the expulsion of NW-3B from the slot waveguide, as illustrated by the AFM image scan displayed in Figure 5.23(c). Despite being damaged, the photonic crystal membrane did not collapse entirely after this attempted removal procedure, and so PL measurements were performed on the remaining nanowires in the slot waveguide of this device. During PL characterisation of the two nanowires, it was found that NW-3C had no observable PL emission features, even at relatively high excitation powers (>5uW). As a consequence, PL measurements were carried out only on NW-3A after nanomanipulation, and the PL emission spectrum collected with the excitation spot centred at the approximate mid-point of this nanowire is depicted by the blue-trace in Figure 5.23(d). The emission spectrum was again seen to be dominated by a broad feature encompassing a similar wavelength range to that observed before nanomanipulation, but, perhaps as a consequence of the damage caused to the photonic crystal device during removal of debris from its surface, there was no evidence of cavity-enhanced emission from this structural arrangement.

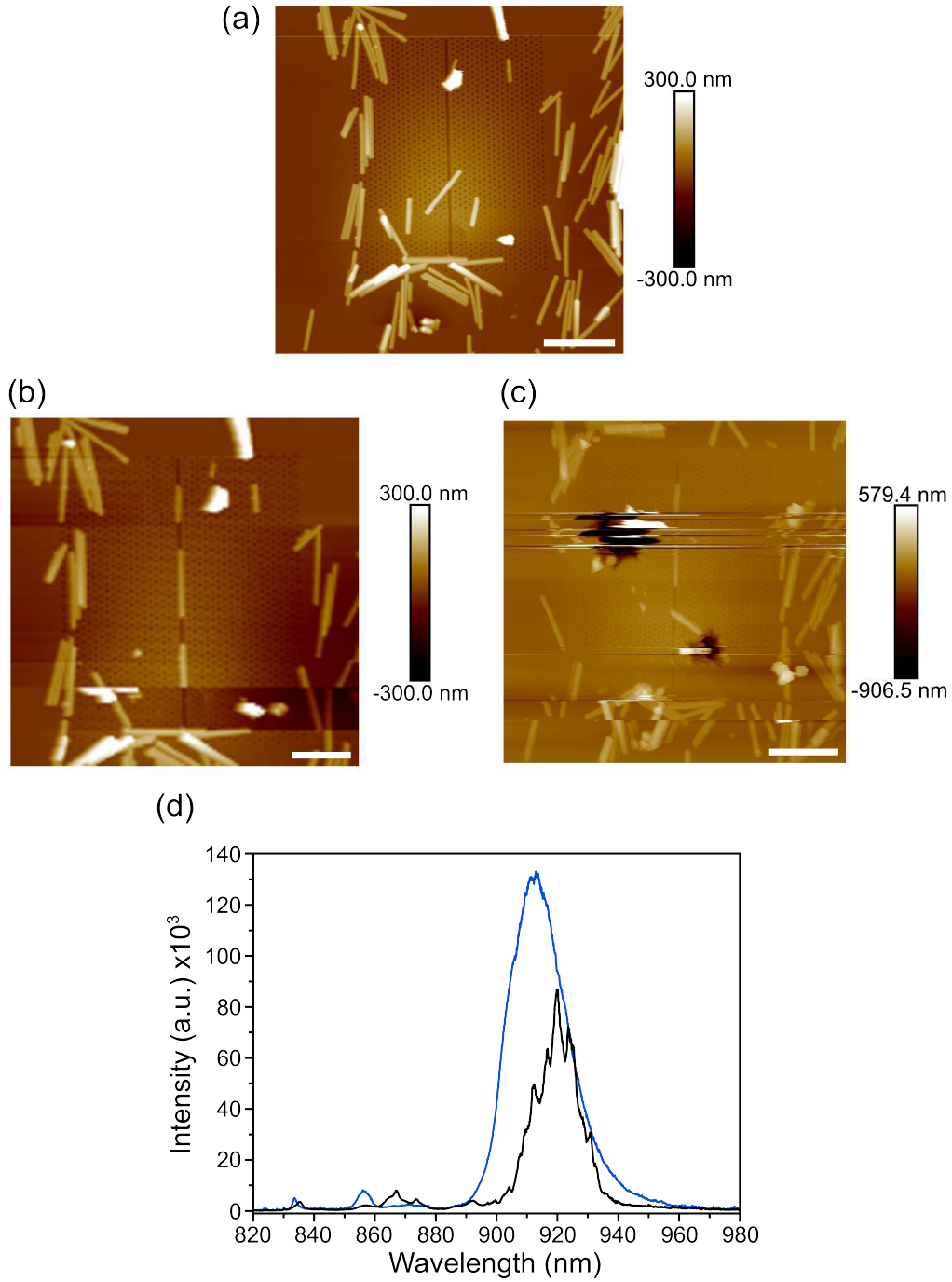

Figure 5.23: Optical characterisation of candidate nanowires on Device 3 before and after nanomanipulation. AFM images show location of nanowires NW-3A, NW-3B and NW-3C (a) before (b) and after nanomanipulation (c) and then after subsequent attempts at removing nanowire bunches and debris fragments from surface of Device 3. Dark regions in (c) correspond to areas of Device 3 where the GaAs membrane has ruptured due to the lateral force exerted by the AFM cantilever tip while in lift mode; (d) PL spectra obtained from combination of all three nanowires before nanomanipulation (black-trace) and NW-3A only after nanomanipulation (blue-trace). For both spectra, an excitation power of ~5µW was used. Scale bars 3µm.

After suitable nanowire candidates were determined following nanowire deposition, NW-1A was selected as the test specimen on which to perform the AFM nanomanipulation technique presented in Section 5.4.3. The emission spectra of NW-1A, therefore, was not obtained before this first attempt at moving it into the slot waveguide of Device 1 had been carried out. However, as NW-1A was successfully transferred into the slot waveguide after nanomanipulation (see Figure 5.21), PL measurements were performed on this coupled system to identify whether or not it exhibited any cavity-like emission behaviour. The PL spectrum collected from NW-1A after nanomanipulation is displayed in Figure 5.24(a). Away from the wetting layer, a sharp emission peak centered at a wavelength close to the resonant wavelength of the optimised cavity design (~878nm) was observed at low excitation powers, with a calculated Q-factor of ~1000. Power dependent PL measurements undertaken on this nanowire, however, revealed that the emission peak did not exhibit behaviour expected for a resonant cavity mode (i.e. its intensity did not sharply increase with increasing excitation power) with it instead beginning to saturate at a relatively low excitation power (~300nW). It was also found that the count rate of the emission peak was maximised when the excitation spot was displaced slightly from the nanowire structure. Taking into account these two observations, it was posited that the origin of this emission peak was not related to nanowire emission enhanced by the formation of a cavity system, but instead resulted from a weakly confined photonic crystal defect mode that was produced by fabrication imperfections in the photonic crystal device [188, 189]. Further support of this emission peak origin is provided by the PL map displayed in Figure 5.24(b), which was generated through calculation of the integrated PL intensity in the wavelength range defined by the width of the emission peak, collected using a manual raster scan technique over a region encompassing the nanowire and a section of the surrounding photonic crystal device. It is observed in this PL map that the regions where the collected PL intensity in this wavelength range is highest are all located somewhere in the surrounding photonic crystal device and not in the nanowire. No evidence of cavity-enhanced nanowire emission at other wavelengths was observed from this structural arrangement.

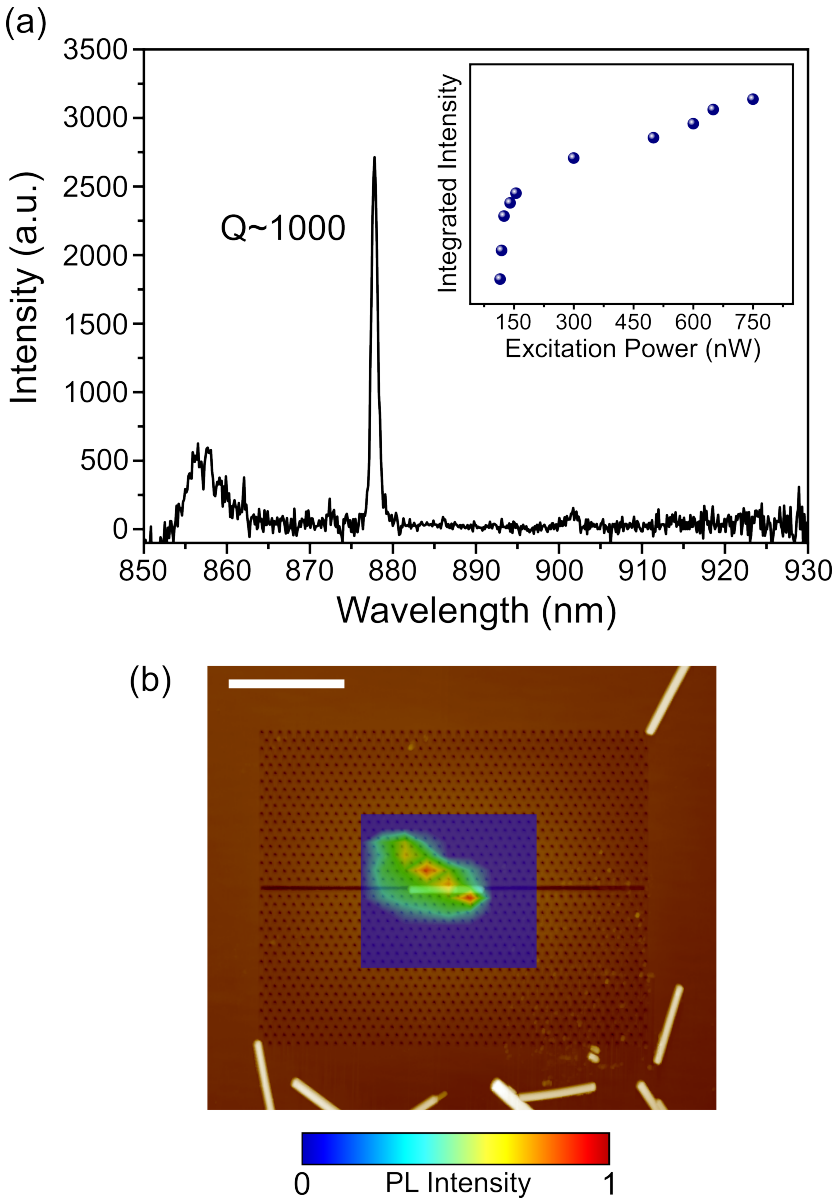

Figure 5.24: Optical characterisation of NW-1A after nanomanipulation. (a) At low excitation powers, the PL spectrum collected from the nanowire contains a narrow isolated emission peak centred at ~878nm, with a Q-factor of ~1000. Inset: Normalised integrated intensity of emission peak as a function of excitation power. Peak is seen to begin to saturate at excitation powers of ~300nW; (b) PL map of area around NW-1A obtained from a manual raster scan of PCslots-5A sample relative to fixed excitation and collection paths of PL setup. Highest PL intensity regions are observed to be located exclusively in the photonic crystal device. Scale bar 3µm.

In addition to the nanowire candidates described above, PL measurements were also carried out on a number of other nanowires deposited on the surface of PCslots-5A. PL spectra obtained from separate groups of clumped nanowires complemented that seen in previous

nanowire characterisation on this sample (see Figure 2.16(d)), with broadband emission observed over the majority of the energy range bounded by available ZB/WZ transitions. However, as well as being considerably less intense in comparison, emission from most of the single isolated nanowires characterised on this sample was found to occur predominately around the low temperature WZ band edge energy ($\lambda \approx 833$nm) only. The broadband emission observed from groups of clumped nanowires on this sample would suggest that these single isolated nanowires do not necessarily consist of a single crystalline phase, but the lack of emission seen at energies lower than the WZ bandgap energy may indicate that either emission corresponding to available range of indirect ZB/WZ transitions is much weaker than that of the direct WZ transition or the stacking fault density in these nanowires is low. An example of the typical PL spectrum obtained from a group of clumped nanowires and a single isolated nanowire on PCslots-5A is displayed in Figure 5.25.

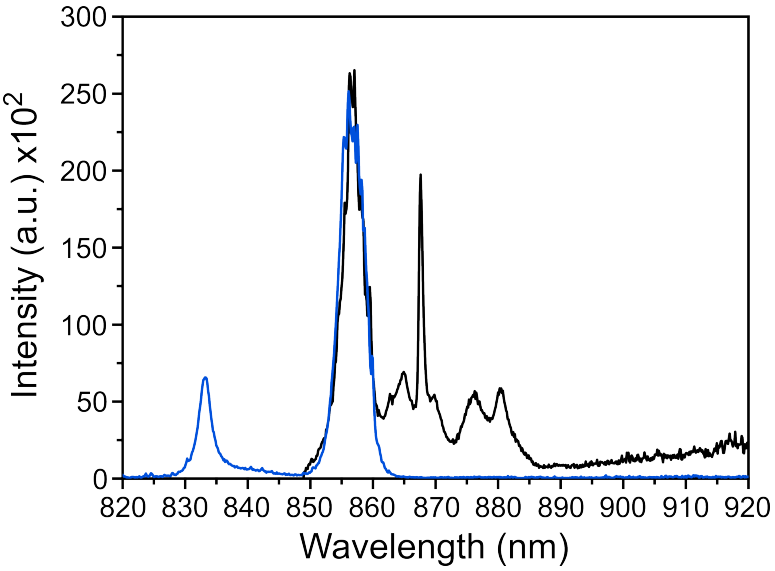

Figure 5.25: PL spectra obtained from a group of clumped nanowires (black-trace) and a single isolated nanowire (blue-trace) deposited on the surface of PCslots-5A using excitation powers of ~700nW and ~2μW, respectively.

5.6 Reflectivity Measurements to Determine Cavity Resonance Wavelength

As no evidence of cavity formation was observed in the PL spectra from the three nanocavity systems described in Section 5.5, the setup previously used for μ-PL measurements was modified so that polarisation resolved reflectivity measurements could instead be performed on these three systems. Cavity formation in polarisation resolved reflectivity measurements is detected through a change in the polarisation of light reflected from the cavity system relative to that of the light incident upon it at a wavelength coincident with the fundamental cavity resonance wavelength. This type of measurement therefore allows for confirmation of nanowire cavity formation irrespective of the emission properties of the nanowire forming the cavity.

The setup utilised for polarisation resolved reflectivity measurements is outlined schematically in Figure 5.26. To enable cavity detection over a broad spectral range, a tuneable Ti:Saph ultrashort pulsed laser (Tsunami, Spectra Physics) was used as the excitation source in this setup. In an effort to decrease the amount of background signal in these measurements (i.e. light not reflected by the cavity), the non-polarising beam splitter in the previous PL setup was replaced by a polarising beam-splitter (PBS), which acted to suppress the transmission to the spectrometer of reflected light from the cavity that has same polarisation as that incident upon it. Further quenching of the unwanted background signal was attempted by also placing a half wave plate (HWP) and linear polariser (LP) in both the collection and excitation paths.

To calibrate the setup and evaluate its suitability for optical characterisation of the nanowire cavity systems, reflectivity measurements were first performed on an L3 photonic crystal cavity device, which was fabricated in a wafer with the same layer structure as shown in Figure 5.12, using a similar fabrication procedure to that described in Section 5.4.1[§]. This

[§]Fabrication of L3 photonic crystal cavity device used for reflectivity measurements was performed by Dr. Ben Royall.

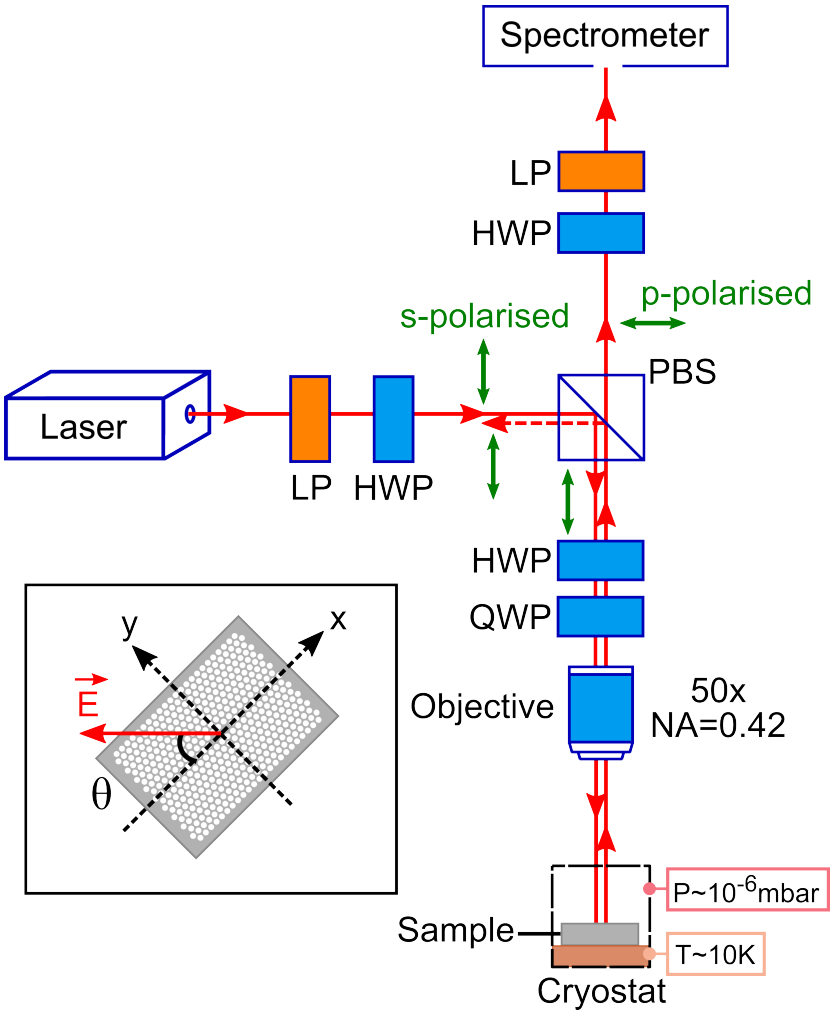

Figure 5.26: Schematic overview of the experimental setup used for reflectivity measurements. *s*-polarised light, prepared by the linear polariser (LP) and half-wave plate (HWP), is reflected by the polarising beam-splitter (PBS) onto the sample. The HWP in-between the PBS and objective is used to rotate the polarisation of the incident light relative to the L3 cavity direction. Light reflected by the sample which is polarised perpendicularly to the light incident upon it is transmitted through the PBS into the spectrometer, whilst reflected light which is co-polarised with the incident light is reflected by the PBS. An additional HWP and LP pair are placed between the PBS and spectrometer as a further barrier to any residual light transmitted through the PBS which has the same polarisation as the incident beam. The quarter-wave plate (QWP) is included to correct for birefringence of the sample and the optics in the excitation path. Red arrows indicate the light beam paths in the reflectivity setup, with green arrows specifying the polarisation degree of freedom of the light before and after interaction with the PBS. Inset illustrates how the polarisation angle of the incident light θ, is defined relative to the L3 cavity direction.

device was chosen for initial testing of the reflectivity setup as there is a relatively wide spectral separation between the (single) fundamental mode resonance and higher order mode resonances of an L3 cavity [158, 159], and the quasi-continuum of excitonic transitions of

the QD ensemble in the wafer allowed for the cavity resonance wavelength to be determined from PL measurements beforehand. The PL spectrum obtained from the L3 photonic crystal device utilised for reflectivity measurements is shown in Figure 5.27(a).

In this experimental arrangement, the number of reflected cavity photons transmitted through the PBS is maximised when the incident polarisation is oriented at 45° (or 135°) relative to the L3 cavity axis (i.e. the direction coincident with the line of missing holes) [190–192]. As it was not possible to rotate the L3 sample after it had been mounted on the cryostat coldfinger, a HWP was placed between the PBS and objective (in the excitation path) to allow for rotation of the incident light polarisation relative to the L3 cavity axis. A quarter wave plate (QWP) was also placed in the excitation path, between the HWP and objective. A previous report in the literature had specified that placing a QWP in this location had further aided in the suppression of unwanted background in their measurements, by acting to correct for any birefringence of the optics in the excitation path and also the cavity sample itself [193].

The HWP rotation angle that oriented the polarisation of the incident light at ~45° to the L3 cavity axis was determined by monitoring the PL signal of the cavity resonance peak as the HWP was rotated and identifying the angle at which this signal was maximised. Reflectivity measurements were then performed with the pulsed laser tuned to the wavelength corresponding to the centre of the cavity resonance peak. With the incident light polarisation oriented at approximately 45° relative to the L3 cavity direction, the reflectivity lineshape of the cavity resonance was observed to be asymmetric as shown in Figure 5.27(b). Upon rotation of the HWP away from this 45° position however (towards θ=0°), the reflectivity line was seen to gradually switch from an asymmetrical shape to a symmetrical shape in the manner depicted by the reflectivity spectra shown in Figures 5.27(c), (d) and (e).

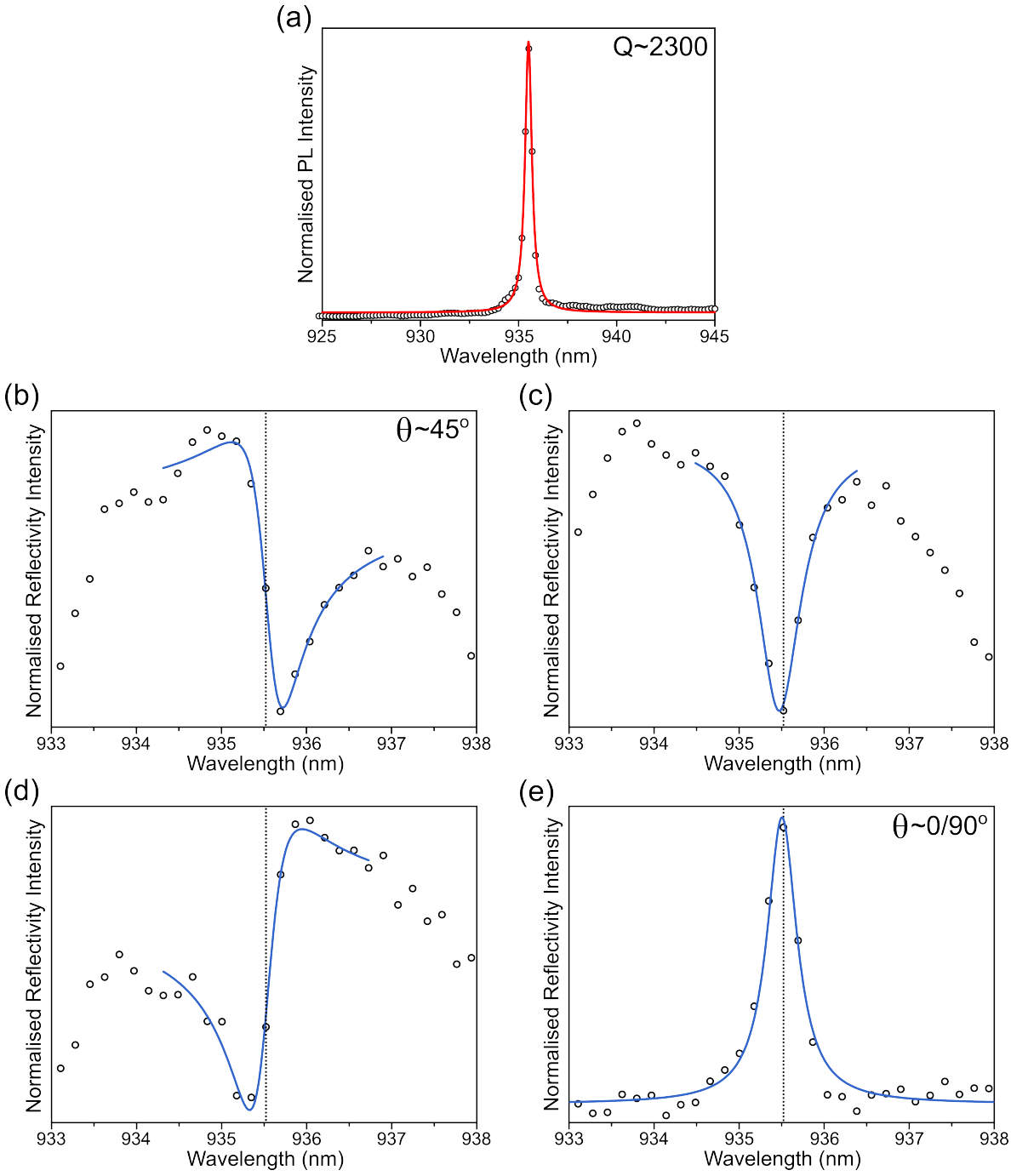

Figure 5.27: Polarisation resolved reflectivity measurements on an L3 photonic crystal cavity. (a) Normalised PL spectrum of the fundamental L3 cavity mode. Experimental data (circles) was fitted with a single Lorentzian function; (b,c,d,e) Representative normalised reflectivity spectra obtained from the L3 sample at four different incident light polarisations. The θ values denoted in (b) and (e) are defined relative to the L3 cavity direction (as illustrated in Figure 5.26). Experimental data (circles) in (b,c,d,e) was fitted with a Breit-Wigner-Fano function as described in Ref [194]. The black dashed lines in (b,c,d,e) indicate the centre of the PL cavity mode peak displayed in (a).

As has been reported previously in the literature, the observed change in the reflectivity lineshape as the HWP was rotated is the behaviour expected when a Fano interference phenomenon is occurring. The asymmetric reflectivity lineshape observed in Figure 5.27(b) is a result of interference between the electric field of the light reflected by the cavity (scattering by a discrete state) and the electric field of the light reflected by the surrounding photonic crystal (scattering to the continuum), which was also impinged upon by the incident light in this case [195, 196]. As the HWP is rotated, the relative strength of the scattering by the discrete state with respect to the scattering to the continuum is modified, leading first to the formation of a symmetrical lineshape as a consequence of destructive interference between the light reflected by the cavity and surrounding photonic crystal (Figure 5.27(c)) and then subsequently an asymmetrical lineshape that is the reverse of that seen in Figure 5.27(b). The shape of the reflectivity line then becomes symmetric again when the incident light polarisation is oriented parallel or perpendicular to the L3 cavity direction (Figure 5.27(e)). In Fano interference, the symmetric lineshape seen in Figure 5.27(e) emerges when the continuum channel contribution is much greater than that of the discrete state. Taking into account the cross-polarised configuration of the setup, when the incident light is polarised perpendicularly to the cavity direction, the reflected light is collected along the direction in which emission from the cavity is low with respect to the continuum contribution. Similarly, when the polarisation orientation of the incident light is parallel to the cavity direction, the cavity mode is not excited efficiently and thus the continuum once again dominates. Although it was not possible to determine accurately the relative angle between the incident light polarisation and the L3 cavity direction for the spectra shown in Figures 5.27(c) and (d), PL measurements confirmed that the symmetrical lineshape observed in Figure 5.27(e) occurred when the incident light polarisation was oriented either parallel or perpendicular to the L3 cavity direction. It is noted that the Q-factor of the cavity resonance determined from these reflectivity measurements was found to be approximately the same as that determined from PL measurements (~2300).

Although the fundamental cavity mode was successfully observed during reflectivity measurements performed on this L3 photonic crystal cavity, for other L3 devices on the same sample that had a slightly lower cavity Q-factor (measured using PL), detection of the cavity mode did not occur. Even with the cross-polarised signal collection approach utilised in this setup, the suppression of the background signal was apparently not strong enough for the cavity resonance to be visible for these lower-Q devices. As seen in Figure 5.28(a), the calculated Q-factor for nanocavity arrangements with parameters matching those of the experimental devices presented in Table 5.1 (with the parameters of NW-3A used in the case of Device 3) using FDTD simulations ranged from $12000 \lesssim Q \lesssim 57000$, with Device 1 possessing the largest. However, SEM images revealed that for Device 1 the nanowire after nanomanipulation was located against one of the sidewalls of slot waveguide rather than its centre (Figure 5.28(b)). FDTD simulations showed that for an arrangement where the nanowire is located at this position within the slot, as well as resulting in a modification of the cavity mode field profile (as seen in Figures 5.28(c) and (d)), a relative order of magnitude reduction in the resonance Q-factor occurs ($Q \approx 1700$). Accordingly, no observation of a cavity resonance was observed during reflectivity measurements on Device 1. No observation of a cavity resonance was observed during reflectivity measurements on Devices 2 and 3 either, indicating that the experimental Q-factors of these devices were also lower than that of the L3 device from which the spectra in Figure 5.27 were obtained.

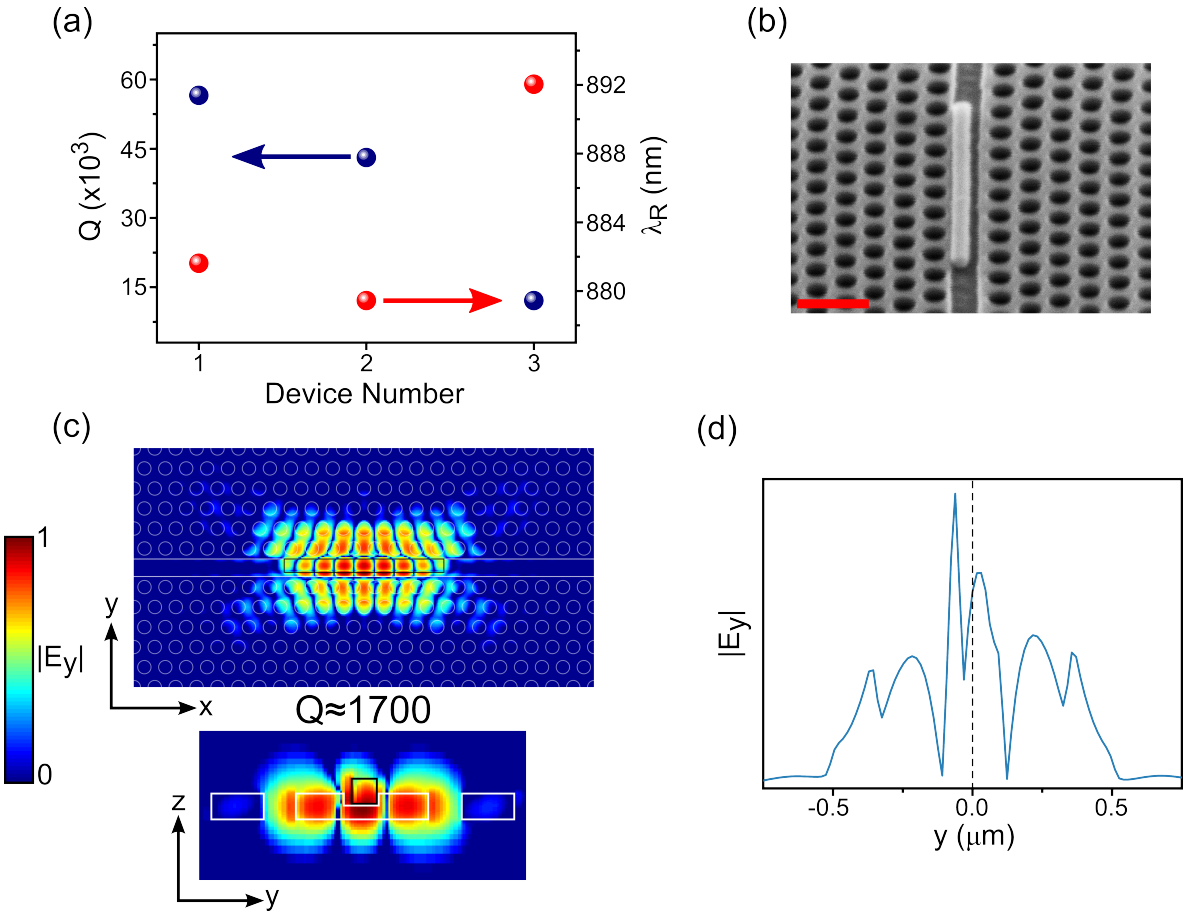

Figure 5.28: Calculated resonant mode properties of experimental nanocavity devices. (a) Summary of calculated Q and λ_R values for nanocavity arrangements with photonic crystal and nanowire parameters corresponding to those measured for Devices 1, 2 and 3; (b) Angled SEM image of Device 1 after nanomanipulation. Scale bar 500nm; (c) Calculated electric field profile in the x-y and y-z planes of an arrangement with photonic crystal and nanowire parameters corresponding to those of Device 1, with the nanowire positioned against one of the slot sidewalls. The colour scale is logarithmic and the field profiles are normalised to the source power. Photonic crystal and nanowire structures are depicted by white and black solid lines, respectively; (d) Development of $|\mathbf{E_y}|$ along the y-direction for the arrangement in (c) at the centre of the nanowire in x and z.

5.7 Cavity Resonance at the InP WZ Bandgap Energy

5.7.1 Optimisation of the Cavity Design

The lack of any observation of cavity enhanced nanowire emission during PL measurements performed on Devices 1, 2 and 3 may have been the result of a number different factors. Although, in the case of Device 2, the calculated Q-factor of the nanocavity mode was ~55000, there was a considerable mismatch between nanowire diameter and slot width, and therefore the spatial overlap of the electric field with the nanowire volume was likely to be very small. Also, after nanomanipulation, destruction of a considerable region of the photonic crystal structure of device 3 had occurred, and as observed in Figure 5.28(b), the nanowire comprising device 1 was located against one of the sidewalls of the slot waveguide rather than in the centre which FDTD simulations showed led to a significant reduction in the Q-factor of the cavity system. In addition, the lack of evidence of cavity formation in reflectivity measurements provides a hint that, for all of the experimental devices, the Q-factor of the cavity mode was not high enough to allow for detection of cavity enhanced emission during PL measurements. However, even if there had been a larger sample size of devices to study and the parameters of these devices had matched exactly those of the ideal arrangements modelled in Section 5.3, the observation that emission from individual nanowires transferred to the device substrate did not match that seen previously in ensemble PL measurements (Section 2.4.3), and instead occurred predominately only around the InP WZ bandgap energy means that the probability of observing cavity enhanced nanowire emission would still have been small even for these ideal nanocavity devices.

Therefore, in order to maximise the probability of realising cavity-enhanced nanowire emission in this design scheme, a cavity arrangement with a resonance around the wavelength corresponding to the InP WZ bandgap energy emission which was observed from the ma-

jority of individual single nanowires characterised on PCslots-5A, was required. As before, optimisation of cavity parameters for this resonance wavelength was first performed using numerical calculations. Taking note of the previous simulation results presented in Section 5.3, blue-shifting of the previous target resonance wavelength to that of the InP WZ bandgap energy emission was achieved (with a slab thickness again of 140nm) by decreasing a and W to 235nm and $0.96\sqrt{3}a$, respectively, while r was kept at 80nm. As in the previous simulations, the ideal scenario of w=d was simulated with h again set to 60nm. The nanowire parameters also remained as d=100nm and L=2µm. For this design, λ_R was calculated to be ~833nm, with the calculated value of Q somewhat higher than that for the equivalent design previously described whose λ_R≈870nm (Q≈110000) and a calculated V value that was slightly smaller (V≈$0.62(\lambda/n)^3$). There was no difference, however, in the calculated value of C_y between these two designs (C_y≈0.15). The mode profile of the cavity resonance for this arrangement is shown in Figure 5.29.

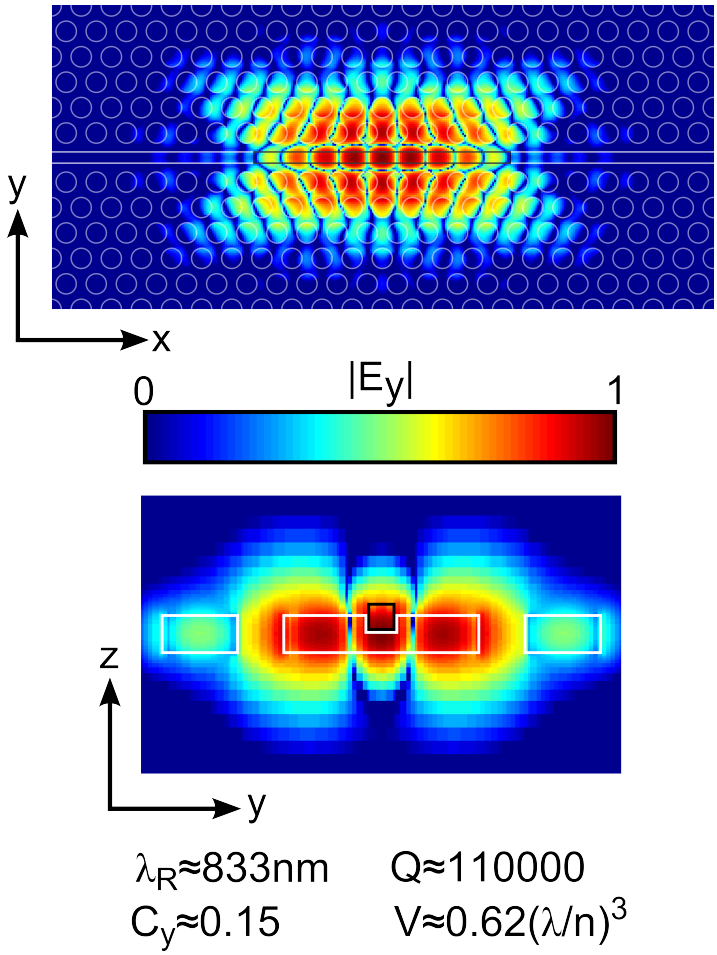

Figure 5.29: Calculated electric field profile of a nanowire-photonic crystal waveguide fundamental cavity mode with a resonance wavelength λ_R≈833nm in the x-y and y-z planes. The colour scale is logarithmic and the field profiles are normalised to the source power. Photonic crystal and nanowire structures are depicted by white and black solid lines, respectively. Parameters of the nanocavity system are described in the main text.

5.7.2 Photonic Crystal Slot Waveguide Device Fabrication

Fabrication of the photonic crystal slot waveguide arrangement optimised for λ_R≈833nm presented above was attempted using a similar approach outlined in Section 5.4.1. Although there is a considerable wavelength separation between the resonance of the optimised cavity in this instance and the centre of the wetting layer emission observed in all previous PL measurements on PCslots-5A ($\Delta\lambda$≈22nm), there was still a possibility that this wetting layer emission may obscure to some extent observation of cavity-enhanced nanowire emission (as

it may have done previously also), especially at higher excitation powers and if the cavity resonance is shifted slightly to longer wavelengths as a result of variations in device parameters after fabrication. A different wafer therefore, with the same layer structure as VN2782 but containing no embedded InAs QDs, was utilised for photonic crystal fabrication here. This wafer layer structure (Growth Reference: VN2891) is depicted schematically in Figure 5.30(a).

As the spectral width of the sole InP WZ bandgap emission peak is considerably smaller than that of the wavelength range encompassing all of the available ZB/WZ energy transitions in a polytypic nanowire, a new photonic crystal device array design was implemented on this sample in an effort to maximise the probability of spectral overlap between the emission from a transferred nanowire and the resonance wavelength of the cavity system produced after nanowire placement into the slot waveguide. In this design, which is outlined schematically in Figure 5.30(b) and Figure 5.30(c), a single slot waveguide encompasses three separate photonic crystal devices whose patterned hole radii are incrementally increased by 1nm from the leftmost device to the rightmost device, which — with the ability of being able to push a nanowire along the slot waveguide demonstrated in Section 5.4.3 — provides three opportunities to achieve successful spectral overlap of the cavity resonance and emission of the single nanowire placed into the slot. This scheme is repeated for a total of five rows, with the patterned air hole radius of the left-most crystal in each successive row set to be 1nm larger than the right-most crystal of the row below, forming a 'chain' of devices with incrementally increasing hole sizes.

The capability to pattern a single slot waveguide extending over three photonic crystal devices (with similar dimensions to those patterned on the previous sample) without any interruptions due to write-field stitching errors, was provided by the use of a newer EBL system[¶], which offered a patterning step size comparable to the previous system for a greatly enlarged write-field size of 500x500µm^2. The newer EBL system also promised a better overlay accuracy of ~20nm.

[¶]EBL system used for device patterning in this instance – Raith Voyager

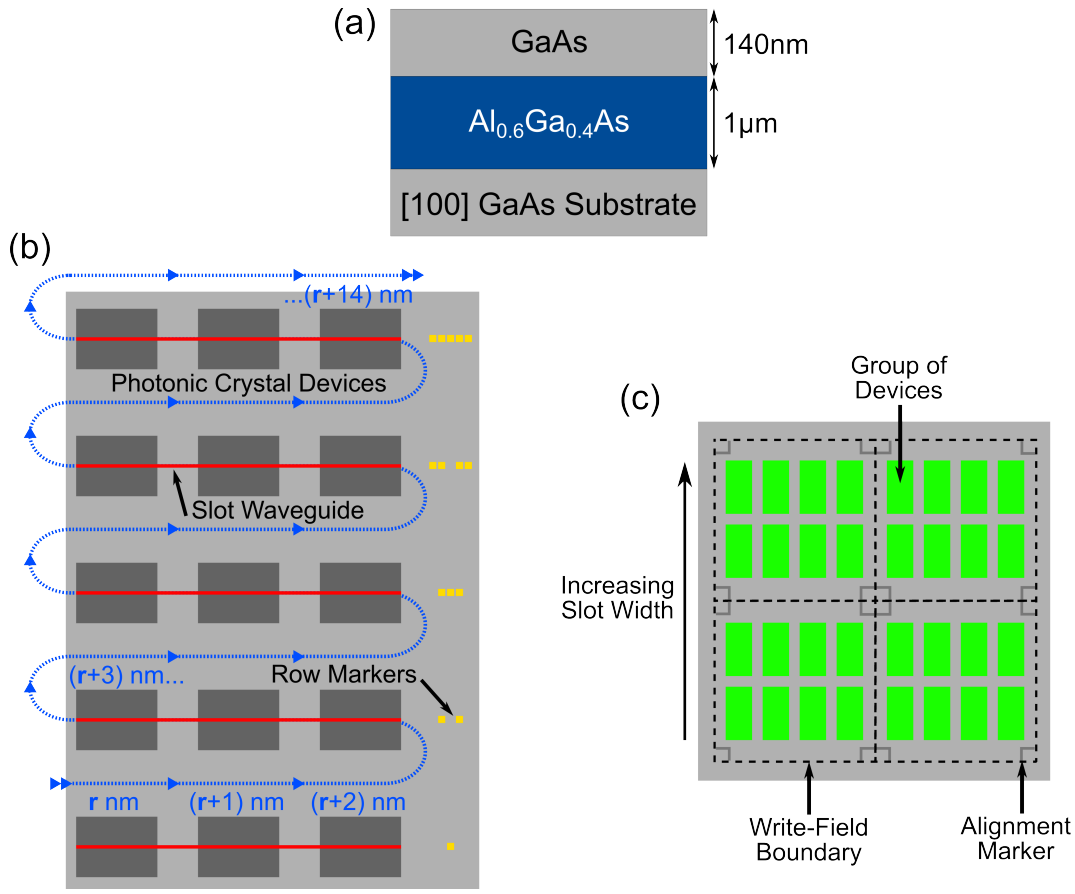

Figure 5.30: Fabrication of photonic crystal slot waveguide devices on sample PCslots-5B. Schematic diagrams show overviews of (a) the epitaxially grown wafer structure used for photonic crystal slot waveguide device fabrication; (b) the 'chain' of photonic crystal devices that form a single device group. The patterned hole radius of each device is increased incrementally by 1nm from device-to-device in the sequence depicted by the blue dashed line (where r corresponds to the smallest hole radius in the device 'chain'). A single slot waveguide (red solid lines) encompasses all three of the photonic crystal devices (dark grey squares) forming a row to provide multiple opportunities for successful realisation of cavity enhanced nanowire emission with a single nanowire. Square markers (yellow squares) are patterned to the right of each row in order to specify device row number and also to clearly indicate where one group of devices begins and another finishes (when looking along successive rows of device groups); (c) a region of a single device array patterned on PCslots-5B. Alignment markers sit in each of the four corners of an individual write-field (illustrated here by black dashed lines), which contains a total of 8 device groups.

As before, alignment markers were patterned at the edges of each write-field in the same patterning run as the photonic crystal devices, in preparation for subsequent overlay of the slot waveguides. The patterned slot waveguide width was kept constant for the five row group of photonic crystal devices and then increased successively by 5nm for a total of four

device groups in recognition of the fact that there will be a certain variation in the diameter of individual nanowires transferred onto the device substrate (which was indeed observed after transfer on the previous experimental devices). This four device group arrangement was repeated once more (vertically) and then these eight rows of device groups were duplicated across 16 columns to give a final array design that contained 1920 patterned photonic crystal devices and 640 slot waveguides. Multiple device arrays were patterned on a cleaved piece of VN2891 (herein referred to as sample PCslots-5B) using an EBL accelerating voltage of 50kV and a beam aperture size of 40um, with the exposure dose varied from array to array. The feature resolution limit provided by these beam settings (with the same resist thickness of ~340nm), was ~40nm. In addition to the features described above, a separate set of slots with the same width increments as those patterned in the device arrays were also patterned on this sample (away from the main arrays), so that the approximate depth of the slot waveguides in the photonic crystal devices could be characterised after fabrication using a similar method to that described in Section 5.4.1 .

Figure 5.31 displays SEM images of a selection of example photonic crystal slot waveguide structures (before the final HF underetch step) on PCslots-5B produced by the fabrication procedure presented in Section 5.4.1 with the new EBL system described above. The number of air hole repeats in x for these structures was 47, and in y the number of repeats, separated by the line defect, was 20. As well as allowing for the realisation of an uninterrupted etched slot waveguide that spans a region encompassing three photonic crystal devices, the use of the new EBL system for device patterning also prevented the appearance of the periodically repeating nodules that were present along the length of the slot waveguides in the previously fabricated structures on PCslots-5A. Although there was still some random displacement of the etched slot from the exact centre of the photonic crystal line defect after fabrication, the overall slot overlay accuracy was observed to be greater in comparison to the previously fabricated devices on PCslots-5A. This sample was therefore deemed suitable for attempts at experimentally realising the optimised cavity system described in the previous section.

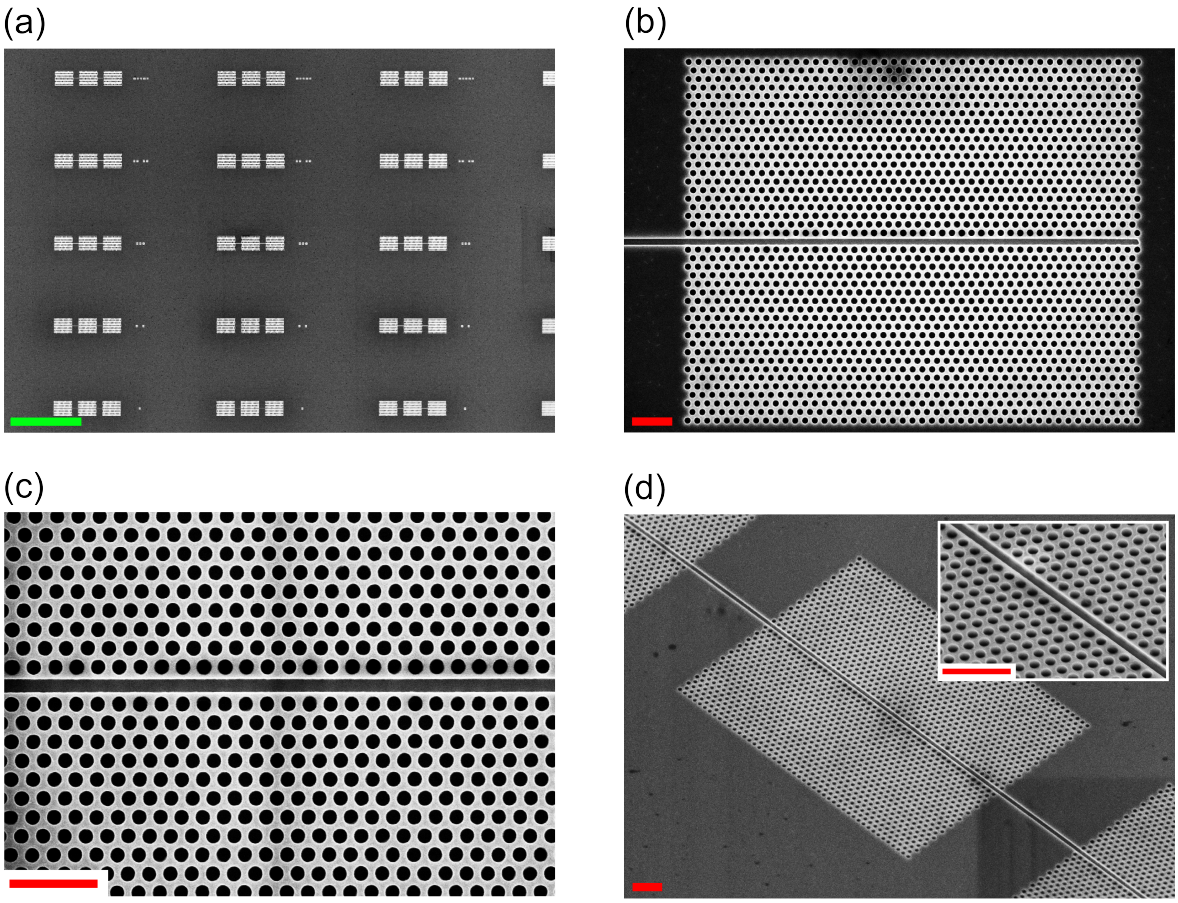

Figure 5.31: SEM images of photonic crystal slot waveguide devices fabricated on PCslots-5B using the process described in the main text. Top-down SEM images show, (a) a region encompassing a number of device groups within a single device array, (b) the right most photonic crystal waveguide device in the group of three for which a single slot waveguide extends and (c) a higher magnification image of a similar device to that shown in (b); (d) An angled SEM image of the central photonic crystal slot waveguide device in the group of three for which a single slot waveguide extends. Inset: Higher magnification image of the device displayed in (d), showing in more detail the depth of the slot waveguide and the air holes comprising the surrounding photonic crystal. Scale bars (a) 50µm (b-d) 1µm.

5.7.3 InP Nanowire Fabrication and Growth

Following the transfer of nanowires from Sample 2F to PCslots-5A using the technique described in Section 5.4.2, the majority of nanowires with a diameter suitable for experimental realisation of the optimised cavity design in Section 5.7.1 had been removed from the growth substrate. Therefore, fabrication and growth of a new InP sample was required in order to perform nanowire transfer onto PCslots-5B.

Preparation of Sample 5A[‖] for growth followed a similar process to that used for all of the previous InP growth samples discussed in Chapter 2. To better facilitate nanowire transfer (taking into consideration the previously used transfer technique), large groups of many individual arrays containing nanoholes of the same diameter and pitch were patterned on this sample. Across the array groups, the nanohole diameter was varied from ~50 to ~95nm. As defect formation and nanowire morphology variance was observed to increase significantly for nanohole pitches greater than 1µm on Sample 2F, nanoholes were patterned only with a pitch of either 0.5µm or 1µm on this sample. Due to the fact that both large groups of nanohole arrays were to be patterned on this sample, and alignment of these holes did not have to coincide with individual SiO_2 squares on the sample surface (as the growth mask was full coverage), fabrication of gold alignment markers was not performed on Sample 5A. This greatly simplified the overall fabrication process and reduced the amount of unavoidable wafer contamination that occurs during the preparation of samples for growth. SEM characterisation of nanoholes after EBL patterning and subsequent etching revealed that final nanohole diameters on this sample were on average ~80nm larger than the target patterned diameters. This considerable difference between the target and final nanohole diameter here was thought to be most likely a result of either some variation in chamber conditions during the RIE step in the fabrication procedure, or exposure of the growth mask to HF for too long when attempting to remove the final remnants of SiO_2 that may have been present in the nanoholes after the preceding RIE step.

As for the previous InP nanowire growth runs described in Chapter 2, one of the main aims for nanowire growth in this case was to produce pure phase stacking fault free nanowires. Production of pure phase nanowires would mean that there was an approximately uniform emission energy range across the entire sample which coincided with the fundamental resonance energy of the optimised nanowire-photonic crystal cavity system. Stacking faults in nanowires are observed to increase in the proximity of heterostructure interfaces [197], and SEM images of previously grown InP nanowire samples revealed that the attempted incorpo-

[‖]Sample 5A corresponds to growth sample reference MR3867.

ration of a NWQD during growth led to a subsequent abrupt change in nanowire morphology. Owing to the fact that the resonance of the cavity system design in this case was optimised to coincide with the previously observed InP WZ transition energy, there was no practical reason for trying to incorporate a NWQD in each nanowire during growth. Therefore, in an effort to increase the probability of producing pure phase nanowires here, incorporation of a NWQD during nanowire growth was not attempted.

Nanowire growth on Sample 5A followed the same scheme as that for Sample 2F, but with the AsH_3 step used to produce the InAsP segment within each nanowire omitted. The wafer was first annealed at 680°C for 9 minutes under a PH_3 overpressure to remove the native oxide, along with any organic contaminants that may have been introduced during the previous processing of the substrate. Following this annealing step, nanowire growth proceeded for a total of ~300s using flow rates of 0.13sccm and 50sccm for TMIn and PH_3, respectively. Nanowire growth was concluded by the closure of the TMIn channel, with the PH_3 (double-dilution) channel remaining open while the sample cooled.

Representative SEM images of nanowires formed from the smallest and largest nanoholes for both 0.5µm and 1µm pitches after growth on Sample 5A are shown in Figure 5.32. As for all previous nanowire growths, the nanowire growth direction on this sample was seen to be perpendicular to the plane of the substrate, with the nanowire structures composed of {110} facets. For both pitches, no obvious tapering of individual nanowires was observed, and the variation in nanowire height was found to decrease as nanohole diameter increased. The relative side length of nanowires was also seen to become more uniform with increasing nanohole diameter for both pitches, though as for previous InP nanowire growths, the overall cross-sectional uniformity was substantially better for 0.5µm pitch nanowires, with the majority of structures formed from the largest nanoholes with this pitch exhibiting a cross-section comparable to that observed for individual (non-elongated) GaAs nanowires discussed in Chapters 2 and 3 (Figures 5.32(c) and (d)). Similar to nanowire cross-sectional uniformity, the number of defects within each array on this sample was observed to decrease as nanowire diameter increased, with the relative defect density considerably lower for nanowires with 0.5µm pitch.

It is noted that for the smallest nanowire diameters, the defect density was comparable to that observed for 0.5µm and 1µm pitch nanowires on Sample 2F.

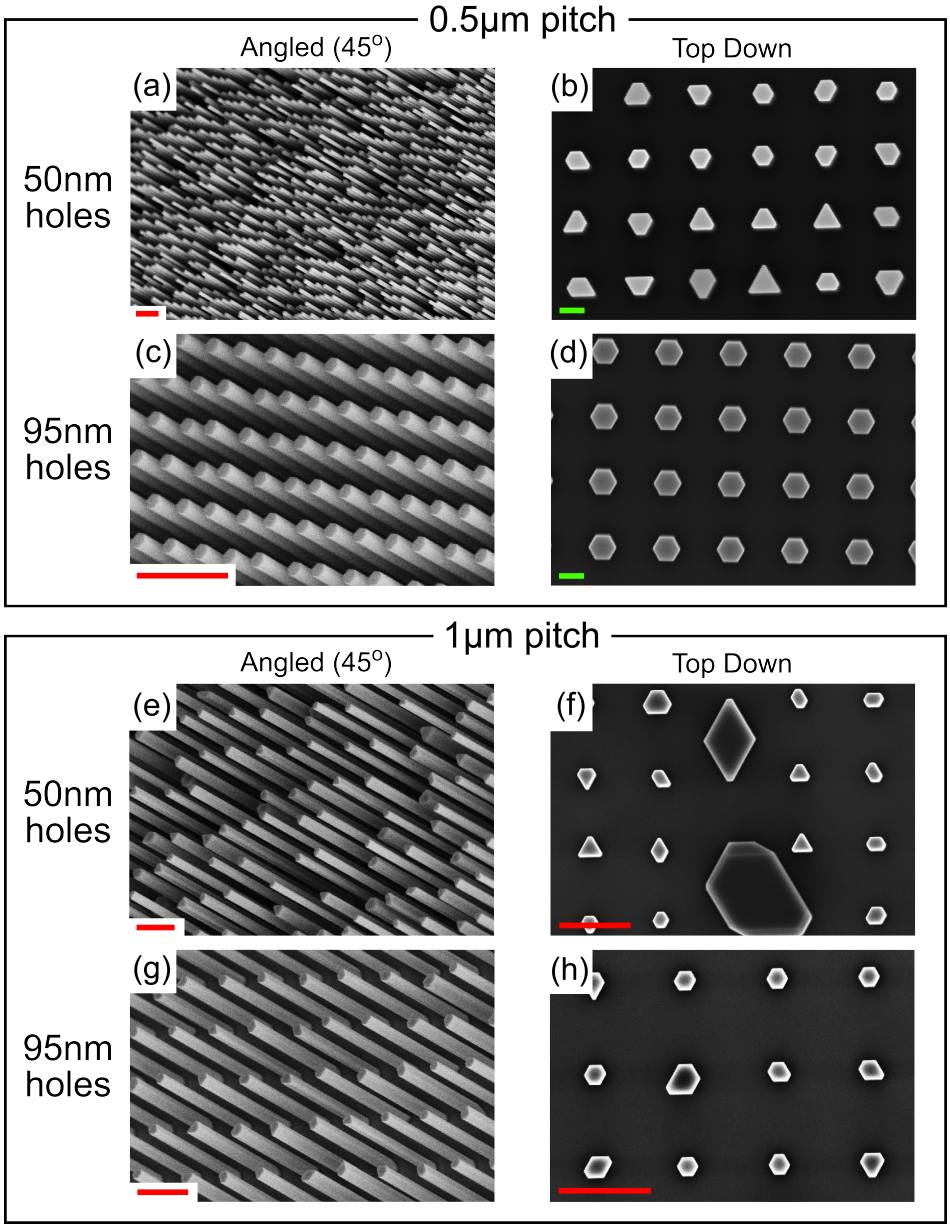

Figure 5.32: SEM images of nanowire growth on Sample 5A. (a,c) 45° and (b,d) top-down overview images of nanowires grown from nanoholes with a pitch of 0.5µm and a patterned diameter of 50nm and 95nm, respectively; (e,g) 45° overview and (f,h) top-down images of nanowires grown from nanoholes with equivalent patterned diameters to those in (a,b,c,d), but with a pitch of 1µm. Scale bars (a,c,e-h) 1µm (b,d) 200nm.

The radial growth rate for nanowires on this sample did not show much variation between the two different pitches, with the average nanowire diameter ~40nm larger than the nanohole from which it had formed. As for previous InP nanowire growth performed on full coverage substrates, it was not possible to determine the heights of nanowires with a pitch of 0.5µm due to the increased growth rate around the edges of each array. For nanowires with a pitch of 1µm, there was an approximately inverse linear relationship between nanowire height and diameter as shown in Figure 5.33. Using a linear growth rate approximation, the axial growth rate varied from ~10nm/s for the largest patterned nanohole diameter to ~21nm/s for the smallest. Although not possible to compare directly, it is noted that the average height of the smallest diameter nanowires on this sample was considerably larger than that measured for nanowires of equivalent pitch on Sample 2F.

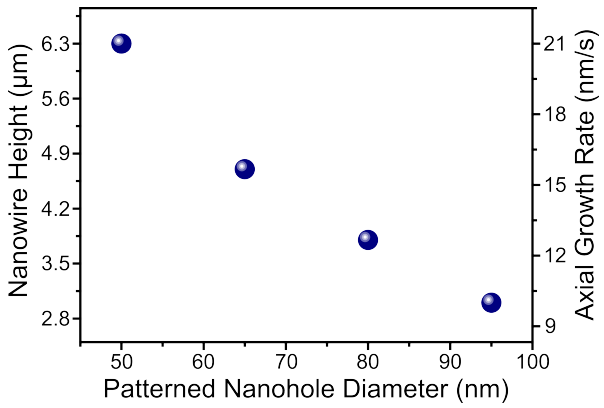

Figure 5.33: Nanowire height versus patterned nanohole diameter for nanowires grown on Sample 5A with a pitch of 1µm. Axial growth rates are calculated using a linear approximation.

Owing to the overetching of the SiO_2 growth mask in nanohole regions during fabrication, even the smallest diameter nanowires on this sample had diameters that were considerably larger than both those on Sample 2F and that of the optimised design described in Section 5.7.1. Indeed, the results of the FDTD simulations presented in Section 5.3 showed that increasing the nanowire diameter beyond 100nm resulted in a dramatic decrease in the resonance Q-factor due to the reduction in the vertical confinement of the cavity mode. However, the observation that, as nanohole diameter decreases on this sample, the uniformity of nanowire side length and height decreases and the number of defects increases shows that obtaining a

high yield of nanowires with a diameter of ~100nm which all exhibit similar morphology using these growth conditions is unlikely.

Although further InP growth studies in addition to those presented in Chapter 2 are ongoing, as demonstrated in that Chapter, obtaining a high yield of nanowires with the ideal parameters described above may simply not be attainable on full coverage SiO_2 wafers using this growth approach. With this in mind, reduction of nanowire diameter on Sample 5A post-growth was attempted using a hydrochloric acid (HCl) wet etch. Etchants based on HCl are widely used for InP semiconductor devices [198, 199] and a number of reports in the literature have shown that the etching of (111)A surfaces proceeds much more slowly than that of {110} surfaces [200–202]. Therefore, with use of a suitably concentrated solution of HCl, a significant increase in nanowire aspect ratio may be achieved.

Etching was performed for two different nanowire diameters ~175nm and ~200nm (grown from patterned nanohole diameters of 65nm and 80nm, respectively), with pitches of both 0.5µm and 1µm. In the first etching attempt, four separate cleaved pieces, which each incorporated a single nanowire array group, were submerged into a beaker containing a 1:10 HCl:H_2O(DI water) solution for 80s and then dried with a nitrogen gun. SEM images revealed that after this etching procedure, however, there was no discernible change in nanowire diameter for any of the four arrays. Therefore etching was performed once again on these same four cleaved pieces, using a significantly higher concentration solution of 1:3 HCl:H_2O and a reduced etching time of 50s. Figure 5.34 shows representative SEM images of the nanowires after this second etch for each of the four cleaved pieces. Nanowire diameter was observed to be reduced to some extent in each of the four individual array groups after etching, with the magnitude of this reduction comparatively larger for 0.5µm pitch nanowires. The average reduction in diameter for nanowires with a pitch of 0.5µm was observed to increase with increasing initial nanowire diameter, rising from ~25nm for ~175nm diameter nanowires to ~40nm for ~200nm diameter nanowires. Nanowires with a pitch of 1µm showed the opposite behaviour, however, with the average reduction in diameter decreasing from ~15nm for ~175nm diameter nanowires to only ~5nm for ~200nm diameter nanowires. As anticipated, a larger reduction

in nanowire diameter resulted in nanowire surfaces that displayed more surface damage, with the 1µm pitch ~200nm diameter nanowires exhibiting almost no surface damage at all. Again, owing to the enhanced growth rate at the edges of each individual array, it was not possible to measure whether there was any difference in nanowire height after etching for nanowires with a pitch of 0.5µm. No appreciable change in the heights of the 1µm pitch nanowires was observed after etching, however.

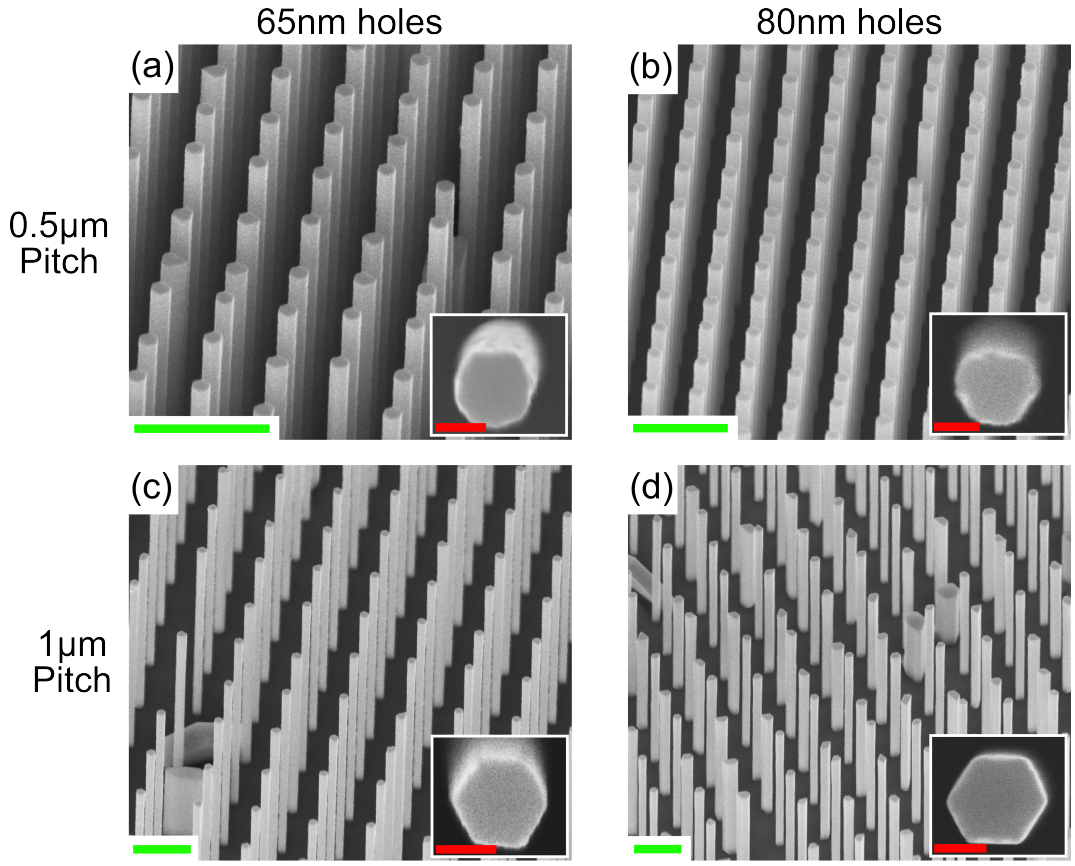

Figure 5.34: SEM images of nanowires on Sample 5A after post-growth wet-etching in a HCl:H_2O solution. 45° overview images of nanowires grown from patterned nanohole diameters of 65nm and 80nm, respectively and a pitch of (a,b) 0.5µm and (c,d) 1µm. Scale bars 1µm. The insets of (a,b,c,d) show shallow angle images of an individual nanowire within each array. Scale bars 1µm.

5.7.4 PL Measurements on InP Nanowires

Although incorporation of an embedded emitter was not attempted during growth on Sample 5A, the surface damage induced by the wet etching process described above still had the

potential to have an impact on the emission properties of individual nanowires [19, 203]. To determine the extent to which nanowire emission was influenced by the presence of this surface damage, PL measurements were undertaken on a cleaved piece of Sample 5A containing arrays of nanowires with a pitch of 1µm grown from nanoholes with a patterned diameter of 65nm before and after HCl etching.

PL measurements were undertaken using the same low temperature non-resonant µ-PL setup outlined in Figure 2.13. The cleaved sample under investigation was installed in an evacuated continuous flow helium cryostat operating at T≈10K, with nanowires excited by a 632.8nm HeNe laser. The laser was focused onto the sample using a 50X microscope objective lens with an NA of 0.42, giving an excitation spot size of ~2µm.

Representative spectra taken at various locations on the cleaved nanowire sample before etching are displayed in Figure 5.35. At low excitation powers (insets of plots in Figure 5.35), although nanowire emission was observed to occur predominately at the low-temperature WZ InP bandgap energy (~833nm), there was also some weaker emission seen at longer wavelengths. Nanowires on this cleaved sample, therefore, did not all consist of a single crystalline phase. However, in contrast to Sample 2F, at higher excitation powers, the spectrum collected from each location on this sample was observed to be dominated by the WZ emission peak. Figure 5.36 shows representative spectra taken at various locations on the cleaved nanowire sample after etching had taken place. The surface damage induced by the wet etching procedure had seemingly little impact on the optical properties of nanowires on this sample, with both the emission spectra and count rates measured by the spectrometer at low and high excitation powers very similar to those observed before etching.

Due to time constraints, it was not possible to optically characterise nanowires on the other cleaved pieces from Sample 5A, or perform further etching of nanowires to reduce their diameter to that required for the optimised cavity design described in Section 5.7.1. However, the results of PL measurements presented here demonstrate that post-growth HCl etching may indeed provide a viable supplementary means of controlling InP nanowire diameter alongside tailoring of growth conditions for nanowires without an incorporated quantum emitter.

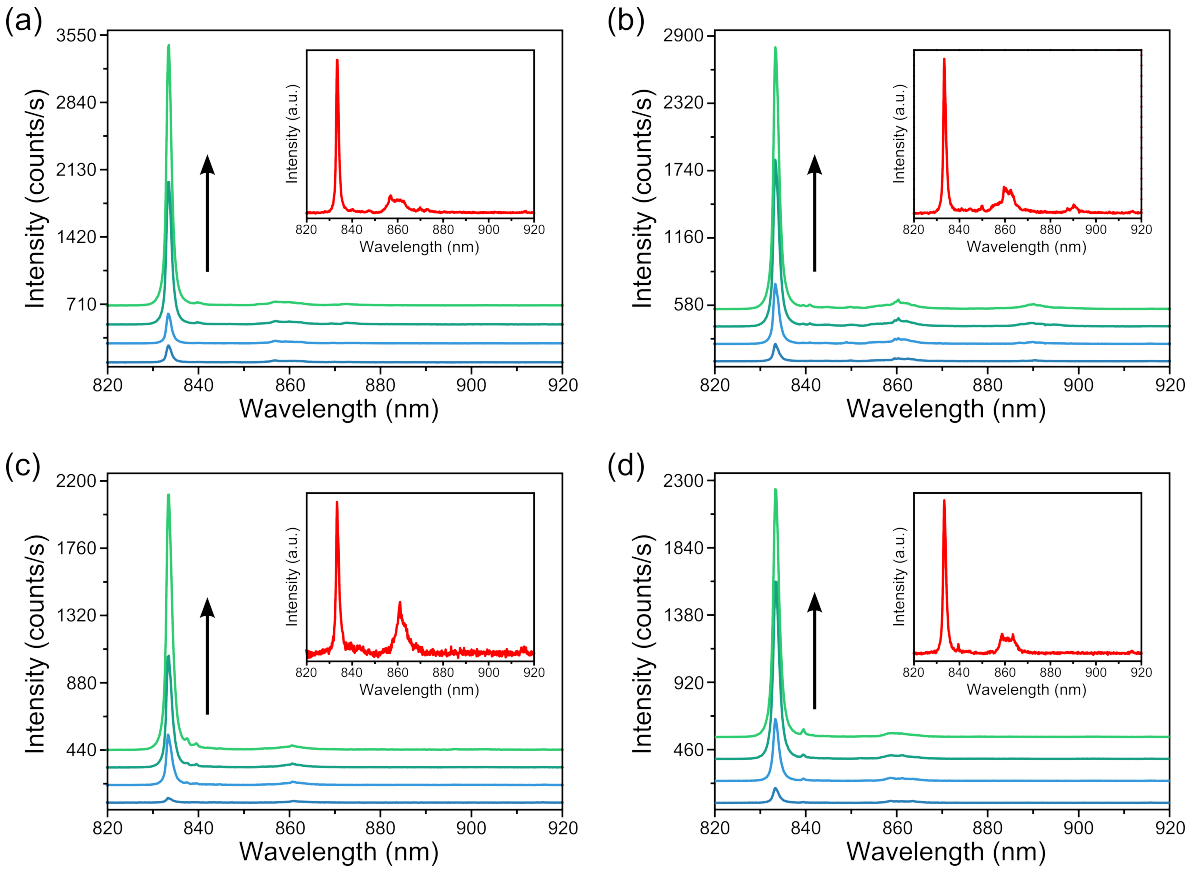

Figure 5.35: PL spectra of InP nanowires with a 1µm pitch grown from nanoholes with a patterned diameter of 65nm. The black arrow in (a,b,c,d) denotes increasing laser excitation power (~20nW, ~50nW, ~100nW and ~200nW, respectively). Spectra are offset in y for clarity. Insets of (a,b,c,d) show the lowest power (~20nW) PL spectra in more detail.

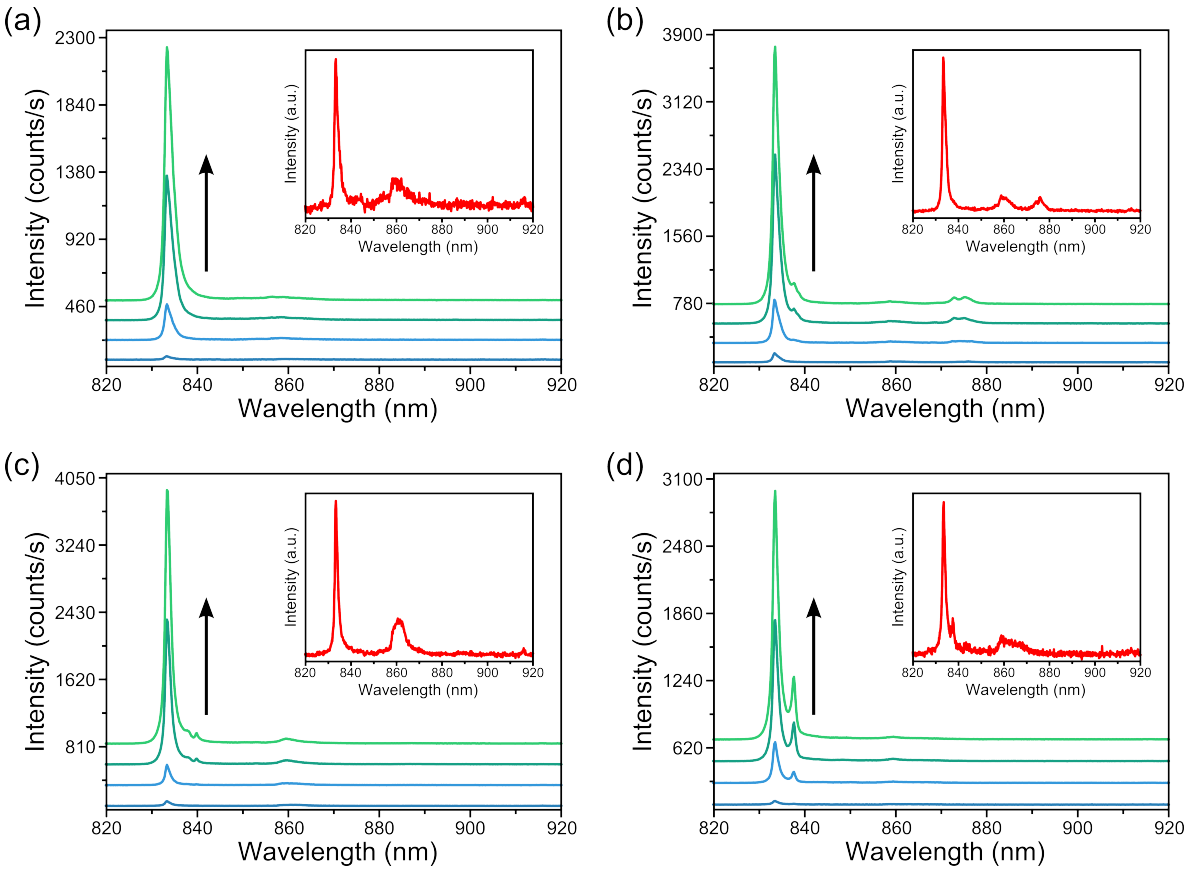

Figure 5.36: PL spectra of InP nanowires with a 1µm pitch grown from nanoholes with a patterned diameter of 65nm after wet etching with a concentrated HCl solution. The black arrow in (a,b,c,d) denotes increasing laser excitation power (~20nW, ~50nW, ~100nW and ~200nW, respectively). Spectra are offset in y for clarity. Insets of (a,b,c,d) show the lowest power (~20nW) PL spectra in more detail.

5.8 Conclusion

A scheme for production of a high-Q, low-V nanocavity arrangement with a sub-micron resonance wavelength has been presented. The cavity arrangement consisted of an InP nanowire placed at the centre of a GaAs photonic crystal slot waveguide. Ensemble PL measurements revealed that the InP nanowires selected for experimental realisation of this nanocavity arrangement were polytypic, and exhibited a broad range of emission wavelengths centred around ~870nm. Therefore, using a combination of frequency-domain and FDTD simulations, an optimised nanocavity design with a calculated cavity resonance corresponding to this wavelength and a Q factor and V of ~76000 and ~$0.65(\lambda/n)^3$, respectively was developed. Fabrication of photonic crystal slot waveguide devices with parameters based on this optimised design was carried out using a two-step lithography process. Nanowires were then transferred onto the device substrate using a dry mechanical dispersion technique. After transfer, placement of five suitable nanowire candidates into the slot waveguide of nearby photonic crystal devices was performed using an AFM system. Subsequent repositioning of a nanowire along the length of the slot waveguide after placement was also demonstrated with this AFM nanomanipulation technique.

Fabricated nanocavity arrangements were characterised using both PL measurements and reflectivity measurements. In each case, however, no evidence of cavity formation was observed. The lack of evidence of cavity formation in reflectivity measurements suggests that the Q-factor of the cavity mode for all experimental devices was not high enough for detection of cavity enhanced emission in PL measurements. In addition, it was found that PL the emission from the majority of individual nanowires deposited on the device substrate occurred predominately around the low-temperature WZ band edge energy ($\lambda\approx$833nm) only. The probability of observing cavity enhanced emission therefore, even if the Q-factors of the experimental devices had been higher, would have been small owing to this wavelength disparity between the observed emission from individual nanowires and the targeted resonance of the nanocavity arrangement. For this reason, FDTD simulations were used to optimise the parameters

for a nanocavity arrangement with a calculated resonance wavelength corresponding to the WZ band edge energy. The calculated V of this blueshifted resonance remained comparable to that of the previous arrangement (~$0.62(\lambda/n)^3$), though the Q-factor was considerably higher (~110000). Fabrication of the re-designed photonic crystal slot waveguide devices was undertaken using a similar process to that adopted previously. No suitable InP nanowires remained on the previously used sample after nanowire deposition, however, and so a new InP sample was grown with the sole aim of producing uniform arrays of nanowires with a single crystalline phase. Owing to a substantial increase in nanohole diameter after fabrication, average nanowire diameters were much larger than desired. Therefore, in an attempt to reduce nanowire diameter post-growth, cleaved sections of the nanowire sample were wet-etched in a concentrated HCl solution. PL measurements performed on a single cleaved section containing nanowires formed from nanoholes of the same diameter (with a fixed pitch) before and after post-growth HCl wet-etching, revealed that this process, although causing appreciable surface damage, did not adversely affect the optical emission properties of the nanowires. In both cases, the emission spectra collected from several locations on the cleaved section demonstrated that the nanowires were not composed of a single crystalline phase. However, unlike the previous sample used for nanocavity formation, ensemble nanowire emission was observed to occur predominately around the low-temperature WZ InP bandgap energy, with the peak centred around this energy dominating at higher excitation powers.

Although the growth conditions used for InP nanowires and subsequent HCl wet-etching procedure has the potential to provide nanowires with suitable structural and optical properties for the re-designed nanocavity arrangement presented here, experimental realisation of cavity enhanced nanowire PL emission is likely to still be very challenging. FDTD simulations performed during the optimisation of nanocavity device parameters showed that any mismatch between the nanowire diameter, d and photonic crystal slot width, w results in a significant reduction in the overlap of the cavity mode with the nanowire volume compared to that when $w{=}d$. In addition, when $w{>}d$ the Q-factor of the cavity mode decreases considerably if the nanowire is not located at the centre of the slot. Production of an experimental nanocavity

arrangement where $w{=}d$ is not feasible, and as observed in Figure 5.28(b), when $w{>}d$, it is more probable that the nanowire after placement is located against one of the sidewalls of the slot rather than at its centre. Experimental evidence of cavity formation, however, has been reported for a similar nanocavity device design (where $w{>}d$) optimised for resonance in the telecommunication wavelength band, and a cavity system such as this operating at sub-micron wavelengths provides the opportunity for future realisation of extremely high quality position-controlled nanowire-based light sources integrated with GaAs photonic circuitry on-chip.

Chapter 6

Conclusions and Outlook

In the following, the key results of Chapters 2-5 are summarised. An outlook giving directions for further progression in some of the research areas discussed in this thesis is then presented.

6.1 Summary of Chapters

This thesis has focused on the theoretical and experimental investigation of the optical and mechanical properties of III-V nanowire structures produced using a selective-area catalyst-free growth approach.

The material systems that were chosen for the study of these properties in this thesis were GaAs and InP. Firstly, the fabrication and growth of GaAs and InP nanowire arrays by selective-area metal-organic chemical vapour deposition was described. Two distinct growth regimes were observed for GaAs nanowires. Initially, when the planar growth in regions surrounding the SiO_2 growth mask was observed to have both a high growth rate and high surface roughness, nanowire heights were seen to vary across individual arrays, and the maximum nanowire heights were measured to be less than 300nm. Through modification of the pre-growth fabrication process, particularly the method by which cleaning of the wafer was performed, smooth planar growth with a much reduced planar growth rate was achieved, and

this resulted in much taller nanowires (~2µm) and a dramatic improvement in the height uniformity across the entire nanowire sample. Taking into consideration the observed influence of planar growth on GaAs nanowire formation, InP nanowire growth was undertaken on InP wafers fully covered by the SiO_2 growth mask (excluding the patterned nanohole growth sites). Control of nanowire radial growth rate was demonstrated through variation of the source material fluxes and the use of a higher growth temperature than that utilised for GaAs growth (680°C). Samples showed PL emission over a broad range of energies, indicating that the nanowires were polytypic in nature.

Through attempts to further develop this bottom-up growth technique, the ability to control the cross-section morphology of GaAs nanowires at the growth stage was achieved. It was shown initially that nanowires with elongated cross-section could be formed through fabrication of nanohole pairs in close proximity. An optically active InGaAs region formed within one of these elongated structures was shown to emit linearly polarised light when measured from the nanowire top facet, with a measured degree of polarisation (DOP) of ~60–75%. The direction of polarisation was observed to be coincident with the elongation axis of the nanowire cross-section. To provide more control over the final cross-section dimensions of the elongated nanowires, fabrication of elongated nanoholes (nanoslots), rather than closely spaced nanohole pairs, was performed prior to growth. PL collected from an InGaAs region formed within nanowires grown from these nanoslot sites demonstrated behaviour expected for emission from a nanowire quantum dot (NWQD), with the measured DOP of emission collected from the nanowire top-facet reaching over 90% for structures oriented in both the $[2\bar{1}1]$ and $[\bar{1}12]$ directions. 3D FDTD simulations showed that the DOP of NWQD emission from the nanowire top facet was largely independent of the NWQD location within the nanowire and remained above 90% over a broad wavelength range. This work represented the first demonstration of emission polarisation control in this manner using a catalyst-free growth approach and presents a promising route for the bottom-up growth of position-controlled linearly polarised single photon sources.

Using this same growth approach which provided a means to control nanowire morphology at the growth stage, the mechanical properties of catalyst-free GaAs nanowires with different cross-section aspect ratios were investigated. It was demonstrated that the ability to manipulate nanowire cross-section morphology allowed for control of the precise direction of motion of the non-degenerate orthogonal modes that exist for each nanowire flexural mechanical mode order. Nanowire motion was characterised using a free-space Michelson interferometer, and was observed to follow closely the behaviour described by Euler-Bernoulli theory for a singly clamped beam. The mechanical Q-factor of the fundamental flexural modes was seen to increase significantly when the temperature of the nanowire was reduced from RT to cryogenic temperatures, in agreement with previous reports in the literature. In an effort to observe non-linear nanowire oscillatory behaviour, the amplitude response of a resonantly driven fundamental flexural nanowire mode was investigated. However, owing to the large oscillatory amplitudes required for transition from the linear to non-linear regime for the fundamental modes, no evidence of non-linear behaviour was detected in this first instance. The control over the direction of motion of the nanowire flexural modes demonstrated in this work, combined with the array-scale uniformity that can also be achieved with the catalyst-free growth approach, offers potential for development of a highly sensitive multi-nanowire force transducer arrangement, collectively oscillating in the same orthogonal directions with well defined frequencies.

Attempts at controlling the optical properties of nanowire structures was also pursued through the theoretical and experimental study of a moveable nanowire-based nanocavity arrangement. The nanocavity arrangement consisted of an InP nanowire placed at the centre of a partially etched GaAs photonic crystal slot waveguide. Using a combination of frequency-domain and FDTD simulations, an optimised nanocavity design with a calculated cavity resonance of ~870nm and a Q factor and mode volume of ~76000 and ~$0.65(\lambda/n)^3$ (where n refers to the refractive index of InP), respectively was developed. This resonance wavelength was selected as it was thought to provide the best possibility of achieving cavity enhanced emission with nanowires from InP nanowire samples grown during this thesis.

Experimental nanocavity devices, based on the parameters of the optimised design, were produced through top-down fabrication of photonic crystal slot waveguide devices, transfer of a selection of the smallest diameter InP nanowires from the previously grown InP samples onto the fabricated device substrate, and subsequent nanomanipulation of a number of suitable nanowire candidates from this selection into the slot waveguide of nearby photonic crystal devices using an atomic force microscopy system. Both PL and reflectivity measurements were employed to characterise the experimental nanocavity devices. In each case, however, no evidence of cavity formation was observed. PL measurements also revealed that the emission from the majority of individual nanowires transferred to the device substrate occurred predominately around the wavelength corresponding the low-temperature InP WZ band edge energy ($\lambda \approx 833$nm). Although it was not considered to be the sole reason for the lack of evidence of cavity formation, it was posited that the substantial mismatch between the PL emission observed from individual nanowires and the designed cavity resonance would have significantly lowered the probability of observing cavity enhanced emission from the experimental devices. Therefore, FDTD simulations were once again utilised to design a modified nanocavity arrangement with a resonance wavelength corresponding to the InP WZ band edge energy. The calculated Q-factor of this blueshifted resonance was considerably higher than that of the previous design (~110000), while the mode volume remained comparatively similar ($\sim 0.62(\lambda/n)^3$). Fabrication of the re-designed photonic crystal slot waveguide devices was undertaken using a similar process to that adopted previously. Due to no suitable nanowires remaining on the sample previously used for nanowire transfer, a new InP sample was grown with the primary aim of forming uniform arrays of nanowires with a single crystalline phase. In an attempt to reduce nanowire diameter on this sample post-growth, a selection of nanowires were wet-etched in a concentrated HCl solution. PL measurements performed on these nanowires before and after post-growth HCl wet-etching, revealed that this process, although causing appreciable surface damage, did not adversely affect the optical emission properties of the nanowires. In both cases, the emission spectra demonstrated that the nanowires were not composed of a single crystalline phase. However, unlike the

previously grown InP nanowire samples, ensemble nanowire emission was observed to occur predominately around the low-temperature WZ InP bandgap energy, with the peak centred around this energy dominating at higher excitation powers.

Although the growth conditions used for InP nanowires on this sample and subsequent post-growth HCl wet-etching procedure showed promise in providing nanowires with suitable structural and optical properties for the re-designed nanocavity arrangement, experimental realisation of cavity enhanced nanowire PL emission with this nanowire-based cavity design is likely to still be a significant challenge due to its sensitivity to unavoidable fabrication imperfections, as demonstrated by FDTD simulations performed during optimisation of the nanocavity design. Experimental evidence of cavity formation, however, has been reported for a similar nanocavity device design optimised for resonance in the telecommunication wavelength band, and a cavity system such as this operating at sub-micron wavelengths provides the opportunity for future realisation of extremely high quality position-controlled nanowire-based light sources integrated with GaAs photonic circuitry on-chip.

6.2 Outlook

The developmental work presented in this thesis has opened up a number of different potential future research directions. Four of these are discussed briefly in the following sections.

6.2.1 Position-Controlled Linearly Polarised Single Photon Emitters

In Chapter 3, it was shown that the ability to tune nanowire morphology enabled polarisation control of the emission from a catalyst-free nanowire heterostructure. PL measurements on highly anisotropic nanowires grown from single elongated apertures (nanoslots) revealed that emission from the optically active InGaAs region within these structures exhibited QD-like behaviour. As discussed in Section 3.5.2 (and also in Ref [7]), this behaviour is thought to result from a reduction in indium incorporation from the centre to the edge of the nanowire during growth of the InGaAs region, leading to the formation of a NWQD of smaller radial extent compared to the surrounding waveguide. However, as the diameter of the embedded emitter is still dictated primarily by the dimensions of the nanowire in the catalyst-free growth scheme, further reduction of its radial dimension whilst also maintaining an appropriate waveguide cross-section for polarisation control at the desired wavelength is challenging.

One possible way of overcoming this limitation would be to initially grow a 'core' nanowire with smaller radial dimensions containing the embedded NWQD and then perform a subsequent radial overgrowth step to increase the dimensions of the surrounding waveguide to those required for polarisation control at the desired wavelength. A realistic minimum nanowire diameter that can be achieved with this growth approach is ~30nm, so forming a structure with a cross-section aspect ratio of 2:1 would require a nanoslot with dimensions of ~30x60nm. However, as shown schematically in Figure 6.1, if the radial growth rate is assumed to be equal on all side facets of the nanowire, increasing the largest dimension of the nanowire to ~200nm would lead to a minor axis length of ~170nm and a final aspect ratio of ~1.2:1. Referring

back to the modal analysis in Section 3.4, this cross-section would obviously not facilitate any kind of polarisation control of the emission. Recovering a similar level of polarisation control observed in the previous PL measurements would require an extension of the long axis dimension of the nanoslot to ~100nm (producing a resultant structure of ~130x200nm), leading to an undesirable increase in the overall radial extent of the embedded emitter.

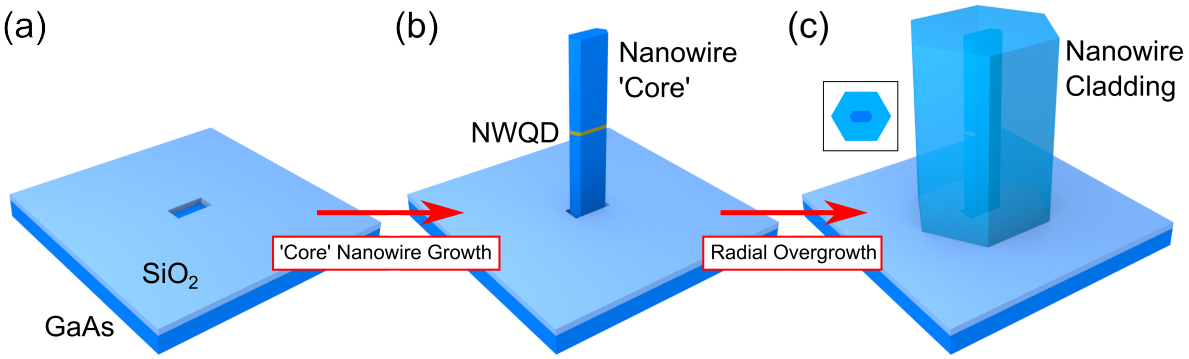

Figure 6.1: Schematic outline of elongated nanowire growth via a two-step catalyst-free growth process. (a) A nanoslot defining desired dimensions of NWQD (here 30x60nm) and final nanowire aspect ratio is patterned and etched into SiO_2 growth mask; (b) A 'core' nanowire containing a elongated NWQD is grown from the nanoslot site; (c) Radial overgrowth is performed to form an elongated nanowire containing an on-axis NWQD. However, assuming radial growth is isotropic, the final nanowire aspect ratio is only ~1.2:1 from the initial 'core' aspect ratio. Inset shows cross-section of final nanowire morphology.

An alternative way of overcoming this limitation would be to employ a combination of catalysed and catalyst-free growth. Although utilisation of a catalyst for nanowire growth risks contamination of the nanowire with some of the catalyst material, it also provides the most promising means by which the radial dimensions of the embedded NWQD can be decoupled from the parameters of the surrounding waveguide structure. This proposed growth approach is outlined schematically in Figure 6.2. A nanoslot is initially patterned into the SiO_2 growth mask with dimensions corresponding to the desired final cross-section of the resultant nanowire. A catalyst nanoparticle (e.g. Au) with radial dimensions of ~10–20nm is then deposited into the nanoslot. After catalyst deposition, growth of a nanowire 'core' can then proceed via the vapour-liquid-solid (VLS) growth mechanism, leading to the formation of a NWQD with the same radial dimensions as that of the catalyst nanoparticle. Through appropriate changing of the growth conditions, a transition from the VLS growth mechanism

to the catalyst-free growth mechanism can be achieved, facilitating the formation of a radial cladding around the 'core' nanowire. It is supposed that, with selection of the right catalyst-free growth conditions, the morphology of the cladding can be dictated by the patterned nanoslot dimensions, leading to the creation of a highly anisotropic nanowire containing a non-elongated and well-confined on-axis embedded NWQD.

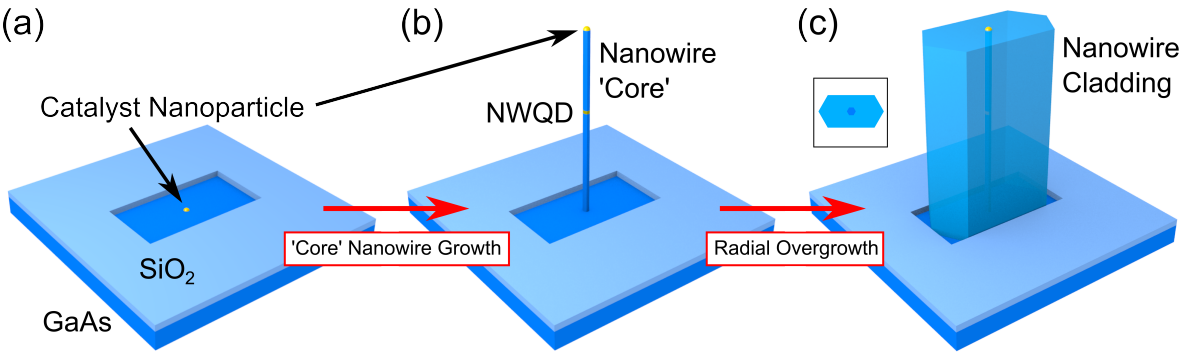

Figure 6.2: Schematic outline of elongated nanowire growth via combined VLS and catalyst-free growth. (a) A catalyst nanoparticle is located at the centre of a nanoslot patterned and etched into the SiO_2 growth mask, which defines desired dimensions of final nanowire structure; (b) A 'core' nanowire containing a NWQD is grown using VLS growth mechanism; (c) Transition to a catalyst-free growth mechanism promotes radial growth to form highly anisotropic nanowire structure containing an on-axis NWQD. Inset shows cross-section of final nanowire morphology.

As in standard catalyst deposition techniques catalyst nanoparticles are randomly deposited, one of the main challenges in the above process is the successful placement of the catalyst nanoparticle at the centre of the nanoslot (to ensure the subsequent NWQD is located on the axis of the final nanowire structure). Improved control over the location of this deposited catalyst nanoparticle may be achieved by initially patterning and etching a nanohole in the SiO_2 growth mask that defines the size and position of the catalyst, and then carrying out a further patterning and etching step to produce a nanoslot around the deposited catalyst nanoparticle that defines the geometry of the surrounding waveguide. A similar process of defining catalyst nanoparticle size and position, and subsequent combined VLS/selective-area growth (without elongation) has been reported elsewhere [5, 204].

6.2.2 A Coupled On-Chip Nanowire-Waveguide System

Owing to the vertical geometry of nanowire structures formed by bottom-up growth techniques, integration of NWQD emission with other photonic elements on-chip — a key requirement for scalable optical quantum information processing [81, 205, 206] — is challenging. Typically, this integration is achieved by transferring the vertically grown nanowires from the growth substrate to another 'device' substrate, where a photonic waveguide structure is subsequently fabricated around a selected nanowire that contains a NWQD with suitable optical properties [1, 154] Achieving strong overlap of the NWQD dipole moment with the fundamental modes of the photonic waveguide in this approach requires the use of intricate nanofabrication techniques, and as the transferred nanowire ensemble is randomly distributed on the device substrate, assembly of structures that are coupled to more than one emitter is not possible. Device processing after nanowire transfer may also adversely affect the optical properties of the selected NWQD, especially if etching is involved. The ability to successfully control nanowire morphology using the growth scheme presented in Chapter 3 offers a potential alternative approach for the coupling of emission from a NWQD in a vertical nanowire to a photonic waveguide structure on-chip. In this approach, waveguide structures are realised through elongated nanowires with extremely high cross-section aspect ratio. One of the main advantages of this approach is that waveguide structures and individual nanowires can be grown in the same growth run, foregoing the need for any additional fabrication steps after growth.

As a simple first demonstration of this new growth scheme, the feasibility of growing a single nanowire structure in close proximity to a highly anisotropic nanowire waveguide was investigated. A schematic overview of this growth arrangement is presented in Figure 6.3(a). The separation between a single circular nanohole and a highly anisotropic nanoslot, d is varied from 0nm upto 250nm. The patterned dimensions of the nanoslot were specified so as to form an elongated structure with a long dimension in the range 1000–2000nm and a cross-section aspect ratio range of 10–20:1 after growth. SEM images of the resulting structures formed

after growth are displayed in Figure 6.3(b) and Figure 6.3(c). The sample on which nanowire growth took place was the same as that referred to as Sample 2B in Chapter 2 (MR3540). It is observed from these images that an extremely anisotropic nanowire waveguide with approximately uniform structure consisting of six {110} facets was successfully formed from the nanoslot site, along with a single normal nanowire in close proximity. Edge-to-edge separations down to ~10nm were measured for this structural pair. Although there was some variation across the sample, the relative heights of the single nanowire and elongated waveguide were found to be approximately the same in most cases, with heights of ~330nm and ~210nm measured for the elongated structures displayed in Figure 6.3(b) (aspect ratio ~8:1) and Figure 6.3(c) (aspect ratio ~14:1), respectively. The variation in height between the two aspect ratios is thought to be a result of the increased lateral size of the nanowire formed from the more anisotropic nanoslot site during growth.

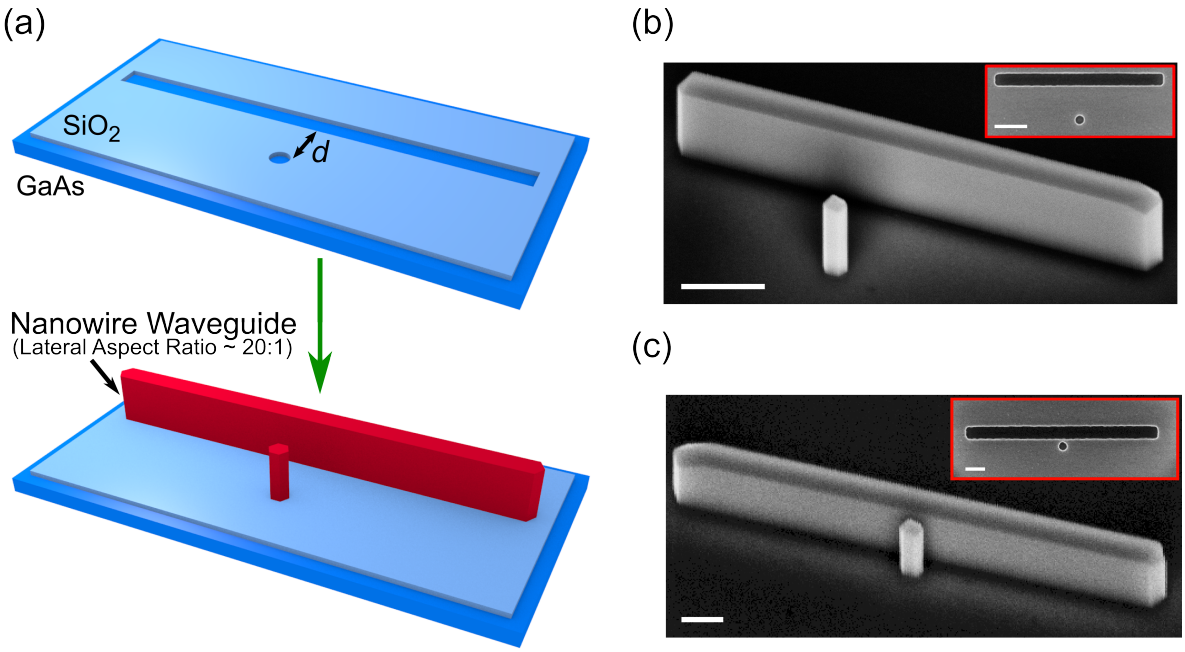

Figure 6.3: Towards integration of a vertically grown NWQD with waveguide circuitry on-chip. (a) Schematic diagram of a nanowire growth scheme where an elongated nanowire formed from a nanoslot with extremely high aspect ratio is grown in close proximity to a single hexagonal nanowire containing a NWQD; SEM images show, after growth, (b) a single nanowire and elongated structure with a cross-section aspect ratio of ~8:1, separated by d~200nm; (c) a single nanowire and elongated structure with a cross-section aspect ratio of ~14:1, separated by d~10nm. Insets in (b) and (c) display fabricated nanoapertures from which the resulting structures were formed. Scale bars 200nm.

As described in Chapter 2, planar growth in the regions of the substrate not covered by the SiO_2 mask was observed to be extremely rough for this sample. PL measurements performed on these structures revealed a lack of emission in the previously observed InGaAs wavelength range, implying that, perhaps as a consequence of this substrate roughness, proper formation of the heterostructure did not occur in these nanowires. Additional growth runs will therefore be required in the future so that the optical properties of the structural pair can be appropriately evaluated, but the experimental realisation of this system has the potential to be an important step towards the coupling of position-controlled single photon emitters and waveguide circuitry on a single photonic device.

6.2.3 Tuning Non-Linear Mechanical Mode Coupling of GaAs Nanowires Through Cross-Section Morphology Control

In Chapter 4, it was shown that the ability to tune the nanowire cross-section aspect ratio using the growth approach presented in Chapter 3 allowed for control of the mechanical properties of GaAs nanowires in the linear regime. Attempts at detecting non-linear nanowire oscillatory behaviour, however, were initially unsuccessful and it was not possible at the time to determine the influence of the cross-section aspect ratio on the non-linear mechanical properties of these structures.

Investigation of the mechanical properties of these nanowire structures continued within the LDSD group after the completion of my research, and non-linear nanowire oscillatory behaviour has now been demonstrated for both the fundamental ($f_1{}^{major}$ & $f_1{}^{minor}$) and second order ($f_2{}^{major}$ & $f_2{}^{minor}$) flexural nanowire modes. Figure 6.4 shows the nanowire amplitude response under swept excitation for the (a) $f_1{}^{major}$ and (b) $f_2{}^{minor}$ modes of a nanowire with a cross-section aspect ratio of 1.17 (same as that for NW-4A in Chapter 4). The 'shark fin' response observed at larger drive amplitudes is characteristic of a nonlinear oscillator [123].

Of particular interest was the demonstration of mechanical coupling between orthogonal flexural modes, whereby the frequency of one mode is dependent on the amplitude of other

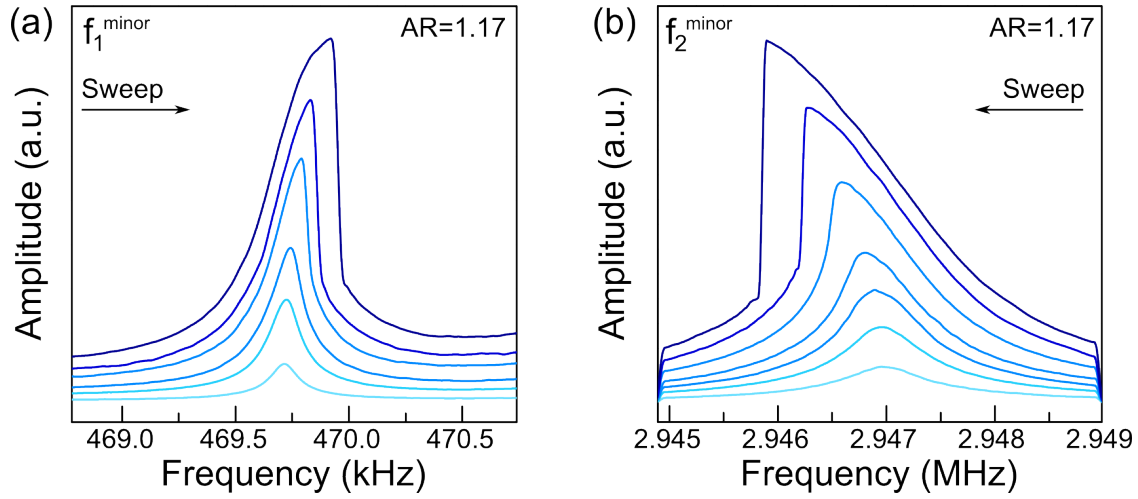

Figure 6.4: Nanowire response amplitude under swept excitation for the (a) fundamental flexural mode, $f_1{}^{minor}$ and (b) second order flexural mode, $f_2{}^{minor}$ of a nanowire with a cross-section aspect ratio of 1.17. The drive amplitude increases from the bottom trace (light blue) to the top trace (dark blue) in both cases.

(coupled) modes. Recent measurements showed that the sign of the frequency shift when driving one of the fundamental flexural modes and recording the frequency of the other flexural mode is dependent on the degree of anisotropy of the nanowire cross section. The ability to tune the nanowire cross-section aspect ratio therefore provides a new route to control the mode coupling in nano- and micro-cantilevers which is of particular interest for applications such as vectorial force sensing [13]. It has also been demonstrated that, independent of the aspect ratio of the nanowire cross section, the dependence of the frequency of one mode on the squared amplitude of the coupled mode becomes linear above a certain driving amplitude, which may be relevant for amplitude to frequency conversion applications.

The results discussed above were obtained from experiments undertaken by Dr. Andrew Foster and Joseph Maguire and were recently published in Nano Letters [126]. One future avenue of study being considered in this area is investigating how the surface and growth quality affects the non-linear oscillatory behaviour of the nanowires.

6.2.4 Experimental Realisation of a Position-Controlled High-Q Nanocavity Operating at Sub-Micron Wavelengths

In Chapter 5, experimental realisation of a nanowire-based cavity system which consisted of an InP nanowire placed in a partially etched GaAs photonic crystal slot waveguide was attempted. No evidence of cavity formation, however, was observed in either PL or reflectivity measurements performed on fabricated devices. In addition to the spectral mismatch between the PL emission observed from individual nanowires deposited on the device substrate and the target resonance wavelength of the optimised nanocavity design, the lack of evidence of cavity formation in this instance was attributed to the small number of fully assembled experimental device arrangements that were produced and also the sensitivity of the nanocavity design, demonstrated by FDTD simulations, to differences between the nanowire diameter d, and slot width w, and the position of the nanowire in the slot when $w>d$.

With the new photonic crystal device array design presented in Section 5.7.2, and the fact that the nanomanipulation technique described in Section 5.4.3 has now been established, the efficiency with which cavity arrangements are produced in future attempts should be significantly improved. Coupled with the demonstrated ability to reduce nanowire diameter after growth through HCl wet-etching with minimal impact on the nanowire emission properties, this improvement in the rate of production of cavity arrangements therefore increases the potential for realising an experimental device arrangement that exhibits evidence of cavity formation. To take full advantage of this design, however, nanowires containing well-confined NWQDs exhibiting high quality optical properties are desired. Owing to the difficulties in controlling the nanowire growth rate on full coverage substrates, as described in Chapter 2, attempts at incorporation of an InAsP NWQD in catalyst-free InP nanowires in the LDSD group have so far been unsuccessful. GaAs/InGaAs heterostructures may present a viable alternative, as highly uniform arrays of GaAs nanowires containing InGaAs NWQDs which exhibit evidence of photon antibunching have been demonstrated in this group [7] and FDTD simulations have shown that high-Q, low mode volume cavity resonances can be achieved over

the InGaAs NWQD emission wavelength range observed in Ref [7] and in Chapter 3 with a GaAs nanowire placed in a partially etched GaAs photonic crystal slot waveguide. Using InP as the host nanowire material though, offers the potential for development of NWQDs with superior optical properties relative to the GaAs materials system due to the low surface recombination velocity of InP nanowires [207] and the demonstrated ability to grow pure phase structures using the catalyst-free technique [28].

With this in mind, methods of controlling the growth rate of catalyst-free InP nanowires on full coverage substrates is the subject of ongoing study in the group. In addition to tailoring of the conditions and material flows used for nanowire growth, the improved capabilities of the newly installed electron-beam lithography system may provide another means of manipulating the nanowire growth rate. Sub-100nm diameter nanohole arrays on InP (111)A substrates spanning areas upto 500x500µm^2 with pitches down to 0.25µm have recently been achieved by the author with this system in time frames comparable to that for patterning of the InP nanowire arrays discussed in Chapter 2 using the old EBL system. Reducing InP nanowire growth rates could also be accomplished through growth on partially covered rather than full coverage substrates, but this is expected to consequently impact on the repeatability of nanowire growth between samples. While still at the early stages of research, combination of the nanocavity design described above and nanowires containing NWQDs in this materials system would provide the opportunity for creation of position-controlled quantum light sources of extremely high optical quality that could be potentially integrated with other on-chip GaAs photonic structures that have been developed in this group.

Bibliography

[1] H.-G. Park, C. J. Barrelet, Y. Wu, B. Tian, F. Qian, and C. M. Lieber, Nature Photonics **2**, 622 (2008).

[2] C. J. Barrelet, J. Bao, M. Lončar, H.-G. Park, F. Capasso, and C. M. Lieber, Nano Letters **6**, 11 (2005).

[3] M. D. Birowosuto, A. Yokoo, G. Zhang, K. Tateno, E. Kuramochi, H. Taniyama, M. Takiguchi, and M. Notomi, Nature materials **13**, 279 (2014).

[4] S. N. Dorenbos, H. Sasakura, M. P. Van Kouwen, N. Akopian, S. Adachi, N. Namekata, M. Jo, J. Motohisa, Y. Kobayashi, K. Tomioka, T. Fukui, S. Inoue, H. Kumano, C. M. Natarajan, R. H. Hadfield, T. Zijlstra, T. M. Klapwijk, V. Zwiller, and I. Suemune, Applied Physics Letters **97**, 13 (2010).

[5] D. Dalacu, K. Mnaymneh, J. Lapointe, X. Wu, P. J. Poole, G. Bulgarini, V. Zwiller, and M. E. Reimer, Nano Letters **12**, 5919 (2012).

[6] J. Tatebayashi, Y. Ota, S. Ishida, M. Nishioka, S. Iwamoto, and Y. Arakawa, Applied Physics Letters **100**, 1 (2012).

[7] M. N. Makhonin, A. P. Foster, A. B. Krysa, P. W. Fry, D. G. Davies, T. Grange, T. Walther, M. S. Skolnick, and L. R. Wilson, Nano letters **13**, 861 (2013).

[8] A. J. Shields, Nature Photonics **1**, 215 (2007).

[9] D. Loss and D. P. DiVincenzo, Physical Review A **57**, 12 (1998).

[10] A. Lundskog, C.-W. Hsu, K. Fredrik Karlsson, S. Amloy, D. Nilsson, U. Forsberg, P. Olof Holtz, and E. Janzén, Light: Science & Applications **3**, e139 (2014).

[11] H. M. Kim, Y. H. Cho, H. Lee, S. I. I. Kim, S. R. Ryu, D. Y. Kim, T. W. Kang, and K. S. Chung, Nano Letters **4**, 1059 (2004).

[12] C. Couteau, A. Larrue, C. Wilhelm, and C. Soci, Nanophotonics **4**, 90 (2015).

[13] N. Rossi, F. R. Braakman, D. Cadeddu, D. Vasyukov, G. Tütüncüoglu, A. Fontcuberta i Morral, and M. Poggio, Nature Nanotechnology [Online early access]. DOI: 10.1038/nnano.2016.189. Published Online: Oct 17, 2016. http://www.nature.com/nnano/journal/vaop/ncurrent/full/nnano.2016.189.html (accessed Dec 10, 2016).

[14] A. Gloppe, P. Verlot, E. Dupont-Ferrier, A. G. Kuhn, A. Siria, P. Poncharal, G. Bachelier, P. Vincent, and O. Arcizet, Nature Nanotechnology **9**, 920 (2014).

[15] Y. Cui, Q. Wei, H. Park, and C. Lieber, Science **293**, 1289 (2001).

[16] J. Hahm and C. M. Lieber, Nano Letters **4**, 51 (2004).

[17] K. Tomioka, M. Yoshimura, and T. Fukui, Nature **488**, 189 (2012).

[18] H. Kim, A. C. Farrell, P. Senanayake, W. J. Lee, and D. L. Huffaker, Nano Letters **16**, 1833 (2016).

[19] E. M. Clausen, H. G. Craighead, J. M. Worlock, J. P. Harbison, L. M. Schiavone, L. Florez, and B. Van der Gaag, Applied Physics Letters **55**, 1427 (1989).

[20] J. Yang, T. Ono, and M. Esashi, Applied Physics Letters **77**, 3860 (2000).

[21] K. A. Dick, K. Deppert, L. S. Karlsson, L. R. Wallenberg, L. Samuelson, and W. Seifert, Advanced Functional Materials **15**, 1603 (2005).

[22] J. E. Ayers, T. Kujofsa, P. Rago, and J. Raphael, *Heteroepitaxy of Semiconductors: Theory, Growth, and Characterization, Second Edition*, 2nd ed. (CRC Press, 2016).

[23] K. Ikejiri, T. Sato, H. Yoshida, K. Hiruma, J. Motohisa, S. Hara, and T. Fukui, Nanotechnology **19**, 265604 (2008).

[24] J. Motohisa, J. Noborisaka, J. Takeda, M. Inari, and T. Fukui, Journal of Crystal Growth **272**, 180 (2004).

[25] K. Hiruma, M. Yazawa, T. Katsuyama, K. Ogawa, K. Haraguchi, M. Koguchi, and H. Kakibayashi, Journal of Applied Physics **77**, 447 (1995).

[26] P. Kusch, *Band Gap and Symmetry of Wurtzite GaAs A Resonant Raman Study*, Ph.D. thesis, Freie Universität Berlin (2014).

[27] P. Mohan, J. Motohisa, and T. Fukui, Nanotechnology **16**, 2903 (2005).

[28] Y. Kitauchi, Y. Kobayashi, K. Tomioka, S. Hara, K. Hiruma, T. Fukui, and J. Motohisa, Nano letters **10**, 1699 (2010).

[29] P. Caroff, J. Bolinsson, and J. Johansson, IEEE Journal on Selected Topics in Quantum Electronics **17**, 829 (2011).

[30] N. Akopian, G. Patriarche, L. Liu, J.-C. Harmand, and V. Zwiller, Nano letters **10**, 1198 (2010).

[31] Y. Chen, T. Burgess, X. An, Y.-W. Mai, H. H. Tan, J. Zou, S. P. Ringer, C. Jagadish, and X. Liao, Nano letters **16**, 1911 (2016).

[32] S. Varoutsis, S. Laurent, I. Sagnes, A. Lemaître, L. Ferlazzo, C. Mériadec, G. Patriarche, I. Robert-Philip, and I. Abram, Journal of Vacuum Science & Technology B: Microelectronics and Nanometer Structures **23**, 2499 (2005).

[33] M. D. Henry, S. Walavalkar, A. Homyk, and A. Scherer, Nanotechnology **20**, 255305 (2009).

[34] R. S. Wagner and W. C. Ellis, Applied Physics Letters **4**, 89 (1964).

[35] N. Han, F. Wang, A. T. Hui, J. J. Hou, G. Shan, F. Xiu, T. Hung, and J. C. Ho, Nanotechnology **22**, 285607 (2011).

[36] S. Ambrosini, M. Fanetti, V. Grillo, A. Franciosi, and S. Rubini, AIP Advances **1**, 042142 (2011).

[37] M. Inari, J. Takeda, J. Motohisa, and T. Fukui, Physica E: Low-Dimensional Systems and Nanostructures **21**, 620 (2004).

[38] K. Tomioka, K. Ikejiri, T. Tanaka, J. Motohisa, S. Hara, K. Hiruma, and T. Fukui, Journal of Materials Research **26**, 2127 (2011).

[39] L. Dupré, D. Buttard, C. Leclere, H. Renevier, and P. Gentile, Chemistry of Materials **24**, 4511 (2012).

[40] D. E. Perea, J. E. Allen, S. J. May, B. W. Wessels, D. N. Seidman, and L. J. Lauhon, Nano Letters **6**, 181 (2006).

[41] N. Li, T. Y. Tan, and U. Gösele, Applied Physics A: Materials Science and Processing **90**, 591 (2008).

[42] K. A. Dick, J. Bolinsson, B. M. Borg, and J. Johansson, Nano Letters **12**, 3200 (2012).

[43] J. N. Shapiro, A. Lin, P. S. Wong, A. C. Scofield, C. Tu, P. N. Senanayake, G. Mariani, B. L. Liang, and D. L. Huffaker, Applied Physics Letters **97**, 1 (2010).

[44] S. Fujisawa, T. Sato, S. Hara, J. Motohisa, K. Hiruma, and T. Fukui, Japanese Journal of Applied Physics **50**, 04DH03 (2011).

[45] J. Tatebayashi, Y. Ota, S. Ishida, M. Nishioka, S. Iwamoto, and Y. Arakawa, Applied Physics Letters **105**, 103104 (2015).

[46] J. Noborisaka, J. Motohisa, S. Hara, and T. Fukui, Applied Physics Letters **87**, 093109 (2005).

[47] P. Mohan, J. Motohisa, and T. Fukui, Applied Physics Letters **88**, 1 (2006).

[48] Q. Gao, D. Saxena, F. Wang, L. Fu, S. Mokkapati, Y. Guo, L. Li, J. Wong-Leung, P. Caroff, H. H. Tan, and C. Jagadish, Nano Letters **14**, 5206 (2014).

[49] H. Kim, W.-J. Lee, A. C. Farrell, P. Senanayake, and D. L. Huffaker, arXiv , 1701.02763 (2017).

[50] E. D. Minot, F. Kelkensberg, M. Van Kouwen, J. A. Van Dam, L. P. Kouwenhoven, V. Zwiller, M. T. Borgström, O. Wunnicke, M. A. Verheijen, and E. P. A. M. Bakkers, Nano Letters **7**, 367 (2007).

[51] M. J. Holmes, K. Choi, S. Kako, M. Arita, and Y. Arakawa, Nano Letters **14**, 982 (2014).

[52] K. Tomioka, Y. Kobayashi, J. Motohisa, S. Hara, and T. Fukui, Nanotechnology **20**, 145302 (2009).

[53] M. T. Björk, H. Schmid, C. M. Breslin, L. Gignac, and H. Riel, Journal of Crystal Growth **344**, 31 (2012).

[54] P. D. Kanungo, H. Schmid, M. T. Björk, L. M. Gignac, C. Breslin, J. Bruley, C. D. Bessire, and H. Riel, Nanotechnology **24**, 225304 (2013).

[55] A. P. Foster, *Theoretical and Experimental Investigation of III-V Semiconductor Nanowire Heterostructures*, Ph.D. thesis, University of Sheffield (2013).

[56] S. Ando and T. Fukui, Journal of Crystal Growth **98**, 646 (1989).

[57] S. Ando, S. S. Chang, and T. Fukui, Journal of Crystal Growth **115**, 69 (1991).

[58] S. Ando, Journal of Crystal Growth **145**, 302 (1994).

[59] K. Ikejiri, J. Noborisaka, S. Hara, J. Motohisa, and T. Fukui, Journal of Crystal Growth **298**, 616 (2007).

[60] R. Dobrushin, R. Kotecký, and S. Sholsman, *Wulff Construction: A Global Shape from Local Interactions* (American Mathematical Society, 1992).

[61] H. J. Joyce, Q. Gao, H. Hoe Tan, C. Jagadish, Y. Kim, J. Zou, L. M. Smith, H. E. Jackson, J. M. Yarrison-Rice, P. Parkinson, and M. B. Johnston, Progress in Quantum Electronics **35**, 23 (2011).

[62] H. Asai, Journal of Crystal Growth **80**, 425 (1987).

[63] D. Biegelsen, R. Bringans, J. Northrup, and L.-E. Swartz, Physical Review Letters **65**, 452 (1990).

[64] P. J. Harshman and S. Wang, Journal of Applied Physics **71**, 5531 (1992).

[65] J. Noborisaka, J. Motohisa, and T. Fukui, Applied Physics Letters **86**, 213102 (2005).

[66] D. H. Reep and S. Ghandhi, Journal of The Electrochemical Society **130**, 675 (1983).

[67] T. Sato, J. Motohisa, J. Noborisaka, S. Hara, and T. Fukui, Journal of Crystal Growth **310**, 2359 (2008).

[68] S. Hertenberger, D. Rudolph, M. Bichler, J. J. Finley, G. Abstreiter, and G. Koblmüller, Journal of Applied Physics **108**, 114316 (2010).

[69] K. Tomioka, P. Mohan, J. Noborisaka, S. Hara, J. Motohisa, and T. Fukui, Journal of Crystal Growth **298**, 644 (2007).

[70] A. Li, J. Zou, and X. Han, Science China Materials **59**, 51 (2016).

[71] K. Kumakura, K. Nakakoshi, M. Kishida, J. Motohisa, T. Fukui, and H. Hasegawa, Journal of Crystal Growth **145**, 308 (1994).

[72] K. Hiruma, K. Tomioka, P. Mohan, L. Yang, J. Noborisaka, B. Hua, A. Hayashida, S. Fujisawa, S. Hara, J. Motohisa, and T. Fukui, Journal of Nanotechnology **2012**, 169284 (2012).

[73] K. Tomioka, J. Motohisa, S. Hara, and T. Fukui, Nano letters **8**, 3475 (2008).

[74] O. D. D. Couto, D. Sercombe, J. Puebla, L. Otubo, I. J. Luxmoore, M. Sich, T. J. Elliott, E. A. Chekhovich, L. R. Wilson, M. S. Skolnick, H. Y. Liu, and A. I. Tartakovskii, Nano Letters **12**, 5269 (2012).

[75] Y. Calahorra, Y. Greenberg, S. Cohen, and D. Ritter, Nanotechnology **23**, 245603 (2012).

[76] J. M. Jancu, K. Gauthron, L. Largeau, G. Patriarche, J. C. Harmand, and P. Voisin, Applied Physics Letters **97**, 041910 (2010).

[77] M. Bouwes Bavinck, K. D. Jöns, M. Zieliński, G. Patriarche, J.-C. Harmand, N. Akopian, and V. Zwiller, Nano Letters **16**, 1081 (2016).

[78] A. Casadei, E. A. Llado, F. Amaduzzi, E. Russo-Averchi, D. Rüffer, M. Heiss, L. D. Negro, L. Dal Negro, and A. Fontcuberta i Morral, Scientific Reports **5**, 7651 (2015).

[79] R. Röder, D. Ploss, A. Kriesch, R. Buschlinger, S. Geburt, U. Peschel, and C. Ronning, Journal of Physics D: Applied Physics **47**, 394012 (2014).

[80] G. Bulgarini, M. E. Reimer, M. Bouwes Bavinck, K. D. Jöns, D. Dalacu, P. J. Poole, E. P. A. M. Bakkers, and V. Zwiller, Nano Letters **14**, 4102 (2014).

[81] E. Knill, R. Laflamme, and G. J. Milburn, Nature **409**, 46 (2001).

[82] R. N. Patel, T. Schröder, N. Wan, L. Li, S. L. Mouradian, E. H. Chen, and D. R. Englund, Light: Science & Applications **5**, e16032 (2016).

[83] M. Munsch, J. Claudon, J. Bleuse, N. S. Malik, E. Dupuy, J.-M. Gérard, Y. Chen, N. Gregersen, and J. Mørk, Physical Review Letters **108**, 1 (2012).

[84] I. Stranski and L. Krastanow, Akademie der Wissenschaften Wien **146**, 797 (1958).

[85] M. Bayer and A. Forchel, Physical Review B **65**, 041308 (2002).

[86] C. Santori, M. Pelton, G. Solomon, Y. Dale, and Y. Yamamoto, Physical Review Letters **86**, 1502 (2001).

[87] R. M. Stevenson, R. J. Young, P. Atkinson, K. Cooper, D. A. Ritchie, and A. J. Shields, Nature **439**, 179 (2006).

[88] N. Akopian, N. H. Lindner, E. Poem, Y. Berlatzky, J. Avron, D. Gershoni, B. D. Gerardot, and P. M. Petroff, Physical Review Letters **96**, 7 (2006).

[89] T. Yoshie, A. Scherer, J. Hendrickson, G. Khitrova, H. M. Gibbs, G. Rupper, C. Ell, O. B. Shchekin, and D. G. Deppe, Nature **432**, 9 (2004).

[90] M. Heiss, Y. Fontana, A. Gustafsson, G. Wust, C. Magen, D. D. O'Regan, J. W. Luo, B. Ketterer, S. Conesa-Boj, A. V. Kuhlmann, J. Houel, E. Russo-Averchi, J. R. Morante, M. Cantoni, N. Marzari, J. Arbiol, A. Zunger, R. J. Warburton, and A. Fontcuberta i Morral, Nature Materials **12**, 439 (2013).

[91] Z. Yan, X. Zhang, X. Ren, X. Lv, J. Li, Q. Wang, S. Cai, and Y. Huang, Nano letters **12**, 1851 (2012).

[92] C. S. S. R. Kumar, *Semiconductor Nanomaterials*, Nanomaterials for Life Sciences (John Wiley & Sons, 2010).

[93] R. Singh and G. Bester, Physical Review Letters **103**, 1 (2009).

[94] N. Panev, A. I. Persson, N. Sköld, and L. Samuelson, Applied Physics Letters **83**, 2238 (2003).

[95] M. T. Borgström, V. Zwiller, E. Müller, and A. Imamoglu, Nano Letters **5**, 1439 (2005).

[96] J. Renard, R. Songmuang, G. Tourbot, C. Bougerol, B. Daudin, and B. Gayral, Physical Review B **80**, 2 (2009).

[97] M. H. Bouwes Bavnick, *Engineering The Optical Properties Of Nanowire Quantum Dots*, Ph.D. thesis, Delft University of Technology (2016).

[98] M. E. Reimer, G. Bulgarini, N. Akopian, M. Hocevar, M. B. Bavinck, M. A. Verheijen, E. P. A. M. Bakkers, L. P. Kouwenhoven, and V. Zwiller, Nature Communications **3**, 737 (2012).

[99] I. Friedler, C. Sauvan, J. P. Hugonin, P. Lalanne, J. Claudon, and J.-M. Gérard, Optics express **17**, 2095 (2009).

[100] J. Bleuse, J. Claudon, M. Creasey, N. S. Malik, J.-M. Gérard, I. Maksymov, J.-P. Hugonin, and P. Lalanne, Physical Review Letters **106**, 103601 (2011).

[101] J. Claudon, J. Bleuse, N. S. Malik, M. Bazin, P. Jaffrennou, N. Gregersen, C. Sauvan, P. Lalanne, and J.-M. Gérard, Nature Photonics **4**, 174 (2010).

[102] G. Bulgarini, M. E. Reimer, T. Zehender, M. Hocevar, E. P. A. M. Bakkers, L. P. Kouwenhoven, and V. Zwiller, Applied Physics Letters **100**, 121106 (2012).

[103] T. Jemsson, H. Machhadani, K. F. Karlsson, C. W. Hsu, and P. O. Holtz, Applied Physics Letters **105** (2014).

[104] N. Gisin, G. Ribordy, W. Tittel, and H. Zbinden, Reviews of Modern Physics **74**, 145 (2002).

[105] T. J. Pfau, A. Gushterov, J. P. Reithmaier, I. Cestier, G. Eisenstein, E. Linder, and D. Gershoni, Applied Physics Letters **95**, 243106 (2009).

[106] A. P. Foster, J. P. Bradley, K. Gardner, A. B. Krysa, B. Royall, M. S. Skolnick, and L. R. Wilson, Nano Letters **15**, 1559 (2015).

[107] M. H. M. van Weert, N. Akopian, F. Kelkensberg, U. Perinetti, M. P. van Kouwen, J. G. Rivas, M. T. Borgström, R. E. Algra, M. A. Verheijen, E. P. A. M. Bakkers, L. P. Kouwenhoven, and V. Zwiller, Small **5**, 2134 (2009).

[108] J. D. Joannopoulos, S. G. Johnson, J. N. Winn, and R. D. Meade, *Photonic Crystals - Molding the Flow of Light* (Princeton University Press, 2007).

[109] S. Johnson and J. Joannopoulos, Optics Express **8**, 173 (2001).

[110] H. J. Kimble, Nature **453**, 1023 (2008).

[111] A. Kuhn, "Cavity Induced Interfacing of Atoms and Light," in *Engineering the Atom-Photon Interaction*, edited by A. Predojević and W. M. Mitchell (Springer International Publishing, 2015) pp. 3–38.

[112] D. K. Armani, T. J. Kippenberg, S. M. Spillane, and K. J. Vahala, Nature **421**, 925 (2003).

[113] E. Moreau, I. Robert, J.-M. Gérard, I. Abram, L. Manin, and V. Thierry-Mieg, Applied Physics Letters **79**, 2865 (2001).

[114] A. Dousse, J. Suffczyński, R. Braive, A. Miard, A. Lemàtre, I. Sagnes, L. Lanco, J. Bloch, P. Voisin, and P. Senellart, Applied Physics Letters **94**, 12 (2009).

[115] J. Yuan, H. Wang, R. P. J. Van Veldhoven, J. Wang, T. De Vries, B. Smalbrugge, C. Y. Jin, P. Nouwens, E. J. Geluk, A. Y. Silov, and R. Nötzel, Applied Physics Letters **98**, 15 (2011).

[116] Lumerical Solutions Inc., "FDTD Solutions," (2015).

[117] X. L. Feng, R. He, P. Yang, and M. L. Roukes, Nano Letters **7**, 1953 (2007).

[118] J. M. Nichol, R. Budakian, E. R. Hemesath, and L. J. Lauhon, Applied Physics Letters **93**, 193110 (2008).

[119] J. H. Ko, J. Jeong, J. Choi, and M. Cho, Applied Physics Letters **98**, 1 (2011).

[120] K. L. Ekinci and M. L. Roukes, Review of Scientific Instruments **76**, 061101 (2005).

[121] S. Rast, C. Wattinger, U. Gysin, and E. Meyer, Nanotechnology **11**, 169 (2000).

[122] E. Gil-Santos, D. Ramos, J. Martínez, M. Fernández-Regúlez, R. García, A. San Paulo, M. Calleja, and J. Tamayo, Nature nanotechnology **5**, 641 (2010).

[123] F. R. Braakman, D. Cadeddu, G. Tütüncüoglu, F. Matteini, D. Rüffer, A. Fontcuberta i Morral, and M. Poggio, Applied Physics Letters **105**, 1 (2014).

[124] D. Cadeddu, F. R. Braakman, G. Tütüncüoglu, F. Matteini, D. Rüffer, A. Fontcuberta i Morral, and M. Poggio, Nano Letters **16**, 926 (2016).

[125] M. Montinaro, G. Wüst, M. Munsch, Y. Fontana, E. Russo-Averchi, M. Heiss, A. Fontcuberta i Morral, R. J. Warburton, and M. Poggio, Nano Letters **14**, 4454 (2014).

[126] A. P. Foster, J. K. Maguire, J. P. Bradley, T. P. Lyons, A. B. Krysa, A. M. Fox, M. S. Skolnick, and L. R. Wilson, Nano Letters **16**, 7414 (2016).

[127] A. N. Rasmussen, *Optomechanics with Semiconductor Nanomembranes*, Ph.D. thesis, University of Copenhagen (2013).

[128] W. Hallstrom, M. Lexholm, D. B. Suyatin, G. Hammarin, D. Hessman, L. Samuelson, L. Montelius, M. Kanje, and C. N. Prinz, Nano Letters **10**, 782 (2010).

[129] J. M. Nichol, E. R. Hemesath, L. J. Lauhon, and R. Budakian, Applied Physics Letters **95**, 123116 (2009).

[130] O. A. Bauchau and J. I. Craig, "Euler-Bernoulli beam theory," in *Structural Analysis*, edited by O. A. Bauchau and J. I. Craig (Springer Netherlands, Dordrecht, 2009).

[131] Y. Jiang, T. Ono, and M. Esashi, Journal of Micromechanics and Microengineering **19**, 065030 (2009).

[132] K. Y. Yasumura, T. D. Stowe, E. M. Chow, T. Pfafman, T. W. Kenny, B. C. Stipe, and D. Rugar, Journal of Microelectromechanical Systems **9**, 117 (2000).

[133] H. Okamoto, D. Ito, K. Onomitsu, and H. Yamaguchi, Physica Status Solidi (C) **5**, 2920 (2008).

[134] R. Lifshitz and M. L. Roukes, Physical Review B **61**, 10 (1999).

[135] U. Gysin, S. Rast, P. Ruff, E. Meyer, D. Lee, P. Vettiger, and C. Gerber, Physical Review B **69**, 1 (2004).

[136] R. Sandberg, W. Svendsen, K. Mølhave, and A. Boisen, Journal of Micromechanics and Microengineering **15**, 1454 (2005).

[137] E. J. Boyd, L. Li, R. Blue, and D. Uttamchandani, Sensors and Actuators A: Physical **198**, 75 (2013).

[138] D. Rugar and P. Grütter, Physical Review Letters **67**, 699 (1991).

[139] R. Almog, S. Zaitsev, O. Shtempluck, and E. Buks, Applied Physics Letters **88**, 27 (2006).

[140] A. Erbe, H. Krömmer, A. Kraus, R. H. Blick, G. Corso, and K. Richter, Applied Physics Letters **77**, 3102 (2000).

[141] R. Almog, S. Zaitsev, O. Shtempluck, and E. Buks, Physical Review Letters **98**, 1 (2007).

[142] S. Schmid, L. G. Villanueva, and M. L. Roukes, "Resonance Frequency," in *Fundamentals of Nanomechanical Resonators* (Springer International Publishing, Cham, 2016).

[143] C. Bentham, I. E. Itskevich, R. J. Coles, B. Royall, E. Clarke, J. O'Hara, N. Prtljaga, A. M. Fox, M. S. Skolnick, and L. R. Wilson, Applied Physics Letters **106**, 221101 (2015).

[144] A. Tandaechanurat, S. Iwamoto, M. Nomura, N. Kumagai, and Y. Arakawa, Optics Express **16**, 448 (2008).

[145] Y. Akahane, T. Asano, B.-S. Song, and S. Noda, Nature **425**, 944 (2003).

[146] M. Danang Birowosuto, A. Yokoo, H. Taniyama, E. Kuramochi, M. Takiguchi, and M. Notomi, Journal of Applied Physics **112**, 113106 (2012).

[147] A. Larrue, C. Wilhelm, G. Vest, S. Combrié, A. de Rossi, and C. Soci, Optics Express **20**, 7758 (2012).

[148] J.-M. Lourtioz, H. Benisty, V. Berger, J.-M. Gérard, D. Maystre, and A. Tchelnokov, *Photonic Crystals: Towards Nanoscale Photonic Devices*, 2nd ed. (Springer-Verlag Berlin Heidelberg, 2003).

[149] A. Faraon, A. Majumdar, D. Englund, E. Kim, M. Bajcsy, and J. Vučković, New Journal of Physics **13**, 055025 (2011).

[150] W. H. Chang, W. Y. Chen, H. S. Chang, T. P. Hsieh, J. I. Chyi, and T. M. Hsu, Physical Review Letters **96**, 3 (2006).

[151] M. Notomi, A. Shinya, S. Mitsugi, E. Kuramochi, and H. Ryu, Optics Express **12**, 1551 (2004).

[152] R. Chen, T. Tran, K. Ng, and W. Ko, Nature Photonics **5** (2011).

[153] H. Sun, F. Ren, K. W. Ng, T. T. D. Tran, K. Li, and C. J. Chang-Hasnain, ACS Nano **8**, 6833 (2014).

[154] I. Esmaeilzadeh, A. W. Elshaari, K. D. Jöns, A. Fognini, D. Dalacu, P. J. Poole, M. E. Reimer, and V. Zwiller, Nano Letters **16**, 2289 (2016).

[155] H. G. Park, F. Qian, C. J. Barrelet, and Y. Li, Applied Physics Letters **91**, 2005 (2007).

[156] B. Mayer, L. Janker, B. Loitsch, J. Treu, T. Kostenbader, S. Lichtmannecker, T. Reichert, S. Morkötter, M. Kaniber, G. Abstreiter, C. Gies, G. Koblmüller, and J. J. Finley, Nano Letters (2015).

[157] Y. S. Choi, M. T. Rakher, K. Hennessy, S. Strauf, A. Badolato, P. M. Petroff, D. Bouwmeester, and E. L. Hu, Applied Physics Letters **91**, 2007 (2007).

[158] A. R. A. Chalcraft, S. Lam, D. O'Brien, T. F. Krauss, M. Sahin, D. Szymanski, D. Sanvitto, R. Oulton, M. S. Skolnick, A. M. Fox, D. M. Whittaker, H. Y. Liu, and M. Hopkinson, Applied Physics Letters **90**, 13 (2007).

[159] W. Fan, Z. Hao, E. Stock, J. Kang, Y. Luo, and D. Bimberg, Semiconductor Science and Technology **26**, 014014 (2010).

[160] C. Sauvan, P. Lalanne, and J. P. Hugonin, Physical Review B **71**, 1 (2005).

[161] A. F. Oskooi, D. Roundy, M. Ibanescu, P. Bermel, J. D. Joannopoulos, and S. G. Johnson, Computer Physics Communications **181**, 687 (2010).

[162] S. Hara, S. Sakita, and M. Yatago, Japanese Journal of Applied Physics **51**, 1 (2012).

[163] K. Kato, Y. Hasumi, A. Kozen, and J. Temmyo, Journal of Applied Physics **65**, 1947 (1989).

[164] D. A. Woolf, D. I. Westwood, and R. H. Williams, Semiconductor Science and Technology **8**, 1075 (1999).

[165] J. Heo, W. Guo, and P. Bhattacharya, Applied Physics Letters **98**, 2011 (2011).

[166] A. Das, J. Heo, M. Jankowski, W. Guo, L. Zhang, H. Deng, and P. Bhattacharya, Physical Review Letters **107**, 1 (2011).

[167] A. Yokoo, T. Tanabe, E. Kuramochi, and M. Notomi, Nano Letters **11**, 3634 (2011).

[168] F. Intonti, S. Vignolini, V. Türck, M. Colocci, P. Bettotti, L. Pavesi, S. L. Schweizer, R. Wehrspohn, and D. Wiersma, Applied Physics Letters **89**, 10 (2006).

[169] F. Intonti, S. Vignolini, F. Riboli, M. Zani, D. S. Wiersma, L. Balet, L. H. Li, M. Francardi, A. Gerardino, A. Fiore, and M. Gurioli, Applied Physics Letters **95**, 2007 (2009).

[170] M. Notomi, K. Yamada, A. Shinya, J. Takahashi, C. Takahashi, and I. Yokohama, Physical Review Letters **87**, 1 (2001).

[171] A. Di Falco, L. O'Faolain, and T. Krauss, Photonics and Nanostructures - Fundamentals and Applications **6**, 38 (2008).

[172] S. Jeon, B.-S. Song, S. Yamada, Y. Yamaguchi, J. Upham, T. Asano, and S. Noda, Optics Express **23**, 4523 (2015).

[173] M. Notomi, Reports on Progress in Physics **73**, 96501 (2010).

[174] M. Notomi and H. Taniyama, Optics Express **16**, 18657 (2008).

[175] M. W. Lee, C. Grillet, S. Tomljenovic-Hanic, E. C. Mägi, D. J. Moss, B. J. Eggleton, X. Gai, S. Madden, D.-Y. Choi, D. A. P. Bulla, and B. Luther-Davies, Optics Letters **34**, 3671 (2009).

[176] B.-S. Song, S. Noda, T. Asano, and Y. Akahane, Nature materials **4**, 207 (2005).

[177] S. Tomljenovic-Hanic, M. J. Steel, C. Martijn de Sterke, and D. J. Moss, Optics Letters **32**, 542 (2007).

[178] A. M. Fox, *Optical Properties of Solids*, 2nd ed. (Oxford University Press, 2010).

[179] N. Prtljaga, R. J. Coles, J. O'Hara, B. Royall, E. Clarke, A. M. Fox, and M. S. Skolnick, Applied Physics Letters **104**, 2014 (2014).

[180] J. Vučković, M. Lončar, H. Mabuchi, and A. Scherer, Physical Review E **65**, 1 (2002).

[181] T. Yamamoto, M. Notomi, H. Taniyama, E. Kuramochi, Y. Yoshikawa, Y. Torii, and T. Kuga, Optics Express **16**, 13809 (2008).

[182] N. Tajik, Z. Peng, P. Kuyanov, and R. R. LaPierre, Nanotechnology **22**, 225402 (2011).

[183] Bruker AFM Probes, "Olympus AC160TS-R3 AFM Tip," `http://www.brukerafmprobes.com/p-3864-otespa-r3.aspx` (2016).

[184] A. Schirmeisen, B. Anczykowski, H. Hölscher, and H. Fuchs, *Springer Handbook of Nanotechnology*, 2nd ed. (Springer-Verlag Berlin Heidelberg, 2010).

[185] B. Voigtländer, *Scanning Probe Microscopy: Atomic Force Microscopy and Scanning Tunneling Microscopy*, 1st ed. (Springer-Verlag Berlin Heidelberg, 2015).

[186] R. García, Surface Science Reports **47**, 197 (2002).

[187] B. Mayer, D. Rudolph, J. Schnell, S. Morkötter, J. Winnerl, J. Treu, K. Müller, G. Bracher, G. Abstreiter, G. Koblmüller, and J. J. Finley, Nature Communications **4**, 2931 (2013).

[188] L. Sapienza, H. Thyrrestrup, S. Stobbe, P. D. Garcia, S. Smolka, and P. Lodahl, Science **327**, 1352 (2010).

[189] R. Faggiani, A. Baron, X. Zang, L. Lalouat, S. A. Schulz, B. O'Regan, K. Vynck, B. Cluzel, F. de Fornel, T. F. Krauss, and P. Lalanne, Scientific Reports **6**, 27037 (2016).

[190] W. C. Stumpf, T. Asano, T. Kojima, M. Fujita, Y. Tanaka, and S. Noda, Physical Review B **82**, 75119 (2010).

[191] Y. Nazirizadeh, J. Müller, U. Geyer, D. Schelle, E.-B. Kley, A. Tünnermann, U. Lemmer, and M. Gerken, Optics Express **16**, 7153 (2008).

[192] R. Bose, T. Cai, K. Choudhury, G. Solomon, and E. Waks, Nature Photonics **8**, 858 (2014).

[193] K. Müller, K. A. Fischer, A. Rundquist, C. Dory, K. G. Lagoudakis, T. Sarmiento, Y. A. Kelaita, V. Borish, and J. Vučković, Physical Review X **5**, 1 (2015).

[194] Origin Lab, "Breit-Wigner-Fano Line Shape Documentation," `http://www.originlab.com/doc/Origin-Help/BWF-PAFunc` (2016).

[195] P. T. Valentim, J. P. Vasco, I. J. Luxmoore, D. Szymanski, H. Vinck-Posada, A. M. Fox, D. M. Whittaker, M. S. Skolnick, and P. S. S. Guimarães, Applied Physics Letters **102**, 111112 (2013).

[196] J. P. Vasco, H. Vinck-Posada, P. T. Valentim, and P. S. S. Guimãraes, Optics express **21**, 31336 (2013).

[197] V. Zwiller, N. Akopian, M. van Weert, M. van Kouwen, U. Perinetti, L. Kouwenhoven, R. Algra, J. Gómez Rivas, E. Bakkers, G. Patriarche, L. Liu, J. C. Harmand, Y. Kobayashi, and J. Motohisa, Comptes Rendus Physique **9**, 804 (2008).

[198] P. H. L. Notten, Journal of The Electrochemical Society **131**, 2641 (1983).

[199] F. Pearton, S. J. Abernathy, C. R. Ren, "Wet and Dry Etching of III-V Semiconductors," in *Topics in Growth and Device Processing of III-V Semiconductors* (World Scientific, 1996).

[200] C. J. Novotny, *A Study of InP Nanowires: Growth, Material Properties, and Application in Optoelectronics*, Ph.D. thesis, UC San Diego (2007).

[201] Institution of Electrical Engineers, *Properties, processing and applications of indium phosphide*, edited by T. P. Pearsall (Institution of Electrical Engineers, 2000).

[202] B. Tuck and A. J. Baker, Journal of Materials Science **8**, 1559 (1973).

[203] T. J. Pfau, A. Gushterov, J. P. Reithmaier, I. Cestier, G. Eisenstein, E. Linder, and D. Gershoni, Applied Physics Letters **95**, 93 (2009).

[204] D. Dalacu, K. Mnaymneh, X. Wu, J. Lapointe, G. C. Aers, P. J. Poole, and R. L. Williams, Applied Physics Letters **98**, 251101 (2011).

[205] P. Kok, W. J. Munro, K. Nemoto, T. C. Ralph, J. P. Dowling, and G. J. Milburn, Reviews of Modern Physics **79**, 135 (2007).

[206] J. L. O'Brien, A. Furusawa, and J. Vuckovic, Nature Photonics **3**, 687 (2009).

[207] H. J. Joyce, J. Wong-Leung, C. K. Yong, C. J. Docherty, S. Paiman, Q. Gao, H. H. Tan, C. Jagadish, J. Lloyd-Hughes, L. M. Herz, and M. B. Johnston, Nano Letters **12**, 5325 (2012).